Atomically dispersed iridium electrocatalysts for the oxygen evolution reaction



Po-Yuan Huang

St Edmund Hall

University of Oxford

A thesis submitted for the degree of

Doctor of Philosophy

Trinity 2024

Abstract

Proton-exchange membrane (PEM) water electrolysers can efficiently integrate with renewable energy sources for green hydrogen production. With the increasing occurrence of surplus renewable electricity periods, there is a growing market for PEM water electrolysers. However, the scalability of these water electrolysers faces a bottleneck due to the use of costly Ir-based catalysts for the anodic oxygen evolution reaction (OER). To address this cost issue and to enhance catalytic efficiency, research efforts are shifting towards exploring atomically dispersed Ir electrocatalysts for the acidic OER.

While in theory, the atomically dispersed Ir electrocatalysts exhibit enhanced mass-specific activity due to the maximum utilisation of the Ir, in practice, they often show poor stability during synthesis and operation. Their degradation can be traced back to the aggregation of the atomically dispersed Ir into larger particles, i.e., a reduction of the catalytically active surface area of Ir. Enhancing catalyst stability requires a deeper understanding of the mobility, agglomeration behaviour, and bonding environment of Ir during synthesis and usage.

This thesis focuses on the synthesis and the characterisation of the atomically dispersed Ir on TiO_2 anatase nanosheets for the acidic OER. In the first half of this work, a facile synthesis strategy for preparing atomically dispersed Ir on TiO_2 anatase with minimised Ir agglomeration is developed. Utilising in-situ heating annular dark field scanning transmission electron microscopy (ADF-STEM) microscopy, combined with X-ray absorption fine structure (XAFS), the Ir agglomeration behaviour and mobility on TiO_2 with increasing synthesis temperature is correlated with the evolution of the bonding environment of the Ir, offering critical insights into the synthesis mechanism.

In the second half of this thesis, a comparative study of OER performance between atomically dispersed Ir on TiO_2 and oxidised Ir clusters is presented. By employing high-angle annular dark field scanning transmission electron microscopy (HAADF-STEM) to establish a statistically significant representation of the Ir dispersion on TiO_2, correlated with the XAFS analysis of the local environment of Ir, this work provides a fundamental understanding of the structure-activity-stability of the atomically dispersed Ir on TiO_2 anatase for the acidic OER.

Acknowledgements

Firstly, I would like to thank my supervisor Prof. Mauro Pasta for offering me the opportunity to join his group. I am grateful for your valuable advice and for sharing your rigorous approach to tackling scientific challenges.

I would like to thank my second supervisor Prof. Jonathan Yates for offering me the opportunity to join his group.

I am grateful to my college advisor, Prof. Sergio Lozano-Perez, for his constructive feedback during the early stages of my research.

My DPhil is fully funded by the Oxford-Taiwan Graduate Scholarship, sponsored by the University and the Ministry of Education, Taiwan. I am also grateful for financial support from the Department of Materials, St Edmund Hall and the Electrochemical Society.

A special thank you to Dr Johannes Ihli for his guidance and support on my research project and to Dr Peng Tang for the fruitful collaboration at the early stage of my DPhil.

Thank you Dr Kai Wang for sharing with me your incredible synthesis skills and all the exciting discussions.

Thank you Dr Guillaume Matthews for your assistance on the SEM measurements and your amazing friendship and positivity, which truely inspires me.

Thank you Yi Liang for your amazing support with the XPS measurements and all the good laughs.

Thank you Yvonne Chart for helping me with the FIB and for the late-night EM sessions. I would also like to thank members at the David Cockayne Centre for Electron Microscopy for their technical support.

To Brigita, Max, Soochan, Krish, and Jacob thank you for your friendship and companionship. Lorenz and Shobhan, thank you for all the good laughs and companionship as well. I would also like to thank all the members of the Pasta group for their supportive atmosphere and insightful scientific discussions.

A special thank you to Han for being an incredible friend and companion throughout my time here. Thank you, Tim, for being such an inspiration towards the end of my DPhil, Julie for being a great housemate throughout the years, and thanks to all my other Taiwanese friends here in Oxford.

Finally, I would like to thank my family—Shelly, Elaine, and Wendy—for their unwavering support and faith in me throughout all these years. Without your love, none of this would have been possible.

Disclaimer

I declare that the work presented in this thesis, unless otherwise stated, is the result of my original work and is written entirely by myself.

Contents

Abstract i

Acknowledgements ii

Originality Declaration iv

List of Figures ix

List of Tables xx

1 Introduction 1

1.1 Green hydrogen production via proton-exchange membrane (PEM) water electrolysis . . . 1

1.2 Supports for atomically dispersed Ir electrocatalysts . . . 4

1.2.1 OER stability and conductivity . . . 5

1.2.2 Stability of Ir atomic dispersion . . . 7

1.2.3 Characterisation of the Ir dispersion . . . 8

1.3 Synthesis strategies for the atomically dispersed Ir on metal oxides . . 11

1.4 Structure-activity relationship of atomically dispersed metal catalysts and clusters . . . 14

1.5 Thesis objective . . . 18

1.6 Nomenclatures used in this work . . . 20

2 Methods 39

2.1 Synthesis of atomically dispersed Ir on TiO_2 . . . 39

2.1.1 Strong electrostatic absorption (SEA) . . . 39

2.1.2 Thermolysis in inert atmosphere . . . 40

2.2 Determination of Ir atomic dispersion . . . 41

2.2.1 Aberration-corrected scanning transmission electron microscopy (AC-STEM) . . . 41

2.3 Chemical state and local environment characterisation of Ir 44
2.3.1 X-ray absorption fine structure (XAFS) 44
2.3.2 X-ray photoelectron spectroscopy (XPS) 47
2.4 Investigation of Ir mobility with in-situ heating annular dark field scanning transmission electron microscopy (ADF-STEM) 50
2.4.1 Setup of in-situ heating ADF-STEM experiments 50
2.4.2 Image processing 52
2.4.3 Ir tracking 54
2.5 Electrochemical characterisation 55
2.5.1 Electrochemical setup 56
2.5.1.1 Reference electrode 56
2.5.1.2 Working electrode 57
2.5.1.3 Counter electrode 59
2.5.2 Characterisation of OER performance 59

3 Synthesis and characterisation of atomically dispersed Ir on TiO_2 anatase nanosheets 67
Introduction 67
3.1 Synthesis of atomically dispersed Ir on TiO_2 using $[IrCl_6]^{2-}$ as precursor 70
3.2 Characterisation of Ir dispersion on TiO_2 76
3.2.1 Small angle X-ray scattering of Ir on TiO_2 76
3.2.2 Preparation of TiO_2 nanosheets 77
3.3 Optimised Ir dispersion on TiO_2 nanosheets 83
Conclusions 92
Experimental details 93

4 Synthesis mechanism of atomically dispersed Ir on TiO_2 anatase nanosheets 101
Introduction 101
4.1 Synthesis mechanism of atomically dispersed Ir on TiO_2 102
4.1.1 Evolution of Ir bonding environment during heating 102
4.1.2 Data analysis workflow for the in-situ heating ADF-STEM experiments 109
4.1.3 Thermal induced Ir mobility on TiO_2 114
4.2 Limitations of the in-situ heating ADF-STEM analysis 124
4.2.1 Temperature-driven Ir transport dynamics 125
4.2.2 Temperature relevance to synthesis conditions 128

4.2.3 Accuracy of image registration 128
Conclusions 133
Experimental details 145

5 Oxygen evolution reaction properties of atomically dispersed Ir on TiO_2 nanosheets 150
Introduction 150
5.1 Analysis of Ir dispersion on TiO_2 151
5.1.1 Statistically analysis from HAADF-STEM images 152
5.1.2 Atomic dispersion analysis from XAFS 154
5.1.3 Chemical state analysis of Ir-TiO_2 156
5.2 OER performance 158
5.2.1 Activity 158
5.2.2 Stability 166
5.2.3 Improvements of the support 168
Conclusions 173
Experimental details 175

6 Conclusions and future work 182

Publication list

Some of the work presented here is being prepared for the submission of this manuscript:

- **Po-Yuan Huang**, Kai Wang, Yi Liang, Guillaume Matthews, David Hopkinson, Donato Decarolis, Johannes Ihli, Mauro Pasta. "Transport and degradation mechanism of atomically dispersed Ir on TiO_2 nanosheets." *In preparation.*

List of publications that are not included in this thesis:

- Peng Tang*, **Po-Yuan Huang***, Jack E. N. Swallow, Chenbo Wang, Diego Gianolio, Hua Guo, Jamie H. Warner, Robert S. Weatherup, and Mauro Pasta. "Structure-property relationship of defect-trapped Pt single-site electrocatalysts for the hydrogen evolution reaction" *ACS Catalysis* vol. 13 no. 14, 9558-9566, 2023. *Equal contribution.

- Peng Tang, Hyeon Jeong Lee, Kevin Hurlbutt, **Po-Yuan Huang**, Sudarshan Narayanan, Chenbo Wang, Diego Gianolio, Rosa Arrigo, Jun Chen, Jamie H. Warner, and Mauro Pasta. "Elucidating the Formation and Structural Evolution of Platinum Single-Site Catalysts for the Hydrogen Evolution Reaction" *ACS Catalysis* vol. 12 no. 5, 3173-3180, 2022.

List of Figures

1.1 Projected global production and demand of hydrogen in the net zero emission (NEZ) scenario. Reprinted from IEA [1]. Licensed under Creative Commons Attribution CC BY 4.0. 2
1.2 Schematic of a proton-exchange membrane (PEM) water electrolyser stack with the electrochemical reactions splitting of water highlighted in the middle. Reprinted from [3]. Licensed under Creative Commons Attribution CC BY 4.0. 3
1.3 Representative aberration-corrected scanning transmission electron microscopy (AC-STEM) images of the commercially available IrO_x from Alfa Aesar (99.99%) at (a) low-magnification and (b) high-magnification. 4
1.4 (a) Modeled FT-EXAFS data for Pt/CeO_2 single atom catalyst (SAC) structure and oxidized $Pt_{14}O_{37}$ cluster. The peak at 2.75 Å is from the Pt-O-Ce scattering path specific to the SAC, and the peak at 3.4 Å is the Pt-O-Pt bonds characteristic of the oxidised Pt clusters. (b) Fitting R-factor as a function of the proportion of SAC in the mixture using the SAC structural model for the fit. Reprinted with permission from [41]. Copyright 2020 American Chemical Society. 10
1.5 Synthesis of single-site catalysts using SOMC-TMP. (a) A schematic of the SOMC-TMP. Adapted with permission from [50]. Copyright 2019 American Chemical Society. (b) An example of utilisation of SOMC-TMP for the preparation of atomically dispersed Ir on indium tin oxide (Ir_{SAC}-ITO) for the acidic oxygen evolution (top). High-angle annular dark field (HAADF) scanning transmission electron microscopy (STEM) images show the [Ir(COD)(IMes)(OH)] grafted on ITO (bottom left) and the Ir_{SAC}-ITO (bottom right). Adapted with permission from [14]. Copyright 2020 American Chemical Society. 13

1.6 Synthesis of ultra-high density (UHD) single-atom catalysts (SACs) using the two-step annealing strategy. (a) Literature survey of the Ni content in Ni SACs. (b) Comparison between the sizes of Ni on nitrogen-doped carbon (NC) prepared with one-step annealing and two-step annealing as a function of the Ni content. Ni precursor is loaded with the conventional impregnation method. (c) HAADF-STEM images of 10 wt% the Ni on NC prepared with one-step annealing (top) and a two-step annealing (bottom). Scale bars are 100 nm (inset: 1 nm). (d) A schematic of the two-step annealing protocol for the synthesis of UHD-SACs. (e) Metal loadings of the SAC prepared on nitrogen-doped carbon (NC), polymeric carbon nitride (PCN) and CeO_2. Reprinted with permission from [51]. Copyright 2022 Nature Publishing Group. 15

1.7 An platinum single-site catalysts (Pt-SSCs) example demonstrating the difference in intrinsic activity between the trapped Pt-SSC and the commercial Pt/C for the hydrogen evolution reaction (HER). (a) HAADF-STEM images of Pt on nitrogen-doped graphitic carbon with increasing Pt weight loading, with 1 wt% as the trapped Pt-SSC and 20 wt% as the commercial Pt/C. (b) Pt-mass-normalised HER current responses of the samples are shown in (a). (c) DFT free energy diagram for the hydrogen evolution on the Pt-SSC sample with the corresponding relaxed structures of hydrogen adsorbed on the Pt site, N site, C site on the Pt-SSC and FCC site on Pt(111) surface. Adapted from [53]. Copyright 2023 The Authors. Published by American Chemical Society. 17

1.8 A mechanistic OER kinetics study comparing $Ir_{Molecular}$ and IrO_x to highlight the role of Ir's local environment in regulating OER kinetics. (a) Structure of $Ir_{Molecular}$, (b) schematic of IrO_x and (c) Tafel plot comparing the sample in (a) and (b) with current measured at steady state, normalised to per mol of electrochemically active iridium. Reprinted with permission from [54]. Copyright 2022 The Authors. Published by American Chemical Society. 18

1.9 Schematic of the synthesis strategy for the atomically dispersed Ir on TiO_2 nanosheets used in this study. The synthesis begins with the loading of $[IrCl_6]^{2-}$ on the TiO_2 nanosheets using the strong electrostatic absorption (SEA), followed by a thermolysis step in N_2 to decompose $[IrCl_6]^{2-}$ and remove the Cl^- for the formation of atomically dispersed Ir on TiO_2 nanosheets (Ir-TiO_2). Schematic produced with the Vesta 3 software [65]. 19
1.10 Schematic of the categorisation of single-atom catalysts (SACs), single-sit catalysts (SSCs) and atomically dispersed metal catalysts as a function of the metal's oxidation state and local environment [69]. 22

2.1 (a) Simplified RPA model-predicted $[PtCl_6]^{2-}$ uptake by alumina as a function of pH value. The solid curve is the surface zeta potential that corresponds to the left y-axis, and the other dashed curve is the surface coverage of $[PtCl_6]^{2-}$ that reads the right-hand y-axis. (b) Comparison between the experimentally observed and the RPA model-predicted $[PtCl_6]^{2-}$ uptakes. Adapted from [2] with permission. Copyright 2003 Elsevier Inc. 40
2.2 (a) Schematic of the electron-probe-forming lenses in a STEM. Adapted with permission from [5]. (b) Schematic of the electron detectors in a STEM. Adapted with permission from [4]. Copyright 2009 Springer Science Business Media, LLC. 44
2.3 XAFS analysis of IrO_2 highlighting the measured XANES and EXAFS regions along with the determination of the edge step $\Delta\mu_0(E)$. 46
2.4 XANES analysis of Ir reference samples. (a) Normalised XANES spectra. (b) Integrated white line intensity of the Ir reference samples as a function of the number of Ir 5d holes. The integration of the WL of the (c) IrO_2, (d) Ir and (e) $IrCl_3$. Raw data of the spectra is plotted with the scattered hollow circles. Background arc-tangent function fit to the spectra is shown as the red curve, and the integrated area is the grey-shaded area. 48
2.5 Fitting of the pristine TiO_2 nanosheets for the determination of the Ti 3s peak shape. 51

2.6 In-situ heating ADF-STEM setup. (a) Schematic of the DENS Wildfire in-situ heating Nano-Chip, showing the metallic microheater spiral with the suspended SiN membrane. Windows with 20 nm of SiN membranes are used as the support for the sample of interest(b) Simulated temperature profile across the metallic microheater, demonstrating a temperature uniformity of 98%. Adapted from [16] with permission. Copyright 2018 Elsevier B.V. (c) Representative image of the Nano-Chip used for the in-situ heating STEM experiments in this study, where the SiN membrane for supporting the powder Ir-TiO_2 sample is highlighted. The red dashed circle highlights the area of interest in the sample, where the SiN membrane underneath it was etched away using a focused ion beam (FIB) to remove background contrast from SiN. FIB is performed in collaboration with Yvonne Chart and Dr Phani Karamched (University of Oxford). 53

2.7 Overview of the image registration process using a 19-frame image stack obtained from the in-situ heating ADF-STEM experiment. (a) Two consecutive image frames showing the drift of the STEM holder, manifested as a displacement of the Ir cluster towards the bottom-right corner of the image, highlighted in the green circle and the arrow. (b) The average image of a registered image stack is then used to generate the Ir displacement trajectory relative to the TiO_2 support [18]. . . . 56

2.8 A schematic of the three-electrode setup used in this thesis. 57

2.9 Schematic plot of the OER current density response (j) to the applied potential (E) on the electrode. The red vertical line denotes the thermodynamic equilibrium potential for the OER (1.23 V vs RHE). The blue line highlights the potential where a current density of 10 mA cm^{-2} is achieved. The potential difference between the red and blue vertical lines represents the overpotential. 60

3.1 Thermolysis of $[IrCl_6]^{2-}$. (a) TGA-MS analysis of $H_2IrCl_6 \cdot xH_2O$ in Ar with a heating rate of 10 °C min^{-1}. (b) Cl 2p XPS measurements of the post-SEA, as-synthesised TiO_2, treated at 300 °C and 500 °C in N_2 for 4 hours with a heating rate of 1 °C min^{-1}. The XPS measurements were performed in collaboration with Yi Liang (University of Oxford). 73

3.2 HAADF-STEM images of (a) post-SEA, as-synthesised TiO_2 and (b) post-SEA, as-synthesised TiO_2 loaded on a TEM grid and baked at 150 °C in a vacuum. (c) High- and (d) low-magnification HAADF-STEM images of post-SEA, as-synthesised TiO_2 treated at 500 °C in N_2 for 4 hour with a heating rate of 1 °C min^{-1}. 75
3.3 SAXS experiments of the Ir-TiO_2 samples at 0.5 wt% and 2 wt%. (a) HAADF-STEM images of the 0.5 wt% and 2 wt% Ir-TiO_2 samples. (b) Ir size distribution analysis for the 2 wt% Ir-TiO_2 sample. SAXS spectra of the bare 5 nm TiO_2, 0.5 wt% and 2 wt% within the q range (c) from 0 to 7 nm^{-1} and (d) from 0 to 2.5 nm^{-1}. SAXS experiments were performed in collaboration with Dr Thomas Zinn (Diamond Light Source), Dr Johannes Ihli (University of Oxford) and Dr Matthew Burton (University of Oxford). 78
3.4 Synthesis of TiO_2 nanosheets. (a) Schematic of the synthesis process. (b) XRD analysis of the nanosheets synthesised at 300 °C, 550 °C, 600 °C, 700 °C and 800 °C. The schematic was created with Vesta 3 software [25]. 79
3.5 ADF-STEM images of the TiO_x-loaded rGO treated at (a) and (b) 300 °C, (c) and (d) 550 °C, and (e) and (f) at 800 °C. 81
3.6 ADF-STEM images of the TiO_x-loaded rGO treated at 550 °C. (a) Image captured at the beginning and (b) after 1 minute of the STEM imaging. 82
3.7 Characterisation of the TiO_2 nanosheets prepared with at 550 °C after the toluene/ethanol wash. (a) Low-magnification and (b) high-magnification ADF-STEM images. (c) Rietveld refinement of the XRD pattern. (d) AFM height map and (e) corresponding line profiles from (d). The AFM measurements were performed in collaboration with Ben Jagger (University of Oxford). 84
3.8 (a) HAADF-STEM image of $[IrCl_6]^{2-}$ loaded on TiO_2 nanosheets. The yellow boxes highlight representative regions of the TiO_2 nanosheets with different exposed lattice planes. Scale bar denotes 2 nm. (b) Fast Fourier Transform (FFT) images of regions i, ii, and iii in (a). Scale bar denotes 10 nm^{-1}. (c) Gaussian fits of the FFT peaks in (b), with the corresponding lattice plane spacings calculated from the fits. The error represents the standard deviation of the Gaussian fits. 86

3.9 EDX analysis of bright spots in HAADF-STEM images. HAADF-STEM image and corresponding EDX spectra (inset) of Ir-TiO_2 nanosheet sample. 88
3.10 Determination of the actual Ir weight loading on TiO_2 using UV-Vis spectroscopy. (a) UV-Vis spectra of $[IrCl_6]^{2-}$ at various concentrations at pH 3. (b) Absorbance at 488 nm as a function of $[IrCl_6]^{2-}$ concentration. Error bars in (b) are calculated from at least three independent measurements. (c) UV-Vis spectra of the freshly prepared and the post-SEA $[IrCl_6]^{2-}$ solution for a 0.5 wt% nominal Ir loading. 89
3.11 Ir dispersion of Ir-TiO_2 samples. (a) Representative HAADF-STEM and (b) HAADF-SEM images of Ir-TiO_2-1C. (c) Representative HAADF-STEM and (d) HAADF-SEM images of Ir-TiO_2-10C. (e) Representative HAADF-STEM and (f) HAADF-SEM images of Ir-TiO_2-flash. These samples were prepared on FTO glass electrodes for further OER characterisation, which will be discussed in Chapter 5. HAADF-SEM experiments were performed in collaboration with Dr. Guillaume Matthews (University of Oxford). 91

4.1 Bonding environment analysis. (a) Ir L_3-edge k^3-weighted FT-EXAFS spectra for the 80 °C, 150 °C, 300 °C, 500 °C and the reference samples. Spectra fits of the (b) 80 °C, (c) 150 °C, (d) 300 °C and (e) 500 °C sample, respectively. 106
4.2 XANES analysis. (a) XANES spectra and (b) corresponding fits at Ir L_3 edge for the 80 °C, 150 °C, 300 °C, 500 °C and the reference samples. Integration of the WL is shown for the (c) 80 °C, (d) 150 °C, (e) 300 °C and (f) 500 °C sample, respectively. Raw data of the spectra is plotted with the scattered hollow circles. The background arc-tangent function fit to the spectra is shown as the red curve, and the integrated area is shown as the grey-shaded region. 108
4.3 Representative ADF-STEM images captured at (a) 300 °C and (b) 500 °C on a DENS Wildfire Nano-Chip. Red, orange and green boxes highlight the presence of Ir_1, $Ir_{2\text{-}6}$ and $Ir_{>6}$, respectively. 111

4.4 Intensity line profile of a representative in-situ heating ADF-STEM image. (a) Raw image before processing. The white dashed line indicates the location of the line profile. (b) Zoomed-in view of the centre of the image (a). (c) Intensity line profile along the dashed line in (a) and (b). The green circle highlights the signal from the Ir at approximately X = 400, and the red circles highlight the noise in the image. 112
4.5 Detection of the atomically resolved Ir in the ADF-STEM images. (a) Representative $Ir_{>10}$ detected, highlighted in red boxes and labelled with their sizes in nanometers. (b) Representative $Ir_{1\text{-}10}$ detected, highlighted with white dots. 113
4.6 Representative set of linked Ir trajectories at 500 °C. (a) Ir_1 trajectories, (b) $Ir_{2\text{-}6}$ trajectories and (c) $Ir_{>6}$ trajectories. (d) Total number of Ir tracked as a function of Ir size (e) Total number of Ir displacements tracked as a function of temperature and Ir size. 115
4.7 Ir mobility analysis as a function of temperature and Ir size. Histograms showing displacement velocities for Ir_1, $Ir_{2\text{-}6}$ and $Ir_{>6}$ across 80, 150 °C, 300 °C and 500 °C. The displacement velocities are calculated over 100 ± 10-second intervals, meaning a displacement velocity of 0.01 nm s^{-1} corresponds to a total 1 nm displacement within this time interval. The vertical line marks the displacement velocities at 0.005 nm s^{-1}. 117
4.8 Time-resolved Ir_1 mobility analysis. Histograms showing displacement velocities at 300 °C (top) and 500 °C (bottom) as a function of time (0-1200 seconds and >1200 seconds). The vertical line marks the displacement velocities at 0.005 nm s^{-1}. 119
4.9 Time-resolved ADF-STEM images of a representative (a) Ir_2 and (b) Ir_3 captured at 80 °C. Scale bars are 2 nm. Ir_3 in (b) are highlighted in red dash-line circles of the same sizes in each image set to demonstrate their proximity to one another. 120
4.10 Time-resolved ADF-STEM images of a representative (a) Ir_2 and (b) Ir_3 captured at 300 °C. Scale bars are 2 nm. Ir_x are highlighted in red dash-line circles of the same sizes in each image set to demonstrate their proximity to one another. 121

4.11 Time-resolved ADF-STEM images of a representative Ir_2 on TiO_2 with the edges of (a) (004) planes and (b) (101) planes shown. Images were captured at 500 °C. Scale bars are 2 nm. Ir_2 are highlighted in red dash-line circles of the same sizes in each image set to demonstrate their proximity to one another. 122
4.12 Time-resolved ADF-STEM images of two Ir_x coalescing into one large cluster at 500 °C. Scale bars are 2 nm. 123
4.13 Summed Ir displacement lengths as a function of 2D radial directions of the displacement for Ir_1, $Ir_{2\text{-}6}$ and $Ir_{>6}$ across 80 °C, 150 °C, 300 °C and 500 °C. 130
4.14 (a) and (b) show two consecutive image frames from a registered image stack captured at 500 °C. Highlighted in the red circles are Ir_1, which is presumed to be the same. (c) shows the highlighted Ir_1 in (a) and (b) projected onto the registered and averaged image of the stack. . . 132
4.15 Overview of the image processing using the raw image shown in Figure 4.4 as an example. (a) Padded and windowed raw image. (b) FFT spectrum of the padded and windowed image. (c) Inverse FFT image after applying bandpass filtering in Fourier domain. (d) Corresponding intensity line profile along the horizontal white line in (c). (e) Inverse FFT image after lattice suppression in Fourier domain. (f) Corresponding intensity line profile along the horizontal white line in (e). (g) Intensity-thresholded image. (h) Corresponding intensity line profile along the horizontal white line in (g). 137
4.16 Selection of bandpass filter. (a) Bandpass filter for the detection of $Ir_{1\text{-}10}$. (b) Line profile of the proportion of the signal that can pass through the mask as a function of feature length for the $Ir_{1\text{-}10}$ and $Ir_{>10}$ bandpass filters. (c) FFT spectrum of the raw image in Figure 4.4 after the masking with the $Ir_{1\text{-}10}$ bandpass filter and (d) the corresponding inverse FFT image. (e) FFT spectrum of the raw image in Figure 4.4 after the masking with the $Ir_{>10}$ bandpass filter and (f) the corresponding inverse FFT image. 139

4.17 Lattice suppression process. (a) FFT spectrum of the raw image in Figure 4.4 with its centre signal masked and (b) the corresponding thresholded image. (c) Detected lattice reflection peaks from (b). (d) FFT spectrum of the Figure 4.16c with lattice reflections masked. (e) F1, recall and precision scores of the detection of the lattice reflection peaks in the FFT spectrum as functions of the threshold. 142
4.18 Intensity thresholding process. (a) F1, recall and precision scores of the detection of $Ir_{1\text{-}10}$. (b) Thresholded image of $Ir_{1\text{-}10}$ and (c) $Ir_{>10}$ from the raw image in Figure 4.4, both after the padding/windowing and bandpass filtering and lattice suppressing process. 144

5.1 Ir size distribution statistics from HAADF-STEM images. (a) Atomic percentages of Ir_1 and Ir_x for Ir-TiO_2-1C and Ir-TiO_2-10C. (b) Size distribution of Ir_x for Ir-TiO_2-1C and Ir-TiO_2-10C normalised to the total counts of Ir_x. 153
5.2 Bonding environment analysis of Ir-TiO_2 samples using Ir L_3-edge k^3-weighted FT-EXAFS spectra for Ir-TiO_2-1C and Ir-TiO_2-10C. 155
5.3 XANES analysis of different Ir size distribution. (a) XANES spectra and (b) corresponding fits at Ir L_3-edge for the Ir-TiO_2-1C, Ir-TiO_2-10C and the reference samples. Integration of the WL is shown in (c)for the Ir-TiO_2-10C sample. The raw data of the spectra are plotted with the scattered hollow circles. Background arc-tangent function fitted to the spectra is shown as the red curve, and the integrated area is shown as the grey-shaded region. 157
5.4 XANES linear combination analysis of Ir-TiO_2-10C conducted using (a) a mixture of Ir-TiO_2-1C and Ir metal spectra and (b) a mixture of IrO_2 and Ir metal spectra from 11175 eV to 11315 eV. 158
5.5 Morphology of the TiO_2-coated OER electrode investigated with SEM micrographs. (a) Top and (b) cross-sectional view of the electrode. . . 159

5.6 Electrochemical properties of the Ir-TiO_2 samples. (a) PEIS of Ir-TiO_2-1C. (b) shows in the low impedance region in (a). Inset showing a R_1-p(R_2-CPE) circuit for the fitting of the spectrum at 1.76 V, with CPE as the constant phase element to represent the non-ideal capacitive behaviour. (c) CV of Ir-TiO_2-1C, Ir-TiO_2-10C and TiO_2 below OER potentials, performed in Ar-saturated 0.5 M H_2SO_4 with a scan rate of 100 mV s^{-1}. The CV scans start from OCV (∼0.9 V) first cathodically, then anodically, and finally back to OCV. 161

5.7 Evaluation of OER performance of Ir-TiO_2-1C and Ir-TiO_2-10C performed using 10 consecutive CVs between 1.3 and 2.1 V vs RHE in O_2-saturated 0.5 M H_2SO_4. OER current responses are normalised to the total Ir mass on the electrode, typically ranging from 0.1 to 0.2 μg. (a) shows the 1^{st}, (b) 3^{rd} and (c) 10^{th} CV. (d) summarises the Ir mass-normalised OER activities across all three samples at 1.55 V vs RHE. Averaged OER current densities and error bars are calculated using at least three independent measurements. In each measurement, the OER current density is extracted from the average of the forward and the backward CV sweep to cancel out the capacitive charging in the current response [6]. 163

5.8 Evaluation of OER performance of Ir-TiO_2-1C, Ir-TiO_2-10C and TiO_2 performed using 10 consecutive CVs between 1.3 and 2.1 V vs RHE in O_2-saturated 0.5 M H_2SO_4. OER current is normalised to 0.5 cm^2, the geometric surface area of the electrode. (a) shows the 1^{st}, (b) 3^{rd} and (c) 10^{th} CV. (d) summarises the geometric OER activities across all three samples at 1.55 V vs RHE. Averaged OER current densities and error bars are calculated using at least three independent measurements. In each measurement, the OER current density is extracted from the average of the forward and the backward CV sweep to cancel out the capacitive charging in the current response [6]. 165

5.9 HAADF-STEM analysis of the post-OER samples. Representative (a) high- and (b) low-magnification HAADF-STEM images of the post-OER Ir-TiO_2-1C. Representative (c) high- and (d) low-magnification HAADF-STEM images of the post-OER Ir-TiO_2-10C. 166

5.10 Ir size distribution statistics from STEM images. (a) Atomic percentage of Ir_1 and Ir_x for post-OER Ir-TiO_2-1C and post-OER Ir-TiO_2-10C. (b) Size distribution of Ir_x for post-OER Ir-TiO_2-1C and post-OER Ir-TiO_2-10C normalised to the total counts of Ir_x. 168
5.11 Chemical state analysis of post-OER Ir-TiO_2-1C (top) comparing with Ir-TiO_2-1C (bottom) using Ir 4f XPS. 169
5.12 Synthesis and physical characterisation of N-TiO_2. (a) XRD of 5 nm TiO_2 treated in 50 sccm NH_3 with increasing temperature. (b) XPS N 1s spectra, Ti 2p and O 1s spectra of the N-TiO_2 prepared at 575 °C with a flow rate of 200 sccm NH_3. (c) A photo showing the TiO_2 treated at different conditions. The sample on the left is at 600 °C with a flow rate of 200 sccm NH_3, the sample in the middle is at 600 °C with a flow rate of 50 sccm NH_3 and the sample on the right is at 575 °C with a flow rate of 50 sccm NH_3. (d) Representative ADF-STEM images of the N-TiO_2 prepared at 575 °C with a flow rate of 50 sccm NH_3. . . . 172

1 HAADF-STEM images of Ir-TiO_2-1C. 186
2 HAADF-STEM images of Ir-TiO_2-10C. 187
3 HAADF-STEM images of Ir-TiO_2-flash. 188
4 HAADF-STEM images of post-OER Ir-TiO_2-1C. 189
5 HAADF-STEM images of post-OER Ir-TiO_2-10C. 190
6 Experimental EXAFS spectrum of the Ir-TiO_2-1C sample. The black circle and the inset highlight the signal between 11540 and 11560 eV, which corresponds to the W L_2 edge [1]. 191
7 HAADF-STEM image of as-received rGO at (a) low magnification and (b) high magnification. (c) and (d) HAADF-STEM images of the TiO_2 nanosheets. The red circles highlight the high-contrast atomically dispersed species and clusters, which can be attributed to the presence of W impurity. 192
8 k^3-weighted experimental EXAFS data (black), fit (red) and masking window (green) for the (a) 80 °C, (b) 150 °C, (c) 300 °C and (d) 500 °C sample. 193

9 k^3-weighted experimental data (black), fit (red) and masking window (green) for the IrO_2 reference. (a) Fitting conducted with k = 3 to 14 Å^{-1} masked with a Hanning window of δk = 3 Å^{-1}. The EXAFS fit was performed over a R range between 1.0 and 4.2 Å, utilising the first 5 single scattering paths from a rutile IrO_2 reference structure [2]. (b) Fitting conducted with k = 3 to 8.5 Å^{-1} masked with a Hanning window of δk = 0.5 Å^{-1}. The EXAFS fit was performed over a R range between 1.0 and 3.5 Å, utilising the first 3 single scattering paths from a rutile IrO_2 reference structure [2]. 194

List of Tables

1.1 Properties of candidate metal oxide substrates for the preparation of atomically dispersed Ir for acidic OER. 10
1.2 Overview of state-of-the-art atomically dispersed Ir catalysts for the acidic OER. All potentials are referenced vs. the reversible hydrogen electrode (RHE). 23
1.3 Overview of benchmark Ir-based catalysts for the acidic OER. All potentials are referenced vs. the reversible hydrogen electrode (RHE). . 23

4.1 EXAFS fitting results for IrO_2. 103
4.2 Summary of EXAFS fitting results for the 80 °C, 150 °C, 300 °C and 500 °C samples. 107

1 EXAFS fitting results for IrO_2 with k = 3 to 8.5 Å^{-1} masked with a Hanning window of δk = 0.5 Å^{-1}. The EXAFS fit was performed over a R range between 1.0 and 3.5 Å, utilising the first 3 single scattering path from a rutile IrO_2 reference structure [2]. 195

Chapter 1

Introduction

1.1 Green hydrogen production via proton-exchange membrane (PEM) water electrolysis

This thesis work is motivated by the growing demand for green hydrogen in pursuing the global net zero emission. According to International Energy Agency (IEA) statistics shown in Figure 1.1, the global demand production is predicted to grow almost six-fold from 90 million tonnes (Mt) in 2020 to 530 Mt in 2050 [1]. This demand comes primarily from the decarbonisation need from the transport, chemical and steel reforming industries. In the predicted 530 Mt H_2 production in 2050, water electrolysis is projected to account for more than 60 %, requiring 3600 gigawatts (GW) global water electrolyser capacity. This projection suggests a yearly installation rate of the water electrolysers at a GW level is required.

Proton-exchange membrane (PEM) water electrolysers are among the most efficient devices for producing green hydrogen to meet the water electrolyser installation demand. Figure 1.2 shows the critical components of a PEM water electrolyser stack, consisting of a membrane electrode assembly (MEA) to catalyse the reaction, gas diffusion layers (GDL) to facilitate the input of the reactant water vapour and the

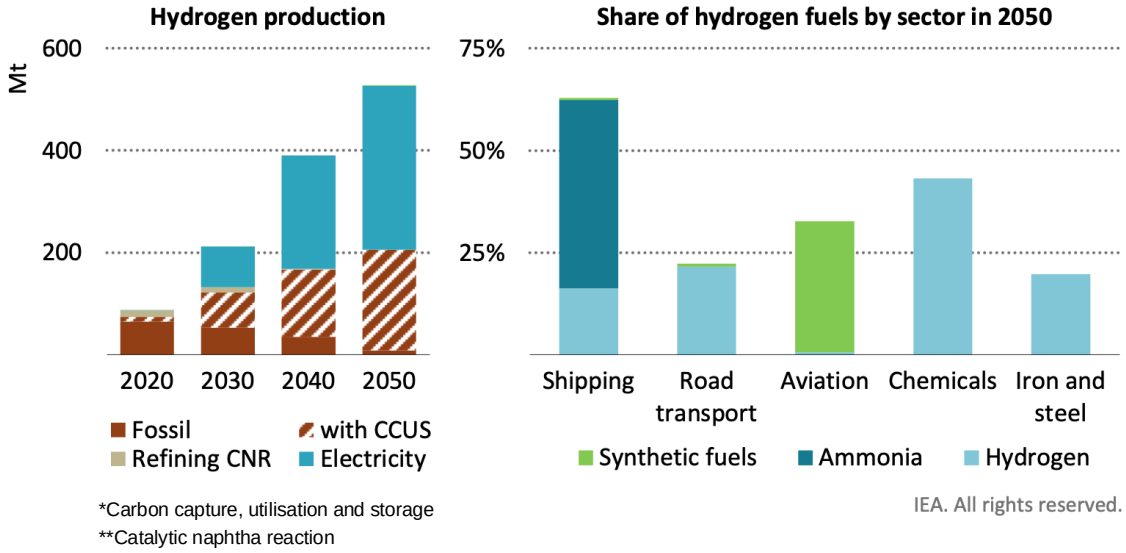


Figure 1.1: Projected global production and demand of hydrogen in the net zero emission (NEZ) scenario. Reprinted from IEA [1]. Licensed under Creative Commons Attribution CC BY 4.0.

extraction of the gas products, and bipolar plates (BP) as the current collectors. The MEA comprises a proton-exchange membrane sandwiched by the anode catalyst for the oxygen evolution reaction and the cathode catalyst for the hydrogen evolution reaction. Commercially, the catalyst for OER is an iridium-based material, and for HER, it is platinum on carbon. The use of these precious metal-based catalysts is due to the need to withstand highly corrosive acidic working conditions [2].

PEM water electrolysers produce high current density (> 1.6 A cm^{-2}) with a millisecond system response time [4]. The latter makes them particularly suitable for coupling with intermittent renewable energy sources, optimising energy use [5]. This is the key advantage of PEM water electrolysers in pursuing the net zero scenario, compared to using the more mature alkaline water electrolysers.

While PEM water electrolysers offer the above advantages, the use of precious metal-based catalysts, specifically the Ir-based catalysts for the OER, is projected to be a bottleneck in scaling up these devices to meet the GW installation rate [6, 7]. This is due to the scarcity and thus the volatile price of Ir, as estimated by multiple

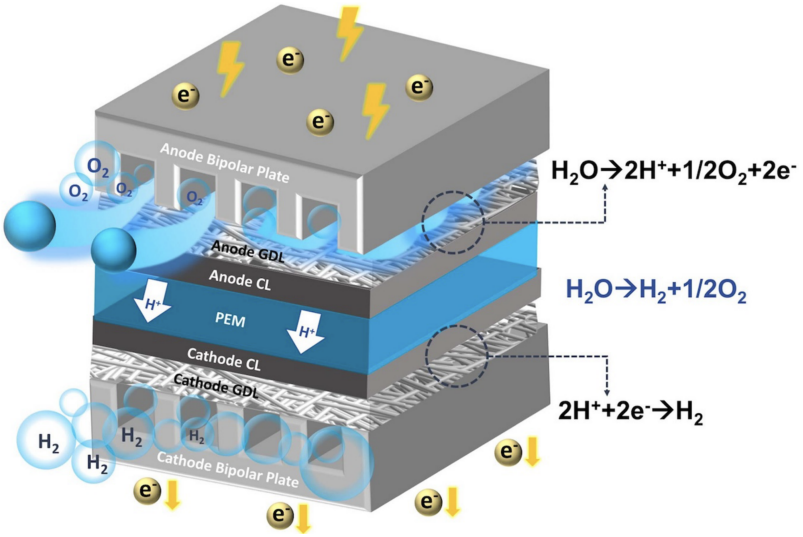


Figure 1.2: Schematic of a proton-exchange membrane (PEM) water electrolyser stack with the electrochemical reactions splitting of water highlighted in the middle. Reprinted from [3]. Licensed under Creative Commons Attribution CC BY 4.0.

reports.

In state-of-the-art PEM water electrolysers, such an IrO_x shown in Figure 1.3 is employed. To produce the target current density, they require an Ir loading of at least 2 mg_{Ir} cm^{-2} [4]. Gasteiger and coworkers estimated a 40-fold reduction of the Ir loading to 0.05 mg_{Ir} cm^{-2} is required for the GW level installation goal [8, 9, 10].

Based on the Butler-Volmer equation, which governs the OER reaction kinetics, only an 80 mV overpotential penalty is required to reduce the Ir loading by 40-fold (see discussion about the reaction kinetics in Section 1.6). However, Gasteiger and coworkers discovered that, despite the use of the IrO_2 on TiO_2 commercial catalyst from Umicore (Elyst Ir75 0480), which has been recognised in literature as a promising catalyst in lowering the Ir loading compared to the IrO_x shown in Figure 1.3, the lowering of the Ir loading significantly degrades the homogeneity of the Ir catalyst layer coated on the PEM, causing inefficient use of the catalyst and resulting in extra overpotential to drive up the reaction current density [9].

Based on the results described above, it is crucial to develop catalysts that expose more Ir active surface area to maximise the utilisation of Ir while maintaining their

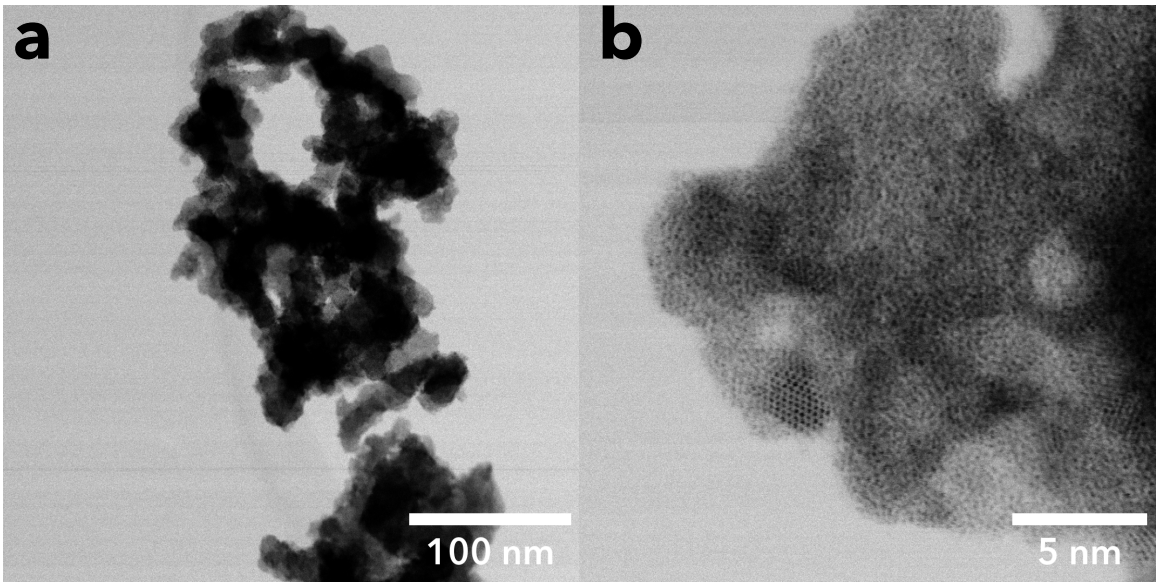


Figure 1.3: Representative aberration-corrected scanning transmission electron microscopy (AC-STEM) images of the commercially available IrO_x from Alfa Aesar (99.99%) at (a) low-magnification and (b) high-magnification.

manufacturability into a homogeneous catalyst layer for PEM application.

The ultimate of this catalyst design strategy is the development of atomically dispersed Ir electrocatalysts, where the Ir are atomically isolated from each other on a support substrate, exposing all the Ir to the reaction [11, 12, 13]. Theoretically, such an atomically dispersed Ir electrocatalyst can realise 100 % of Ir utilisation, lowering the amount needed to achieve the same OER performance.

1.2 Supports for atomically dispersed Ir electrocatalysts

The following section introduces the development of atomically dispersed Ir electrocatalysts.

Pioneering work on atomically dispersed Ir electrocatalysts for the acidic oxygen evolution reaction was reported by Leberev and coworkers [14]. They synthesised the Ir single atoms supported on indium tin oxide (Ir_{SAC}-ITO) and demonstrated a

superior Ir-mass normalised OER activity in an acidic environment to the commercial IrO_x benchmark (Table 1.3 and Table 1.2). This promising OER activity rationalises the development of atomically dispersed Ir electrocatalysts.

Nevertheless, practical implementations of Ir_{SAC}-ITO may be limited by concerns over its long-term stability under PEM conditions. The authors observed degradation of the catalyst due to agglomeration of the atomically dispersed Ir after 2 hours of OER stability test. A follow-up study by Zlater and coworkers [15], using an online inductively coupled plasma mass spectrometry electrochemical setup (ICP-MS), demonstrated a 20-time faster dissolution rate of the Ir for Ir_{SAC}-ITO than that of the IrO_2 benchmark. They attributed this instability to the intense dissolution of the In in ITO during OER, leading to the destabilisation of both the Sn and the Ir supported on top.

Further strategies are required to develop atomically dispersed Ir electrocatalysts with higher stability, particularly by focusing on improving the support for Ir. However, this task is challenging, as evidenced by a limited number of reports found in the literature after Leberev and coworkers' work (Table 1.2). I attribute this to the three critical challenges in developing suitable supports to stablise atomically dispersed Ir. The following section details each of these challenges:

1. Stability and electronic conductivity for OER
2. Uniform synthesis of the atomic dispersion of Ir
3. Rigorous physicochemical characterisation of the dispersion of Ir.

1.2.1 OER stability and conductivity

As observed in the Ir_{SAC}-ITO study, the stability of the substrate is a critical issue that needs to be addressed before the catalyst can be employed in a PEM water electrolyser. Although carbon-based substrates have been shown to have great success

in supporting atomically dispersed Ir [16], they combust and degrade readily under acidic OER conditions [17].

Metal oxides are, in general, more resistant to the acidic OER environment. However, their low electronic conductivity limits their application in PEM. This requirement of electronic conductivity constrains the choice of metal oxides that can serve as a support.

SnO_2-based materials, including indium-doped tin oxide (ITO), fluorine-doped tin oxide (FTO) and antimony-doped tin oxide (ATO), are commonly accepted as stable for OER, as demonstrated by Jaramillo and coworkers [18]. However, these materials remain insufficient for the Ir_{SAC}-ITO and requires further improvement.

An alternative is TiO_2, where its high stability against corrosion under OER conditions is well-known [12, 19]. This stability is why a Ti plate with a nanolayer of native TiO_2 oxide on top is used in PEM water electrolysers as the gas diffusion layer, which is in contact with the OER electrode [9].

Many efforts have been invested in using TiO_2 to support IrO_2, aiming to lower the loading of Ir. One of the most successful developments is the commercially available product from Umicore, the Elyst 75, which reportedly can reduce the Ir content from the IrO_x 85% to 75% while maintaining the activity. Endeavours exploring the further lowering of the loading of Ir on TiO_2 reveal that the gain from the higher Ir use efficiency from the lower Ir loading is being offset by the decrease in the electronic conductivity of the catalyst due to the semi-conductive nature of the TiO_2 [20]. Kasian and coworkers reported an optimal Ir loading at 40 wt%, balancing these two effects [21]. Therefore, further strategies to overcome this electronic conductivity issue, like doping with Nb [22, 23], W [24, 25] and N [26, 27], are being explored.

MnO_2 and Co_3O_4 are also reported as the support for atomically dispersed Ir [28, 29]. Even though they are, in general, less stable than SnO_2 and TiO_2, in particular in the higher potential region ($>$ 1.8 V vs RHE), they are OER active on their

own [30, 31]. Therefore, several reports leverage the OER activity of these substrates and combine it with the activity of atomically dispersed Ir on top to drive sufficiently high current densities in the low potential region, reducing the rate of degradation of the support.

1.2.2 Stability of Ir atomic dispersion

The synthesis of uniform atomic dispersion of Ir on a metal oxide support without agglomeration is the critical challenge to be addressed to achieve the theoretical 100% Ir atom efficiency. Surface oxygen of the metal oxide support can form strong bonds to the atomically dispersed Ir, thereby stabilising the Ir [32]. However, due to the high surface energy of such atomic dispersion of the Ir precursor and the resulting atomically dispersed Ir catalyst, they both tend to agglomerate during synthesis [33, 34].

The synthesis of atomically dispersed Ir on the metal oxide is commonly carried out by decomposing an Ir precursor (typically H_2IrCl_6 [33, 35, 36, 37]) into an oxidised Ir species, which subsequently bonds to the surface of the metal oxide. Agglomeration of the Ir can occur either before the Ir precursor bonds to the support surface or after the oxidised Ir species bonds to the metal oxide, particularly if the Ir–O bond strength is insufficient to resist sintering at the synthesis temperature.

The bonding strength between oxidised Ir and the support is governed by the Lewis basicity of the surface oxygen in the metal oxide support: higher Lewis basicity of the surface oxygen that provides greater electron density to share with Ir results in a stronger Ir–O bond, reducing the probability of Ir agglomeration during synthesis. This is evidenced by density-functional theory (DFT) calculations from Uzun and coworkers, which revealed that Ir bonds more strongly to surface oxygen that is a strong electron donor, such as MgO, CeO_2 and TiO_2 [38]. These electrondoating supports, therefore, provide the Ir with a higher thermal sintering resistance. In

contrast, Ir supported on metal oxide with surface oxygen that acts as a weaker and median electron donor, such as like SiO_2 and Al_2O_3, tends to agglomerate during synthesis.

1.2.3 Characterisation of the Ir dispersion

The last challenge in the study of the atomically dispersed Ir electrocatalysts is the characterisation of the dispersion of Ir, and arguably the most critial yet its importance is often overlooked in the literature. Without comprehensive and detailed characterisation to confirm the atomic dispersion of the Ir, a biased understanding of the catalyst can be derived, compromising the interpretation of their synthesis mechanism and structure-property relationship. This can significantly hinder the understanding and development of atomically dispersed Ir electrocatalysts.

To confirm the atomic dispersion of the Ir, the high-angle annular dark field scanning transmission electron microscopy (HAADF-STEM) is the indispensable technique, providing sub-angstrom spatial resolution for the visualisation of the position of Ir. HAADF-STEM provides the mass-thickness contrast, also known as Z-contrast, where the intensity in the image is approximately proportional to Z^2. Therefore, to "see" the atomically dispersed metal on the support, there should ideally be a significant difference in the atomic number between the support and the metal (empirically, a difference of at least two rows in the periodic table is needed) [39]. Additionally, the support is required to be sufficiently thin (on the order of a few nanometers). The requirement of contrast between the Ir and its underlying support in a HAADF-STEM imagelimits the choice of support. Specifically, for the characterisation of Ir, 3d TM oxides (TiO_2, Fe_3O_4 and Co_3O_4) or period 3 metal oxides (MgO, Al_2O_3 and SiO_2) are desirable. In contrast, Sn-based oxides are less suitable, as will be shown in Figure 1.5b.

Although HAADF-STEM provides high space resolution, its characterisation length

scale is limited to the thinnest sample regions, where the greatest mass-thickness contrast is obtained. Therefore, the representativeness of the observed sample morphology towards the entire sample is questionable.

Extended X-ray absorption fine structure (EXAFS) from an X-ray absorption spectroscopy (XAS) measurement is used as a standard technique to complement HAADF-STEM, providing knowledge on the local bonding environment of the X-ray absorbing species at micrometre to millimetre length scales.

For the study of atomic dispersion of Ir, a standard characterisation procedure is to first use HAADF-STEM to identify the presence of the atomically dispersed Ir, complemented by the use of EXAFS to confirm the bonding environment of the Ir. Using the absence of scattering signals associated with Ir-Ir or Ir-O-Ir bonds in the EXAFS analysis, the absence of Ir agglomeration can be concluded.

However, a number of reports reveal that EXAFS can be insensitive to the difference between the bonding environment of an atomically dispersed metal and oxidised clusters of the same metal [40, 41]. Specifically, Finzel and coworkers modelled the Fourier-transformed (FT)-EXAFS data of a mixture of the Pt/CeO_2 single-atom catalyst (SAC) structure and oxidised $Pt_{14}O_{37}$ clusters, showing that 10 % mixture of the oxidised Pt clusters into the single atoms did not significantly alter the EXAFS spectra (Figure 1.4a). The EXAFS spectra of up to 40% of the oxidised cluster, i.e., the 60% SAC in Figure 1.4a, can be fitted with the SAC model with a r-factor below 1% (Figure 1.4b).

This work highlights the risk of using EXAFS as the bulk technique for characterising the metal dispersion in atomically dispersed metal catalysts, urging extra care should be taken when interpreting the EXAFS data. Not to mention, in an actual sample measurement, a low Ir loading is usually used to prepare these atomically dispersed metal samples, resulting in a low single-to-noise ratio (SNR) for the analysis of Ir-Ir and Ir-O-Ir bonds. This further complicates an accurate interpretation of the

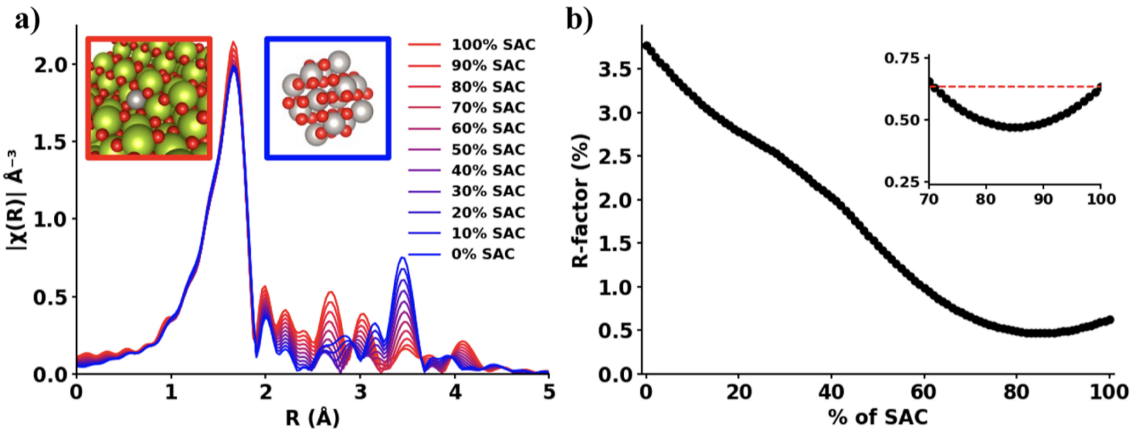


Figure 1.4: (a) Modeled FT-EXAFS data for Pt/CeO_2 single atom catalyst (SAC) structure and oxidized $Pt_{14}O_{37}$ cluster. The peak at 2.75 Å is from the Pt-O-Ce scattering path specific to the SAC, and the peak at 3.4 Å is the Pt-O-Pt bonds characteristic of the oxidised Pt clusters. (b) Fitting R-factor as a function of the proportion of SAC in the mixture using the SAC structural model for the fit. Reprinted with permission from [41]. Copyright 2020 American Chemical Society.

bonding environment and the dispersion of Ir using EXAFS.

The conductivity values of the candidate metal oxide substrates, the Lewis basicity of the oxygen in the metal oxide substrate, and the atomic number difference between the substrate and Ir (δZ) are compiled in Table 1.1. In summary, the above three subsections describe the critical aspects of selecting a suitable substrate, and all aspects are interconnected. The combination of these three challenges hampers the development of the OER, requiring more efforts to push this field ahead.

Table 1.1: Properties of candidate metal oxide substrates for the preparation of atomically dispersed Ir for acidic OER.

Metal Oxide	**Conductivity (S m^{-1})**	**Stability in acidic OER [42]**	**Lewis basicity of the oxygen**	**δZ with Ir (rows in periodic table)**
SnO_2 (doped)	10^4 to 10^5 [43]	High	Medium	2
Co_3O_4	10^2 to 10^4 [44]	Medium	Medium	1
CeO_2	10^{-4} [45]	Moderate	Medium	0
MnO_2	10^{-2} to 10^{-4} [46]	Low	Medium	1
TiO_2	10^{-6} to 10^{-1} [47]	High	High	1
ZrO_2	10^{-10} [45]	High	High	1
Al_2O_3	10^{-12} [48]	Low	Low	2
MgO	10^{-12} [49]	Low	High	3
SiO_2	10^{-16} [48]	Low	Low	2

1.3 Synthesis strategies for the atomically dispersed Ir on metal oxides

The following section summarises the synthesis techniques of atomically dispersed Ir on metal oxides. As discussed in Section 1.2.2, one of the key challenges in studying atomically dispersed Ir on metal oxides is the prevention of agglomeration of the Ir precursor and the resulting atomically dispersed Ir during synthesis.

The most rigorous and reproducible synthesis method that addresses this agglomeration challenge is the surface organometallic chemistry coupled with thermolytic molecular precursors (SOMC-TMP) synthesis strategy advanced by Copéret and coworkers [50]. Using SOMC-TMP, the so-called single-site catalysts (SSCs) with a single well-defined bonding environment of the metal can be produced.

SOMC-TMP is a three-step method, first involving a support preparation step with heat treatment, usually carried out in a vacuum. A grafting step is then employed to anchor a metal complex precursor on a metal oxide support of choice, followed by a post-treatment of the sample to remove the ligands on the precursor, activating the metal site on the support surface for the further reaction of interest, as summarised in Figure 1.5a.

During the grafting step, the metal precursor (ML_nX_m, where M is metal, L is any ligands and X is the anionic ligand) undergoes a ligand exchange reaction with the surface OH group, i.e., the protonolysis of one anionic X ligand in the metal complex, and becomes bonded to the oxo group on the surface of the support. To promote the efficiency of the post-treatment step, TMPs that have labile organic moieties as their ligands (L in ML_nX_m) are used to enable readily ligand removal during the heat treatment step. In this synthesis strategy, the density of the metal can be controlled by tuning the density of the surface OH groups. When the metal loading is sufficiently low, the atomic dispersion of the metal is achieved.

Using this SOMC-TMP, Leberev and coworkers synthesised the Ir_{SAC}-ITO that was mentioned previously by using an Ir(COD)(IMEs)(OH) complex grafted on ITO, followed by a heat treatment step in the air at 400 °C to remove the organic moiety. Using HAADF-STEM, they confirmed the atomic dispersion of Ir and reported an Ir loading of 0.86 wt% (Figure 1.5b).

Despite the excellent control over the metal dispersion that SOMC-TMP can provide, this technique is highly technical, posing challenges in scaling up the synthesis of atomically dispersed Ir electrocatalysts using SOMC-TMP for the application in PEM water electrolysers. This challenge is due to the intricate procedure of surface treatment of the substrate and the delicate design of the metal complex to enable the grafting step necessary in SOMC-TMP. The low metal density (0.86 wt% as seen in the Ir_{SAC}-ITO case) may further hamper its practical use in a PEM water electrolyser, as such low Ir metal loading requires a more significant total amount of catalyst to achieve the target reaction rate, thickening the catalyst layer and resulting in more considerable ohmic loss.

Hai and coworkers proposed a two-step annealing method, aiming to maximise the loading of the atomically dispersed metal while taking the synthesis scalability into account (Figure 1.6) [51]. In their two-step annealing strategy, they used a stepwise removal of the ligand of the metal precursor to minimise the agglomeration of the metal precursor, achieving atomic dispersion of the metal with high metal loadings. Specifically, they first load metal chlorides as the precursor using wet impregnation, and the high-density atomic dispersion is achieved by first promoting anchoring of the metal precursor on the support with a low-temperature annealing step at a temperature below the decomposition temperature of the metal precursor. They showed that this step promoted the bonding of metal precursors to the high-energy surface sites on the support surface. Subsequently, a washing step was introduced to remove the unbounded metal precursors, followed by a second annealing step to remove the

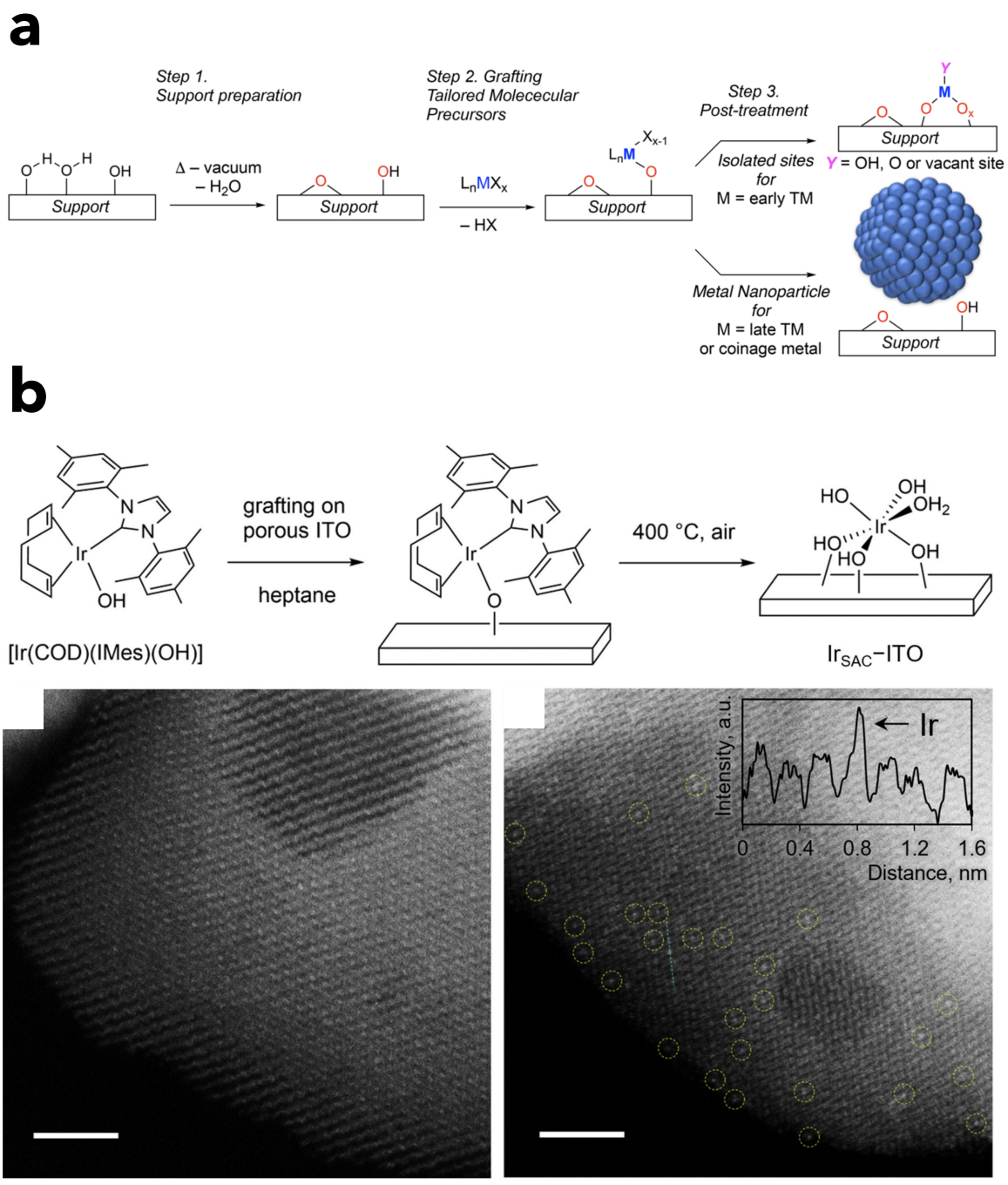


Figure 1.5: Synthesis of single-site catalysts using SOMC-TMP. (a) A schematic of the SOMC-TMP. Adapted with permission from [50]. Copyright 2019 American Chemical Society. (b) An example of utilisation of SOMC-TMP for the preparation of atomically dispersed Ir on indium tin oxide (Ir_{SAC}-ITO) for the acidic oxygen evolution (top). High-angle annular dark field (HAADF) scanning transmission electron microscopy (STEM) images show the [Ir(COD)(IMes)(OH)] grafted on ITO (bottom left) and the Ir_{SAC}-ITO (bottom right). Adapted with permission from [14]. Copyright 2020 American Chemical Society.

ligand on the metal precursor altogether (Figure 1.6d).

In their report, using the Ni supported on nitrogen-doped carbon as an example, they demonstrated a significant difference in the metal dispersion between the sample prepared with one-step and two-step annealing methods (Figure 1.6a-c). Ni is atomically dispersed on the support using the two-step annealing method at 10 wt% of Ni loading. In contrast, Ni nanoparticles (NP) of approximately 100 nm are observed using the one-step annealing method at the same Ni loading. Using this two-step annealing method, they demonstrated an atomically dispersed Ir on CeO_2 sample with an Ir loading of 10 wt% (Figure 1.6e). They also showed the ability to scale this synthesis towards kilogram productions, demonstrating its potential in industrial application.

Other synthetic strategies, such as photochemical synthesis [52] removing the ligands on Ir precursor by a UV treatment of the sample to produce Ir single atoms on NiFe oxyhydroxides, or the oxidative ligand exchange from K_2IrCl_6 with MnO_2 to trap the Ir into MnO_2 surface, were reported [28]. These strategies are more specific to the material's chemistry and less broadly applicable to all other substrates.

1.4 Structure-activity relationship of atomically dispersed metal catalysts and clusters

As emphasised in Section 1.2.3, it can be challenging to characterise if oxidised metal clusters are present in the presumed atomically dispersed metal sample. This ambiguity in the determination of the metal dispersion can lead to biased interpretations of the structure-property relationship of atomically dispersed metal catalysts, as oxidised metal clusters have been shown to exhibit significantly different activity compared to their atomically dispersed counterparts.

One example is the different intrinsic activity between the trapped Pt single-site

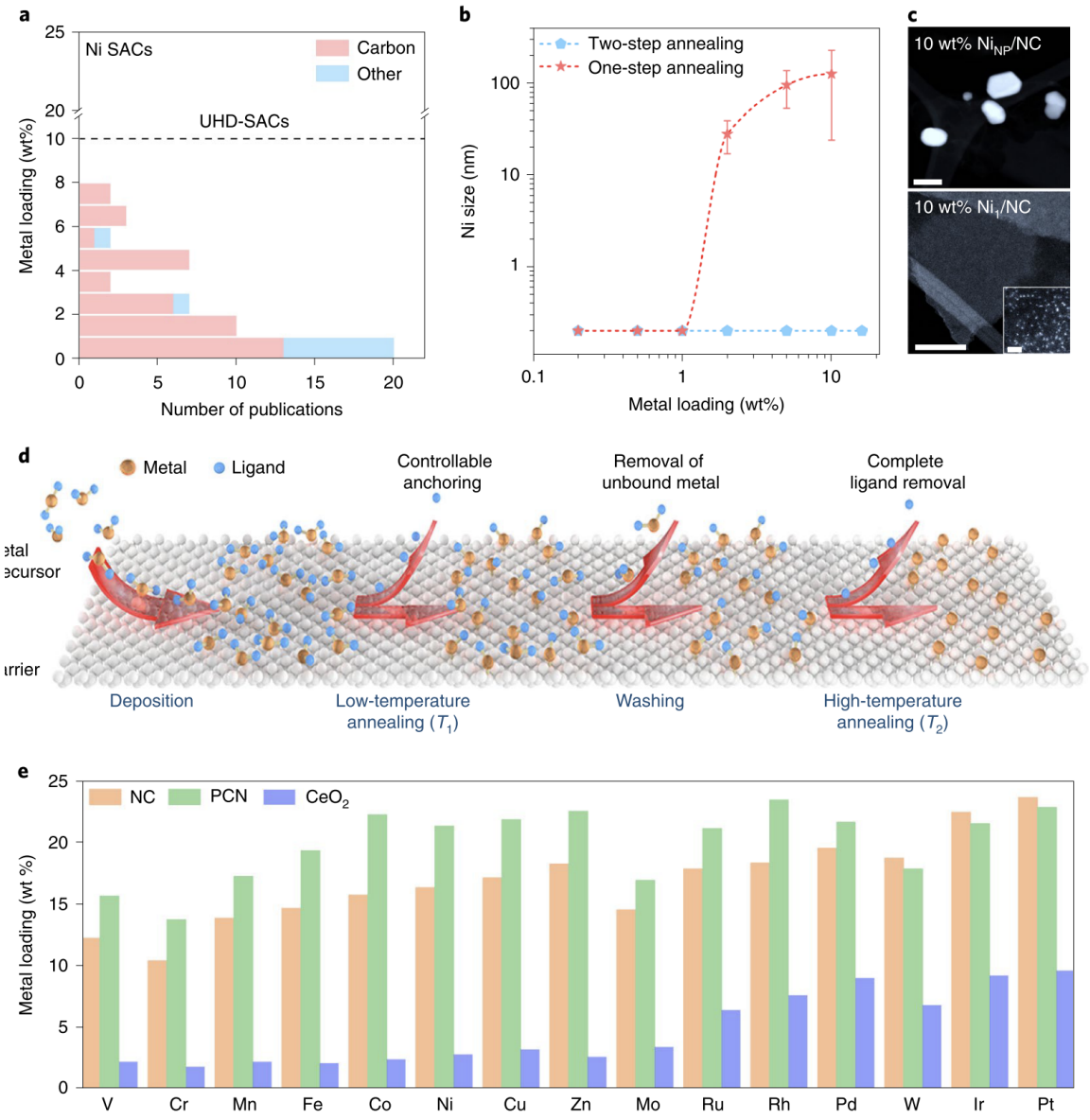


Figure 1.6: Synthesis of ultra-high density (UHD) single-atom catalysts (SACs) using the two-step annealing strategy. (a) Literature survey of the Ni content in Ni SACs. (b) Comparison between the sizes of Ni on nitrogen-doped carbon (NC) prepared with one-step annealing and two-step annealing as a function of the Ni content. Ni precursor is loaded with the conventional impregnation method. (c) HAADF-STEM images of 10 wt% the Ni on NC prepared with one-step annealing (top) and a two-step annealing (bottom). Scale bars are 100 nm (inset: 1 nm). (d) A schematic of the two-step annealing protocol for the synthesis of UHD-SACs. (e) Metal loadings of the SAC prepared on nitrogen-doped carbon (NC), polymeric carbon nitride (PCN) and CeO_2. Reprinted with permission from [51]. Copyright 2022 Nature Publishing Group.

catalysts (Pt-SSCs) in a nitrogen-doped graphitic support compared to Pt nanoparticles (PtNP) supported on the same support for the HER (Figure 1.7) [53]. As shown by Huang and coworkers, they synthesised an array of Pt samples on the same nitrogen-doped graphitic substrate. By varying the Pt loading, they presented the 1 wt% sample as the trapped Pt-SSCs. Increasing the Pt loading to 10 wt%, the sample becomes PtNP dominant (Figure 1.7a). Comparing their HER activities in acid, normalised to the total Pt mass, they discovered that despite the higher Pt metal dispersion, the activity of the trapped Pt-SSC is lower than that of the PtNP (Figure 1.7b). Their DFT calculation revealed that this inferior activity of the trapped Pt-SSCs results from a less favourable hydrogen absorption energy at their Pt sites compared to that at metallic Pt(111) surfaces, leading to a less unfavourable HER thermodynamics (Figure 1.7c).

For the acidic OER, Bozal-Ginesta and coworkers investigated the OER kinetics on an Ir molecular catalyst ($Ir_{Molecular}$) and an IrO_x catalyst using operando UV-Vis spectroscopy (Figure 1.8) [54]. They revealed that $Ir_{Molecular}$ exhibited a potential-independent reaction kinetics, whereas the IrO_x showed a potential-dependent kinetics. They proposed that the $Ir_{Molecular}$ activity was regulated by the ligands bonded to the Ir, stabilising the t_{2g} d-orbital of the Ir, leading to a decrease in the bonding strength between Ir and O. This weaker Ir-O bond lowers the reaction barrier for the OOH formation on Ir, which is well accepted as the rate-determining step for OER on Ir-based materials [55]. While for the IrO_x, the OER potential drives surface hole (*O) accumulation, resulting in a decrease of the reaction barrier for the rate determination step and showing a cooperative effect between neighbouring Ir, in agreement with Nong and coworkers and Liang and coworkers observations [56, 57].

These results motivate the investigation of the OER mechanism of atomically dispersed Ir supported on metal oxide supports. Particularly, insights into the metal oxide support that influences the OER activity of atomically dispersed Ir are desired.

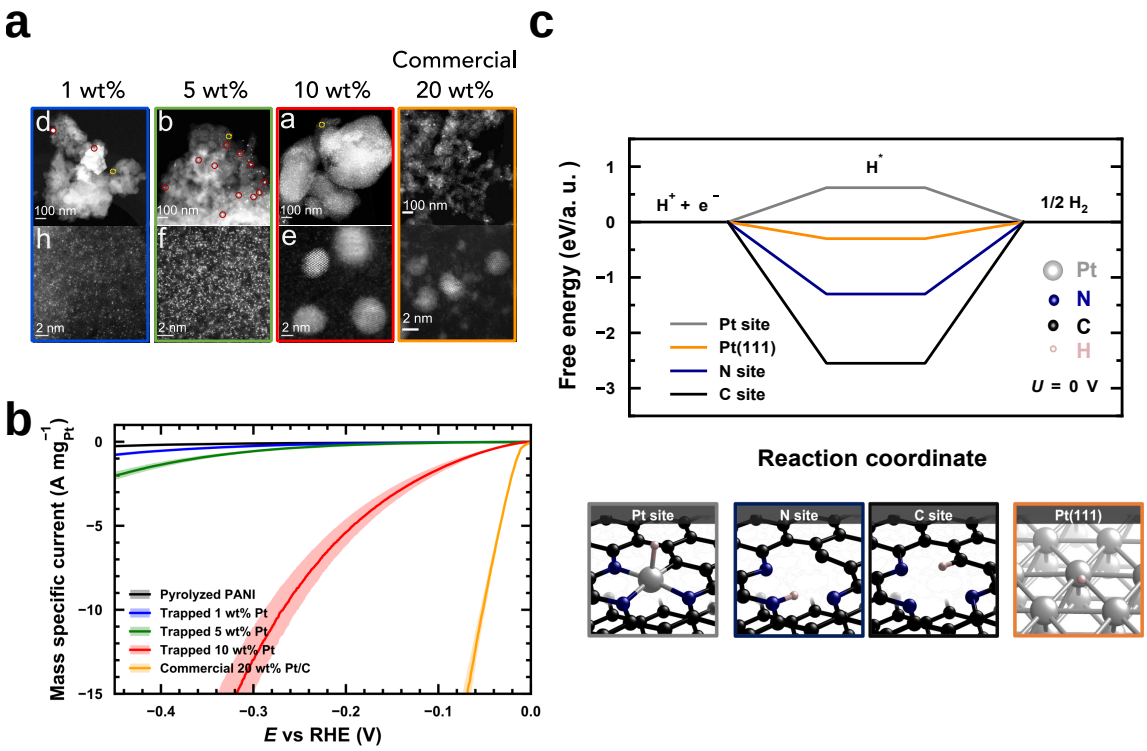


Figure 1.7: An platinum single-site catalysts (Pt-SSCs) example demonstrating the difference in intrinsic activity between the trapped Pt-SSC and the commercial Pt/C for the hydrogen evolution reaction (HER). (a) HAADF-STEM images of Pt on nitrogen-doped graphitic carbon with increasing Pt weight loading, with 1 wt% as the trapped Pt-SSC and 20 wt% as the commercial Pt/C. (b) Pt-mass-normalised HER current responses of the samples are shown in (a). (c) DFT free energy diagram for the hydrogen evolution on the Pt-SSC sample with the corresponding relaxed structures of hydrogen adsorbed on the Pt site, N site, C site on the Pt-SSC and FCC site on Pt(111) surface. Adapted from [53]. Copyright 2023 The Authors. Published by American Chemical Society.

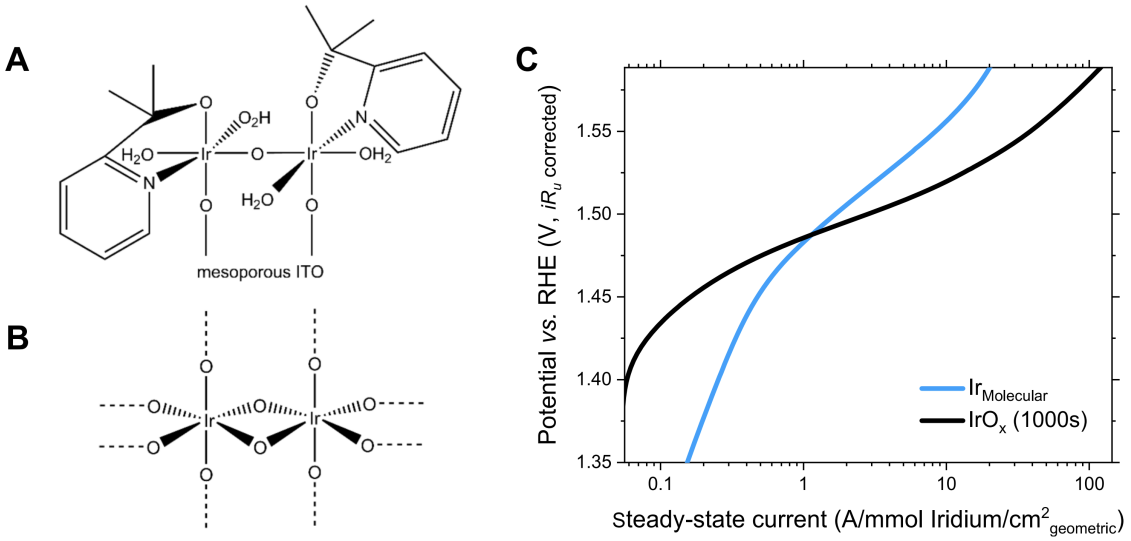


Figure 1.8: A mechanistic OER kinetics study comparing $Ir_{Molecular}$ and IrO_x to highlight the role of Ir's local environment in regulating OER kinetics. (a) Structure of $Ir_{Molecular}$, (b) schematic of IrO_x and (c) Tafel plot comparing the sample in (a) and (b) with current measured at steady state, normalised to per mol of electrochemically active iridium. Reprinted with permission from [54]. Copyright 2022 The Authors. Published by American Chemical Society.

However, such a study is only valid until a rigorous and representative characterisation of the Ir dispersion can be established. Therefore, again, it highlights the need to develop more advanced characterisation strategies.

1.5 Thesis objective

In light of the limited number of reports on the synthesis and structural-activity-stability relationship of atomically dispersed Ir electrocatalysts for the acidic OER, I dedicate this thesis to providing a fundamental understanding of the development of the atomically dispersed Ir on TiO_2 anatase nanosheets for the acidic OER. This material system is chosen based on the stability of the TiO_2 for the acidic OER and the large Z-contrast of Ir against Ti for the HAADF-STEM characterisation of the Ir dispersion. Nanosheet support morphology further enables a larger characterisation length scale in HAADF-STEM. The anatase phase is chosen for its high surface area

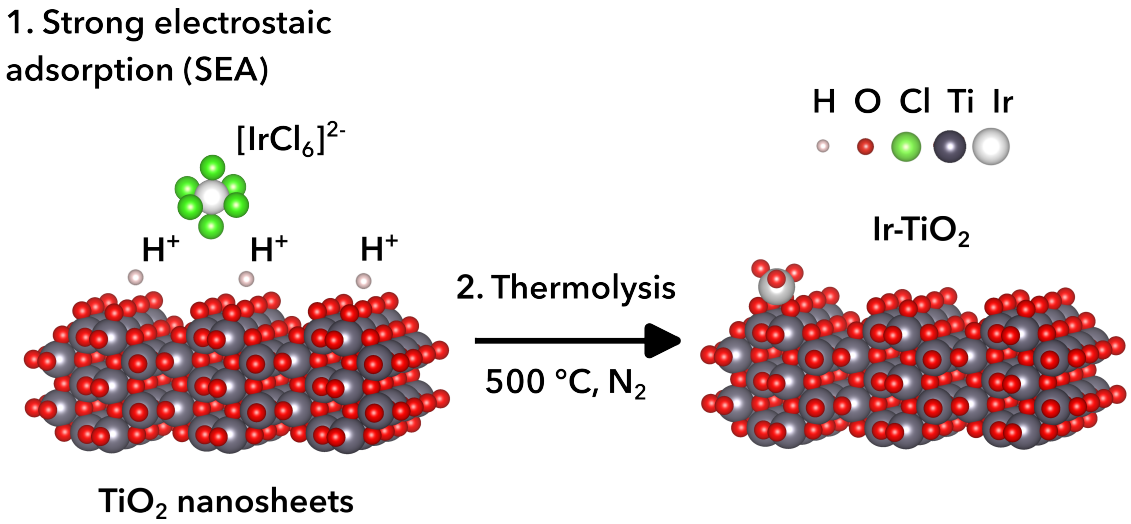


Figure 1.9: Schematic of the synthesis strategy for the atomically dispersed Ir on TiO_2 nanosheets used in this study. The synthesis begins with the loading of $[IrCl_6]^{2-}$ on the TiO_2 nanosheets using the strong electrostatic absorption (SEA), followed by a thermolysis step in N_2 to decompose $[IrCl_6]^{2-}$ and remove the Cl^- for the formation of atomically dispersed Ir on TiO_2 nanosheets (Ir-TiO_2). Schematic produced with the Vesta 3 software [65].

relative to the rutile phase, enabling larger Ir loading [58].

In this thesis, I investigate a synthesis method using the strong electrostatic absorption (SEA) to load $[IrCl_6]^{2-}$ onto TiO_2, followed by a one-step thermolysis in N_2 to remove ligands and stabilise atomically dispersed Ir on TiO_2, as shown in Figure 1.9. This method is motivated by the following considerations: Firstly, SEA can uniformly load metal complexes from aqueous solutions onto metal oxide surfaces [59, 60, 61]. Second, N_2 is used to minimize modifications to the TiO_2 surface, particularly to avoid introducing surface defects, which have been shown to influence the stability of the anchored Ir [62]. Lastly, $[IrCl_6]^{2-}$ is chosen based on successful synthesis outcomes reported previously [33, 34, 35, 36, 37, 63, 64].

In more detail, the objectives of this thesis work in each chapter are as follows: Chapter 3: Synthesis and characterisation of atomically dispersed Ir on TiO_2 anatase nanosheets

- Develop a synthesis method to prepare atomically dispersed Ir on TiO_2

- Optimise the framework for the characterisation of Ir dispersion on TiO_2

Chapter 4: Synthesis mechanism of atomically dispersed Ir on TiO_2 anatase nanosheets

- Determine the chemical states and bonding environment of Ir at different stages of the synthesis temperature using XAFS analysis
- Investigate the behaviour of Ir agglomeration and the evolution of Ir mobility with increasing temperature
- Unravel the synthesis mechanism of the atomically dispersed Ir on TiO_2

Chapter 5: Oxygen evolution reaction properties of atomically dispersed Ir on TiO_2 nanosheets

- Establish a statistically significant representation of Ir dispersion on TiO_2
- Elucidate the structure-activity-stability relationship of the atomically dispersed Ir on TiO_2 for the acidic OER

1.6 Nomenclatures used in this work

Using atomically dispersed metal catalysts has been an exciting front for heterogeneous catalysis, with numerous reports discovering significant activity improvements to traditional nanoparticle-based catalysts [66, 67]. These catalysts are commonly referred to as the single-atom catalyst (SAC), whose definition is from the observation of the atomically isolated features in HAADF-STEM. A lack of sub-categorising these SACs with their chemical nature, i.e., their oxidation states and local bonding environments that are key to their catalytic activities, renders a literature comparison between catalysts confusing [68].

Therefore, during my literature search, I subcategorised the atomically dispersed metal catalysts by their oxidation states and local environments (Figure 1.10). The metallic atoms, regardless of their single or multiple bonding environments, belong as the SACs. When the atomically dispersed metal catalysts have rigorously a single bonding environment uniform throughout the sample, they can be categorised as SSCs, regardless of their oxidation states. The SSCs resemble the hetereogeneised metallorganic molecular catalysts with single metal active sites, which is the ideal system for reaction mechanistic study. Whenever the atomically dispersed metal catalysts do not belong to either SACs or SSCs due to the presence of a distribution of multiple types of bonding environments for the metal centre or the metal centre is not in its metallic state, it would be more accurate to call the sample an atomically dispersed metal catalyst as a general note. The atomically dispersed Ir electrocatalysts developed in this thesis work show an Ir oxidation state of +4, and the Ir can be found in various local environments (at the terrace and step edges of the TiO_2 nanosheets). Therefore, they cannot be categorised as SAC and SSC. Hence, I name them as atomically dispersed Ir electrocatalysts.

For the clarity of this thesis, I avoid the use of the term Ir "atoms" when describing the atomic features with high contrast against the TiO_2 substrate in the HAADF-STEM images, since this implies that these features are Ir in their metallic atom form, which cannot be confirmed from HAADF-STEM images alone. Until spatially resolved spectroscopic analysis like EELS is performed to confirm the oxidation state of these atomically dispersed Ir and their bonding environments, or annular bright field (ABF) images are leveraged to locate the positions of light elements such as Cl and O that are surrounding the Ir, I refer to these atomic features as atomically dispersed Ir, or Ir_1 for brevity, regardless of their chemical structures. This reference is based on the observed size of the features, which is consistent with a single Ir atom, ion or complex, and their high contrast against the TiO_2 substrate. Complementing

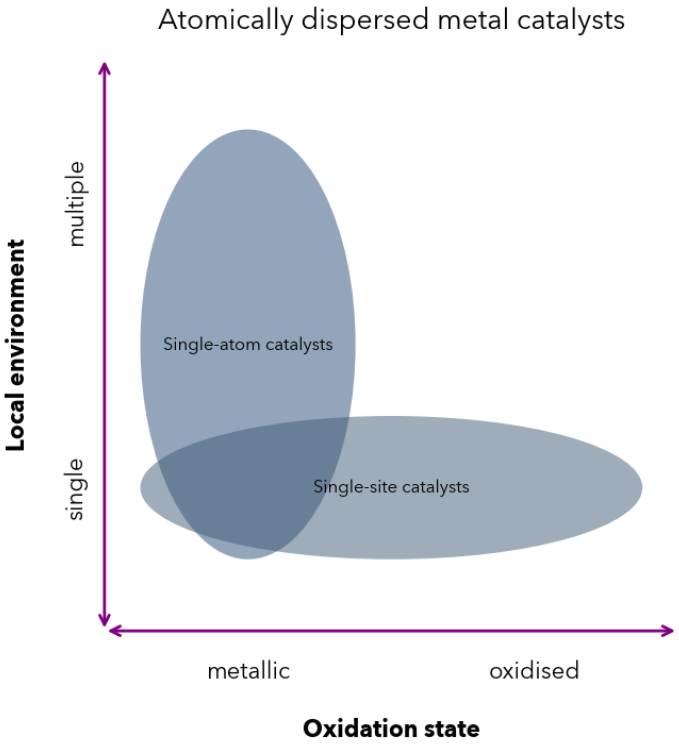


Figure 1.10: Schematic of the categorisation of single-atom catalysts (SACs), single-sit catalysts (SSCs) and atomically dispersed metal catalysts as a function of the metal's oxidation state and local environment [69].

the spatially resolved HAADF-STEM analysis, I determined the chemical bonding environments of these metal species using XAS and XPS in this work, assuming they are homogeneous throughout the sample.

This nomenclature is essential for discussing the in-situ heating ADF-STEM experiments in Chapter 4, where I compare the mobility of Ir at different temperatures. Following the description above, I refer to the isolated atomic features in the ADF-STEM images at both 80 °C and 500 °C as Ir_1, even though the later XAFS analysis suggests that the Ir_1 corresponds to $[IrCl_6]^{2-}$ at 80 °C, and the Ir_1 at 500 °C is a six-fold O-coordinated structure.

Table 1.2: Overview of state-of-the-art atomically dispersed Ir catalysts for the acidic OER. All potentials are referenced vs. the reversible hydrogen electrode (RHE).

Catalyst	**η @ 10 mA cm^{-2}_{geo} (mV)**	**Mass activity (A g_{Ir}^{-1})**	**Electrolyte**	**Reference**
Ir_{SAC}-ITO	220 ± 5	156 ± 13 @ 1.51 V	0.1 M $HClO_4$	Lebedev et al. [14]
TiO_xN_y-Ir	/	450 @ 1.55 V	0.1 M $HClO_4$	Suhadolnik et al. [70]
Ir-MnO_2	218	766 @ 1.53 V	0.5 M H_2SO_4	Shi et al. [71]
Ir-$MnCo_2O_{4.5}$	238	57 @ 1.5 V	0.5 M H_2SO_4	Hua et al. [72]
Ir_1/V_o-CoOOH	200	605.4 @ 1.53 V	0.5 M H_2SO_4	Zhang et al. [73]
Ir-Co_3O_4	236	3343.37 @ 1.53 V	0.5 M H_2SO_4	Zhu et al. [29]
Ir_1-Co_3O_4-NS	226	6318 @ 1.53 V	0.5 M H_2SO_4	Liu et al. [74]
$Ir_{0.06}Co_{2.94}O_4$	∼295	2511 @ 1.53 V	0.5 M H_2SO_4	Shan et al. [75]
Ir^{VI}-ado	20 mA cm^{-2}_{geo} @ 1.5 V in PEM cell	∼250 @ 1.55 V (from plot)	1 M H_2SO_4	Li et al. [28]

Table 1.3: Overview of benchmark Ir-based catalysts for the acidic OER. All potentials are referenced vs. the reversible hydrogen electrode (RHE).

Catalyst	**Ir (wt%)**	**Mass Activity (A g_{Ir}^{-1})**	**Electrolyte**	**Reference**
IrO_x (Alfa Aesar)	84.5	139 ± 6 @ 1.55 V	0.5 M H_2SO_4	Hoffmeister et al. [13]
IrO_x (Alfa Aesar)	84.5	279 @ 1.55 V	0.1 M $HClO_4$	Van Pham et al. [19]
IrO_x (Alfa Aesar)	84.5	557.9 ± 28.5 @ 1.55 V	0.5 M H_2SO_4	Baik et al. [11]
IrO_2-TiO_2-Umicore	75	14 ± 4 @ 1.525 V	0.5 M H_2SO_4	Oakton et al. [12]
IrO_2-TiO_2-Umicore	75	10.6 ± 0.6 @ 1.55 V	0.5 M H_2SO_4	Hoffmeister et al. [13]
IrO_2-TiO_2-Umicore	75	47 @ 1.55 V	0.1 M $HClO_4$	Van Pham et al. [19]
IrO_2-TiO_2-Umicore	75	420 @ 1.8 V	0.1 M $HClO_4$	Regmi et al. [76]
TiO_2@IrO_x	40	49 ± 6 @ 1.55 V	0.5 M H_2SO_4	Hoffmeister et al. [13]
IrO_2-TiO_2	56	70 @ 1.55 V	0.5 M H_2SO_4	Oakton et al.[12]
IrO_2-TiO_2	75	112 @ 1.55 V	0.1 M $HClO_4$	Van Pham et al. [19]
Ir/TiO_2	30	209.0 ± 16.9 @ 1.55 V	0.5 M H_2SO_4	Baik et al. [11]

Basics of electrochemical splitting of water

Reaction thermodynamics

The total reaction of the electrochemical splitting of water in acidic media is given as:

$$\mathrm{H_2O_{(l)}} \longrightarrow \frac{1}{2}\mathrm{O_{2(g)}} + \mathrm{H_{2(g)}}, \quad E_{\mathrm{cell}}, \tag{1.1}$$

where the half-cell reaction at the anode is the oxygen evolution reaction (OER)

$$\mathrm{H_2O_{(l)}} \longrightarrow \frac{1}{2}\mathrm{O_{2(g)}} + 2\,\mathrm{H_{(aq)}}^{+} + 2\,\mathrm{e}^{-}, \quad E_{\mathrm{anode}}, \tag{1.2}$$

and at the cathode is the hydrogen evolution reaction (HER) with a half-reaction potential

$$2\,\mathrm{H_{(aq)}}^{+} + 2\,\mathrm{e}^{-} \longrightarrow \mathrm{H_{2(g)}}, \quad E_{\mathrm{cathode}}. \tag{1.3}$$

The standard cell potential (E_{cell}) can be written as:

$$E_{\mathrm{cell}} = E_{\mathrm{cathode}} - E_{\mathrm{anode}}. \tag{1.4}$$

The Gibbs free energy change of the full reaction governs the cell potential:

$$\Delta G = \Delta H - T\Delta S = -nFE_{\mathrm{cell}}. \tag{1.5}$$

where ΔG is the Gibbs free energy change, n is the moles of electrons transferred in the reaction, F is the Faraday constant, ΔH is the reaction enthalpy change, T is the absolute temperature, and ΔS is the reaction entropy change.

To split water at standard conditions (25 °C and 1 bar pressure), a Gibbs free energy change of $+237.18\,\mathrm{kJ\ mol^{-1}}$ is required. This corresponds to a cell potential ($E^{\circ}_{\mathrm{cell}}$) of 1.23 V. When referencing against the standard hydrogen electrode (SHE)

at 0 V, the standard electrode potential for OER equals 1.23 V.

When the half-cell reactions deviate from standard conditions, the electrode potential can be described with the Nernst equation:

$$E = E^{\circ} + \frac{RT}{nF} \ln \left(\frac{\prod (a_i^{v_i})_{\text{oxidised}}}{\prod (a_i^{v_i})_{\text{reduced}}} \right), \tag{1.6}$$

where R is the gas constant, T is the temperature in kelvins, n is the number of moles of electrons transferred in the reaction, F is the Faraday constant, a_i is the activity of species i, and v_i is the stoichiometric coefficient of species i. For the acidic OER, this equation rewrites as:

$$\begin{aligned} E_{(\mathrm{O_2/H_2O})} &= E^{\circ}_{(\mathrm{O_2/H_2O})} + \frac{RT}{2F} \ln \left(\frac{(a_{\mathrm{O_2}})^{0.5} \cdot (a_{\mathrm{H^+}})^2}{a_{\mathrm{H_2O}}} \right) \\ &= E^{\circ}_{(\mathrm{O_2/H_2O})} - 0.059 \cdot \mathrm{pH} + 0.015 \cdot \log \left(\frac{p_{\mathrm{O_2}}}{p^{\circ}_{\mathrm{O_2}}} \right). \end{aligned} \tag{1.7}$$

Equation 1.7 entails that the OER electrode potential vs SHE is pH-dependent. The reversible hydrogen electrode (RHE) is commonly used as the potential reference to remove this variation for a direct comparison of OER at different pH values, where $E_{\mathrm{RHE}} = E_{\mathrm{SHE}} + 0.059 \cdot \mathrm{pH}$.

Reaction kinetics

The kinetics of a electrochemical reaction is govern by the Butler-Volmer equation, which describes the correlation between the reaction current density and overpotential [77, 78, 79]:

$$i = i_0(T, c_O, c_R) \cdot \mathrm{rf} \cdot \left[\exp \left(\frac{\alpha \cdot n \cdot F \cdot \eta}{R \cdot T} \right) - \exp \left(\frac{(1-\alpha) \cdot n \cdot F \cdot \eta}{R \cdot T} \right) \right], \tag{1.8}$$

where i is the current density (A cm^{-2}), $i_0(T, c_O, c_R)$ is the exchange current density as a function of temperature T, oxidant concentration c_O, and reductant concentration

c_R, rf is the roughness factor, which describes the ratio between the actual surface area of the catalyst and the geometric surface area of the catalyst-loaded electrode, α is the charge transfer coefficient, n is the number of electrons transferred, and η is the overpotential, which is the difference between the operation potential of an electrode against the reaction equilibrium potential.

Note here I adopt Vilestich's nomenclature to separate the rf from the geometric density, aiming to emphasise the intrinsic activity of the catalyst, which scales with the real catalyst surface area instead of the geometric area of the electrode, on which catalysts are coated [77].

The Bulter-Volmer equation can be approximated as the Tafel equation at high overpotentials, where either the anodic or the cathodic part of the Bulter-Volmer equation is dominant:

$$\eta = a + b\log(i), \tag{1.9}$$

where a is a constant and b is the Tafel slope (mV decade^{-1}), which entails the overpotential that is required to increase the reaction current density by 10-fold.

Lowering the catalyst loading by a factor of 40 equals a reduction of the rf in Equation 1.8 by 40-fold. Considering the use of a typical IrO_2 catalyst with a Tafel slope of 50 mV decade^{-1} [56], the overpotential penalty with the 40-fold reduction of the Ir loading can be written using the Tafel equation as $\Delta\eta = 50 \cdot \log(40) = 80\,\mathrm{mV}$.

References

[1] IEA. Net Zero by 2050. 2021.

[2] Charles C.L. McCrory, Suho Jung, Jonas C. Peters, and Thomas F. Jaramillo. Benchmarking heterogeneous electrocatalysts for the oxygen evolution reaction. *Journal of the American Chemical Society*, 135(45):16977–16987, 11 2013.

[3] Xinlong Lin, Justin Zhu Yeow Seow, and Zhichuan J. Xu. A brief introduction of electrode fabrication for proton exchange membrane water electrolyzers. *JPhys Energy*, 5(3), 7 2023.

[4] Marie Francine Lagadec and Alexis Grimaud. Water electrolysers with closed and open electrochemical systems. *Nature Materials*, 19(11):1140–1150, 2020.

[5] IEA. The Future of Hydrogen. Technical Report June, 2019.

[6] McKenzie A. Hubert, Laurie A. King, and Thomas F. Jaramillo. Evaluating the Case for Reduced Precious Metal Catalysts in Proton Exchange Membrane Electrolyzers. *ACS Energy Letters*, 7(1):17–23, 2022.

[7] Jakob Kibsgaard and Ib Chorkendorff. Considerations for the scaling-up of water splitting catalysts. *Nature Energy*, 4(6):430–433, 2019.

[8] Maximilian Bernt, Alexandra Hartig-Weiß, Mohammad Fathi Tovini, Hany A. El-Sayed, Carina Schramm, Jonas Schröter, Christian Gebauer, and Hubert A. Gasteiger. Current Challenges in Catalyst Development for PEM Water Electrolyzers. *Chemie-Ingenieur-Technik*, 92(1-2):31–39, 2020.

[9] Maximilian Bernt, Armin Siebel, and Hubert A. Gasteiger. Analysis of Voltage Losses in PEM Water Electrolyzers with Low Platinum Group Metal Loadings. *Journal of The Electrochemical Society*, 165(5):F305–F314, 2018.

[10] Ugljesa Babic, Michel Suermann, Felix N. Büchi, Lorenz Gubler, and Thomas J. Schmidt. Critical Review—Identifying Critical Gaps for Polymer Electrolyte Water Electrolysis Development. *Journal of The Electrochemical Society*, 164(4):F387–F399, 2017.

[11] Chaekyung Baik, Jinwon Cho, Jeong In Cha, Youngin Cho, Seung Soon Jang, and Chanho Pak. Electron-rich Ir nanostructure supported on mesoporous Ta2O5 for enhanced activity and stability of oxygen evolution reaction. *Journal of Power Sources*, 575, 8 2023.

[12] Emma Oakton, Dmitry Lebedev, Mauro Povia, Daniel F. Abbott, Emiliana Fabbri, Alexey Fedorov, Maarten Nachtegaal, Christophe Copéret, and Thomas J. Schmidt. IrO2-TiO2: A High-Surface-Area, Active, and Stable Electrocatalyst for the Oxygen Evolution Reaction. *ACS Catalysis*, 7(4):2346–2352, 4 2017.

[13] Darius Hoffmeister, Selina Finger, Lena Fiedler, Tien Ching Ma, Andreas Körner, Matej Zlatar, Birk Fritsch, Kerstin Witte Bodnar, Simon Carl, Alexander Götz, Benjamin Apeleo Zubiri, Johannes Will, Erdmann Spiecker, Serhiy Cherevko, Anna T.S. Freiberg, Karl J.J. Mayrhofer, Simon Thiele, Andreas Hutzler, and Chuyen van Pham. Photodeposition-Based Synthesis of TiO2@IrOx Core–Shell Catalyst for Proton Exchange Membrane Water Electrolysis with Low Iridium Loading. *Advanced Science*, 11(30), 8 2024.

[14] Dmitry Lebedev, Roman Ezhov, Javier Heras-Domingo, Aleix Comas-Vives, Nicolas Kaeffer, Marc Willinger, Xavier Solans-Monfort, Xing Huang, Yulia Pushkar, and Christophe Copéret. Atomically Dispersed Iridium on Indium Tin Oxide Efficiently Catalyzes Water Oxidation. *ACS Central Science*, 6(7):1189–1198, 7 2020.

[15] Matej Zlatar, Darryl Nater, Daniel Escalera-López, Rani Mary Joy, Paulius

Pobedinskas, Ken Haenen, Christophe Copéret, and Serhiy Cherevko. Evaluating the stability of Ir single atom and Ru atomic cluster oxygen evolution reaction electrocatalysts. *Electrochimica Acta*, 444, 3 2023.

[16] Qiaoqiao Zhang and Jingqi Guan. Single-Atom Catalysts for Electrocatalytic Applications. *Advanced Functional Materials*, 30(31):1–53, 2020.

[17] Sean J. Ashton and Matthias Arenz. A DEMS study on the electrochemical oxidation of a high surface area carbon black. *Electrochemistry Communications*, 13(12):1473–1475, 2011.

[18] Jesse D. Benck, Blaise A. Pinaud, Yelena Gorlin, and Thomas F. Jaramillo. Substrate selection for fundamental studies of electrocatalysts and photoelectrodes: Inert potential windows in acidic, neutral, and basic electrolyte. *PLoS ONE*, 9(10), 10 2014.

[19] Chuyen Van Pham, Melanie Bühler, Julius Knöppel, Markus Bierling, Dominik Seeberger, Daniel Escalera-López, Karl J.J. Mayrhofer, Serhiy Cherevko, and Simon Thiele. IrO2 coated TiO2 core-shell microparticles advance performance of low loading proton exchange membrane water electrolyzers. *Applied Catalysis B: Environmental*, 269, 7 2020.

[20] Petr Mazúr, Jakub Polonský, Martin Paidar, and Karel Bouzek. Non-conductive TiO 2 as the anode catalyst support for PEM water electrolysis. *International Journal of Hydrogen Energy*, 37(17):12081–12088, 9 2012.

[21] Olga Kasian, Tong Li, Andrea M. Mingers, Kevin Schweinar, Alan Savan, Alfred Ludwig, and Karl Mayrhofer. Stabilization of an iridium oxygen evolution catalyst by titanium oxides. *JPhys Energy*, 3(3), 7 2021.

[22] Guoying Chen, Simon R. Bare, and Thomas E. Mallouk. Development of Sup-

ported Bifunctional Electrocatalysts for Unitized Regenerative Fuel Cells. *Journal of The Electrochemical Society*, 149(8):A1092–A1099, 8 2002.

[23] Chuanpu Hao, Hong Lv, Cangen Mi, Yukun Song, and Jianxin Ma. Investigation of Mesoporous Niobium-Doped TiO2 as an Oxygen Evolution Catalyst Support in an SPE Water Electrolyzer. *ACS Sustainable Chemistry and Engineering*, 4(3):746–756, 3 2016.

[24] Chinmayee V. Subban, Qin Zhou, Anthony Hu, Thomas E. Moylan, Frederick T. Wagner, and Francis J. Disalvo. Sol-gel synthesis, electrochemical characterization, and stability testing of Ti0.7W0.3O2 nanoparticles for catalyst support applications in proton-exchange membrane fuel cells. *Journal of the American Chemical Society*, 132(49):17531–17536, 12 2010.

[25] Shuai Zhao, Allison Stocks, Brian Rasimick, Karren More, and Hui Xu. Highly Active, Durable Dispersed Iridium Nanocatalysts for PEM Water Electrolyzers. *Journal of The Electrochemical Society*, 165(2):F82–F89, 2018.

[26] Marjan Bele, Kevin Stojanovski, Primoz Jovanovič, Leonard Moriau, Gorazd Koderman Podboršek, Jože Moškon, Polona Umek, Melita Sluban, Goran Dražič, Nejc Hodnik, and Miran Gaberšček. Towards Stable and Conductive Titanium Oxynitride High-Surface-Area Support for Iridium Nanoparticles as Oxygen Evolution Reaction Electrocatalyst. *ChemCatChem*, 11(20):5038–5044, 10 2019.

[27] Léonard Moriau, Gorazd Koderman Podboršek, Angelja Kjara Surca, Sorour Semsari Parpari, Martin Šala, Urša Petek, Marjan Bele, Primož Jovanovič, Bostjan Genorio, and Nejc Hodnik. Enhancing Iridium Nanoparticles' Oxygen Evolution Reaction Activity and Stability by Adjusting the Coverage of Titanium Oxynitride Flakes on Reduced Graphene Oxide Nanoribbons' Support. *Advanced Materials Interfaces*, 8(17), 9 2021.

[28] Ailong Li, Shuang Kong, Kiyohiro Adachi, Hideshi Ooka, Kazuna Fushimi, Qike Jiang, Hironori Ofuchi, Satoru Hamamoto, Masaki Oura, Kotaro Higashi, Takuma Kaneko, Tomoya Uruga, Naomi Kawamura, Daisuke Hashizume, and Ryuhei Nakamura. Atomically dispersed hexavalent iridium oxide from MnO2 reduction for oxygen evolution catalysis. *Science*, 384(6696):666–670, 5 2024.

[29] Yiming Zhu, Jiaao Wang, Toshinari Koketsu, Matthias Kroschel, Jin Ming Chen, Su Yang Hsu, Graeme Henkelman, Zhiwei Hu, Peter Strasser, and Jiwei Ma. Iridium single atoms incorporated in Co3O4 efficiently catalyze the oxygen evolution in acidic conditions. *Nature Communications*, 13(1), 12 2022.

[30] Alejandra Ramírez, Philipp Hillebrand, Diana Stellmach, Matthias M. May, Peter Bogdanoff, and Sebastian Fiechter. Evaluation of MnOx, Mn2O3, and Mn 3O4 electrodeposited films for the oxygen evolution reaction of water. *Journal of Physical Chemistry C*, 118(26):14073–14081, 7 2014.

[31] Hsin Yi Wang, Sung Fu Hung, Ying Ya Hsu, Lulu Zhang, Jianwei Miao, Ting Shan Chan, Qihua Xiong, and Bin Liu. In situ spectroscopic identification of μ-OO bridging on spinel Co3O4 water oxidation electrocatalyst. *Journal of Physical Chemistry Letters*, 7(23):4847–4853, 2016.

[32] Rui Lang, Xiaorui Du, Yike Huang, Xunzhu Jiang, Qian Zhang, Yalin Guo, Kaipeng Liu, Botao Qiao, Aiqin Wang, and Tao Zhang. Single-Atom Catalysts Based on the Metal-Oxide Interaction, 11 2020.

[33] Aiping Jia, Wei Zhang, Hantao Peng, Yunshang Zhang, Tongyang Song, Lei Li, Yanwen Ye, Yu Wang, Mengfei Luo, De Li Chen, Weixin Huang, and Ji Qing Lu. Selective hydrogenation of crotonaldehyde over Ir/TiO2 catalysts: Unraveling the metal-support interface related reaction mechanism. *Journal of Catalysis*, 425:57–69, 9 2023.

[34] Haofei Wu, Zheng Li, Qiwen Zhang, Luozhen Jiang, Chen Hou, Shufen Chu, Jing Feng, Wenwu Xu, Lina Li, Fang Song, Mingwei Chen, and Pan Liu. Chloride ligand stablizes single-atom on nanoporous metal oxides in a pyrolysis process. *Chemical Engineering Journal*, 497, 10 2024.

[35] Xue Peng Yin, Hong Juan Wang, Shang Feng Tang, Xiu Li Lu, Miao Shu, Rui Si, and Tong Bu Lu. Engineering the Coordination Environment of Single-Atom Platinum Anchored on Graphdiyne for Optimizing Electrocatalytic Hydrogen Evolution. *Angewandte Chemie - International Edition*, 57(30):9382–9386, 2018.

[36] Shubo Tian, Wanbing Gong, Wenxing Chen, Na Lin, Youqi Zhu, Quanchen Feng, Qi Xu, Qiang Fu, Chun Chen, Jun Luo, Wensheng Yan, Huijun Zhao, Dingsheng Wang, and Yadong Li. Regulating the Catalytic Performance of Single-Atomic-Site Ir Catalyst for Biomass Conversion by Metal-Support Interactions. *ACS Catalysis*, 9(6):5223–5230, 6 2019.

[37] Coogan B. Thompson, Liping Liu, Denis S. Leshchev, Adam S. Hoffman, Jiyun Hong, Simon R. Bare, Raymond R. Unocic, Eli Stavitski, Hongliang Xin, and Ayman M. Karim. CO Oxidation on Ir1/TiO2: Resolving Ligand Dynamics and Elementary Reaction Steps. *ACS Catalysis*, 13(12):7802–7811, 6 2023.

[38] Alper Uzun, Samira F. Kurtoglu, Adam S. Hoffman, Deniz Akgül, Melike Babucci, Viktorya Aviyente, Bruce C. Gates, and Simon R. Bare. Electronic structure of atomically dispersed supported iridium catalyst controls iridium aggregation. *ACS Catalysis*, 10(21):12354–12358, 11 2020.

[39] Shufang Ji, Yuanjun Chen, Xiaolu Wang, Zedong Zhang, Dingsheng Wang, and Yadong Li. Chemical Synthesis of Single Atomic Site Catalysts, 11 2020.

[40] Kun Feng, Huizhen Zhang, Jin Gao, Jiabin Xu, Yuming Dong, Zhenhui Kang,

and Jun Zhong. Single atoms or not? The limitation of EXAFS. *Applied Physics Letters*, 116(19):191903, 2020.

[41] Jordan Finzel, Kenzie M. Sanroman Gutierrez, Adam S. Hoffman, Joaquin Resasco, Phillip Christopher, and Simon R. Bare. Limits of Detection for EXAFS Characterization of Heterogeneous Single-Atom Catalysts. *ACS Catalysis*, 13(9):6462–6473, 5 2023.

[42] Jesse D. Benck, Blaise A. Pinaud, Yelena Gorlin, and Thomas F. Jaramillo. Substrate selection for fundamental studies of electrocatalysts and photoelectrodes: Inert potential windows in acidic, neutral, and basic electrolyte. *PLoS ONE*, 9(10), 10 2014.

[43] Matthias Batzill and Ulrike Diebold. The surface and materials science of tin oxide, 2005.

[44] Shi Yuan Zhang, Ting Ting Li, Hong Lin Zhu, and Yue Qing Zheng. Co3O4 polyhedrons with enhanced electric conductivity as efficient water oxidation electrocatalysts in alkaline medium. *Journal of Materials Science*, 53(6):4323–4333, 3 2018.

[45] J.-H Lee, S M Yoon, B.-K Kim, H.-W Lee, and H S Song. Electrical conductivity and defect structure of CeO 2-ZrO 2 mixed oxide. *Journal of Materials Science*, 37:1665, 2002.

[46] Michael M Thackeray. MANGANESE OXIDES FOR LITHIUM BATTERIES. Technical report, 1997.

[47] Akira Fujishima and Xintong Zhang. Titanium dioxide photocatalysis: present situation and future approaches. *Comptes Rendus. Chimie*, 9(5-6):750–760, 2006.

[48] Cem Sevik and Ceyhun Bulutay. Theoretical study of the insulating oxides and nitrides: SiO2, GeO2, Al2O3, Si3N4, and Ge3N4. *Journal of Materials Science*, 42(16):6555–6565, 8 2007.

[49] Jaroslav Hornak, Pavel Trnka, Petr Kadlec, Ondřej Michal, Václav Mentlík, Pavol Šutta, Gergely Márk Csányi, and Zoltán Ádám Tamus. Magnesium oxide nanoparticles: Dielectric properties, surface functionalization and improvement of epoxy-based composites insulating properties. *Nanomaterials*, 8(6), 6 2018.

[50] Christophe Copéret. Single-Sites and Nanoparticles at Tailored Interfaces Prepared via Surface Organometallic Chemistry from Thermolytic Molecular Precursors. *Accounts of Chemical Research*, 52(6):1697–1708, 6 2019.

[51] Xiao Hai, Shibo Xi, Sharon Mitchell, Karim Harrath, Haomin Xu, Dario Faust Akl, Debin Kong, Jing Li, Zejun Li, Tao Sun, Huimin Yang, Yige Cui, Chenliang Su, Xiaoxu Zhao, Jun Li, Javier Pérez-Ramírez, and Jiong Lu. Scalable two-step annealing method for preparing ultra-high-density single-atom catalyst libraries. *Nature Nanotechnology*, 17(2):174–181, 2 2022.

[52] Xueli Zheng, Jing Tang, Alessandro Gallo, Jose A Garrido Torres, Xiaoyun Yu, Constantine J Athanitis, Emily May Been, Peter Ercius, Haiyan Mao, Sirine C Fakra, Chengyu Song, Ryan C Davis, Jeffrey A Reimer, John Vinson, Michal Bajdich, and Yi Cui. Origin of enhanced water oxidation activity in an iridium single atom anchored on NiFe oxyhydroxide catalyst. *Proceedings of the National Academy of Sciences*, 118(36):e2101817118, 9 2021.

[53] Peng Tang, Po-Yuan Huang, Jack E.N. Swallow, Chenbo Wang, Diego Gianolio, Hua Guo, Jamie H. Warner, Robert S. Weatherup, and Mauro Pasta. Structure-Property Relationship of Defect-Trapped Pt Single-Site Electrocatalysts for the Hydrogen Evolution Reaction. *ACS Catalysis*, 13(14):9558–9566, 7 2023.

[54] Carlota Bozal-Ginesta, Reshma R. Rao, Camilo A. Mesa, Yuanxing Wang, Yanyan Zhao, Gongfang Hu, Daniel Antón-García, Ifan E.L. Stephens, Erwin Reisner, Gary W. Brudvig, Dunwei Wang, and James R. Durrant. Spectroelectrochemistry of Water Oxidation Kinetics in Molecular versus Heterogeneous Oxide Iridium Electrocatalysts. *Journal of the American Chemical Society*, 2022.

[55] J. Rossmeisl, Z. W. Qu, H. Zhu, G. J. Kroes, and J. K. Nørskov. Electrolysis of water on oxide surfaces. *Journal of Electroanalytical Chemistry*, 607(1-2):83–89, 9 2007.

[56] Hong Nhan Nong, Lorenz J. Falling, Arno Bergmann, Malte Klingenhof, Hoang Phi Tran, Camillo Spöri, Rik Mom, Janis Timoshenko, Guido Zichittella, Axel Knop-Gericke, Simone Piccinin, Javier Pérez-Ramírez, Beatriz Roldan Cuenya, Robert Schlögl, Peter Strasser, Detre Teschner, and Travis E. Jones. Key role of chemistry versus bias in electrocatalytic oxygen evolution. *Nature*, 587(7834):408–413, 11 2020.

[57] Caiwu Liang, Reshma R. Rao, Katrine L. Svane, Joseph H.L. Hadden, Benjamin Moss, Soren B. Scott, Michael Sachs, James Murawski, Adrian Malthe Frandsen, D. Jason Riley, Mary P. Ryan, Jan Rossmeisl, James R. Durrant, and Ifan E.L. Stephens. Unravelling the effects of active site density and energetics on the water oxidation activity of iridium oxides. *Nature Catalysis*, 7 2024.

[58] Florian Kraushofer and Gareth S. Parkinson. Single-Atom Catalysis: Insights from Model Systems, 9 2022.

[59] Leo DeRita, Joaquin Resasco, Sheng Dai, Alexey Boubnov, Ho Viet Thang, Adam S. Hoffman, Insoo Ro, George W. Graham, Simon R. Bare, Gianfranco Pacchioni, Xiaoqing Pan, and Phillip Christopher. Structural evolution of atom-

ically dispersed Pt catalysts dictates reactivity. *Nature Materials*, 18(7):746–751, 7 2019.

[60] Christopher Foo, Yiyang Li, Konstantin Lebedev, Tianyi Chen, Sarah Day, Chiu Tang, and Shik Chi Edman Tsang. Characterisation of oxygen defects and nitrogen impurities in TiO2 photocatalysts using variable-temperature X-ray powder diffraction. *Nature Communications*, 12(1), 12 2021.

[61] Chithra Asokan, Mingjie Xu, Sheng Dai, Xiaoqing Pan, and Phillip Christopher. Synthesis of Atomically Dispersed Rh Catalysts on Oxide Supports via Strong Electrostatic Adsorption and Characterization by Cryogenic Infrared Spectroscopy. *Journal of Physical Chemistry C*, 126(44):18704–18715, 2022.

[62] Jiawei Wan, Wenxing Chen, Chuanyi Jia, Lirong Zheng, Juncai Dong, Xusheng Zheng, Yu Wang, Wensheng Yan, Chen Chen, Qing Peng, Dingsheng Wang, and Yadong Li. Defect Effects on TiO2 Nanosheets: Stabilizing Single Atomic Site Au and Promoting Catalytic Properties. *Advanced Materials*, 30(11), 3 2018.

[63] Jian Lin, Aiqin Wang, Botao Qiao, Xiaoyan Liu, Xiaofeng Yang, Xiaodong Wang, Jinxia Liang, Jun Li, Jingyue Liu, and Tao Zhang. Remarkable performance of Ir1/FeOx single-atom catalyst in water gas shift reaction. *Journal of the American Chemical Society*, 135(41):15314–15317, 10 2013.

[64] Qi Wang, Xiang Huang, Zhi Liang Zhao, Maoyu Wang, Bin Xiang, Jun Li, Zhenxing Feng, Hu Xu, and Meng Gu. Ultrahigh-Loading of Ir Single Atoms on NiO Matrix to Dramatically Enhance Oxygen Evolution Reaction. *Journal of the American Chemical Society*, 142(16):7425–7433, 4 2020.

[65] Koichi Momma and Fujio Izumi. VESTA3 for three-dimensional visualization of crystal, volumetric and morphology data. *Journal of Applied Crystallography*, 44(6):1272–1276, 12 2011.

[66] Seunghyun Weon, Dahong Huang, Kali Rigby, Chiheng Chu, Xuanhao Wu, and Jae-Hong Kim. Environmental Materials beyond and below the Nanoscale: Single-Atom Catalysts. *ACS ES&T Engineering*, 1(2):157–172, 2021.

[67] Selina K. Kaiser, Zupeng Chen, Dario Faust Akl, Sharon Mitchell, and Javier Pérez-Ramírez. Single-Atom Catalysts across the Periodic Table. *Chemical Reviews*, 2020.

[68] Yuanjun Chen, Shufang Ji, Chen Chen, Qing Peng, Dingsheng Wang, and Yadong Li. Single-Atom Catalysts: Synthetic Strategies and Electrochemical Applications. *Joule*, 2(7):1242–1264, 2018.

[69] Aiqin Wang, Jun Li, and Tao Zhang. Heterogeneous single-atom catalysis. *Nature Reviews Chemistry*, 2(6):65–81, 2018.

[70] Luka Suhadolnik, Marjan Bele, Miha Čekada, Primož Jovanovič, Nik Maselj, Anja Lončar, Goran Dražić, Martin Šala, Nejc Hodnik, Janez Kovač, Tiziano Montini, Michele Melchionna, and Paolo Fornasiero. Nanotubular TiOxNy-Supported Ir Single Atoms and Clusters as Thin-Film Electrocatalysts for Oxygen Evolution in Acid Media. *Chemistry of Materials*, 35(6):2612–2623, 3 2023.

[71] Zhaoping Shi, Ying Wang, Ji Li, Xian Wang, Yibo Wang, Yang Li, Weilin Xu, Zheng Jiang, Changpeng Liu, Wei Xing, and Junjie Ge. Confined Ir single sites with triggered lattice oxygen redox: Toward boosted and sustained water oxidation catalysis. *Joule*, 5(8):2164–2176, 8 2021.

[72] Kang Hua, Xiaoke Li, Zhiyan Rui, Xiao Duan, Yongkang Wu, Deren Yang, Jia Li, and Jianguo Liu. Integrating Atomically Dispersed Ir Sites in MnCo2O4.5 for Highly Stable Acidic Oxygen Evolution Reaction. *ACS Catalysis*, 14(5):3712–3724, 3 2024.

[73] Zhirong Zhang, Chen Feng, Dongdi Wang, Shiming Zhou, Ruyang Wang, Sunpei Hu, Hongliang Li, Ming Zuo, Yuan Kong, Jun Bao, and Jie Zeng. Selectively anchoring single atoms on specific sites of supports for improved oxygen evolution. *Nature Communications*, 13(1), 12 2022.

[74] Yang Liu, Yawei Chen, Xulin Mu, Zhongyi Wu, Xu Jin, Jianming Li, Yanzhi Xu, Li Yang, Xiaoke Xi, Haeseong Jang, Zhanwu Lei, Qinghua Liu, Shuhong Jiao, Pengfei Yan, Xiyu Li, and Ruiguo Cao. Spinel-Anchored Iridium Single Atoms Enable Efficient Acidic Water Oxidation via Intermediate Stabilization Effect. *ACS Catalysis*, 13(6):3757–3767, 3 2023.

[75] Jieqiong Shan, Chao Ye, Shuangming Chen, Tulai Sun, Yan Jiao, Lingmei Liu, Chongzhi Zhu, Li Song, Yu Han, Mietek Jaroniec, Yihan Zhu, Yao Zheng, and Shi Zhang Qiao. Short-Range Ordered Iridium Single Atoms Integrated into Cobalt Oxide Spinel Structure for Highly Efficient Electrocatalytic Water Oxidation. *Journal of the American Chemical Society*, 143(13):5201–5211, 4 2021.

[76] Yagya N. Regmi, Eden Tzanetopoulos, Guosong Zeng, Xiong Peng, Douglas I. Kushner, Tobias A. Kistler, Laurie A. King, and Nemanja Danilovic. Supported Oxygen Evolution Catalysts by Design: Toward Lower Precious Metal Loading and Improved Conductivity in Proton Exchange Membrane Water Electrolyzers. *ACS Catalysis*, 10(21):13125–13135, 11 2020.

[77] W. Vielstich, Arnold. L., and H. A. Gasteiger. Handbook of Fuel Cells : Fundamentals, Technology, and Applications., 2003.

[78] Allen J. Bard and L. R. Faulkner. *Electrochemical Methods: Fundamentals and Applications*, volume 2nd. 1995.

[79] J Newman and K. E. Thomas-Alyea. *ELECTROCHEMICAL SYSTEMS*. John Wiley & Sons, 2004.

Chapter 2

Methods

2.1 Synthesis of atomically dispersed Ir on TiO_2

2.1.1 Strong electrostatic absorption (SEA)

Strong electrostatic absorption (SEA) is used to uniformly load $[IrCl_6]^{2-}$ onto the surface of TiO_2. In this process, the metal oxide support is dispersed in an aqueous solution containing the precursor metal complex to be loaded and the loading of this complex is carried out by tuning the pH value of the solution. Below the pH value of their points of zero charge (PZC), the surface of the metal oxides becomes protonated and thus positively charged. With this surface charge, anionic metal complexes in the solution are attracted through electrostatic interaction, resulting in the adsorption of the complex. At a pH value above the PZC, the surface is negatively charged and capable of absorbing the cationic metal complexes. The key advantage of using SEA is that the electrostatic interaction is strong enough to withstand the capillary forces of the solution during drying, avoiding agglomeration of the metal complexes adsorbed, which is a well-known challenge for the wet impregnation method [1].

In summary, by knowing the PZC of the metal oxide support of interest, control over the adsorption amount can be achieved by tuning the pH value of the solution

containing the metal complex precursor of interest. The electrostatic interaction between the metal complex and the metal oxide support enables uniform dispersion of the metal complex on the surface of the metal oxide.

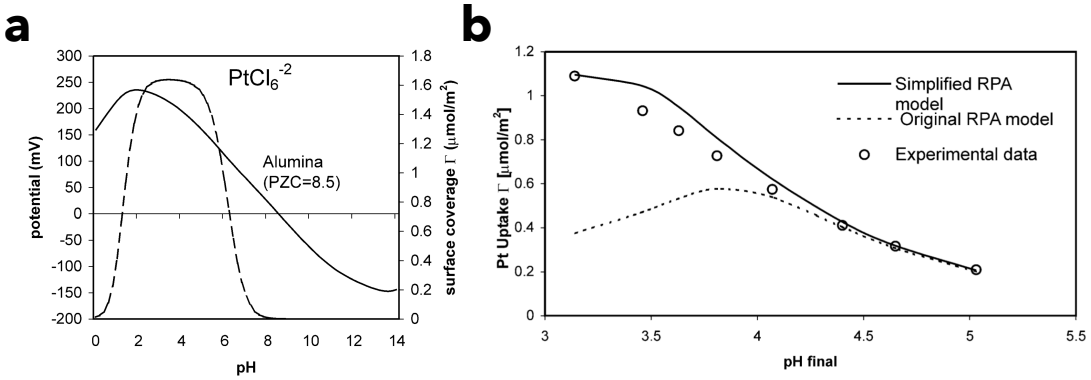


Figure 2.1: (a) Simplified RPA model-predicted $[PtCl_6]^{2-}$ uptake by alumina as a function of pH value. The solid curve is the surface zeta potential that corresponds to the left y-axis, and the other dashed curve is the surface coverage of $[PtCl_6]^{2-}$ that reads the right-hand y-axis. (b) Comparison between the experimentally observed and the RPA model-predicted $[PtCl_6]^{2-}$ uptakes. Adapted from [2] with permission. Copyright 2003 Elsevier Inc.

2.1.2 Thermolysis in inert atmosphere

Following the SEA of $[IrCl_6]^{2-}$, a thermolysis step, also known as thermal decomposition, is performed to decompose $[IrCl_6]^{2-}$, removing the chloride ligands on the Ir and promoting bonding between the Ir and surface O on TiO_2. In this work, the thermolysis was performed in N_2. Powder samples and the sample-coated FTO glass for electrochemical testing are placed in an alumina crucible at the centre of a quartz tube. The two ends of the quartz tube are connected to a N_2 gas cylinder on one end and the exhaust in a fume cupboard on the other end using Swagelok connectors. The sample is heated up in a tube furnace to the target temperature with a constant flow of N_2, approximately at 50 standard cubic centimetres per minute (sccm).

Thermolysis can be performed in different reaction atmospheres, such as inert gases (N_2, Ar), oxidative (O_2), reductive (H_2 in Ar), or a vacuum. The choice of

the atmosphere significantly impacts not only the decomposition mechanism of the precursor metal complex but also the surface termination of the support. Particularly when the metal oxide support is redox-active, such as TiO_2 and Fe_3O_4, changes in their surface structure and electronic structure can occur, thus dictating the bonding between the resulting metal and the support surface. For example, DeRita and coworkers showed that the surface adsorbed Pt single atom preferentially substituting Ti in the lattice of TiO_2 anatase when it undergoes the thermolysis in an oxidative environment, while in a reductive H_2/Ar, the Pt is found at the step edges and on the terrace of the TiO_2 surface [3].

Thermolysis in a vacuum can accelerate the removal of the surface hydroxyl group on the metal oxide support, as commonly used in the surface organometallic chemistry coupled with thermolytic molecular precursors (SOMC-TMP) as a pretreatment of the support surface to control the grafting density of the precursor metal complex. A thermolysis process in a vacuum can, therefore, influence the bond formation between the precursor metal complex and the metal oxide, compared to the sample prepared in an inert atmosphere. This is one crucial aspect to be considered in this work, where I attempt to correlate the in-situ heating annular dark field scanning transmission electron microscopy (ADF-STEM) analysis of the Ir mobility performed in a vacuum with the observation from the synthesis performed in N_2. A detailed discussion of this will be found in Chapter 4.

2.2 Determination of Ir atomic dispersion

2.2.1 Aberration-corrected scanning transmission electron microscopy (AC-STEM)

Aberration-corrected scanning transmission electron microscopy (AC-STEM) is the core characterisation technique used in this work for the investigation of the spatial

distribution of Ir on TiO_2, determining whether Ir is atomically dispersed on the support. This unique technique with sub-angstrom spatial resolution is well suited for this purpose. In a STEM, unlike a parallel electron beam used in a TEM in standard imaging mode, a focused electron probe rasters through the sample of interest and a detector after the sample plane collects the electron that passes through the sample, forming the images of the sample. The following section summaries the working principles for the AC-STEM from William and Carter's seminal textbook on electron microscopy [4].

A combination of condenser lenses and an aberration corrector is installed in a STEM after the electron source to form the focused electron beam probe. The sets of condenser lenses bend the travelling direction of the electron to form a focused beam (Figure 2.2a). However, imperfect lens configuration introduces aberration to the beam, which degrades the image formed.

Typical aberration types observed in a STEM electron probe are as follows. 2-fold astigmatism occurs when the horizontal axis of the beam is focused differently than the vertical axis. Coma is the beam's asymmetrical focus towards the far side of the beam, leading to distortion to images shaped like a comet. A spherical aberration occurs when the centre of the beam is focused differently than the edge of the beam. Higher-order aberrations are also present, which are related to more complex interactions between the electron beam and the lenses.

As the name AC-STEM suggested, an aberration corrector is used to rectify the above aberration. Because of the advancement of the aberration corrector design, STEM enters the sub-angstrom resolution regime and, therefore, enables the development of atomically dispersed supported metal catalysts.

The interaction between the electron beam and the sample can be categorised into elastic and inelastic scattering, both of which can be coherent in inducing interference of the scattered electron from samples with periodic atomic ordering or

simply incoherent. These scattered electrons from the sample thus provide a wealth of information regarding the type of element and its chemical state that is probed, as the scattering behaviour depends on these factors. How to effectively collect the scattered electrons and interpret them is the key to material characterisation, both in microscopy and spectroscopy.

In ADF-STEM, the imaging is based on collecting scattered electrons from the samples. Different imaging modes controlled by the angle of the detector to the beam travelling direction, namely the low-, medium- and high-angle annular dark field (LAADF, MAADF and HAADF, respectively) imaging, can be used to separate the coherently scattered electrons from the incoherently scattered electrons, to provide different contrast to the image, as shown in Figure 2.2b.

When the detector is placed at a small angle to the direct beam, the LAADF, a large amount of coherently scattered electrons are collected, forming images with diffraction contrast for samples with periodic lattice. Whereas, when the detector is placed at a larger angle from the beam direction, the HAADF, incoherently scattered electrons are collected, with the contrast of in the image entirely based on the intensity of Rutherford scattering of electron from the atoms in the sample, which approximately scales with Z^2, where Z is the atomic number of the scattering atom. This is also known as the mass-thickness contrast or the Z-contrast.

The approximate differentiation between the LAADF, MAADF and HAADF imaging is calculated as the ratio between the inner semi-collection angle (β_1) of the annular detector and the incident electron beam angle, as known as probe semi-convergence angle α. When β_1/α is below 1, it is classified as LAADF. When β_1/α is over 3, HAADF is named. With β_1/α in between 1 and 2, it is the MAADF.

For locating the atomically dispersed Ir on TiO_2, HAADF imaging is advantageous due to the high Z-contrast of Ir against Ti. In addition, the incoherent nature of the scattered electron excludes the image contrast from electron diffraction. Therefore,

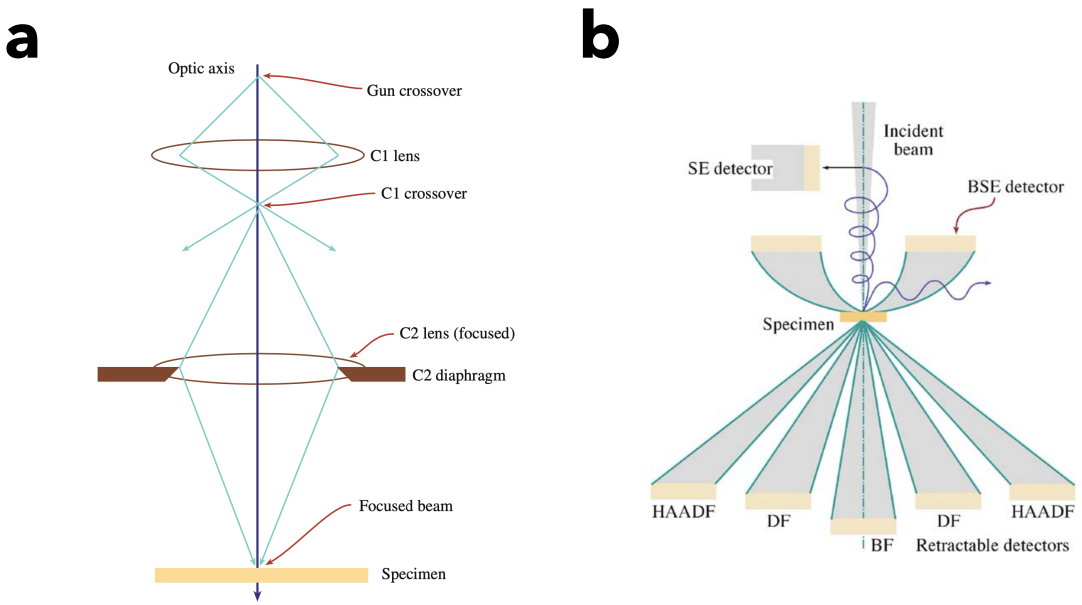


Figure 2.2: (a) Schematic of the electron-probe-forming lenses in a STEM. Adapted with permission from [5]. (b) Schematic of the electron detectors in a STEM. Adapted with permission from [4]. Copyright 2009 Springer Science Business Media, LLC.

this enables the direct determination of the position of the atomically dispersed Ir relative to the TiO_2 support.

2.3 Chemical state and local environment characterisation of Ir

2.3.1 X-ray absorption fine structure (XAFS)

X-ray absorption fine structure (XAFS) is used to investigate the chemical state and local environment characterisation of Ir on TiO_2, where the extended X-ray absorption fine structure (EXAFS) is used to probe the local environment of Ir, in particular, to identify the evolution of the Ir-Cl bond and the formation of Ir-O bond and the X-ray absorption near edge structure (XANES) is to probe the oxidation state of Ir. XAFS spectra are acquired by X-ray absorption spectroscopy (XAS) experiments [6, 7]. XAS is a technique based on the photoelectric effect using X-ray

as the probing source. When the incident X-ray energy is equivalent to the binding energy of a core-level electron of an atom, the X-ray is absorbed with a photoelectron ejected. The absorption is governed by the Beer-Lambert Law, with the absorption coefficient as a function of the X-ray energy written as:

$$\mu(E) = \log\left(\frac{I_0}{I}\right), \tag{2.1}$$

where $\mu(E)$ is the X-ray absorption coefficient at energy E, I_0 is the intensity of the incident X-ray, and I is the intensity of X-ray transmitted through the sample. In a typical XAS spectrum, a sharp rise in adsorption that corresponds to the binding energy of the probed atom can be observed, which is called the absorption edge or the white line (WL). From the absorption edge to 30 eV above, this edge is typically characterised as the XANES region; after that is the EXAFS (Figure 2.3).

The oscillating behaviour observed in the EXAFS is caused by the interference of the back-scattered photoelectron wave with the absorption of the X-ray. When the ejected photoelectron propagates and is scattered off the neighbouring atoms, the photoelectron wave travels back to the absorbing atom, introducing interference with the X-ray absorption. Due to this back-scattering behaviour from the neighbouring atoms, the EXAFS reflects the local geometry and coordination structure of the probed atom.

The EXAFS fine-structure function $\chi(k)$ is first defined as:

$$\chi(E) = \frac{\mu(E) - \mu_0(E)}{\Delta\mu_0(E)}, \tag{2.2}$$

where $\mu_0(E)$ is the absorption coefficient of the smooth varying background, and $\Delta\mu_0(E)$ is the height of the absorption edge, calculated from fits of tens of eV below the edge against hundreds of eV above the edge. The energy of the X-ray is commonly

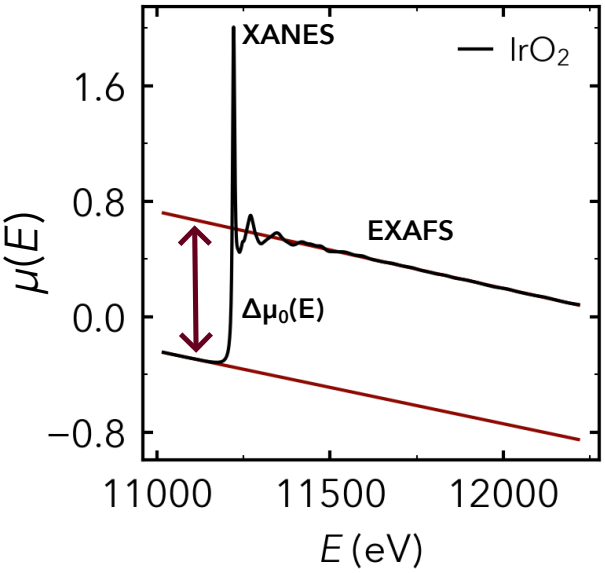


Figure 2.3: XAFS analysis of IrO_2 highlighting the measured XANES and EXAFS regions along with the determination of the edge step $\Delta\mu_0(E)$.

written as in k as wavenumbers:

$$k = \sqrt{\frac{2m(E - E_0)}{\hbar^2}}, \tag{2.3}$$

where m is the electron mass, E is the energy of the incident X-ray, E_0 is the energy of the absorption edge, and $\hbar$ is the reduced Planck's constant. After substituting k with E with some detailed derivation, the EXAFS equation can be written as:

$$\chi(k) = \sum_j \frac{N_j f_j(k) e^{-2k^2\sigma_j^2}}{kR_j^2} \sin\left(2kR_j + \delta_j(k)\right), \tag{2.4}$$

where N_j is the number of neighbouring atom j, R_j is the distance between absorbing and neighbouring atoms, σ_j^2 is the disorder in R_j (Debye-Waller factor) and $f_j(k)$ and $\delta_j(k)$ is the scattering amplitude and the phase shift from the neighbouring atom, respectively. When knowing the $f_j(k)$ and $\delta_j(k)$, which can be calculated from first principles using a FEFF code, the coordination number of the absorbing atom with the neighbouring atom, along with their bonding distance, can be estimated.

XANES analysis is further performed to investigate the oxidation state of the Ir, where the integrated WL intensity at the Ir L_3 edge is demonstrated to be proportional to the number of the holes in the Ir d orbital [8]. Qualitatively comparing the XANES spectra of Ir (oxidation state = 0), $IrCl_3$ (oxidation state of +3) and IrO_2 (oxidation state of +4) shows significant differences between the WLs, as can be observed in Figure 2.4a.

The integration of the WL intensity is carried out using the procedure proposed by Clancy and coworkers [9] and illustrated in Figure 2.4b and c. Firstly, the background of the edge is determined by fitting an arctangent function to the edge jump, where the edge step $\Delta\mu_0(E)$ is normalised to 1. The centre of this arctangent function is placed at the inflection point of the edge, i.e., the adsorption edge position. Then, a numerical integration between WL and the background fit is performed for each spectrum. The error bars are calculated by allowing a $\pm$ 1 eV shift in the centre of the arctangent function for the background fit. Finally, the integrated WL intensity is plotted as a function of the 5d holes in the Ir and used to calculate a regression model to determine the number of 5d holes (the number of missing 5d electrons from Ir) for the sample of interest, deriving the oxidation state of Ir.

In addition to the oxidation state analysis from XANES, a linear combination of known spectra of reference samples can be used to investigate the proportion of these reference structures in an unknown sample. This analysis is performed in Chapter 5 to determine the similarity between the atomically dispersed Ir sample and the cluster-rich Ir sample, using the XANES spectra of the atomically dispersed Ir sample and that of Ir metal to analyse the cluster-rich Ir sample.

2.3.2 X-ray photoelectron spectroscopy (XPS)

X-ray photoelectron spectroscopy (XPS) is used for the characterisation of the probe the oxidation state of Ir for the OER electrode prepared with the Ir-TiO_2 samples.

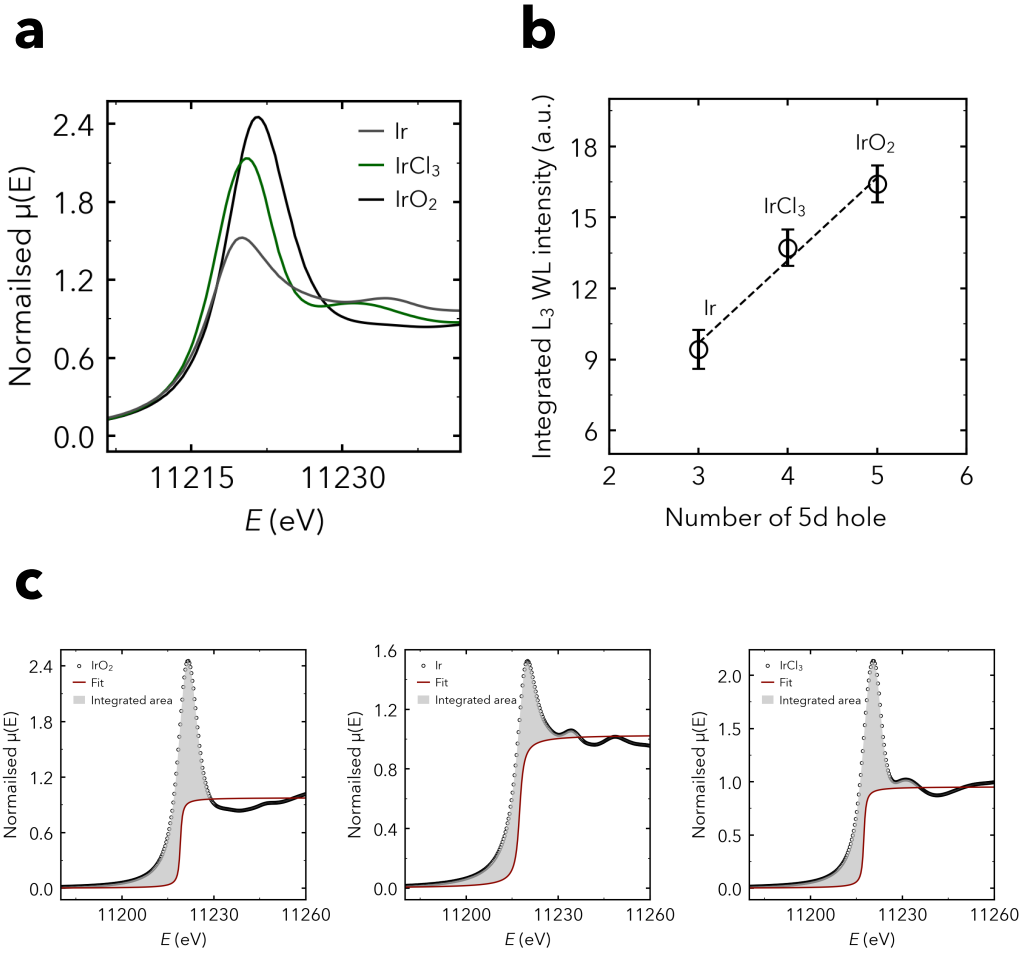


Figure 2.4: XANES analysis of Ir reference samples. (a) Normalised XANES spectra. (b) Integrated white line intensity of the Ir reference samples as a function of the number of Ir 5d holes. The integration of the WL of the (c) IrO_2, (d) Ir and (e) $IrCl_3$. Raw data of the spectra is plotted with the scattered hollow circles. Background arc-tangent function fit to the spectra is shown as the red curve, and the integrated area is the grey-shaded area.

XPS is a more lab-accessible technique than XAS, which utilises a synchrotron source. Similar to XAS, the working principle of XPS is based on the photoelectric effect between an incident X-ray and the probed atom in the sample [10]. Instead of measuring the absorbance of the X-ray, XPS collects and analyses the kinetic energy of the elastically scattered photoelectron emitted from the sample. The binding energy (E_b) of this emitted photoelectron can be calculated as:

$$E_\mathrm{b} = h\nu - E_\mathrm{k}, \tag{2.5}$$

where $h\nu$ is the energy of the incident X-ray and (E_k) is the kinetic energy of the emitted photoelectron. Since the binding energy is sensitive to the chemical state of the probe atom, shifts in binding energy in the acquired spectra reflect the probed atom's oxidation state.

In practice, binding energy requires calibration, as the photoelectron is collected by the spectrometer. Equation 2.5 rewrites as:

$$E_\mathrm{b} = h\nu - (E_\mathrm{k} + \phi), \tag{2.6}$$

where ϕ is the work function of the spectrometer [11]. This work function is experimentally calculated using the core-level excitation of a known reference sample with its Fermi level aligned with that of the spectrometer, which is defined as 0. A common choice is the Au 4f peak at 84.0 eV.

The binding energy calibration of the Ir-TiO_2 samples was performed by aligning the Ti $2p_{3/2}$ peaks in each sample to a Ti(IV) binding energy of TiO_2 anatase of 458.6 eV extracted from literature [10, 12]. This was carried out based on the TiO_2 remains at Ti(IV), and the as-measured binding energy of the Ti 2p peaks varies within 0.05 eV.

Unfortunately, the Ti 3s peak overlaps with the major Ir 4f at around 60 eV.

Therefore, the XPS measurements were carried out using a long measurement time (400 minutes) for each sample to collect the data with a decent signal-to-noise ratio for the Ir 4f peak analysis. Due to the peak overlap, the accurate analysis of the Ir 4f peaks is highly dependent on the fitting of the Ti 3s peak. To ensure consistency, I follow the fitting workflow proposed by Van der Merwe and coworkers for studies of the oxidation state of Ir in an Ir/Ti mixture [13].

The peak shape, position and area of Ti 3s are constrained by the Ti 3p peak at 37.1 eV. The same Gauissan-Lorenzian peak shape is used for both the Ti 3s and Ti 3p. The binding energy difference is confined as 25 eV [14]. The peak area is constrained using the photoionisation cross-section ratio between Ti 3s and Ti 3p ($\sigma_{3s}/\sigma_{3p} = 0.53$) calculated using the SESSA software [15]. The peak shape for both Ti 3s and Ti 3p is fitted using the pristine TiO_2 sample and adapted to the Ir-TiO_2 samples to analyse the Ir 4f peaks. The overall fitting process is illustrated in Figure 2.5.

2.4 Investigation of Ir mobility with in-situ heating annular dark field scanning transmission electron microscopy (ADF-STEM)

2.4.1 Setup of in-situ heating ADF-STEM experiments

The in-situ heating annular dark field scanning transmission electron microscopy (ADF-STEM) experiments were performed with the DENSsolutions Wildfire Nano-Chips. Figure 2.6 shows the setup for the experiment, and detailed design logic can be found in Van Omme and coworkers' work [16]. In short, the in-situ heating is realised with a metallic microheater spiral design on a suspended SiN membrane. The spiral is electrically connected to the dedicated TEM holder with four pins, with two

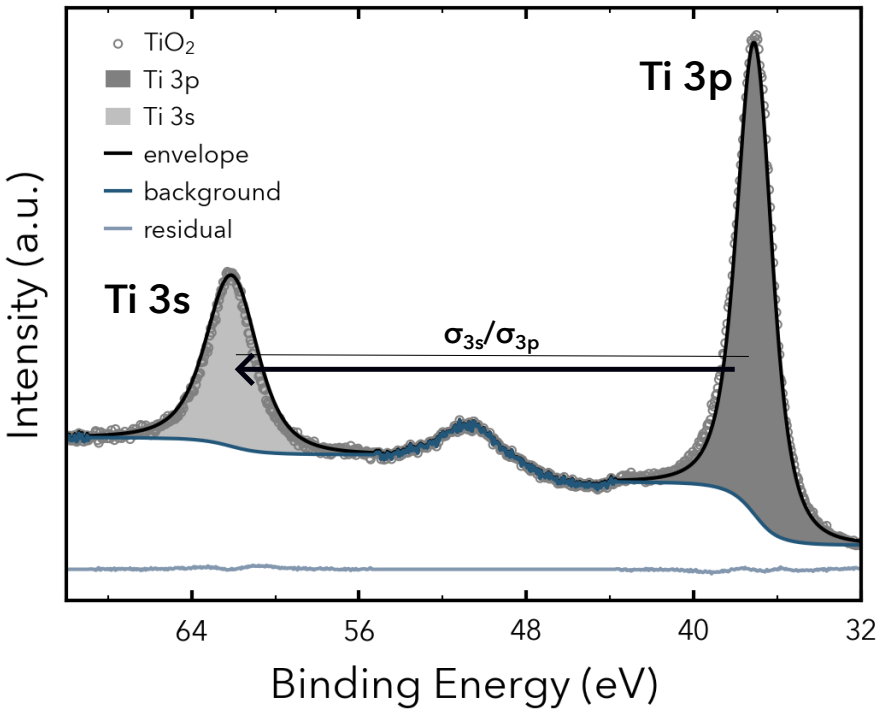


Figure 2.5: Fitting of the pristine TiO_2 nanosheets for the determination of the Ti 3s peak shape.

accounting for passing the current for the Joule heating and the other two measuring the resistance of the microheater. The heat produced can be expressed using the current and resistance measured:

$$P = I^2 R, \tag{2.7}$$

where P is power dissipated as heat, I is the current, and R is the resistance. The temperature induced by the microheater can be obtained using the factory power-to-temperature calibration.

According to the manufacturer, a small stage drift < 0.3 nm min^{-1} upon heating enables the continuous monitoring of the sample area of interest. Figure 2.6c shows a representative image of the Ir-TiO_2 sample loaded on the SiN support. A portion of the SiN support is etched away to prepare the Nano-Chip for the experiments, forming a window in the middle. I selected the sample parts without SiN in the

background of the area of interest to maximise the contrast of Ir, as highlighted in the red circle in Figure 2.6c.

In a typical in-situ heating ADF-STEM experiment, consecutive images of the same sample area are captured, producing an image stack that monitors the evolution of the same over time. To provide a statistically averaged overview of Ir mobility, I acquired image stacks from at least six different sample areas, each tracking Ir displacements for at least 20 minutes at 80 °C, 150 °C, 300 °C and 500 °C.

2.4.2 Image processing

Following the in-situ heating ADF-STEM image collection, an image registration process is required for the time-series image stacks to enable the reconstruction of the Ir trajectories on TiO_2.

Image registration is a procedure used to align images taken at different times, angles or detectors so that corresponding points in the images match and overlap. In this work, image registration is used to prepare the time-series images obtained from the in-situ heating ADF-STEM experiments for further analysis. Although collecting single STEM image is considered instantaneous, tracking the movements of Ir on TiO_2 in the timescale of minutes entails drifts of the sample stage. Therefore, an image registration step is introduced here, correcting the stage drift of the STEM holder so that the actual Ir trajectories with respect to the TiO_2 substrate can be reconstructed.

In common practice, one representative image is chosen from the image series as the reference with known and apparent features and used to align all images to it [17]. However, choosing one of the images is tricky for a low SNR image stack, as subtle artefacts or noisy pixels in any of the images can lead to incorrect registration. Therefore, I refer to the workflow and Python code written by Savitzky and coworkers [18]. They developed a method to perform reference-less image registration, where they

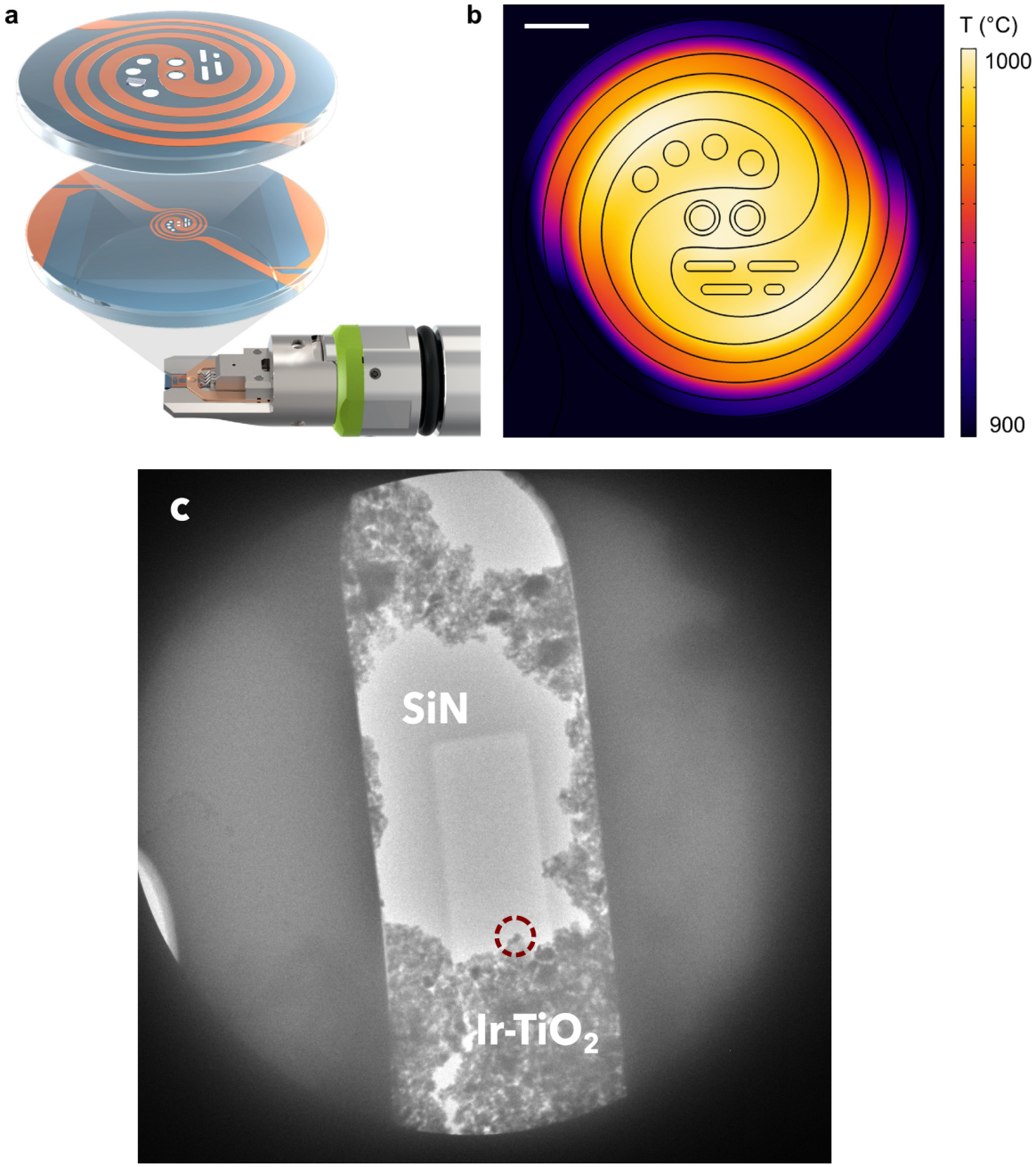


Figure 2.6: In-situ heating ADF-STEM setup. (a) Schematic of the DENS Wildfire in-situ heating Nano-Chip, showing the metallic microheater spiral with the suspended SiN membrane. Windows with 20 nm of SiN membranes are used as the support for the sample of interest(b) Simulated temperature profile across the metallic microheater, demonstrating a temperature uniformity of 98%. Adapted from [16] with permission. Copyright 2018 Elsevier B.V. (c) Representative image of the Nano-Chip used for the in-situ heating STEM experiments in this study, where the SiN membrane for supporting the powder Ir-TiO_2 sample is highlighted. The red dashed circle highlights the area of interest in the sample, where the SiN membrane underneath it was etched away using a focused ion beam (FIB) to remove background contrast from SiN. FIB is performed in collaboration with Yvonne Chart and Dr Phani Karamched (University of Oxford).

proposed to find the best rigid registration matrix for the image stack by maximising the cross-correlation between all image pairs in the stack.

For a stack of N images, the optimal relative shifts between two image pairs (i, j) in both X and Y directions can be calculated by maximising the cross-correlation of the image pairs, giving the shift matrix:

$$\mathbf{R}_{ij} = X_{ij}\hat{x} + Y_{ij}\hat{y}, \tag{2.8}$$

where $\hat{x}$ and $\hat{y}$ are the unit vectors in the x- and y-directions. Then, the optimum shifts $\mathbf{r}_i$ for image i is given as the average of the $\mathbf{R}_{ij}$ in row i as:

$$\mathbf{r}_i = \frac{1}{N}\sum_j \mathbf{R}_{ij}. \tag{2.9}$$

This correlation essentially provides the most probable position of the holder stage, using it as the reference for the alignment of all images in the stack, achieving the reference-less registration.

Figure 2.7 shows an example using this registration pipeline. After this registration step, the averaged image of the registered stack can be produced and used as the invariant reference to reconstruct the Ir trajectories for the analysis of Ir mobility. Detailed mathematical derivation of this method can be found in Savitzky and coworkers' original work [18].

2.4.3 Ir tracking

The tracking of Ir enabled by reconstructing the Ir trajectories was performed using the Python package Trackpy [19], based on the feature detection and linking algorithm developed by Crocker and Grier [20]. This algorithm is used due to the challenges in distinguishing Ir_1 from one another, as there exists no feature nor motion correlation

between the Ir_1.

A radial search distance of 0.8 nm from each Ir_1 is used to perform the nearest neighbour linking. This is guided by the mean Ir areal density in the entire dataset (excluding all Ir_x), which is 0.067 ± 0.002 nm^{-2}. This Ir areal density suggests that starting from any Ir_1, one other Ir_1 is expected to be found within a radial distance of 2.2 nm. The use of 0.8 nm is well below 2.2 nm, minimising false linking of Ir_1 and thus minimising false Ir_1 displacements due to the false linking. In addition, a memory of 3 frames is used to should the Ir_1 to "disappear" in one frame but "re-appear" after. This accounts for the low SNR of the Ir_1 and a high likelihood of instantaneous displacements of the Ir_1 when the electron beam is scanning across, the colloquially known "chasing the single atom" in the STEM imaging literature [21].

Both $Ir_{2\text{-}10}$ and $Ir_{>10}$ are treated as ensembles, and the movement of the centre of mass of the clusters determines their displacements. The centre of mass for $Ir_{2\text{-}10}$ is calculated by the averaged position of the Ir within the cluster. In contrast, for $Ir_{>10}$, it is calculated by the weighted pixel intensity within the detected clusters [22]. Trajectories of $Ir_{2\text{-}10}$ and $Ir_{>10}$ are then produced using the same nearest neighbour algorithm described above.

All the trajectories of the Ir are, in principle, constructed relative to the average positions of all frames, as in the image shown in Figure 2.7b.

2.5 Electrochemical characterisation

Despite the simplicity of the electrochemical splitting of water, a rigorous experimental protocol should be followed to reliably and reproducibly assess the performance of the catalysts for the HER/OER.

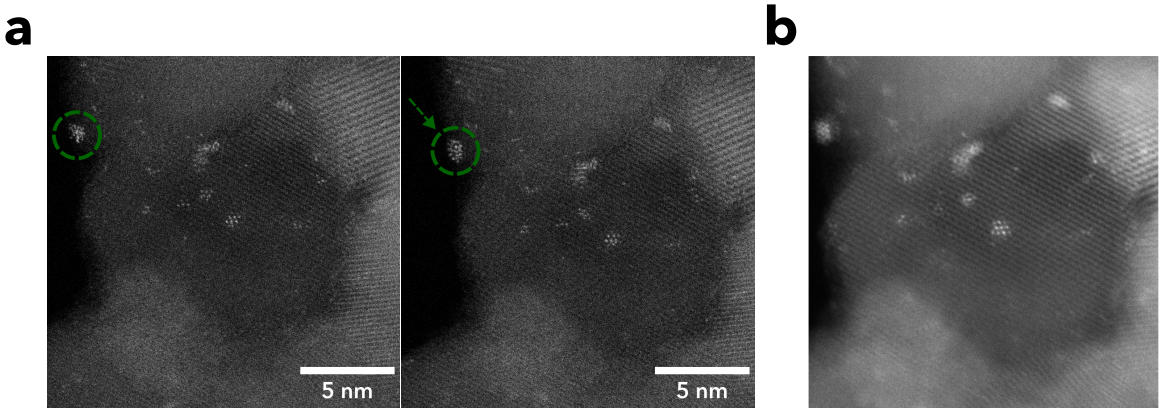


Figure 2.7: Overview of the image registration process using a 19-frame image stack obtained from the in-situ heating ADF-STEM experiment. (a) Two consecutive image frames showing the drift of the STEM holder, manifested as a displacement of the Ir cluster towards the bottom-right corner of the image, highlighted in the green circle and the arrow. (b) The average image of a registered image stack is then used to generate the Ir displacement trajectory relative to the TiO_2 support [18].

2.5.1 Electrochemical setup

Three-electrode cells were used for the OER characterisation. In a three-electrode cell, the choice of reference electrode (RE) and counter electrode (CE) as well as the preparation of the working electrode (WE) are crucial for the quality of the data acquired. A schematic of the three-electrode setup is shown in Figure 2.8.

2.5.1.1 Reference electrode

Saturated calomel electrode (Hg/Hg_2Cl_2) in saturated KCl solution and silver chloride electrode (Ag/AgCl) in KCl solution are the most commonly used RE. Nevertheless, the introduction of Cl^- into the electrochemical system can lead to erroneous current collected for both HER and OER. The strong adsorption of the Cl^- atop the Pt surface was reported to suppress the proton adsorption for HER [23]. Also, the oxidation of Cl^- can compete with the OER, as both reactions occur at a similar potential range [24]. Therefore, I used a mercury/mercury sulfate (Hg/Hg_2SO_4 in satd. K_2SO_4, Supleco, Sigma-Aldrich) reference for water electrolysis in 0.5 M H_2SO_4 (Suprapur, Sigma-Aldrich).

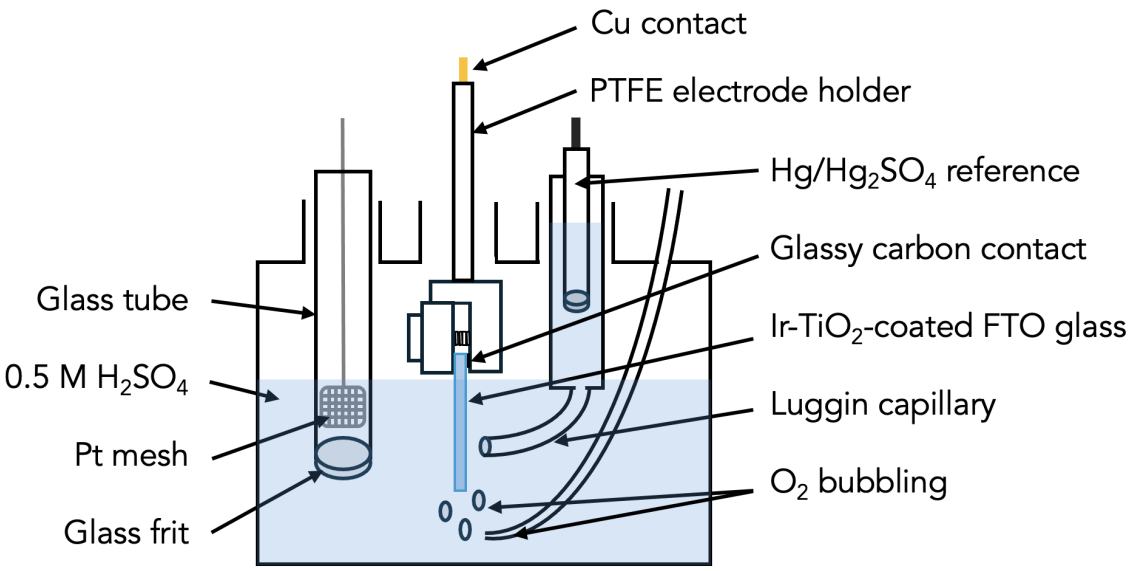


Figure 2.8: A schematic of the three-electrode setup used in this thesis.

The RE was regularly calibrated using the reversible hydrogen electrode (RHE). This was carried out by performing a cyclic voltammetry measurement in the H_2-saturated cell using the same electrolyte in the potential range where hydrogen evolution reaction (HER) and the hydrogen oxidation reaction (HOR) are expected to occur. With a Pt sphere and a Pt mesh as WE and CE, respectively, the value for RHE was read by averaging the potential intercepts at zero current for HER and HOR, as recommended by Wei and coworkers [25]. A slow scan rate of 10 mV s^{-1} is employed to minimised capacitive charging of the electrochemical double layer. Such calibration can offset the voltage loss caused by liquid-junction potential, which is in the range of tens of mV and results from the difference in chemical composition between the reference electrode and the electrolyte solution in the cell [26].

2.5.1.2 Working electrode

Rotating disk electrode (RDE) with glassy carbon (GC) disk inset as the electrode substrate is one of the most widely used WE to examine the performance of electrocatalysts for OER. An ink containing the catalyst of interest and a binder to help

fixate the catalyst is drop-casted to load the catalyst on the GC disk. Typically, Nafion or polytetrafluoroethylene (PTFE) dispersed in aqueous solution are the two binders of choice for the RDE preparation. The hydrophilic Nafion allows efficient proton transfer to the catalyst, essential for HER/OER in acidic medium. Yet, it can be a few hundred times more expensive than PTFE. In contrast, PTFE is a cost-effective option for practical application. Nevertheless, its hydrophobicity can obstruct the wetting of the catalyst with the electrolyte solution. The difference in performance for the two binders is demonstrated by Cheng and coworkers [27]. They reported a 12% reduction of overpotential for ORR at 1 mA cm^2 using Nafion instead of PTFE as binder. Nafion is thus the preferred binder for activity assessments, and a 1:10 (w/w) binder-to-catalyst ratio for a homogeneous distribution of the catalyst is suggested by Vielstich and coworkers [28].

Although the electrochemical stability window of the GC is relatively large, ranging from -0.42 and 1.76 V vs RHE in 0.1 M H_2SO_4 as demonstrated by Jaramillo and coworkers [29]. This is insufficient for the OER test in this work, as shown in Chapter 5. Significant OER current densities begin above 1.8 V for the atomically dispersed Ir on TiO_2 catalysts. Therefore, I chose to use the fluorine-doped tin oxide (FTO) glass, which has been shown to extend the electrochemical stability window to 2.22 V vs RHE [30].

The TiO_2 nanosheet-coated electrodes were prepared with the protocol reported by Lebedev and coworkers [31]. First, a slurry of TiO_2 nanosheets using hydroxypropyl cellulose as a binder (HPC) is prepared. HPC was dissolved and stirred overnight in ethanol, then added and stirred overnight the TiO_2 nanosheets dispersed in ethanol to prepare a 10 wt% HPC suspension. Subsequently, a thin layer of the slurry was coated on the FTO glass (TEC 10, 1mm thickness, 20 mm x 15 mm, 9.39 $\pm$ 0.38 Ω $square^{-1}$, Ossila) using the doctor blade method. Area (0.5 cm^{-2}) and thickness (1-2 μm) of the TiO_2 coating is controlled by the use of one layer of scotch

tape to mask the FTO glass before the doctor blade process. Finally, the electrode was calcined in air at 500 °C at for 1.5 hours with a heating rate of 1 °C min^{-1} to remove the HPC and promote the electrical contact between the TiO_2 and FTO layer. Before use, the FTO glasses were cleaned by successive ultra-sonication in 0.01 M KOH in 2-propanol at 70 °C, followed by water, each for 15 minutes and repeated for 3 times.

Electrical connections to the Ir-TiO_2-coated FTO electrodes were established using an electrode clip, with glassy carbon acting as the electrical contact. The bare FTO part of the electrode, where was not coated with TiO_2, was masked using 3M^{TM} electroplating tape 470 to ensure accurate calculation of the geometric surface area.

2.5.1.3 Counter electrode

The use of CE is to equilibrate the charge produced at the WE. This work uses a Pt mesh with a significantly larger electrochemically active surface area than the WE, ensuring the OER current is not limited by the reaction at the counter electrode. To minimise cross-contamination from the CE, in particular, Pt that can dissolve during the reaction, I placed the CE in a fritted glass tube (Ace gas dispersion tube with a porous fritted glass tip, porosity 4-8 μm) that separates the CE from the WE compartment.

2.5.2 Characterisation of OER performance

Cyclic voltammetry (CV) is the primary technique to characterise the OER activity and stability of the atomically dispersed Ir on TiO_2 nanosheets. In a CV, a voltage bias is applied to the WE with respect to the potential of the RE and the current response is measured. The voltage bias is cycled between the set voltage range, with the rate of the voltage change defined as the scan rate (mV s^{-1}).

This study assesses OER activity and stability by performing ten consecutive

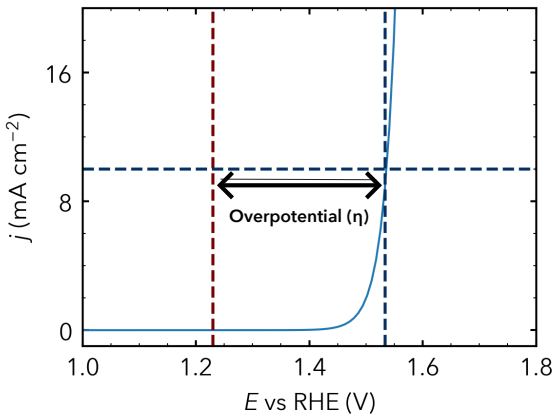


Figure 2.9: Schematic plot of the OER current density response (j) to the applied potential (E) on the electrode. The red vertical line denotes the thermodynamic equilibrium potential for the OER (1.23 V vs RHE). The blue line highlights the potential where a current density of 10 mA cm^{-2} is achieved. The potential difference between the red and blue vertical lines represents the overpotential.

CVs on the electrode between 1.3 and 2.1 V vs RHE at a scan rate of 10 mV s^{-1}. To extract the OER current density at a specific voltage, the averaged current density from the anodic and the cathodic sweep, to offset the capacitive current density, as recommended by Wei and coworkers as an alternative to the use of the steady-state chronoamperometry. This produces a curve describing the relationship between the current density (j) and the applied potential (E) during the OER, as schematically shown in Figure 2.9. Overpotential is the extra voltage required beyond the thermodynamic equilibrium of the reaction (1.23 V vs RHE for the OER) to drive the reaction at a desired rate. The obtained CVs were iR drop corrected using the high-frequency resistance determined using potentiostatic electrochemical impedance spectroscopy (PEIS) between 100 kHz and 1 Hz with a voltage perturbation of 10 mV voltage perturbation.

The OER activity of the atomically dispersed Ir on TiO_2 is reported in two forms in this study: the geometric current density, where the OER current density is normalised to the geometric surface of the electrode, and the mass current density, where the OER current is normalised by the mass loading of Ir.

Geometric current density is conventionally reported in the literature. In particular, the overpotential at a current density of 10 mA per cm^2 of the electrode geometric surface area (denoted as η@10 mA cm^{-2}_{geo}) is commonly used as the metric to assess the OER performance of the catalyst. The use of 10 mA cm^{-2}_{geo} as the benchmark current density derives from the aim of integrating the electrochemical water splitting system with solar cells for the H_2 production [32]. Given that a solar device with a 10% efficiency undergone 1 sun illumination can produce a current density approximately at 10 mA cm^{-2}, the OER performance of the electrocatalysts at this current density is thus crucial for device design.

Despite its practical importance, the geometric activity alone is insufficient to study the intrinsic activity of a catalyst. Jung and coworkers observed a ∼15 mV drop in η@10 mA cm^{-2}_{geo} when the geometric loading of IrO_2 was increased from 0.2 to 0.8 mg cm^{-2} [33]. Even though the same catalyst was used, the geometric activity increased due to increased active material. This implies that the mass activity, in which the current is normalised by the mass loading of the catalytic active metal, should also be reported for insights into the intrinsic activity of the catalysts. Mass activity is also useful to compare the cost-efficiency of different catalysts using identical active materials. This is particularly insightful for comparing the performance of the atomically dispersed Ir electrocatalysts with the benchmark Ir-based catalysts.

References

[1] M Campanati, G Fornasari, and A Vaccari. Fundamentals in the preparation of heterogeneous catalysts. *Catalysis Today*, 77:299–314, 2003.

[2] X. Hao, W. A. Spieker, and J. R. Regalbuto. A further simplification of the revised physical adsorption (RPA) model. *Journal of Colloid and Interface Science*, 267(2):259–264, 11 2003.

[3] Leo DeRita, Joaquin Resasco, Sheng Dai, Alexey Boubnov, Ho Viet Thang, Adam S. Hoffman, Insoo Ro, George W. Graham, Simon R. Bare, Gianfranco Pacchioni, Xiaoqing Pan, and Phillip Christopher. Structural evolution of atomically dispersed Pt catalysts dictates reactivity. *Nature Materials*, 18(7):746–751, 7 2019.

[4] David B Williams and C Barry Carter. The Instrument. In David B Williams and C Barry Carter, editors, *Transmission Electron Microscopy: A Textbook for Materials Science*, pages 141–171. Springer US, Boston, MA, 2009.

[5] David B Williams and C Barry Carter. How to 'See' Electrons. In David B Williams and C Barry Carter, editors, *Transmission Electron Microscopy: A Textbook for Materials Science*, pages 115–126. Springer US, Boston, MA, 2009.

[6] Matthew Newville. Fundamentals of XAFS. *Reviews in Mineralogy and Geochemistry*, 78(1):33–74, 1 2014.

[7] D Norman. X-ray absorption spectroscopy (EXAFS and XANES) at surfaces. Technical report, 1986.

[8] Ailong Li, Shuang Kong, Kiyohiro Adachi, Hideshi Ooka, Kazuna Fushimi, Qike Jiang, Hironori Ofuchi, Satoru Hamamoto, Masaki Oura, Kotaro Higashi, Takuma Kaneko, Tomoya Uruga, Naomi Kawamura, Daisuke Hashizume, and

Ryuhei Nakamura. Atomically dispersed hexavalent iridium oxide from MnO2 reduction for oxygen evolution catalysis. *Science*, 384(6696):666–670, 5 2024.

[9] J. P. Clancy, N. Chen, C. Y. Kim, W. F. Chen, K. W. Plumb, B. C. Jeon, T. W. Noh, and Young June Kim. Spin-orbit coupling in iridium-based 5d compounds probed by x-ray absorption spectroscopy. *Physical Review B - Condensed Matter and Materials Physics*, 86(19), 11 2012.

[10] Mark H. Engelhard, Donald R. Baer, Alberto Herrera-Gomez, and Peter M. A. Sherwood. Introductory guide to backgrounds in XPS spectra and their impact on determining peak intensities. *Journal of Vacuum Science & Technology A: Vacuum, Surfaces, and Films*, 38(6), 12 2020.

[11] Steffen Oswald. X -Ray Photoelectron Spectroscopy in Analysis of SurfacesUpdate based on the original article by Steffen Oswald, Encyclopedia of Analytical Chemistry , © 2000, John Wiley & Sons, Ltd. . In *Encyclopedia of Analytical Chemistry*. Wiley, 3 2013.

[12] Mark C. Biesinger, Leo W.M. Lau, Andrea R. Gerson, and Roger St C. Smart. Resolving surface chemical states in XPS analysis of first row transition metals, oxides and hydroxides: Sc, Ti, V, Cu and Zn. *Applied Surface Science*, 257(3):887–898, 11 2010.

[13] Marianne van der Merwe, Raul Garcia-Diez, Leopold Lahn, R. Enggar Wibowo, Johannes Frisch, Mihaela Gorgoi, Wanli Yang, Shigenori Ueda, Regan G. Wilks, Olga Kasian, and Marcus Bär. The Chemical and Electronic Properties of Stability-Enhanced, Mixed Ir-TiOx Oxygen Evolution Reaction Catalysts. *ACS Catalysis*, 13(23):15427–15438, 12 2023.

[14] M. B. Trzhaskovskaya, V. I. Nefedov, and V. G. Yarzhemsky. Photoelectron angular distribution parameters for elements Z=1 to Z=54 in the photoelectron

energy range 100-5000 eV. *Atomic Data and Nuclear Data Tables*, 77(1):97–159, 2001.

[15] W. S. M. Werner, W. Smekal, and C. J. Powell. Simulation of Electron Spectra for Surface Analysis (SESSA), 2016.

[16] J. Tijn van Omme, Marina Zakhozheva, Ronald G. Spruit, Mariya Sholkina, and H. Hugo Pérez Garza. Advanced microheater for in situ transmission electron microscopy; enabling unexplored analytical studies and extreme spatial stability. *Ultramicroscopy*, 192:14–20, 9 2018.

[17] Barbara Zitová and Jan Flusser. Image registration methods: A survey. *Image and Vision Computing*, 21(11):977–1000, 2003.

[18] Benjamin H. Savitzky, Ismail El Baggari, Colin B. Clement, Emily Waite, Berit H. Goodge, David J. Baek, John P. Sheckelton, Christopher Pasco, Hari Nair, Nathaniel J. Schreiber, Jason Hoffman, Alemayehu S. Admasu, Jaewook Kim, Sang Wook Cheong, Anand Bhattacharya, Darrell G. Schlom, Tyrel M. McQueen, Robert Hovden, and Lena F. Kourkoutis. Image registration of low signal-to-noise cryo-STEM data. *Ultramicroscopy*, 191:56–65, 8 2018.

[19] Daniel B Allan, Thomas Caswell, Nathan C Keim, and Casper M der Wel. soft-matter/trackpy: Trackpy v0.4.2, 10 2019.

[20] John C Crocker and David G Grier. Methods of Digital Video Microscopy for Colloidal Studies. *JOURNAL OF COLLOID AND INTERFACE SCIENCE*, 179:298–310, 1996.

[21] R. F. Egerton and M. Watanabe. Characterization of single-atom catalysts by EELS and EDX spectroscopy. *Ultramicroscopy*, 193:111–117, 10 2018.

[22] F Pedregosa, G Varoquaux, A Gramfort, Michel V., O Grisel, M Blondel, P Prettenhofer, V Dubourg, J Vanderplas, A Passos, D Cournapeau, M Brucher, M Perrot, and E Duchesnay. Scikit-learn: Machine Learning in Python. *Journal of Machine Learning Research*, 12:2825–2830, 2011.

[23] Karl J.J. Mayrhofer, Sean J. Ashton, J. Kreuzer, and M. Arenz. An electrochemical cell configuration incorporating an ion conducting membrane separator between reference and working electrode. *International Journal of Electrochemical Science*, 4(1):1–8, 2009.

[24] Michaela Burke Stevens, Lisa J. Enman, Adam S. Batchellor, Monty R. Cosby, Ashlee E. Vise, Christina D.M. Trang, and Shannon W. Boettcher. Measurement techniques for the study of thin film heterogeneous water oxidation electrocatalysts, 1 2017.

[25] Chao Wei, Reshma R. Rao, Jiayu Peng, Botao Huang, Ifan E.L. Stephens, Marcel Risch, Zhichuan J. Xu, and Yang Shao-Horn. Recommended Practices and Benchmark Activity for Hydrogen and Oxygen Electrocatalysis in Water Splitting and Fuel Cells. *Advanced Materials*, 31(31):1806296, 2019.

[26] Allen J. Bard and L. R. Faulkner. *Electrochemical Methods: Fundamentals and Applications*, volume 2nd. 1995.

[27] Shaoan Cheng, Hong Liu, and Bruce E. Logan. Power densities using different cathode catalysts (Pt and CoTMPP) and polymer binders (Nafion and PTFE) in single chamber microbial fuel cells. *Environmental Science and Technology*, 40(1):364–369, 2006.

[28] W. Vielstich, Arnold. L., and H. A. Gasteiger. Handbook of Fuel Cells : Fundamentals, Technology, and Applications., 2003.

[29] Jesse D. Benck, Blaise A. Pinaud, Yelena Gorlin, and Thomas F. Jaramillo. Substrate selection for fundamental studies of electrocatalysts and photoelectrodes: Inert potential windows in acidic, neutral, and basic electrolyte. *PLoS ONE*, 9(10), 10 2014.

[30] Jesse D. Benck, Blaise A. Pinaud, Yelena Gorlin, and Thomas F. Jaramillo. Substrate selection for fundamental studies of electrocatalysts and photoelectrodes: Inert potential windows in acidic, neutral, and basic electrolyte. *PLoS ONE*, 9(10), 10 2014.

[31] Dmitry Lebedev, Yuliana Pineda-Galvan, Yuki Tokimaru, Alexey Fedorov, Nicolas Kaeffer, Christophe Copéret, and Yulia Pushkar. The Key RuV=O Intermediate of Site-Isolated Mononuclear Water Oxidation Catalyst Detected by in Situ X-ray Absorption Spectroscopy. *Journal of the American Chemical Society*, 140(1):451–458, 1 2018.

[32] Michael G. Walter, Emily L. Warren, James R. McKone, Shannon W. Boettcher, Qixi Mi, Elizabeth A. Santori, and Nathan S. Lewis. Solar water splitting cells. *Chemical Reviews*, 110(11):6446–6473, 2010.

[33] Suho Jung, Charles C.L. McCrory, Ivonne M. Ferrer, Jonas C. Peters, and Thomas F. Jaramillo. Benchmarking nanoparticulate metal oxide electrocatalysts for the alkaline water oxidation reaction. *Journal of Materials Chemistry A*, 4(8):3068–3076, 2016.

Chapter 3

Synthesis and characterisation of atomically dispersed Ir on TiO_2 anatase nanosheets

Introduction

Atomically dispersed Ir on TiO_2 is a promising candidate for the acidic oxygen evolution reaction due to its enhanced mass-specific activity, and the high stability of the TiO_2 under OER conditions. The use of $[IrCl_6]^{2-}$ as the Ir precursor, followed by a heat treatment step to remove the Cl^-, has shown success in the preparation of atomically dispersed Ir anchored on various metal oxide supports, such as FeO_x [1], NiO [2], Co_3O_4 [3], and TiO_2 [4, 5, 6, 7].

Amongst these reports, the representative examples of atomically dispersed Ir on TiO_2 are as follows: Jia and coworkers prepared Ir single atoms (SA) on anatase TiO_2 nanocrystals for the hydrogenation of crotonaldehyde. They dried $[IrCl_6]^{2-}$ on TiO_2 crystals, followed by calcination at 400 °C [4]. They observed that higher Ir loadings resulted in samples with increased agglomeration. Specifically, the Ir SA sample was

prepared at a 0.2 wt% Ir loading, whereas Ir nanoparticles of approximately 2 nm were observed on the TiO_2 when the Ir loading was increased to 12.0 wt%.

Wang and coworkers deposited $[IrCl_6]^{2-}$ on the native amorphous TiO_x layer on Ti mesh using the wet impregnation method, followed by calcination of the Ti mesh in air at 600 °C [5]. Their high-angle annular dark field scanning transmission electron microscopy (HAADF-STEM) analysis showed atomically dispersed Ir at a 0.11 wt% loading. However, their limited HAADF-STEM analysis length-scale and concerns over the crystallisation of TiO_x, which can promote the migration of the Ir into the TiO_2 lattice, remain to be understood and optimised.

The thermal treatment of $[IrCl_6]^{2-}$ in reducing atmospheres has also been reported and shown success in the preparation of atomically dispersed Ir. Tian and coworkers prepared 0.11 wt% single-atomic-site Ir on the defective metastable phase of titanium dioxide nanosheets (Ir_1/def-TiO_2(B)) for the selective hydrogenation of furfural to furfuryl alcohol [6]. They stirred TiO_2 nanosheets with a H_2IrCl_6 solution, followed by the separation of TiO_2 via centrifugation. The $[IrCl_6]^{2-}$-loaded TiO_2 was then heat-treated in 5% H_2/N_2 to remove the Cl^- on the Ir and to reduce the Ir while simultaneously creating a defect-rich TiO_2 surface. Thompson and coworkers employed strong electrostatic absorption (SEA) to load 0.1 wt% Ir on TiO_2 anatase using $[IrCl_6]^{2-}$ as the precursor [7]. The removal of the Cl^- was carried out in a CO atmosphere for the analysis of CO oxidation on the Ir.

Despite these successful synthesis reports of atomically dispersed Ir, mitigating Ir agglomeration during synthesis remains challenging, particularly at higher Ir loadings. The commonly accepted hypothesis is that Ir agglomeration is driven by the tendency to reduce the surface energy of the highly dispersed Ir precursor and/or the resulting atomically dispersed Ir during synthesis [8, 9, 10]. Therefore, elevated synthesis temperatures, which enhance the mobility of the Ir on the support, promote Ir agglomeration.

To design strategies to minimise Ir agglomeration at higher loadings—critical for enhancing catalyst volume efficiency and making these materials more relevant for industrial applications [11, 12]—a deeper understanding of Ir mobility and agglomeration behaviour during synthesis is desired. In this context, the first focus of this thesis work is to develop insights into Ir mobility at synthesis temperatures by utilising in-situ heating annular dark field scanning transmission electron microscopy (ADF-STEM), combined with X-ray absorption fine structure (XAFS) to investigate the evolution of the Ir bonding environment. By correlating the agglomeration behaviour and mobility of Ir on TiO_2 with the evolution of its bonding environment at synthesis temperatures, this work aims to offer critical insights into the synthesis mechanism.

However, this understanding is hindered by the challenges in characterising the mobility of atomically dispersed Ir on the metal oxide support with statistically significant representation in ADF-STEM. These challenges are due to the limited Ir contrast with the metal oxide supports, restricting the characterisation of the Ir dispersion to the thin edges of samples and thus limiting the length scale of the analysis [13]. To enhance the characterisation of Ir dispersion, the first part of this chapter explores characterisation strategies, including the use of small-angle X-ray scattering for detecting Ir clusters and the nanostructuring of TiO_2 into 2D sheets. Subsequently, the second part of this chapter focuses on optimising the synthesis of the strategies mentioned above to produce atomically dispersed Ir with minimised Ir agglomeration.

Summarising the synthesis strategy of atomically dispersed Ir on metal oxide using surface organometallic chemistry coupled with thermolytic molecular precursors (SOMC-TMP) and the two-step annealing method described in Chapter 1 [14, 15], the key to mitigating the agglomeration of Ir during synthesis is to constrain the Ir precursor mobility during the heating-up stage to the target synthesis temperature. Therefore, I hypothesise that by adjusting the synthesis heating rate in the synthesis

described in Figure 1.9, the formation of coordinatively unsaturated Ir precursor and its binding to the TiO_2 surface can be modulated, thereby controlling the rate of Ir agglomeration.

3.1 Synthesis of atomically dispersed Ir on TiO_2 using $[IrCl_6]^{2-}$ as precursor

I firstly tested the synthesis strategy in Figure 1.9 on commercially available 5 nm TiO_2 anatase particles to examine if the SEA of $[IrCl_6]^{2-}$ could be carried out on TiO_2 anatase, and to determine the optimal thermolysis temperature for the removal of the Cl^- without causing agglomeration of Ir. The high surface area ($\sim$290 m^2 g^{-1}) of these 5 nm TiO_2 particles presents as an ideal substrate to maximise the atomic dispersion of Ir [16]. As described in Section 2.1, the SEA was performed by first dispersing TiO_2 in deionised water acidified with hydrochloric acid, followed by drop-wise addition of an aqueous $[IrCl_6]^{2-}$ solution with the desired Ir loading. The mixture was stirred for 1 hour. Then, the TiO_2 is centrifuged, washed with pH 3 HCl solution and dried at 80 °C in an oven overnight. I labelled the sample at this stage as the post-SEA, as-synthesised TiO_2.

The SEA process was carried out in an aqueous solution acidified to pH 3. I selected this pH value based on previously simulated data from Regalbuto and coworkers [17], where for an oxide with a point of zero charges (PZC) at pH 6, such as TiO_2 [18], the uptake of anions by the oxide through the electrostatic adsorption plateaus at pH values between 2 and 3. Here, the choice of pH 3 minimises the amount of Cl^- from the solution remaining on the surface of the TiO_2 after the SEA, ensuring minimal surface contamination for the following HAADF-STEM characterisation of the Ir dispersion. A low nominal Ir weight loading (0.5 wt%) was used to minimise the chance of agglomeration of $[IrCl_6]^{2-}$.

After the SEA, thermogravimetric analysis-mass spectrometry (TGA-MS) was employed to investigate the thermal decomposition behaviour of the $[IrCl_6]^{2-}$ in N_2 to guide the choice of the synthesis temperatures for a complete Cl^- removal. As shown in Figure 3.1, the TG curve can be separated into three stages: room temperature (RT) to 150 °C, 150 to 500 °C and 500 to 900 °C. Between RT and 150 °C, there is a 21.9 % mass drop, with corresponding online MS signals showing evidence of the release H_2O, HCl and Cl_2 gas. Subsequently, between 500 °C, a further 16.3 % mass decrease is observed, followed by the last 21.7 % mass drop to arrive at 39.3 % of the initial mass at 900 °C. The last mass drop is accompanied by strong MS signals of HCl and Cl_2.

The number of Cl^- can be correlated to each mass drop, calculated by back-tracing from the total Ir mass left at 900 °C. This calculation is necessary as the as-received $H_2IrCl_6{\cdot}xH_2O$ is highly hygroscopic and can easily absorb moisture, resulting in a chemical composition of unknown H_2O number. Given the thermolysis was carried out in an inert N_2 atmosphere, and assuming all Cl^- is removed from the Ir, the residual mass at 900 °C should correspond to metallic Ir with an atomic weight of 192.217 g mol^{-1}.

Since the residual metallic Ir consists of 39.3 % of the original mass, the total molecular weight of the $H_2IrCl_6{\cdot}xH_2O$ is estimated at 489.1 g mol^{-1}. With the 6 Cl^- weighing at 210 g mol^{-1}, the total H_2O weight is 87.1 g mol^{-1}, corresponding to an averaged of 4.8 H_2O and accounting for ∼18 % of total mass.

The TGA-MS analysis confirms the $[IrCl_6]^{2-}$ decompose in two main stages, where 3 Cl^- and H_2O are removed from RT to 500 °C, followed by the removal of the rest 3 Cl^- from 500 to 900 °C. This stepwise thermolysis behavior of $[IrCl_6]^{2-}$ agrees with previous reports [3, 19].

Based on the TGA-MS analysis, I concluded that a minimum of 500 °C is required to initiate the second stage of $[IrCl_6]^{2-}$ decomposition, and removing all Cl^- from Ir.

In this work, I chose 500 °C for the thermolysis step, even though the decomposition rate of $[IrCl_6]^{2-}$ is expected to be slow at 500 °C, as this temperature is the onset of the second decomposition stage. This choice is constrained by a maximum reasonable synthesis temperature of 600 °C with the TiO_2 anatase as the support.

The anatase phase transforms into the thermodynamically more favourable rutile phase beginning at 600 °C, which will be discussed in the following Figure 3.4. With the phase transformation of TiO_2 occurring, TiO_2 particles sinter and reduce their surface area for supporting atomically dispersed Ir. In addition, risks of the submersion of the Ir into the TiO_2 bulk increases during the phase transformation of TiO_2, leading to a loss of the Ir active surface. Therefore, I decided to perform the thermolysis at 500 °C in N_2 for 4 hours, using the extended heating duration to ensure the complete Cl^- removal.

Cl 2p XPS measurements were performed to follow the Cl^- removal on the post-SEA, as-synthesised TiO_2 sample treated at 300 °C and 500 °C in N_2 using a heating rate of 1 °C min^{-1}. The Cl 2p spectrum for the post-SEA, as-synthesised sample without heat treatment can be fitted with two sets of double peaks (Cl $2p_{3/2}$ and Cl $2p_{1/2}$), where the Cl $2p_{3/2}$ at 198.6 eV can be attributed to the H-bonded Cl, whereas the peaks at 199.0 eV is the Ir-bonded Cl [20]. The HCl double peaks diminish after treatment at 300 °C with only Ir-Cl peaks remaining. After treatment at 500 °C, no Cl signals are discernible.

The Ir-Cl peaks in the post-SEA, as-synthesised sample suggests the SEA of $[IrCl_6]^{2-}$ was successful. The hydrogen-bonded Cl peaks should be a result of HCl residual from the synthesis solution. The disappearance of all Cl peaks indicates a thorough removal of the Cl^- after the 500 °C treatment of 4 hours.

In summary, combining TGA and XPS measurements, I confirmed that the SEA can be used for loading $[IrCl_6]^{2-}$ onto TiO_2. The thermolysis temperature is selected at 500 °C, staying within the thermal stability window of TiO_2 anatase while providing

sufficient thermal energy to decompose $[IrCl_6]^{2-}$ completely.

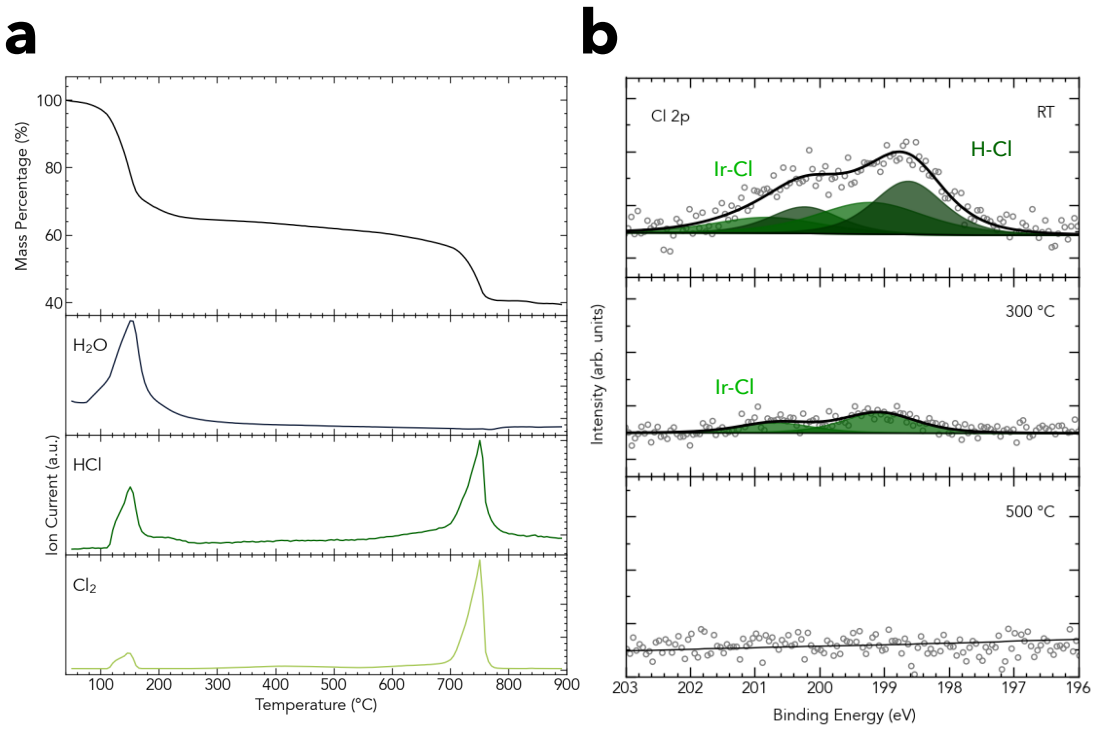


Figure 3.1: Thermolysis of $[IrCl_6]^{2-}$. (a) TGA-MS analysis of $H_2IrCl_6 \cdot xH_2O$ in Ar with a heating rate of 10 °C min^{-1}. (b) Cl 2p XPS measurements of the post-SEA, as-synthesised TiO_2, treated at 300 °C and 500 °C in N_2 for 4 hours with a heating rate of 1 °C min^{-1}. The XPS measurements were performed in collaboration with Yi Liang (University of Oxford).

After the confirmation of the synthesis protocol, the dispersion of Ir synthesised was characterised using HAADF-STEM, shown in Figure 3.2. As observed in Figure 3.2a, there are bright spots in the HAADF-STEM image that can be attributed to atomically dispersed Ir (Ir_1), highlighted in the green circles. However, their contrast with the surrounding TiO_2 signal is relatively low, and the surface of the TiO_2 appears to be covered with contamination, likely due to the residual HCl from the synthesis, resulting in poorly resolved surface features.

To facilitate HAADF-STEM characterisation, I introduce a vacuum baking step at 150 °C to the sample deposited on a TEM grid to remove HCl from the TiO_2 surface. As seen in Figure 3.2b, the TiO_2 surfaces become better resolved after the baking

step. Again, bright spots can be observed on the surface of TiO_2 with no apparent evidence of agglomeration. Based on the higher Z-contrast of Ir than that of Ti, these bright spots can be assigned as Ir_1. The absence of agglomeration indicates a uniform dispersion of the $[IrCl_6]^{2-}$ on TiO_2.

The dispersion of Ir on TiO_2 after the thermolysis at 500 °C is then characterised, shown Figure 3.2c and d. In the high-magnification STEM image, a distribution of Ir_1 and Ir clusters (Ir_x) with sizes ranging from 1 to 2 nm is observed. These clusters seem to be prevalent across the surface of the TiO_2. However, their contrasts with TiO_2 are too low to confirm their precise distribution.

The observation of Ir_1 after the thermolysis at 500 °C confirms that atomically dispersed Ir can be stabilised on TiO_2, which can be attributed to a strong Ir-O binding energy [21]. This result is consistent with Puntscher and coworkers' observation of the presence of thermally stable Ir_1 on TiO_2 (101) investigated with scanning tunnelling microscopy at UHV conditions [22].

Nevertheless, Ir clusters are also present in the 500 °C treated sample. This agglomeration of Ir after the 500 °C treatment agrees with Wu and coworkers' observation, where they reported Ir_1 agglomeration beginning at 350 °C on Co_3O_4 [3]. To design strategies that mitigate the Ir agglomeration, insights into the mobility of Ir during the heating process, in particular the transport and agglomeration behaviour of the Ir induced by increasing temperatures, are desired.

However, these insights cannot be fully obtained with this Ir on 5 nm TiO_2 system using HAADF-STEM. The limited characterisation length scale, typically within a few nanometers at the edge of the TiO_2 particle, constrains the investigation of the Ir dispersion on TiO_2 with a sufficient statistical representation using HAADF-STEM. This constraint is due to the insufficient contrast of the Ir species against TiO_2 support, as shown in Figure 3.2.

Note that the heating rate for the synthesis has a significant influence on the

Ir dispersion on TiO_2, as I hypothesised in the introduction part of this chapter. I observe that although Ir_x are present, the use of a heating rate of 1 °C min^{-1} produces the most uniform Ir dispersion compared to that of higher heating rates. This result confirms my hypothesis. Detailed analysis to provide the evidence for this observation will be briefly discussed at the end of this chapter and further explored in Chapter 4. Here, I present the results obtained at 1 °C min^{-1} for the flow of the discussion.

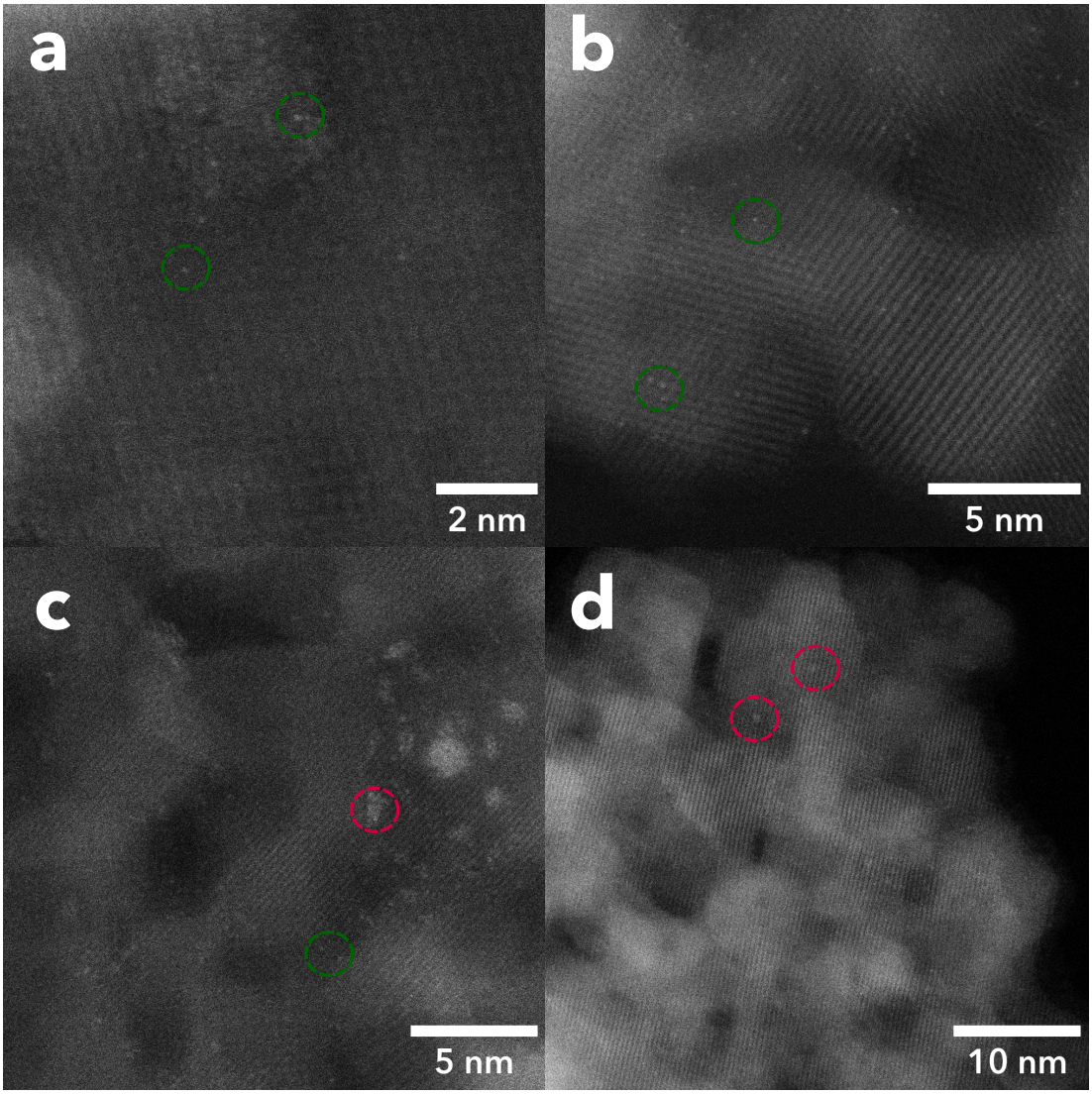


Figure 3.2: HAADF-STEM images of (a) post-SEA, as-synthesised TiO_2 and (b) post-SEA, as-synthesised TiO_2 loaded on a TEM grid and baked at 150 °C in a vacuum. (c) High- and (d) low-magnification HAADF-STEM images of post-SEA, as-synthesised TiO_2 treated at 500 °C in N_2 for 4 hour with a heating rate of 1 °C min^{-1}.

To obtain a statistical representation of the Ir dispersion on TiO_2, I tried the following two methods. Firstly, I employed the small angle X-ray scattering (SAXS) spectroscopy to complement the HAADF-STEM analysis by providing a bulk-averaged characterisation of the Ir dispersion. In parallel, I architected the structure of the TiO_2 support into a uniform 2D nanosheet morphology. The use of nanosheets as the Ir support leverages the Z-contrast of the HAADF-STEM to allow for the differentiation of Ir from the TiO_2 support at an extended length scale, enabling a statistical analysis of the Ir dispersion.

In the following section, I first discuss the observations in the SAXS experiments, followed by the synthesis of the TiO_2 nanosheets and the investigation of the dispersion of Ir on TiO_2 nanosheets.

3.2 Characterisation of Ir dispersion on TiO_2

3.2.1 Small angle X-ray scattering of Ir on TiO_2

SAXS experiments were performed with an offline SAXS instrument at the labSAXS Facility, Diamond Light Source, to investigate if the existence of Ir_x ranging from 1 to 2 nm could be distinguished. I prepared three samples with different Ir dispersions on TiO_2 (Ir-TiO_2). Specifically, the 0.5 wt% Ir-TiO_2 sample as shown in Figure 3.2c and d, where Ir_1 is present with a few Ir_x, a 2 wt% Ir-TiO_2 sample, where Ir_x distribute across the TiO_2, as shown in Figure 3.3a, and the pristine 5 nm TiO_2. All three samples were treated in N_2 at 500 °C for 4 hours.

Size distribution analysis of the 2 wt% Ir-TiO_2 (Figure 3.3b) shows that Ir_x are between 1 and 6 nm in size with the 2 to 3 nm Ir_x dominating. SAXS data is conventionally expressed as the momentum transfer in reciprocal space (q), and its

relationship between the real space distance (d) is given as:

$$q = \frac{2\pi}{d}. \tag{3.1}$$

Using Equation 3.1 on the size distribution of Ir, analysed with the HAADF-STEM image for the 2 wt% Ir-TiO_2 sample, a scattering signal is expected between the q range of 6 to 1 nm^{-1}, with a peak occurring between 3 to 2 nm^{-1} for this sample.

The SAXS results in the q range from 0 to 7 nm^{-1} (Figure 3.3c) show a slight dip in the signal intensity at 2.5 nm^{-1} for the 2 wt% sample comparing to that of the 0.5 wt% sample. This result is consistent with the above estimated scattering q range. However, detailed peak analysis is challenging due to difficulties in reliably subtracting the TiO_2 signal from the total signal, which is primarily due to the size variation of the 5 nm TiO_2 substrate after the 500 °C treatment across sample batches.

Significant signal variations between 0.5 to 1.5 nm^{-1} are observed in Figure 3.3d when comparing the three samples. This corresponds to a size distribution of 4 to 12 nm in real space. Since Ir is not expected to occur within this size range, the signal variation can be attributed to the differences in the sizes of TiO_2.

In conclusion, the SAXS experiments confirm the detection of the Ir scattering signal at a 2 wt% loading. However, further detailed analysis of the Ir size distribution is majorly complicated by baseline signal variations between batches of the 5 nm TiO_2 support as a result of the 500 °C treatments. The low Ir cluster concentration further hinders their detection in SAXS, limiting the use of SAXS as a standard and benchmark characterisation method for Ir dispersion.

3.2.2 Preparation of TiO_2 nanosheets

Given the difficulties in the SAXS analysis, I decided to focus more on the second strategy, i.e., the nanostructuring of TiO_2 into 2D sheets for the HAADF-STEM

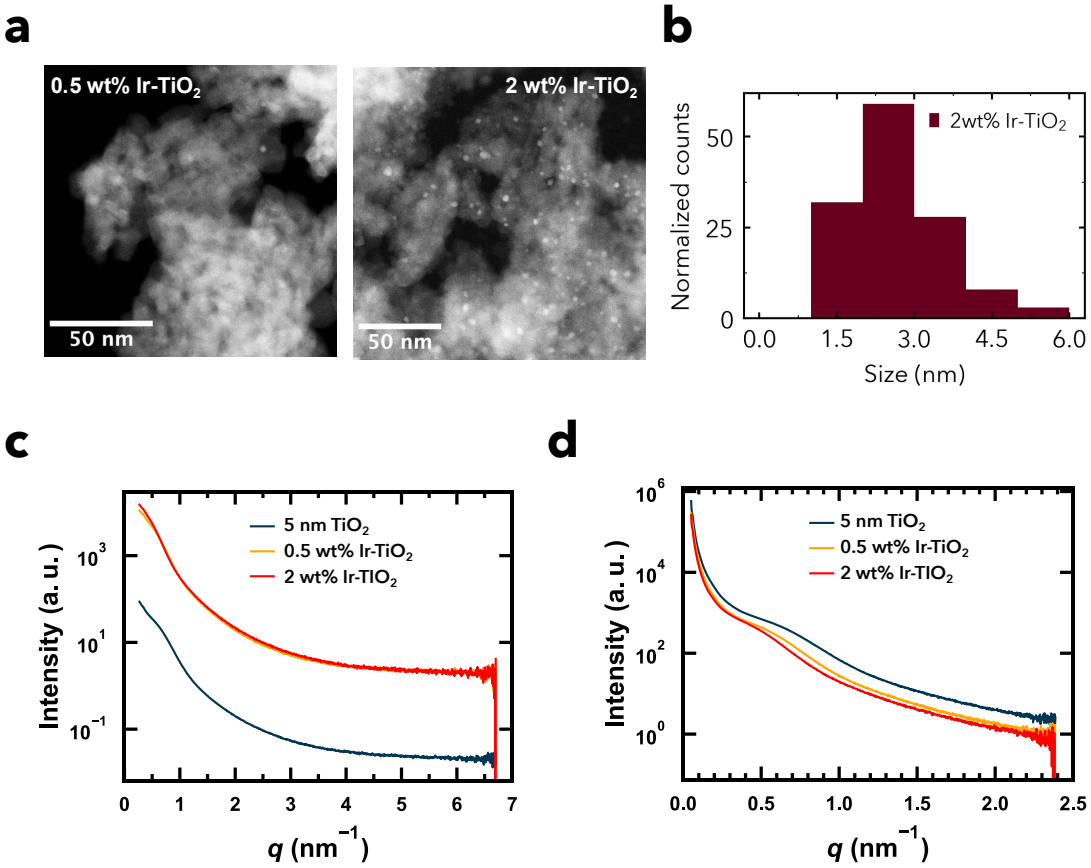


Figure 3.3: SAXS experiments of the Ir-TiO_2 samples at 0.5 wt% and 2 wt%. (a) HAADF-STEM images of the 0.5 wt% and 2 wt% Ir-TiO_2 samples. (b) Ir size distribution analysis for the 2 wt% Ir-TiO_2 sample. SAXS spectra of the bare 5 nm TiO_2, 0.5 wt% and 2 wt% within the q range (c) from 0 to 7 nm^{-1} and (d) from 0 to 2.5 nm^{-1}. SAXS experiments were performed in collaboration with Dr Thomas Zinn (Diamond Light Source), Dr Johannes Ihli (University of Oxford) and Dr Matthew Burton (University of Oxford).

characterisation at an extended length scale.

The TiO_2 anatase nanosheets were synthesised with the method proposed by Zhao and coworkers with modifications [23]. In brief, the synthesis utilises a sacrificial reduced graphene oxide powder (rGO) as a flat template to enable uniform nucleation of TiO_x from the hydrolysis of $TiCl_4$ (TiO_x-loaded rGO), followed by a heat treatment step in O_2, combusting and removing rGO, meanwhile to crystallise TiO_x into TiO_2 anatase [24]. A schematic of the synthesis is shown in Figure 3.4a.

The formation temperature of the anatase phase was investigated with powder

X-ray diffraction (XRD). As shown in Figure 3.4b, diffraction peaks that correspond to the TiO_2 anatase are formed after the 550 °C heat treatment. Further increase of the synthesis temperature to 600 °C promotes the formation of the rutile phase. The anatase to rutile phase transformation is completed at 800 °C. These XRD results determine the use of 550 °C as the target synthesis temperature for the anatase nanosheets.

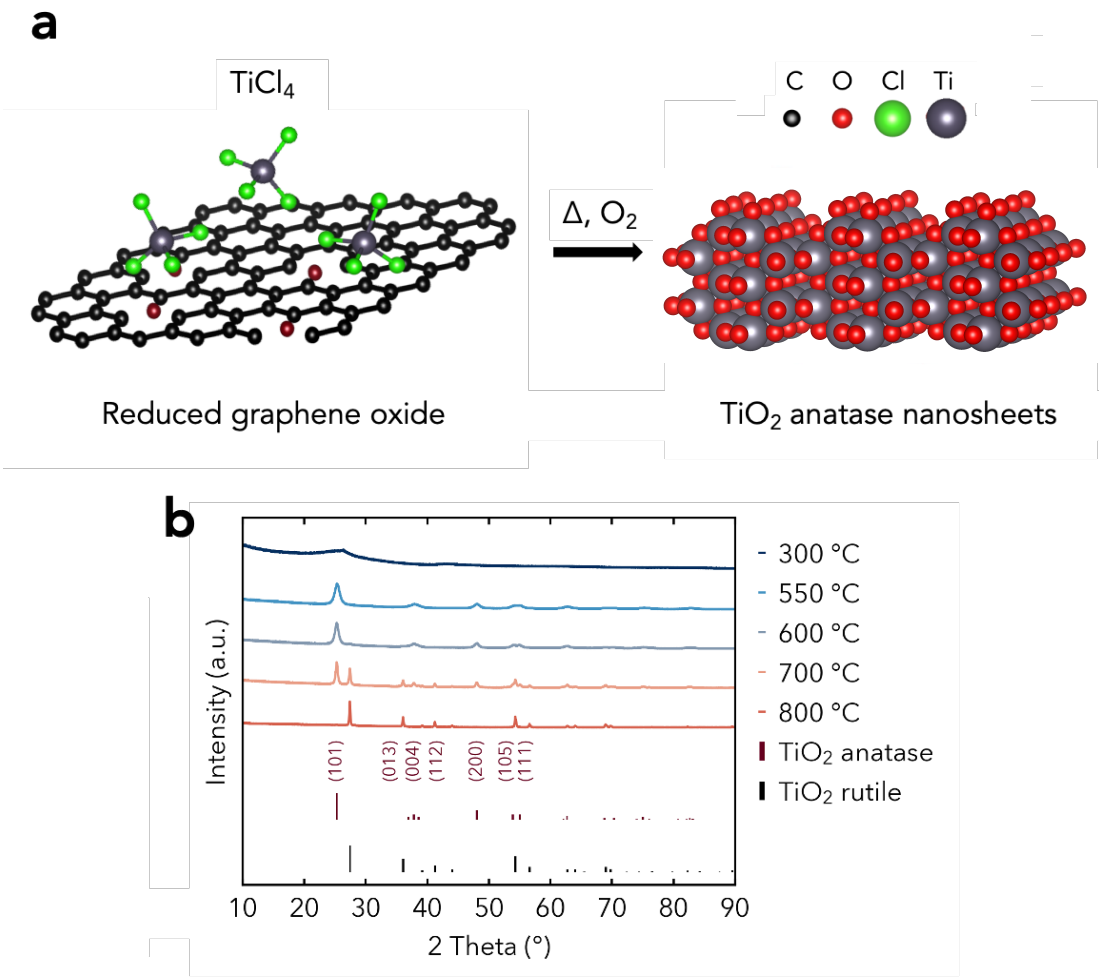


Figure 3.4: Synthesis of TiO_2 nanosheets. (a) Schematic of the synthesis process. (b) XRD analysis of the nanosheets synthesised at 300 °C, 550 °C, 600 °C, 700 °C and 800 °C. The schematic was created with Vesta 3 software [25].

The removal of the rGO and the resulting TiO_2 morphology were further investigated with ADF-STEM images, as shown in Figure 3.5. After the 300 °C treatment,

rGO with its characteristic wrinkled morphology can be seen in the low-magnification ADF-STEM image. An amorphous TiO_x layer can be observed over the rGO, as shown in Figure 3.5b.

At 550 °C, visually, the sample turns from rGO's black colour to the white colour of TiO_2. As shown in Figure 3.5c and d, crystals of sizes between 10 to 20 nm are formed, with the edges of the crystals connected and remaining nearly in the same Z-plane with respect to the electron beam irradiation direction. Although not apparent in the high-magnification image, the characteristic wrinkle of the rGO remains present in the low-magnification image (Fig 3.5c). For the sample treated at 800 °C, 50-150 nm TiO_2 particles are formed, and the rGO characteristic wrinkled morphology disappears (Figure 3.5e and f).

These HAADF-STEM results show that the morphology of the TiO_2 prepared at the 550 °C treatment is well-suited for the STEM characterisation of the Ir dispersion at an extended length scale. However, the characteristic rGO wrinkles that remain observable in the 550 °C sample suggest a risk of incomplete removal of the rGO.

Significant contamination is observed in the ADF-STEM image after one minute of beam irradiation (Figure 3.6a and b): a layer of blurry contrast begins to form over the surface of the 550 °C sample. This additional contrast is likely a condensation of hydrocarbons or polymerisation of organic molecules upon exposure to the electron beam, which is one of the common contaminants that can be observed with STEM imaging [26]. This observation suggests that some carbon residue remains on the TiO_2 nanosheets after the heat treatment, which not only hampers STEM imaging but also interferes with further adsorption of $[IrCl_6]^{2-}$ and the formation of atomically dispersed Ir.

Given that 550 °C is the upper bound of the temperature range for the pure phase anatase synthesis, an alternative strategy is required to ensure that the TiO_2 synthesised is free of rGO or other carbon residue. I explored multiple methods for this

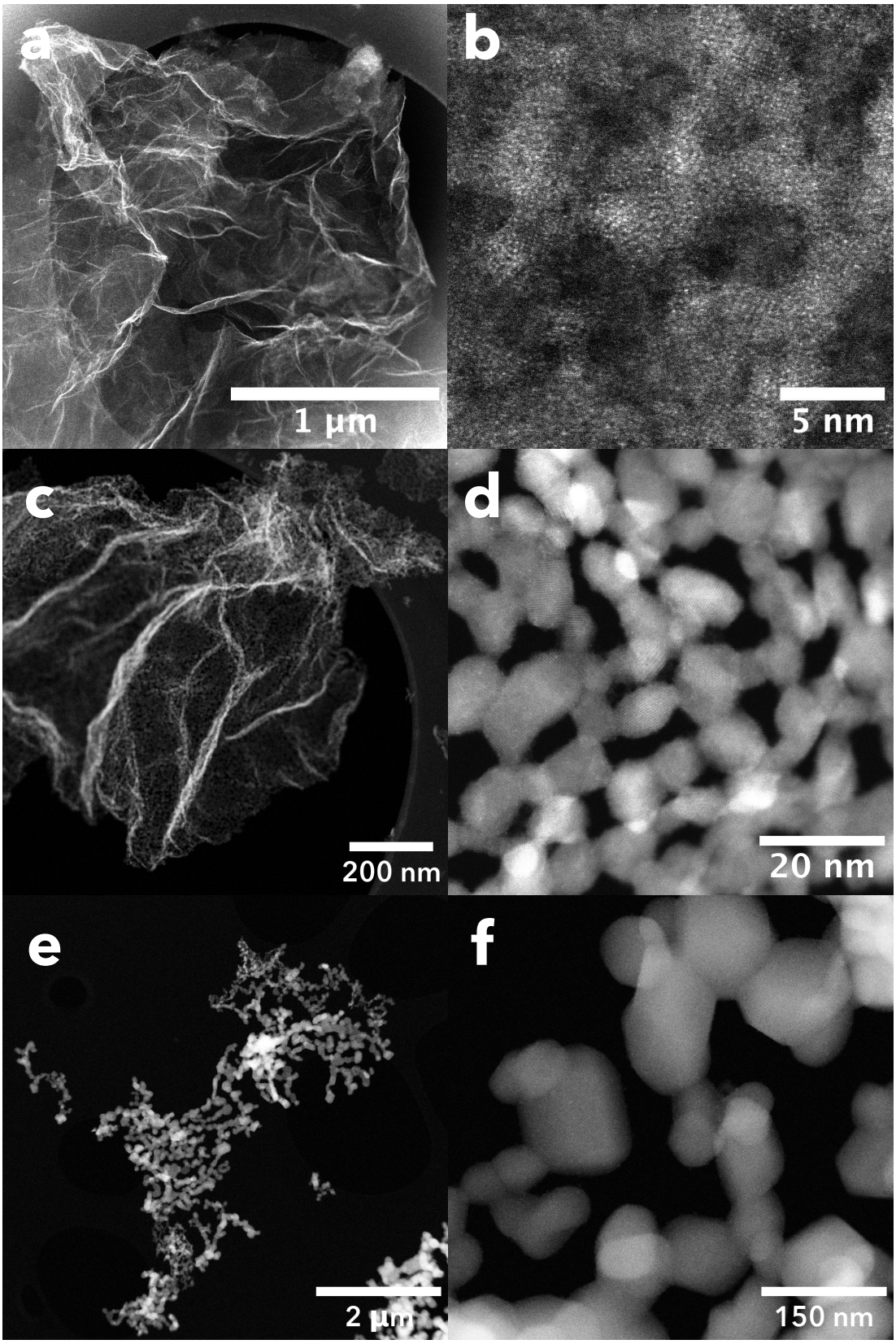


Figure 3.5: ADF-STEM images of the TiO_x-loaded rGO treated at (a) and (b) 300 °C, (c) and (d) 550 °C, and (e) and (f) at 800 °C.

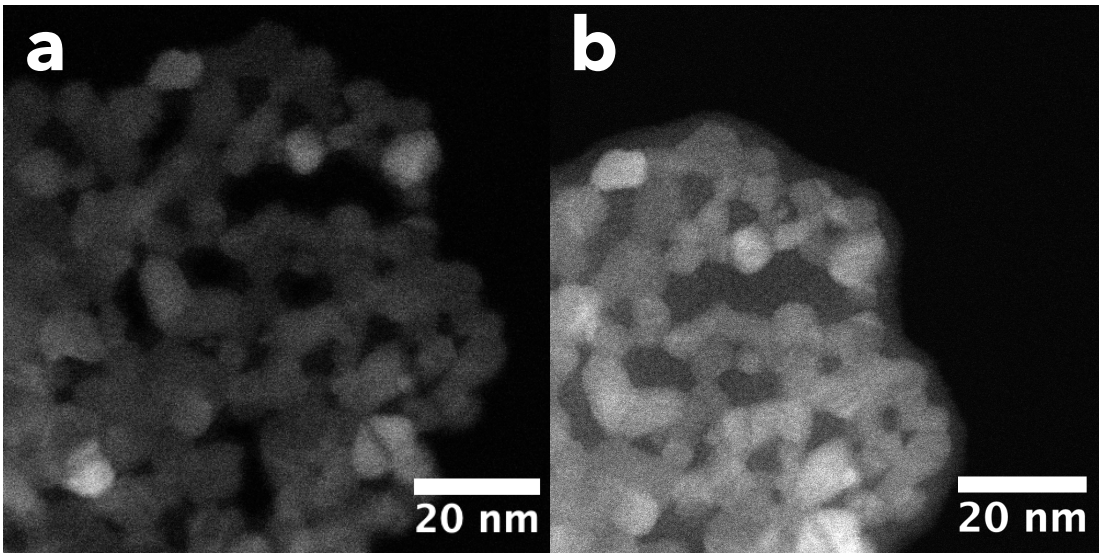


Figure 3.6: ADF-STEM images of the TiO_x-loaded rGO treated at 550 °C. (a) Image captured at the beginning and (b) after 1 minute of the STEM imaging.

purpose, such as plasma cleaning, UV exposure, and chemical washing. I eventually chose chemical washing for its processability of large quantities of sample powder, which is necessary for further preparation of samples for electrochemical tests.

A toluene/ethanol mixture was used for the chemical washing, leveraging the non-polar property of the toluene to dissolve possible aromatic derivatives from the combustion of rGO and the ethanol for the hydrocarbon-related species. Figure 3.7a and b show the morphology of the TiO_2 nanosheets prepared with the 550 °C heat treatment after the chemical wash. The wrinkled morphology of the rGO disappears, and carbon condensation under the electron beam is minimised. The nanosheet crystals begin to stack upon one another compared to the morphology before the chemical washing. These observations suggest a more thorough removal of the rGO and carbon residue on the TiO_2 nanosheets. The stacking of the TiO_2 nanosheets is likely due to the removal of the underlying rGO, which previously stabilised the nanosheets in one single plane. Nevertheless, flat regions, predominantly consisting of a single layer of the TiO_2 nanosheets, remain present.

The mean size of the nanosheets (d is estimated using the Scherrer formula on the

anatase (101) diffraction at 25.30° with the following relationship (Figure 3.7c) [27]:

$$d \approx \frac{0.93\lambda}{b \cdot \cos(\Theta)}, \tag{3.2}$$

where λ is the wavelength of X-ray (Cu Kα source at 1.5406 Å) and b is the full width at half maximum (FWHM) of the diffraction peak, and Θ is the diffraction angle. The analysis shows the mean crystal size of the nanosheets is 11.2 nm.

The thickness of the nanosheet was further determined using atomic force microscopy (AFM). Two line profiles across the TiO_2 are analysed and shown in Figure 3.7d and e. At the thinnest part (profile 1) of the agglomerate, the mean thickness is 4.1 ± 0.5 nm, while at the stacked part of the sample, the mean thickness is 7.8 ± 0.5 nm, approximately double that of profile 1. The thickness of the single layer nanosheet crystal is attributed to be ∼4 nm, as the nanosheets are likely to stack upon each other and show thickness of multiples of 4 nm.

In summary, TiO_2 nanosheets were successfully synthesised by treating the TiO_x-loaded rGO at 550 °C in O_2, followed by a chemical washing step using a toluene/ethanol mixture. The presence of single layer nanosheet regions that are 4 nm thick offers an improvement in the support morphology compared to the commercially available 5 nm nanoparticles. The use of these TiO_2 nanosheets as the support should enable the HAADF-STEM characterisations of the atomically dispersed Ir at an extended length scale.

3.3 Optimised Ir dispersion on TiO_2 nanosheets

With the successful synthesis of TiO_2 nanosheets, I decided to proceed with the use of these nanosheets as the support for the synthesis of atomically dispersed Ir. The aim is to investigate the agglomeration behaviour of Ir during synthesis to develop strategies for optimising the atomic dispersion of Ir.

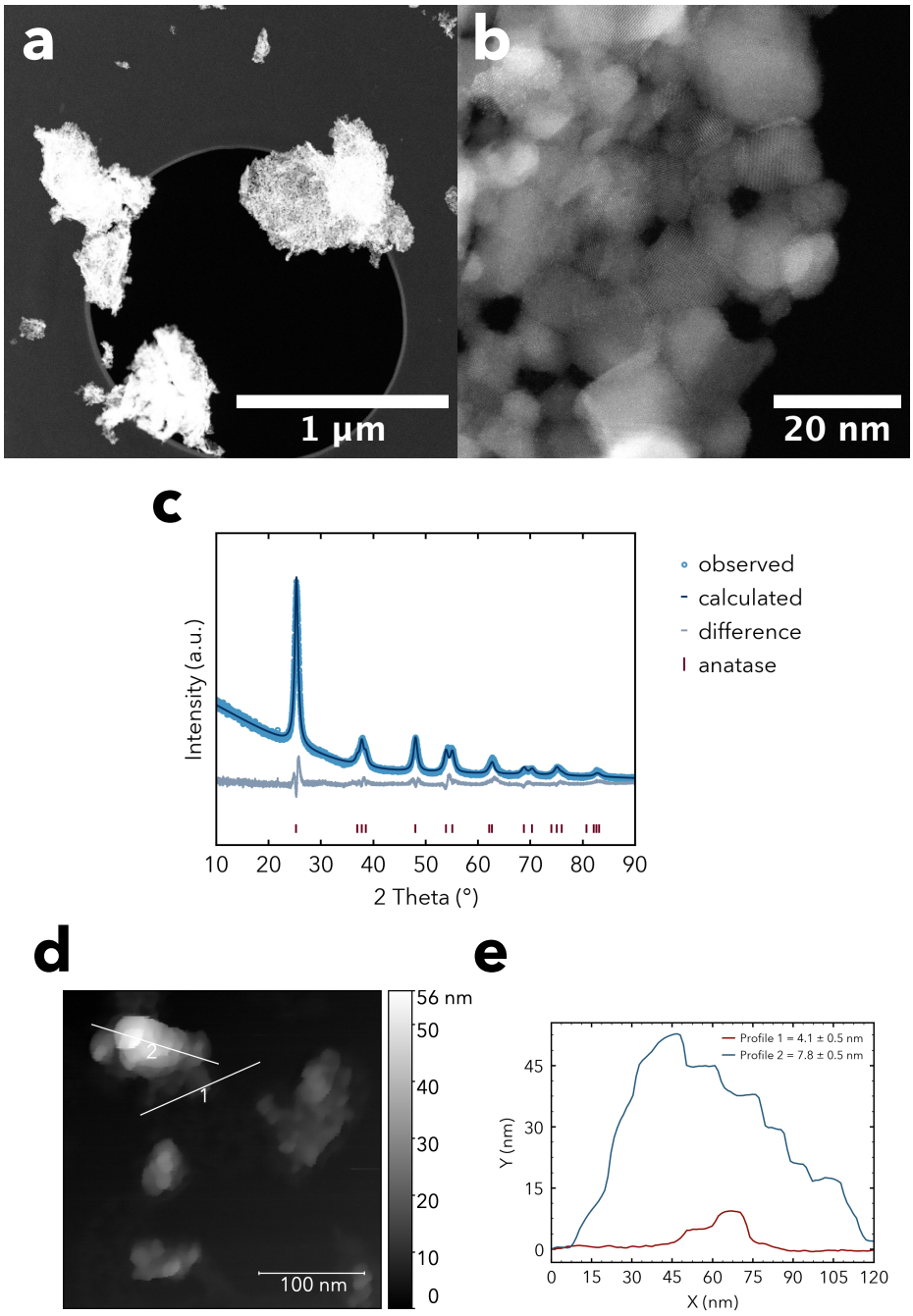


Figure 3.7: Characterisation of the TiO_2 nanosheets prepared with at 550 °C after the toluene/ethanol wash. (a) Low-magnification and (b) high-magnification ADF-STEM images. (c) Rietveld refinement of the XRD pattern. (d) AFM height map and (e) corresponding line profiles from (d). The AFM measurements were performed in collaboration with Ben Jagger (University of Oxford).

The Ir dispersion of the post-SEA, as-synthesised TiO_2 nanosheets was first investigated using ADF-STEM. Figure 3.8a shows representative exposed lattice planes of

the nanosheets, highlighted by the yellow boxes (regions i, ii, and iii), with $[IrCl_6]^{2-}$. Ir_1 are visible with clear contrast in the ADF-STEM image, as highlighted in green circles. The Fast Fourier Transform (FFT) images for regions i, ii, and iii, along with the Gaussian fits of the FFT peaks, confirm the observed lattice spacings are 0.172 ± 0.012 nm, 0.253 ± 0.017 nm and 0.384 ± 0.048 nm, respectively (Figure 3.8b and c). The analysis concludes that lattice planes corresponding to (200), (004), and (101) are observed.

The exposed facets of the TiO_2 nanosheets prepared by the original authors Zhao and coworkers are predominantly the (010) planes. The three planes observed in Figure 3.8 coincide with the major expected reflections from the [010] zone axis, suggesting that all the facets exposed could be close to (010), however slightly misaligned from the axis. This difference in exposed facets is likely a result of different hydrolysis rates of the $TiCl_4$ during the synthesis process.

Although the nanosheets synthesised here do not preferentially expose one single facet, an averaged overview of how the Ir_1 interacts with mixed facets of TiO_2 also provides valuable insights for optimising the Ir dispersion.

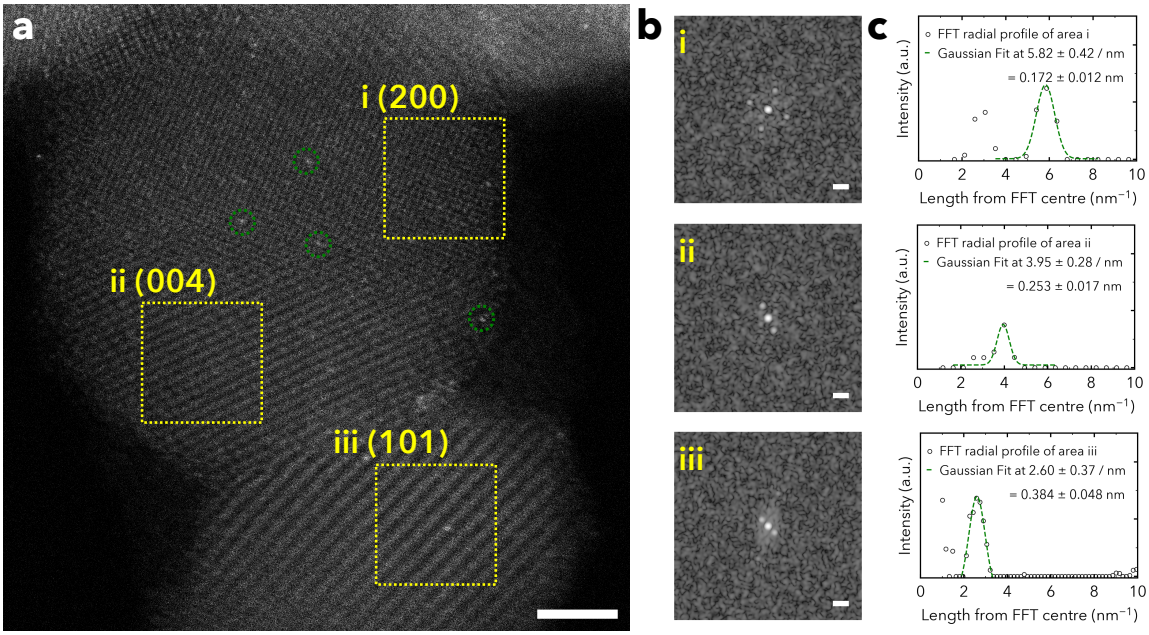


Figure 3.8: (a) HAADF-STEM image of $[IrCl_6]^{2-}$ loaded on TiO_2 nanosheets. The yellow boxes highlight representative regions of the TiO_2 nanosheets with different exposed lattice planes. Scale bar denotes 2 nm. (b) Fast Fourier Transform (FFT) images of regions i, ii, and iii in (a). Scale bar denotes 10 nm^{-1}. (c) Gaussian fits of the FFT peaks in (b), with the corresponding lattice plane spacings calculated from the fits. The error represents the standard deviation of the Gaussian fits.

So far, the assignment of the location of the Ir on the surface of the nanosheets has been solely based on their high contrasts against the TiO_2, i.e., observed as the bright spots in the ADF-STEM images. Spatially resolved chemical characterisation is required to correlate these bright spots with Ir. Single-atom energy dispersive X-ray (EDX) analysis or electron energy loss spectroscopy (EELS) are the desired techniques for this purpose. However, their use for the characterisation of Ir_1 is challenging. Displacements of the atom of interest are promoted by the electron beam when attempting to generate enough spectroscopic signal-to-noise ratio (SNR) [28]. Therefore, I analysed the chemical composition of one of the 1-2 nm clusters in one representative Ir-TiO_2 nanosheet sample to indirectly provide evidence that the bright spots of similar contrast are related to the presence of Ir.

As shown in Fig 3.9, spectrum 5, where the presumed Ir cluster is positioned, exhibits a peak at 2 eV, which corresponds to the X-ray emission from the Ir M edge. In contrast, no signal is observed in the same energy region in spectrum 7, which is collected at the clean TiO_2 region. These EDX results chemically confirm that these bright spots are indeed Ir, rather than contamination.

The Ir loading on TiO_2 nanosheets is calculated by measuring the concentration difference of $[IrCl_6]^{2-}$ in the stirring solution before and after SEA using UV-Vis spectroscopy. $[IrCl_6]^{2-}$ is UV-Vis active and exhibits a strong absorption peak at 488 nm (Fig 3.10a), which can be attributed to a ligand-to-metal charge transfer [29]. Assuming the $[IrCl_6]^{2-}$ is chemically stable and its absorption in the UV-Vis region does not evolve during the SEA process, the absorption intensity should scale linearly with $[IrCl_6]^{2-}$ concentration, as governed by the Beer-Lambert law [30]. The weight loading of Ir on the TiO_2 nanosheets can be calculated using the change in the $[IrCl_6]^{2-}$ solution before and after SEA, along with the known exact weight of the TiO_2 added and the total volume of the stirring solution.

As shown in Fig 3.10b, there is a robust linear relationship between the concen-

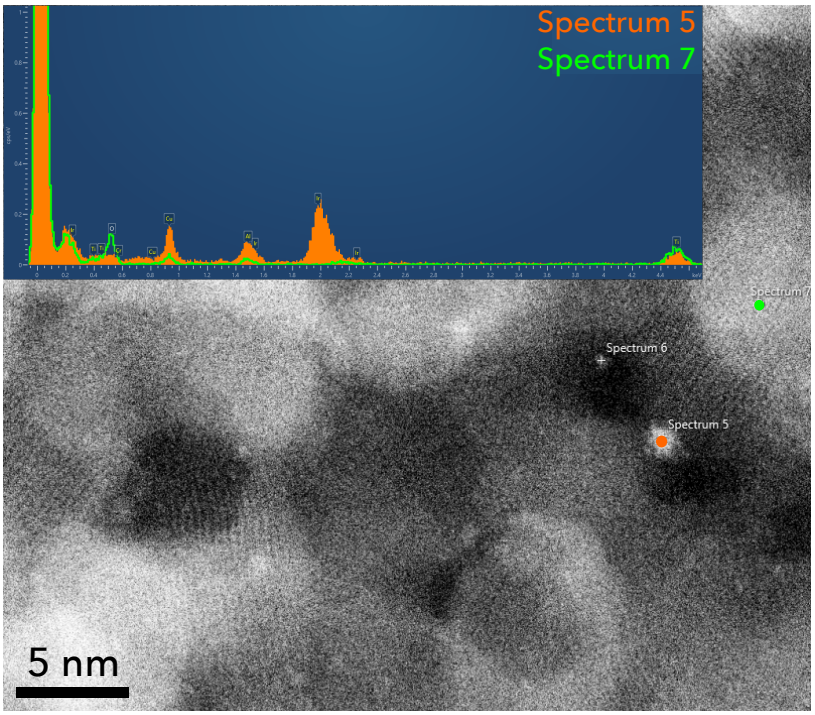


Figure 3.9: EDX analysis of bright spots in HAADF-STEM images. HAADF-STEM image and corresponding EDX spectra (inset) of Ir-TiO_2 nanosheet sample.

tration and absorbance, with a R^2 value of 0.99992. Using this calibration curve, the actual Ir loading on TiO_2 is estimated at 0.18 ± 0.01 wt% with a synthesis targeting a nominal loading of 0.5 wt% (the freshly prepared solution is labelled as "fresh," and the solution after SEA is labelled as "post-SEA" in Figure 3.10c).

The above characterisation of Ir on TiO_2 nanosheets equips me with the necessary details about this materials system, enabling the main objective of this work: investigating the mechanism of the Ir agglomeration during the thermolysis step with a focus on the influence of the heating rate on the Ir dispersion.

I synthesised three Ir-TiO_2 nanosheet samples using heating rates of 1 °C min^{-1} (Ir-TiO_2-1C), 10 °C min^{-1} (Ir-TiO_2-10C) and flash heating (Ir-TiO_2-flash), i.e., step jump to 500 °C. These samples were characterised with HAADF-STEM and HAADF-scanning electron microscopy (SEM) analysis, shown in Figure 3.11.

In the Ir-TiO_2-1C, Ir_1 dominates with a low degree of agglomeration, whereas in the Ir-TiO_2-10C, Ir_x of ∼1 nm in size is dominant, as observed in Figure 3.11a and c,

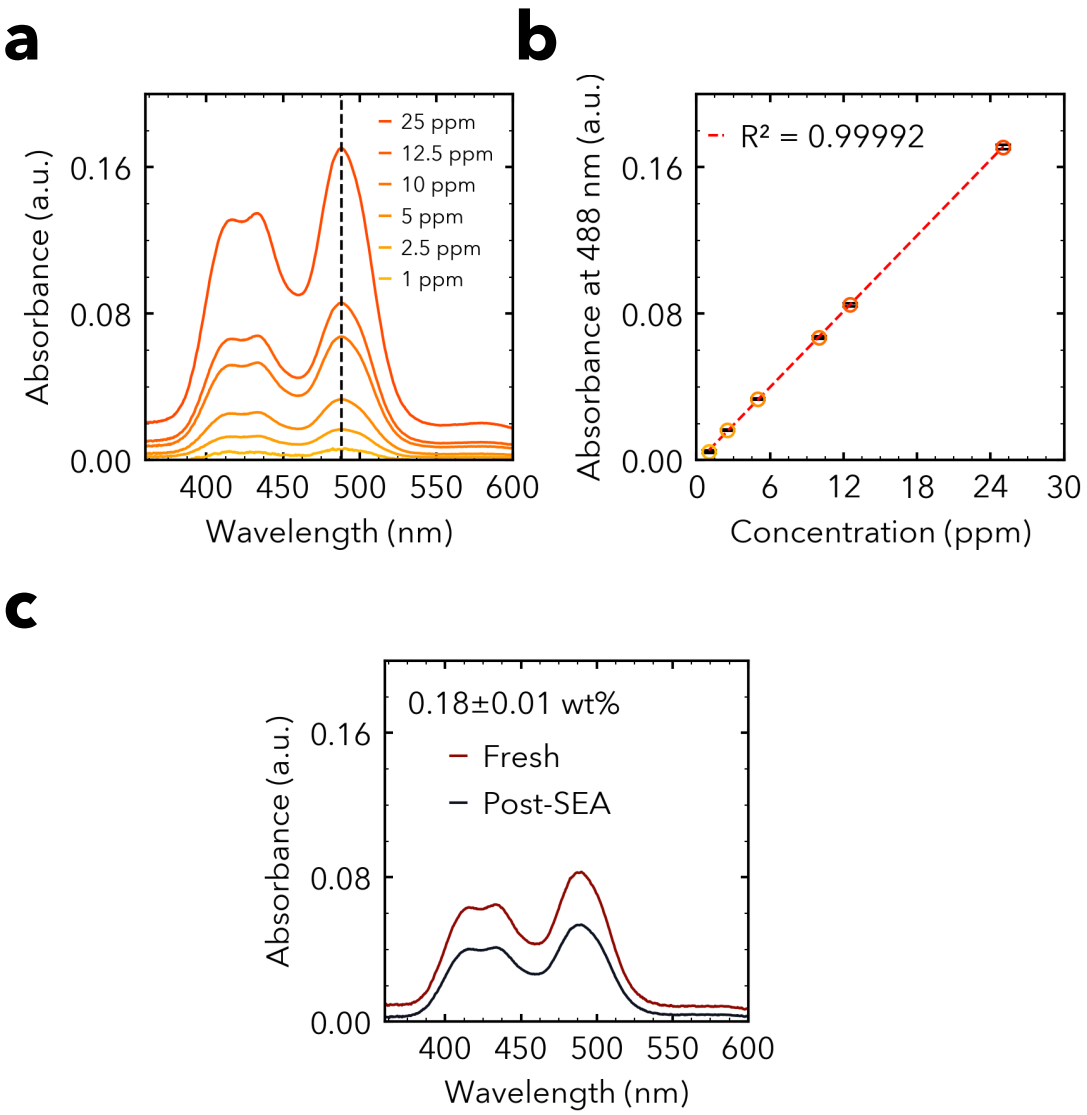


Figure 3.10: Determination of the actual Ir weight loading on TiO_2 using UV-Vis spectroscopy. (a) UV-Vis spectra of $[IrCl_6]^{2-}$ at various concentrations at pH 3. (b) Absorbance at 488 nm as a function of $[IrCl_6]^{2-}$ concentration. Error bars in (b) are calculated from at least three independent measurements. (c) UV-Vis spectra of the freshly prepared and the post-SEA $[IrCl_6]^{2-}$ solution for a 0.5 wt% nominal Ir loading.

respectively. HAADF-SEM images for both Ir-TiO_2-1C (Figure 3.11b) and Ir-TiO_2-10C (Figure 3.11d) show no evidence of large Ir particles. The Ir-TiO_2-flash sample shows a large size distribution of Ir, ranging from a number of Ir_1 along with Ir_x (Figure 3.11e) to particles that are approximately 20 nm, as evident in HAADF-SEM image shown in Figure 3.11f.

This qualitative analysis from the HAADF-STEM images confirms my hypothesis that control over Ir dispersion can be achieved by varying the heating rate of the synthesis. Further investigation into the synthesis mechanism is motivated.

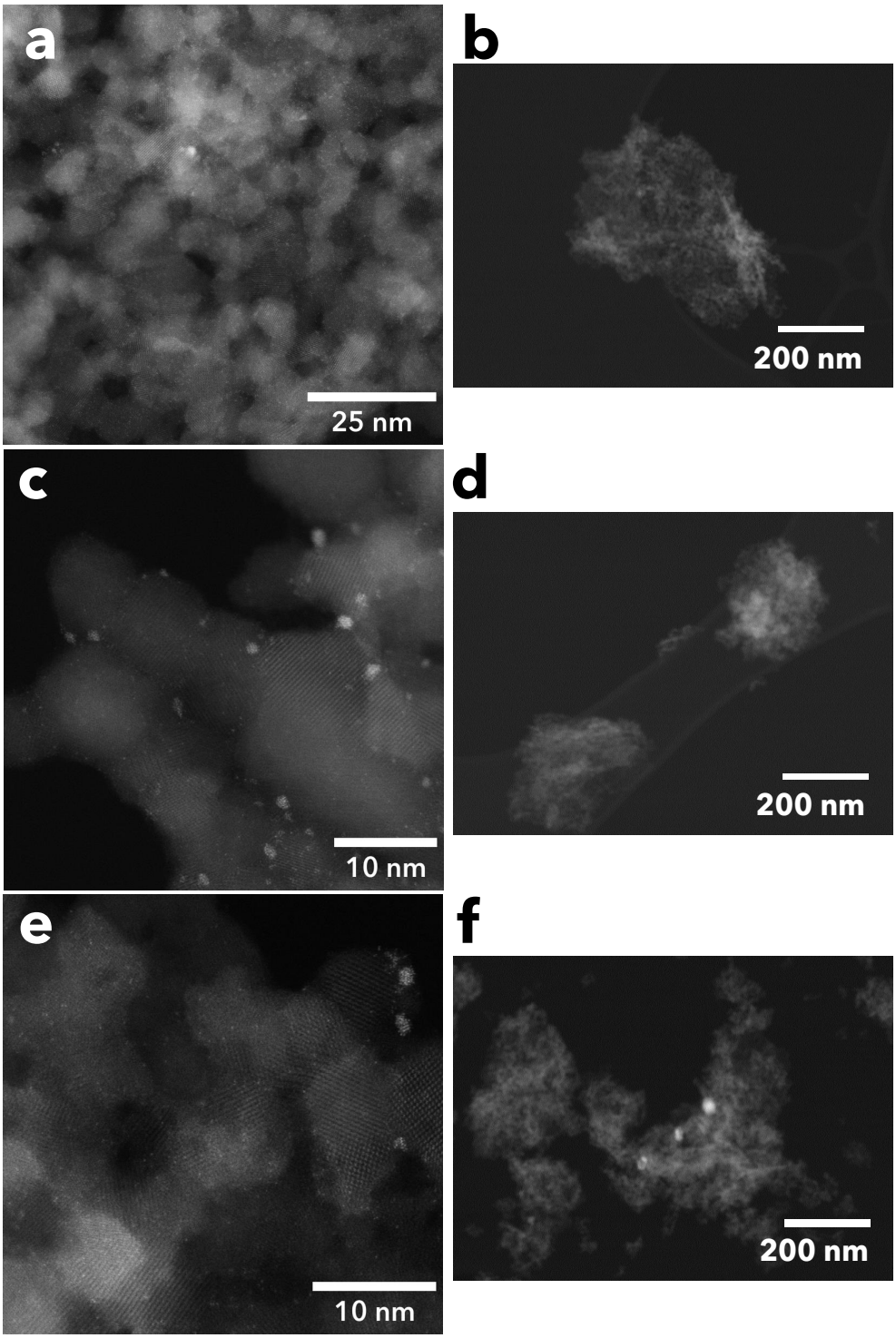


Figure 3.11: Ir dispersion of Ir-TiO_2 samples. (a) Representative HAADF-STEM and (b) HAADF-SEM images of Ir-TiO_2-1C. (c) Representative HAADF-STEM and (d) HAADF-SEM images of Ir-TiO_2-10C. (e) Representative HAADF-STEM and (f) HAADF-SEM images of Ir-TiO_2-flash. These samples were prepared on FTO glass electrodes for further OER characterisation, which will be discussed in Chapter 5. HAADF-SEM experiments were performed in collaboration with Dr. Guillaume Matthews (University of Oxford).

Conclusions

In this chapter, I first show that atomically dispersed Ir can be synthesised on TiO_2 anatase by the thermolysis of $[IrCl_6]^{2-}$ on the TiO_2. However, agglomeration of Ir is observed. A sufficient statistical representation of the Ir dispersion is required for further investigation of the Ir agglomeration behaviour and the Ir mobility during synthesis.

I explore two characterisation strategies: 1. Using SAXS to detect Ir clusters and 2. nanostructuring TiO_2 into 2D morphology for the HAADF-STEM characterisation at an extended length scale. The use of SAXS for the analysis of Ir dispersion on TiO_2 proves to be challenging. Although the experiments confirm the detection of scattering signal at a 2 wt% loading corresponding to the size of Ir clusters, detailed analysis of the scattering signal is hindered by the baseline signal variations between batches of the 5 nm TiO_2 support after the heat treatments. In contrast, the TiO_2 anatase nanosheets with 4 nm monolayer flat regions can be successfully prepared. These nanosheets enable the HAADF-STEM characterisation of Ir dispersion at a larger length scale than commercially available 5 nm nanoparticles.

Finally, using this TiO_2 anatase nanosheets as the support for the Ir, I demonstrate that different Ir dispersions on TiO_2 can be achieved by changing the heating rate of the synthesis. Specifically, atomically dispersed Ir dominates at the 1 °C min^{-1}, while Ir clusters are dominant at a higher heating rate. This observation motivates the in-situ heating ADF-STEM study in Chapter 4, aiming to understand the temperature-induced mobility mechanism and agglomeration behaviour of Ir during synthesis.

Experimental details

TiO_2 nanosheets synthesis

Firstly, reduced graphene oxide (rGO, XFnano) powder was ultrasonically dispersed in glycine-mediated (99%, Sigma-Aldrich) deionized water (18.2 MΩ cm, direct-Q water purification system)/ethylene glycol (99.8%, Sigma-Aldrich) solution at pH 3. The pH value of the mixture was adjusted using hydrochloric acid (36%, Suprapur, Sigma-Aldrich). $TiCl_4$ (99.8%, Sigma-Aldrich) was then gradually added to the mixture, followed by vigorous stirring at 70 °C for 4 hours to promote hydrolysis of the $TiCl_4$ into TiO_x on the surface of the rGO. Subsequently, a heat treatment step was performed in oxygen at 550 °C for 6 hours using a split tube furnace to combust and remove the rGO, meanwhile to crystallise TiO_x into anatase TiO_2. To perform the chemical washing, 50 mg of the synthesised TiO_2 nanosheets were dispersed in 50 mL of toluene/ethanol (3:1 v/v) mixture using an ultrasonication probe at 35% power output (Ultrasonic processors 500W, Sigma-Aldrich) with a 5-second on/off pulse cycle for 20 minutes in an ice bath. TiO_2 nanosheets were collected by centrifuging at 12000 rpm for 5 minutes. This process was repeated two times to ensure complete removal of rGO traces, followed by a drying step at 80 °C in an oven overnight. The synthesis of TiO_2 nanosheets was performed in collaboration with Dr Kai Wang (University of Oxford)

Ir-TiO_2 synthesis

A typical synthesis of the 0.18 wt% Ir-TiO_2 is as follows:

1. SEA of the $[IrCl_6]^{2-}$ on TiO_2: 10 mg of TiO_2 nanosheets or particles were first suspended in 8 mL of pH 3 deionized water, with pH value adjusted using hydrochloric acid. The $[IrCl_6]^{2-}$ solution was separately prepared by dissolving 1 mg of $H_2IrCl_6 \cdot xH_2O$ (99.9%, Sigma-Aldrich) in 3.77 mL of deionized water.

Subsequently, 0.5 mL of the $[IrCl_6]^{2-}$ solution was taken and added to 1.5 mL of deionized water with the mixture adjusted to pH 3. Then, this pH 3 $[IrCl_6]^{2-}$ solution was drop-wise added to the TiO_2 suspension while constant stirring for 1 hour. The $[IrCl_6]^{2-}$-loaded TiO_2 was then centrifuged at 12000 rpm for 10 minutes, followed by washing with pH 3 solution and dried in an oven at 80 °C overnight. This sample is labelled as the post-SEA, as-synthesised TiO_2.

2. Thermolysis: The post-SEA, as-synthesised TiO_2 was then placed in an Al_2O_3 crucible and heat treated in a tube furnace at 500 °C for 4 hours in flowing N_2 with a heating rate of choice.

Aberration-corrected scanning transmission electron microscopy (AC-STEM)

AC-STEM measurements were performed using a JEOL ARM200F microscope at an accelerating voltage of 200 kV. A CL aperture of 20 μm, convergence semiangle of 14.38 mrad, beam current of 69 pA, and detector angle between 78 and 271 mrad were used for HAADF images. A detector angle between 33 and 120 mrad was used for ADF imaging. Samples were deposited on a Cu TEM grid and baked at 150 °C in a vacuum overnight prior to the measurements. EDX measurements were performed using the EDX detector equipped with the JEOL ARM200F microscope (Oxford Instruments).

Scanning electron microscopy (SEM)

SEM measurements were performed using a high-resolution Merlin field-emission scanning electron microscope (Zeiss, Germany). STEM mode and the HAADF detector were used for the imaging. A 30 kV accelerating voltage and a 100 pA beam current were used.

Small angle X-ray scattering (SAXS)

SAXS experiments were performed at the labSAXS facility of the Diamond Light Source using the Xeuss 3.0 with a 9.2 keV Excillium Ga MetalJet source (Xenocs). Samples were packed in quartz capillaries, and the transmission measurement mode was used. Data analysis was performed using the DAWN software [31].

X-ray diffraction (XRD)

XRD measurements were performed using a 3KW diffractometer (Rigaku). A Cu K_α source ($\lambda = 1.5406$ Å) was used. A Nickel filter was used for the removal of Cu K_β radiation. Scans were collected between 10 and 90° with a step size of 0.02°. The surface of the powder sample was lightly levelled using a glass slide. Rietveld refinement was performed using GSAS-II software [32].

UV-Vis spectroscopy

UV-Vis measurements were performed using an Evolution 220 spectrophotometer (Thermo Scientific). A 1 cm quartz cuvette (Mettler Toledo) was used to load the sample solution. Scans between 360 and 700 nm with a step of 0.5 nm were performed. The residual stirring solution after the SEA was filtered with a PTFE syringe filter (Minipore, pore size 0.45 μm, Sigma-Aldrich) before the UV-Vis measurements.

Atomic force microscopy (AFM)

AFM was performed using a Bruker Dimension Icon system. TiO_2 nanosheets were dispersed in ethanol and drop cast on a 1 mm diameter muscovite mica sheet (Electron Microscopy Sciences). The height map was collected using the ScanAsyst imaging mode with a ScanAsyst-Airprobe (Bruker) at a scan rate of 0.5 Hz (256 px × 256 px). Data analysis was performed using the Gwyddion software [33].

References

[1] Jian Lin, Aiqin Wang, Botao Qiao, Xiaoyan Liu, Xiaofeng Yang, Xiaodong Wang, Jinxia Liang, Jun Li, Jingyue Liu, and Tao Zhang. Remarkable performance of Ir1/FeOx single-atom catalyst in water gas shift reaction. *Journal of the American Chemical Society*, 135(41):15314–15317, 10 2013.

[2] Qi Wang, Xiang Huang, Zhi Liang Zhao, Maoyu Wang, Bin Xiang, Jun Li, Zhenxing Feng, Hu Xu, and Meng Gu. Ultrahigh-Loading of Ir Single Atoms on NiO Matrix to Dramatically Enhance Oxygen Evolution Reaction. *Journal of the American Chemical Society*, 142(16):7425–7433, 4 2020.

[3] Haofei Wu, Zheng Li, Qiwen Zhang, Luozhen Jiang, Chen Hou, Shufen Chu, Jing Feng, Wenwu Xu, Lina Li, Fang Song, Mingwei Chen, and Pan Liu. Chloride ligand stablizes single-atom on nanoporous metal oxides in a pyrolysis process. *Chemical Engineering Journal*, 497, 10 2024.

[4] Aiping Jia, Wei Zhang, Hantao Peng, Yunshang Zhang, Tongyang Song, Lei Li, Yanwen Ye, Yu Wang, Mengfei Luo, De Li Chen, Weixin Huang, and Ji Qing Lu. Selective hydrogenation of crotonaldehyde over Ir/TiO2 catalysts: Unraveling the metal-support interface related reaction mechanism. *Journal of Catalysis*, 425:57–69, 9 2023.

[5] Xue Peng Yin, Hong Juan Wang, Shang Feng Tang, Xiu Li Lu, Miao Shu, Rui Si, and Tong Bu Lu. Engineering the Coordination Environment of Single-Atom Platinum Anchored on Graphdiyne for Optimizing Electrocatalytic Hydrogen Evolution. *Angewandte Chemie - International Edition*, 57(30):9382–9386, 2018.

[6] Shubo Tian, Wanbing Gong, Wenxing Chen, Na Lin, Youqi Zhu, Quanchen Feng, Qi Xu, Qiang Fu, Chun Chen, Jun Luo, Wensheng Yan, Huijun Zhao, Dingsheng

Wang, and Yadong Li. Regulating the Catalytic Performance of Single-Atomic-Site Ir Catalyst for Biomass Conversion by Metal-Support Interactions. *ACS Catalysis*, 9(6):5223–5230, 6 2019.

[7] Coogan B. Thompson, Liping Liu, Denis S. Leshchev, Adam S. Hoffman, Jiyun Hong, Simon R. Bare, Raymond R. Unocic, Eli Stavitski, Hongliang Xin, and Ayman M. Karim. CO Oxidation on Ir1/TiO2: Resolving Ligand Dynamics and Elementary Reaction Steps. *ACS Catalysis*, 13(12):7802–7811, 6 2023.

[8] Shufang Ji, Yuanjun Chen, Xiaolu Wang, Zedong Zhang, Dingsheng Wang, and Yadong Li. Chemical Synthesis of Single Atomic Site Catalysts, 11 2020.

[9] Weiming Chen, Xuanli Luo, Thomas J.A. Slater, Yongfang Zhou, Sanliang Ling, Rui Bao, Jesum Alves Fernandes, Jianshe Wang, and Yi Shen. General synthesis of single atom electrocatalysts: via a facile condensation-carbonization process. *Journal of Materials Chemistry A*, 8(48):25959–25969, 2020.

[10] Jiangbo Xi, Hyun Seung Jung, Yun Xu, Fei Xiao, Jong Wook Bae, and Shuai Wang. Synthesis Strategies, Catalytic Applications, and Performance Regulation of Single-Atom Catalysts. *Advanced Functional Materials*, 2008318:1–39, 2021.

[11] Shumin Gong, Yao Meng, Zeying Jin, Hsien-Yi Hsu, Minshu Du, and Feng Liu. Recent Progress on the Stability of Electrocatalysts under High Current Densities toward Industrial Water Splitting. *ACS Catalysis*, pages 14399–14435, 9 2024.

[12] Abhaya K. Datye and Hua Guo. Single atom catalysis poised to transition from an academic curiosity to an industrially relevant technology, 12 2021.

[13] Joaquin Resasco, Sheng Dai, George Graham, Xiaoqing Pan, and Phillip Christopher. Combining In-Situ Transmission Electron Microscopy and Infrared Spectroscopy for Understanding Dynamic and Atomic-Scale Features of Supported

Metal Catalysts. *Journal of Physical Chemistry C*, 122(44):25143–25157, 11 2018.

[14] Christophe Copéret. Single-Sites and Nanoparticles at Tailored Interfaces Prepared via Surface Organometallic Chemistry from Thermolytic Molecular Precursors. *Accounts of Chemical Research*, 52(6):1697–1708, 6 2019.

[15] Chongyi Ling, Yixin Ouyang, Qiang Li, Xiaowan Bai, Xin Mao, Aijun Du, and Jinlan Wang. A General Two-Step Strategy–Based High-Throughput Screening of Single Atom Catalysts for Nitrogen Fixation. *Small Methods*, 3(9):1–8, 2019.

[16] Leo DeRita, Joaquin Resasco, Sheng Dai, Alexey Boubnov, Ho Viet Thang, Adam S. Hoffman, Insoo Ro, George W. Graham, Simon R. Bare, Gianfranco Pacchioni, Xiaoqing Pan, and Phillip Christopher. Structural evolution of atomically dispersed Pt catalysts dictates reactivity. *Nature Materials*, 18(7):746–751, 7 2019.

[17] J R Regalbuto, A Navada, S Shadid, M L Bricker, and Q Chen. An Experimental Verification of the Physical Nature of Pt Adsorption onto Alumina. *Journal of Catalysis*, 184:335–348, 1999.

[18] Min Zeng. Influence of TiO2 surface properties on water pollution treatment and photocatalytic activity. *Bulletin of the Korean Chemical Society*, 34(3):953–956, 3 2013.

[19] Zhangsheng Shi, Wenqing Yang, Yuantong Gu, Ting Liao, and Ziqi Sun. Metal-Nitrogen-Doped Carbon Materials as Highly Efficient Catalysts: Progress and Rational Design. *Advanced Science*, 7(15), 2020.

[20] S. J. Freakley, J. Ruiz-Esquius, and D. J. Morgan. The X-ray photoelectron spectra of Ir, IrO2 and IrCl3 revisited. *Surface and Interface Analysis*, 49(8):794–799, 8 2017.

[21] Satish Kumar Iyemperumal, Thang Duc Pham, Jack Bauer, and N. Aaron Deskins. Quantifying Support Interactions and Reactivity Trends of Single Metal Atom Catalysts over TiO2. *Journal of Physical Chemistry C*, 122(44):25274–25289, 11 2018.

[22] Lena Puntscher, Kevin Daninger, Michael Schmid, Ulrike Diebold, and Gareth S. Parkinson. A study of Pt, Rh, Ni and Ir dispersion on anatase TiO2(101) and the role of water. *Electrochimica Acta*, 449, 5 2023.

[23] Hewei Zhao, Yujie Zhu, Fengshi Li, Rui Hao, Shaoxiong Wang, and Lin Guo. A Generalized Strategy for the Synthesis of Large-Size Ultrathin Two-Dimensional Metal Oxide Nanosheets. *Angewandte Chemie*, 129(30):8892–8896, 7 2017.

[24] Xiaotian Wang, Wenxiong Shi, Shaoxiong Wang, Hewei Zhao, Jie Lin, Zhao Yang, Mo Chen, and Lin Guo. Two-Dimensional Amorphous TiO2 Nanosheets Enabling High-Efficiency Photoinduced Charge Transfer for Excellent SERS Activity. *Journal of the American Chemical Society*, 141(14):5856–5862, 4 2019.

[25] Koichi Momma and Fujio Izumi. VESTA3 for three-dimensional visualization of crystal, volumetric and morphology data. *Journal of Applied Crystallography*, 44(6):1272–1276, 12 2011.

[26] R. F. Egerton, P. Li, and M. Malac. Radiation damage in the TEM and SEM. In *Micron*, volume 35, pages 399–409, 8 2004.

[27] A L Patterson. The Scherrer Formula for X-Ray Particle Size Determination. *Physical Review*, 56(10):978–982, 11 1939.

[28] R. F. Egerton and M. Watanabe. Characterization of single-atom catalysts by EELS and EDX spectroscopy. *Ultramicroscopy*, 193:111–117, 10 2018.

[29] Chr Klixbüll Jørgensen. Electron transfer spectra of lanthanide complexes. *Molecular Physics*, 5(3):271–277, 1962.

[30] D F Swinehart. The Beer-Lambert Law. *Journal of Chemical Education*, 39(7):333, 7 1962.

[31] Mark Basham, Jacob Filik, Michael T. Wharmby, Peter C.Y. Chang, Baha El Kassaby, Matthew Gerring, Jun Aishima, Karl Levik, Bill C.A. Pulford, Irakli Sikharulidze, Duncan Sneddon, Matthew Webber, Sarnjeet S. Dhesi, Francesco Maccherozzi, Olof Svensson, Sandor Brockhauser, Gabor Náray, and Alun W. Ashton. Data Analysis WorkbeNch (DAWN). *Journal of Synchrotron Radiation*, 22:853–858, 5 2015.

[32] Brian H Toby and Robert B Von Dreele. GSAS-II: the genesis of a modern open-source all purpose crystallography software package. *Journal of Applied Crystallography*, 46(2):544–549, 4 2013.

[33] David Nečas and Petr Klapetek. Gwyddion: an open-source software for SPM data analysis. *Central European Journal of Physics*, 10(1):181–188, 2012.

Chapter 4

Synthesis mechanism of atomically dispersed Ir on TiO_2 anatase nanosheets

Introduction

In Chapter 3, I demonstrated that the Ir dispersion on TiO_2 can be controlled by regulating the heating rates of the thermolysis step. Specifically, a higher heating rate leads to a higher degree of Ir agglomeration. In this chapter, I extend the understanding of this observation by investigating the mobility of Ir at the intermediate reaction temperatures using annular dark field scanning transmission electron microscopy (ADF-STEM) and correlating the results with the evolution of Ir oxidation state and bonding environment from the X-ray absorption fine structure (XAFS) analysis.

Firstly, I show the XAFS results of investigating the chemical states and bonding environment of Ir at different stages of the synthesis temperature, specifically at 80 °C, 150 °C, 300 °C and 500 °C. Subsequently, I demonstrate a Python-based

pipeline I developed to analyse the in-situ heating ADF-STEM data from image registration and its validation. Using this analysis pipeline, I investigate the behaviour of Ir agglomeration and the evolution of Ir mobility with increasing temperature. Finally, I propose a synthesis reaction mechanism derived from these results, followed by a dedicated session to discuss the limitations of the in-situ heating ADF-STEM experiments.

As of the writing of this thesis (August 2024), Wu and coworkers reported a successful synthesis of atomically dispersed Ir on Co_3O_4 for alkaline OER using a similar synthesis strategy used in this work, i.e., the thermal decomposition of $[IrCl_6]^{2-}$ to activate the Ir precursor for the synthesis of atomically dispersed Ir [1]. Using X-ray absorption spectroscopy (XAS) and time-of-flight secondary ion mass spectrometry to investigate the effect of temperature on the decomposition of $[IrCl_6]^{2-}$ on Co_3O_4, they concluded that the formation of an Ir-O_3-Cl_3 motif after heat treatment in air at 250 °C is the key to stabilising the Ir. They argued that the remaining Cl^- on Ir restrict reactions amongst the Ir, therefore preventing Ir agglomeration. They found Ir clusters at 350 °C, however, they did not investigate the underlying cause of Ir agglomeration.

Whether the observation reported by Wu and coworkers can be extended to the TiO_2 support will be addressed in this chapter.

4.1 Synthesis mechanism of atomically dispersed Ir on TiO_2

4.1.1 Evolution of Ir bonding environment during heating

To investigate the evolution of the Ir bonding environments at the intermediate thermolysis temperatures, extended X-ray absorption fine structure (EXAFS) analysis at

the Ir L_3 edge was performed on the post-SEA, as-synthesised Ir-TiO_2 samples heated at 80 °C, 150 °C, 300 °C and 500 °C. The 150 °C, 300 °C and 500 °C samples were prepared with a heating rate of 1 °C min^{-1} and held at the target temperatures for 4 hours.

Figure 4.1a shows the k^3-weighted Fourier transform (FT)-EXAFS spectra of the 80 °C, 150 °C, 300 °C and 500 °C samples, while Figure 4.1b-e show the respective fitting results. These samples are labelled in Figure 4.1 after their heating temperatures. The one labelled as 80 °C represents the post-SEA, as-synthesised sample, which was prepared by overnight drying in air at 80 °C after SEA of the $[IrCl_6]^{2-}$. The first-shell coordination peak of Ir is found at 2.24 Å for the 80 °C sample. This peak can be attributed to an Ir-Cl bond since Cl^- is not yet dissociated from Ir, evidenced by TGA and Cl 2p XPS in Figure 3.1. As the heating temperature increases, there is a decrease in this coordination bond length, converging at 2.01 Å for the 500 °C sample.

The fitted Ir-Cl bond length for the 80 °C sample is ∼0.09 Å shorter than that in $[IrCl_6]^{2-}$ (2.33 Å) [2], likely due to the atomically dispersed nature of the $[IrCl_6]^{2-}$ that lacks stabilisation in a crystal lattice, leading to a shortened Ir-Cl bonding. The first shell coordination of the 500 °C sample can be assigned to the Ir-O scattering path, with a bond distance of 2.01 Å, which is consistent with the Ir-O bonding in rutile phase IrO_2 (1.98 Å), as shown in Table 4.1.

Table 4.1: EXAFS fitting results for IrO_2.

Paths	**N**	**R (Å)**	σ^2 **(Å^2)**	ΔE_0 **(eV)**	S_0^2	**R-factor**
Ir-O.1	6	1.98 (0.01)	0.0030 (0.0006)	18 (1)		
Ir-Ir.1	2	3.17 (0.01)	0.0048 (0.0005)	21 (2)		
Ir-Ir.2	8	3.57 (0.01)	0.0048 (0.0005)	21 (2)	0.83 (0.07)	0.02
Ir-O.3	4	3.50 (0.04)	0.0030 (0.0006)	18 (1)		
Ir-O.4	4	3.68 (0.07)	0.0030 (0.0006)	18 (1)		

The fitting results of the FT-EXAFS spectra for all four samples are summarised

in Table 4.2. The fitting of the 80 °C sample was performed using the crystal structure of K_2IrCl_6 to calculate the electronic structure of the Ir-Cl scattering path [2], whereas for the Ir-O, the rutile IrO_2 structure was used for that of the Ir-O scattering path [3]. Fitting for both samples was performed by fixing only the intensity damping factor (S_0^2), determined from the fitting of the IrO_2 reference. Subsequently, the 150 °C and the 300 °C samples were fitted with the parameters for Ir-Cl and Ir-O path fixed, as determined by the fit of the 80 °C and 500 °C samples, respectively, allowing only the coordination number to vary.

The Ir-Cl coordination number for the 80 °C sample is determined to be 7.0 ± 1.6, decreasing to 4.9 ± 0.6, 4.6 ± 0.9 for 150 °C and 300 °C respectively. The Ir-O bond begins to form for the 300 °C sample with a CN of 1.5 ± 0.7 and shows 5.9 ± 1.1 when heated to 500 °C. The gradual decrease in the Ir-Cl coordination number with increasing temperature confirms the progressive decomposition of the $[IrCl_6]^{2-}$, in agreement with the TGA-MS data. Note that the slightly larger than the expected 6 Ir-Cl coordination in the 80 °C sample may be attributed to the residual Cl on the surface of TiO_2 after the SEA, which has a high probability of residing close to the Ir.

While the formation of Ir-O bond at 150 °C is negligible, it becomes apparent from 300 °C. This result is consistent with Wu and coworker observation, where they reported the onset of Ir-O bond formation on Co_3O_4 surface when the $[IrCl_6]^{2-}$ was heated at 250 °C [1]. The summed CN number of the Ir-Cl and Ir-O paths for the 300 °C sample is 6.1 ± 1.6, suggesting that the Ir centre remains 6-fold coordinated, which is the preferred geometry for Ir. The 6-fold O-coordinated structure for the Ir at 500 °C is consistent with the proposed structure of atomically dispersed Ir on the surfaces of various metal oxide supports [4, 5, 6]. In all these reports, Ir is proposed to form three Ir-O bonds with the surface oxygen on the metal oxide supports and the other with three Ir-O bonds likely from water molecules in air, e.g., the one shown

in Figure 1.5b, completing a 6 Ir-O coordination.

Contrary to what is expected from the above proposed Ir structure, where an Ir-Ti scattering corresponding to Ir-O-Ti bonds (∼3 Å) is expected, no discernible peak can be observed at this range of R for both 300 °C and 500 °C samples. This absence of an Ir-Ti scattering is likely due to a low Ir coverage on the surface of TiO_2, thus not producing strong scattering intensity for the analysis on the second-shell bonding environment of Ir. This result is consistent with Finzel and coworkers' observation that for features as small as atomically dispersed metal or clusters, EXAFS may lack sufficient sensitivity to unambiguously determine the second-shell coordination structure of the metal [7]. Although this lack of evidence for Ir second-shell coordination weakens the interpretation of the Ir-O coordination as a formation of bonding between Ir and the surface O from TiO_2, it remains plausible to conclude that the formation of the Ir-O bond corresponds to the coordination of the Ir precursor with the surface oxygen on the TiO_2, as a decrease in Ir mobility is observed beginning of 300 °C, suggesting a firm anchoring of the Ir precursor on the TiO_2 surface, as will be discussed in the following in-situ heating ADF-STEM investigations.

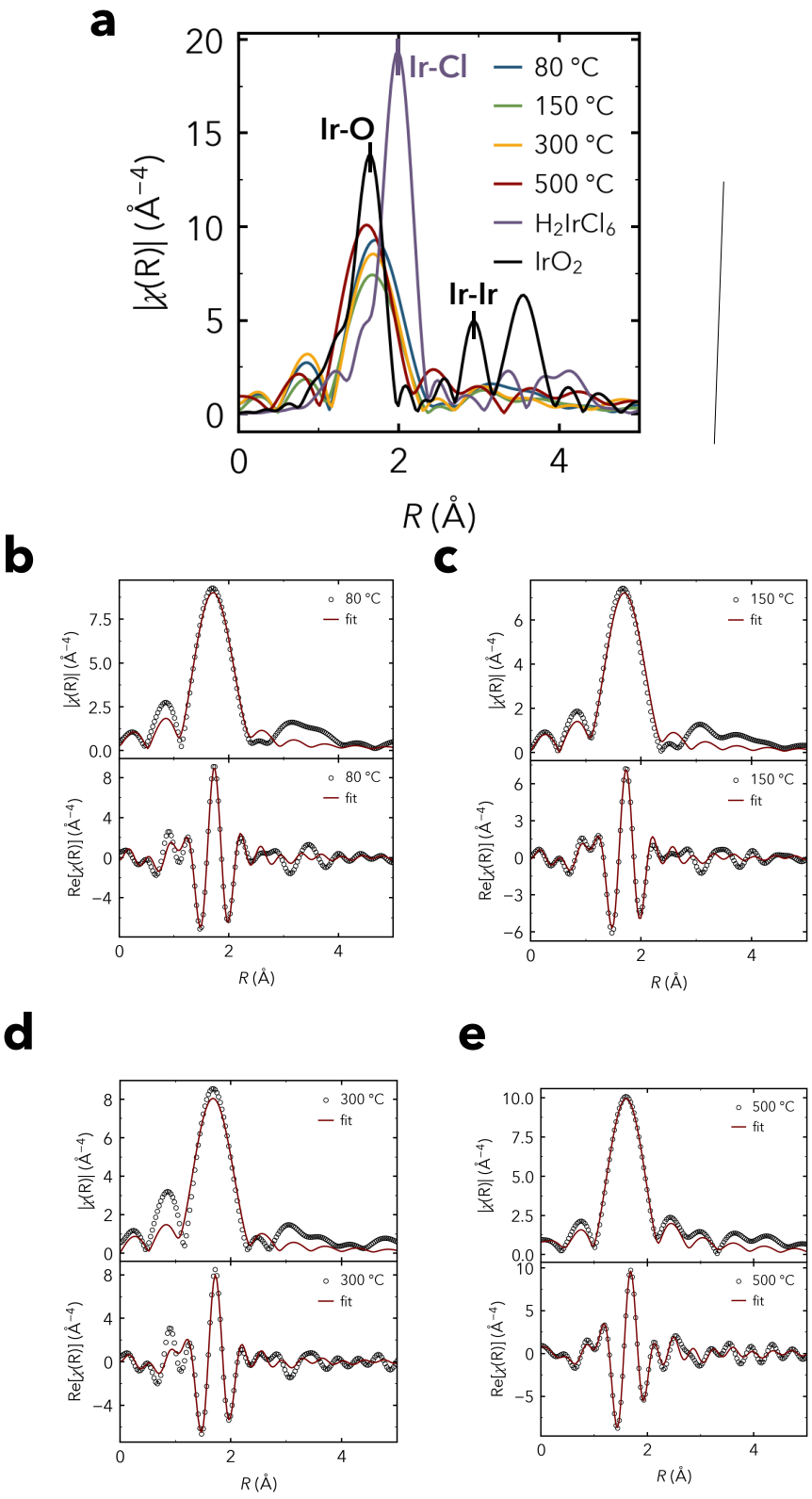


Figure 4.1: Bonding environment analysis. (a) Ir L_3-edge k^3-weighted FT-EXAFS spectra for the 80 °C, 150 °C, 300 °C, 500 °C and the reference samples. Spectra fits of the (b) 80 °C, (c) 150 °C, (d) 300 °C and (e) 500 °C sample, respectively.

Table 4.2: Summary of EXAFS fitting results for the 80 °C, 150 °C, 300 °C and 500 °C samples.

Temperature	**Path**	**N**	**R (Å)**	σ^2 **(Å^2)**	ΔE_0 **(eV)**	S_0^2	**R-factor**
80°C	Ir-Cl	7.0 (1.6)	2.24 (0.02)	0.0089 (0.0028)	3 (3)	0.83	0.04
150°C	Ir-Cl	4.9 (0.6)	2.24 (fixed)	0.0089 (fixed)	3 (fixed)	0.83	0.03
	Ir-O	0.6 (0.5)	2.01 (fixed)	0.0006 (fixed)	16 (fixed)	0.83	0.03
300°C	Ir-Cl	4.6 (0.9)	2.24 (fixed)	0.0089 (fixed)	3 (fixed)	0.83	0.06
	Ir-O	1.5 (0.7)	2.01 (fixed)	0.0006 (fixed)	16 (fixed)	0.83	0.06
500°C	Ir-O	5.9 (1.1)	2.01 (0.02)	0.0006 (0.0021)	16 (2)	0.83	0.03

The oxidation states of these samples are revealed by X-ray absorption near edge structure (XANES) analysis (Figure 4.2). The white line (WL) intensity for each sample is integrated (Figure 4.2c-f), and the oxidation state of Ir is determined by fitting to the WL intensity/number of 5d hole regression relationship determined from the Ir reference samples (Figure 4.2b), as described in Chapter 2. The WL positions are found at 11218.4 eV for all samples at different temperatures, while the intensity of the WL varies, as shown in Figure 4.2a. The oxidation states of 80 °C, 150 °C, 300 °C and 500 °C samples are estimated to be +3.8 ± 0.2, +3.7 ± 0.2, +3.7 ± 0.2 and +4.0 ± 0.2, respectively. The oxidation state of +3.8 ± 0.2 at 80 °C aligns with the expected oxidation state of the precursor $[IrCl_6]^{2-}$. A 0.1 eV reduction for the 150 °C and 300 °C samples can be attributed to the partial removal of the Cl ligands. For the 500 °C sample, Ir is re-oxidised to +4.0, which agrees again with the reported values, when Ir is 6-fold bonded to oxygen [4, 5, 6].

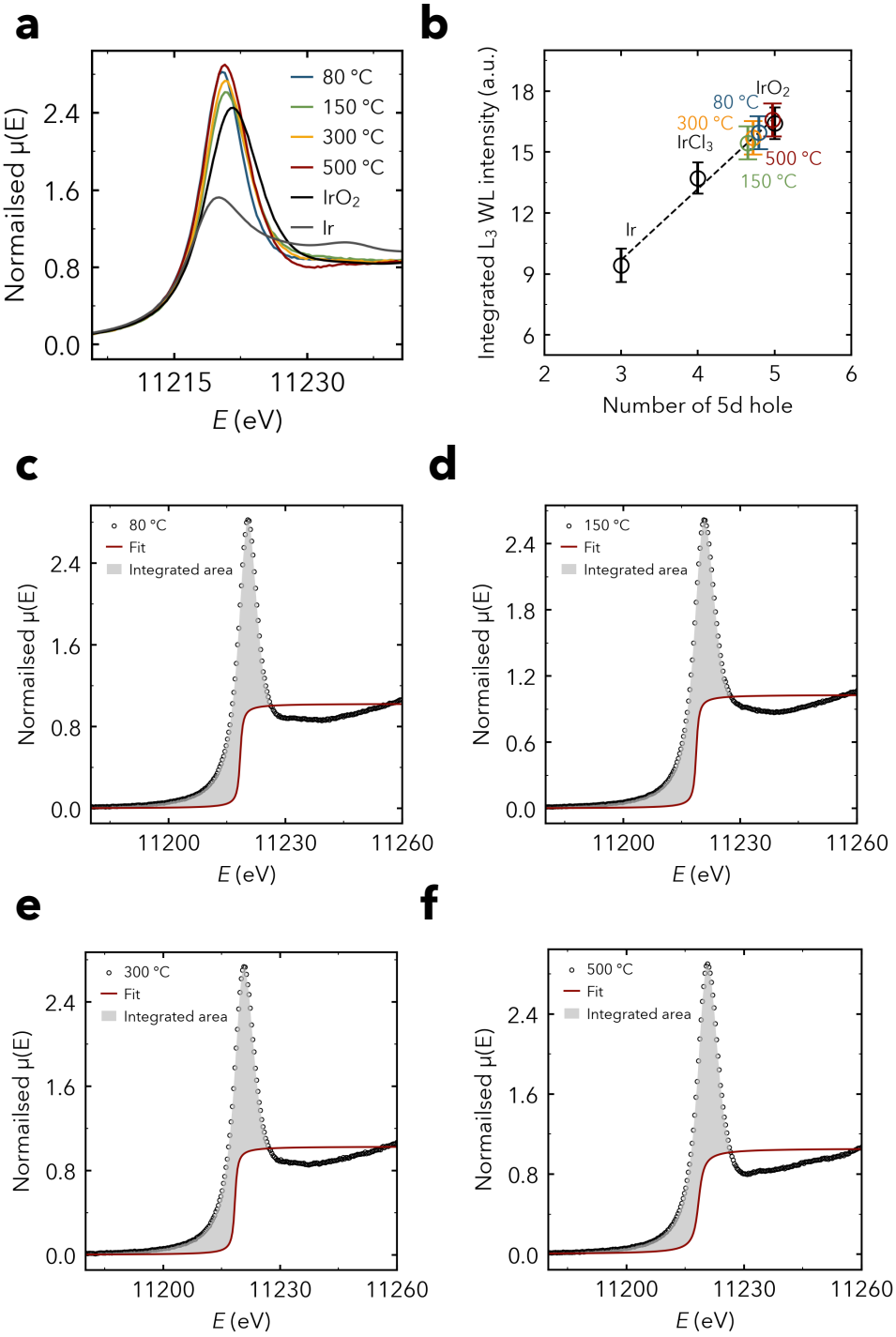


Figure 4.2: XANES analysis. (a) XANES spectra and (b) corresponding fits at Ir L_3 edge for the 80 °C, 150 °C, 300 °C, 500 °C and the reference samples. Integration of the WL is shown for the (c) 80 °C, (d) 150 °C, (e) 300 °C and (f) 500 °C sample, respectively. Raw data of the spectra is plotted with the scattered hollow circles. The background arc-tangent function fit to the spectra is shown as the red curve, and the integrated area is shown as the grey-shaded region.

Overall, the XAFS analysis of the post-SEA, as-synthesised Ir-TiO_2 samples treated at various reaction intermediates temperatures provides an overview of the evolution of the Ir chemical environment during synthesis. FT-EXAFS data demonstrate that the number of Ir-Cl coordination decreases continuously from 80 °C to 500 °C, with Ir-O bonds beginning to form at 300 °C. The oxidation state of Ir is +3.8 at 80 °C, then decreases to +3.7 at 150 °C and 300 °C, subsequently oxidised to +4.0 at 500 °C with a 6-fold Ir-O first-shell coordination confirmed.

As discussed at the end of Chapter 3, time-resolved tracking of the evolution of Ir bonding environments is desired using in-situ heating XAS. However, the low Ir to TiO_2 weight percentage (0.18 wt%) makes the spectrum collection with decent signal-to-noise ratio (SNR) time-intensive. The above ex-situ XAS experiments confirm that each spectrum requires 30 min of collection time. Long measurements pose a risk of insufficient time resolution for the in-situ heating XAS to follow the evolution of the Ir bonding environment, which is expected to be at a time scale of tens of minutes. Therefore, I decided to focus on spending the beamtime collecting ex-situ samples to gather higher-quality spectra more effectively.

4.1.2 Data analysis workflow for the in-situ heating ADF-STEM experiments

This section describes the in-situ heating STEM experiments and their data analysis for the examination of the evolution of Ir mobility on TiO_2 with increasing temperature. The experiments were performed on the post-SEA, as-synthesised sample using the DENS wildfire heating chips described in Chapter 2, and data was collected at 80 °C, 150 °C, 300 °C and 500 °C. To provide a statistically averaged overview of the Ir mobility, I acquired images from at least six different sample areas, each tracking the Ir displacements for at least 20 minutes at all four temperatures.

The workflow for analysing Ir mobility is as follows: firstly, a rigid registration of

the images was performed for all temperatures over time to correct for the drift of the STEM holder and align the TiO_2 substrate to the same position, enabling the tracking of Ir displacements with respect to the TiO_2 support. This step produces image stacks of a specific sample area monitored over time. Then, an image processing pipeline developed by myself is applied to the image stacks to prepare them for the following identification of the Ir and the subsequent tracking of the Ir displacement over time, using the Trackpy Python package [8]. This establishes the Ir displacement trajectories. Lastly, the trajectories are analysed to gain insights into the time- and temperature-resolved mobility of the Ir.

The image registration was performed with its working principles described in Chapter 2. Figure 4.3a and b shows two registered ADF-STEM images collected at 300 °C and 500 °C, respectively. As discussed at the end of Chapter 1, in all the discussions of ADF-STEM data to follow, I categorise the atomically resolved Ir species by their spatial separation from each other, irrespective of their actual chemical state, as this is indistinguishable from the ADF-STEM images alone. When the separation between two atomically resolved Ir is within the distance threshold, set at 3.16 Å based on the Ir-Ir distance in IrO_2, they are considered to be an Ir cluster (Ir_x, where x represents the number of Ir in this cluster). This separation criterion is applied to all the following analyses.

Single Ir (Ir_1), small Ir clusters ($Ir_{2\text{-}6}$) and larger Ir clusters ($Ir_{>6}$) are present. This distribution of Ir sizes is prepared on purpose, aiming to increase the chances of observing the dynamic behaviour of different Ir sizes within a limited microscope time. The sample was prepared by skipping the washing step after SEA of $[IrCl_6]^{2-}$, allowing residual $[IrCl_6]^{2-}$ solution to remain on the TiO_2 surface. One micro-litre of this solution containing the $[IrCl_6]^{2-}$ and TiO_2 was then dropped on the heating STEM chip and rapidly dried using a heat gun, inducing stochastic agglomeration of the $[IrCl_6]^{2-}$ on the surface of TiO_2.

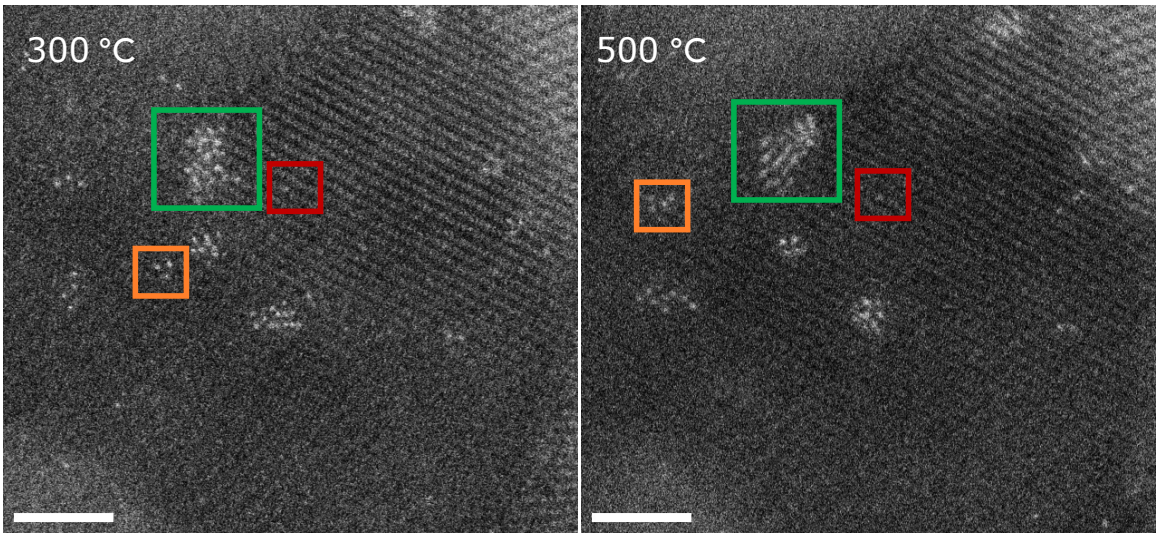


Figure 4.3: Representative ADF-STEM images captured at (a) 300 °C and (b) 500 °C on a DENS Wildfire Nano-Chip. Red, orange and green boxes highlight the presence of Ir_1, $Ir_{2\text{-}6}$ and $Ir_{>6}$, respectively.

After image registration, the next step is to locate the atomically resolved Ir with minimal human interpretation bias. This step is of particular importance for my dataset when attempting to investigate Ir mobility, as the data has a particularly low SNR, shown in the intensity line profile of a representative STEM image in Figure 4.4c. Before image processing, the Ir intensity (highlighted in the green circle) is nearly indistinguishable from the noise and the background intensity of the TiO_2, as highlighted in red circles. Common workflows, such as applying a Gaussian blur to denoise, followed by locating the local intensity maxima across the image, are not sufficiently reliable for my data analysis.

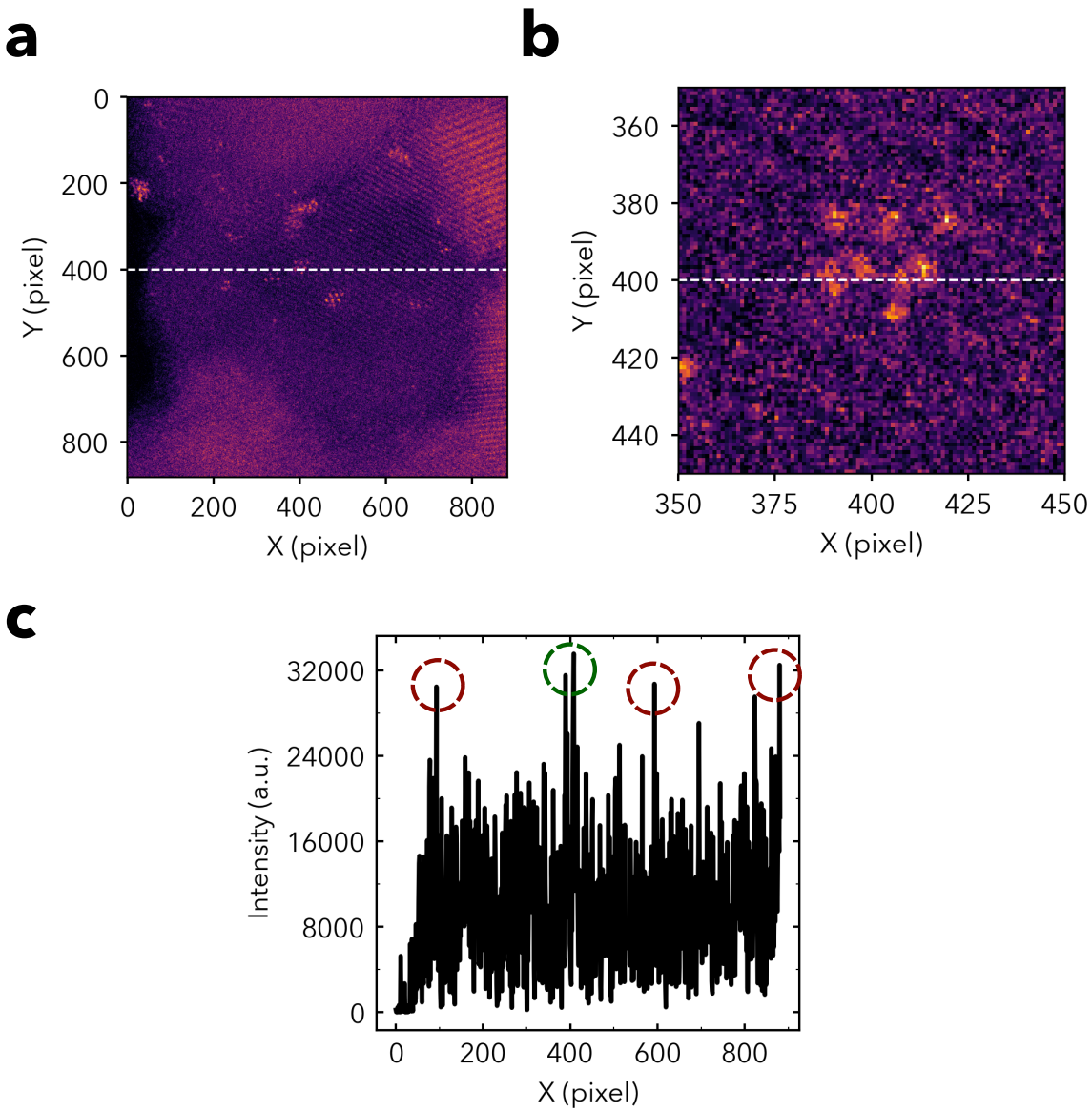


Figure 4.4: Intensity line profile of a representative in-situ heating ADF-STEM image. (a) Raw image before processing. The white dashed line indicates the location of the line profile. (b) Zoomed-in view of the centre of the image (a). (c) Intensity line profile along the dashed line in (a) and (b). The green circle highlights the signal from the Ir at approximately X = 400, and the red circles highlight the noise in the image.

To prepare the images for accurate detection of the atomically resolved Ir, I implemented a Python-based image processing pipeline modified from the workflow developed by Liu and coworkers and Mitchell and coworkers' work [9, 10]. I adapted their workflow to my datasets, where low SNR and lattice fringes complicate the de-

tection and tracking of Ir. A detailed discussion of this pipeline can be found at the end of this chapter.

Figure 4.5b and a shows detection results of $Ir_{1\text{-}10}$ and $Ir_{>10}$, respectively. In Figure 4.5b, atomic features with high contrast, where Ir is expected, are identified without an apparent large number of false positive and negative detections, confirming that the pipeline correctly functions. Subsequently, the classification of Ir_1 and $Ir_{2\text{-}10}$ is performed using the clustering criteria described above. Notice that I separate the detection of $Ir_{>10}$ (on average $>$ 1 nm) from the rest. Instead of using the same Ir detection mechanism, these larger clusters are identified as ensembles. The constituent Ir in these large clusters are constantly shifting their arrangements around each other under the electron beam. Thus, they are not always atomically resolved, despite the fact that most of them are monolayer (highlighted in the red box in Figure 4.5a). Separating $Ir_{>10}$ from the rest improves the overall accuracy of the detection of the atomically resolved Ir and also helps with the following Ir linking.

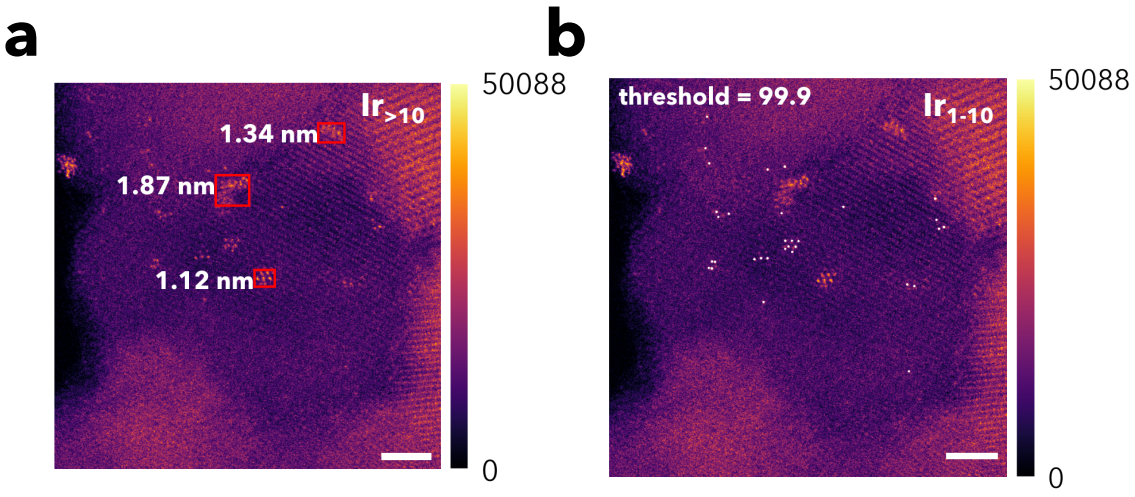


Figure 4.5: Detection of the atomically resolved Ir in the ADF-STEM images. (a) Representative $Ir_{>10}$ detected, highlighted in red boxes and labelled with their sizes in nanometers. (b) Representative $Ir_{1\text{-}10}$ detected, highlighted with white dots.

Following the identification of the Ir positions and the classification of Ir_1, $Ir_{2\text{-}10}$ and $Ir_{>10}$, the mobility of Ir on TiO_2 is investigated by linking the Ir across consecutive

image frames in the image stack using the method as described in Chapter 2. This step enables the Ir mobility analysis in the following section.

4.1.3 Thermal induced Ir mobility on TiO_2

Figure 4.6a-c visualise a representative set of linked Ir trajectories for Ir_1, $Ir_{2\text{-}6}$ and $Ir_{>6}$ at 500 °C over a period of approximately 20 minutes, respectively. Figure 4.6d presents the analysed total counts of the Ir with different sizes at each temperature, with more than 150 counts of Ir_1 analysed at 150 °C, 300 °C and 500 °C and over 90 counts analysed at 80 °C. Figure 4.6e shows the total counts of displacements analysed, with at least 200 displacements analysed for Ir_1 and a few tens counts for $Ir_{2\text{-}6}$ and $Ir_{>6}$ across all four temperatures. Note that I have combined the analysis of Ir_{7-10} with the analysis of $Ir_{>10}$ to become a new $Ir_{>6}$ class for a clearer data presentation, as these two Ir cluster size groups behave similarly for the analysis presented as follows.

Qualitative analysis of Figure 4.6a-c reveals that large displacements (> 0.5 nm) occur more frequently for Ir_1 than for $Ir_{2\text{-}6}$ and $Ir_{>6}$. In addition, none of the displacements show directionality, suggesting Brownian-motion-like mobilities for the Ir species. Note that the trajectories of the Ir_1 are often incomplete throughout the full period of the image frames due to the previously discussed disappearance of Ir_1. Even though a memory of 3 frames is added to rectify this technical challenge, reconstructing full trajectories of all Ir_1 remains difficult. Increasing the number of memories might improve this, but it also increases the likelihood of false Ir linking. Therefore, I maintain the parameters described above.

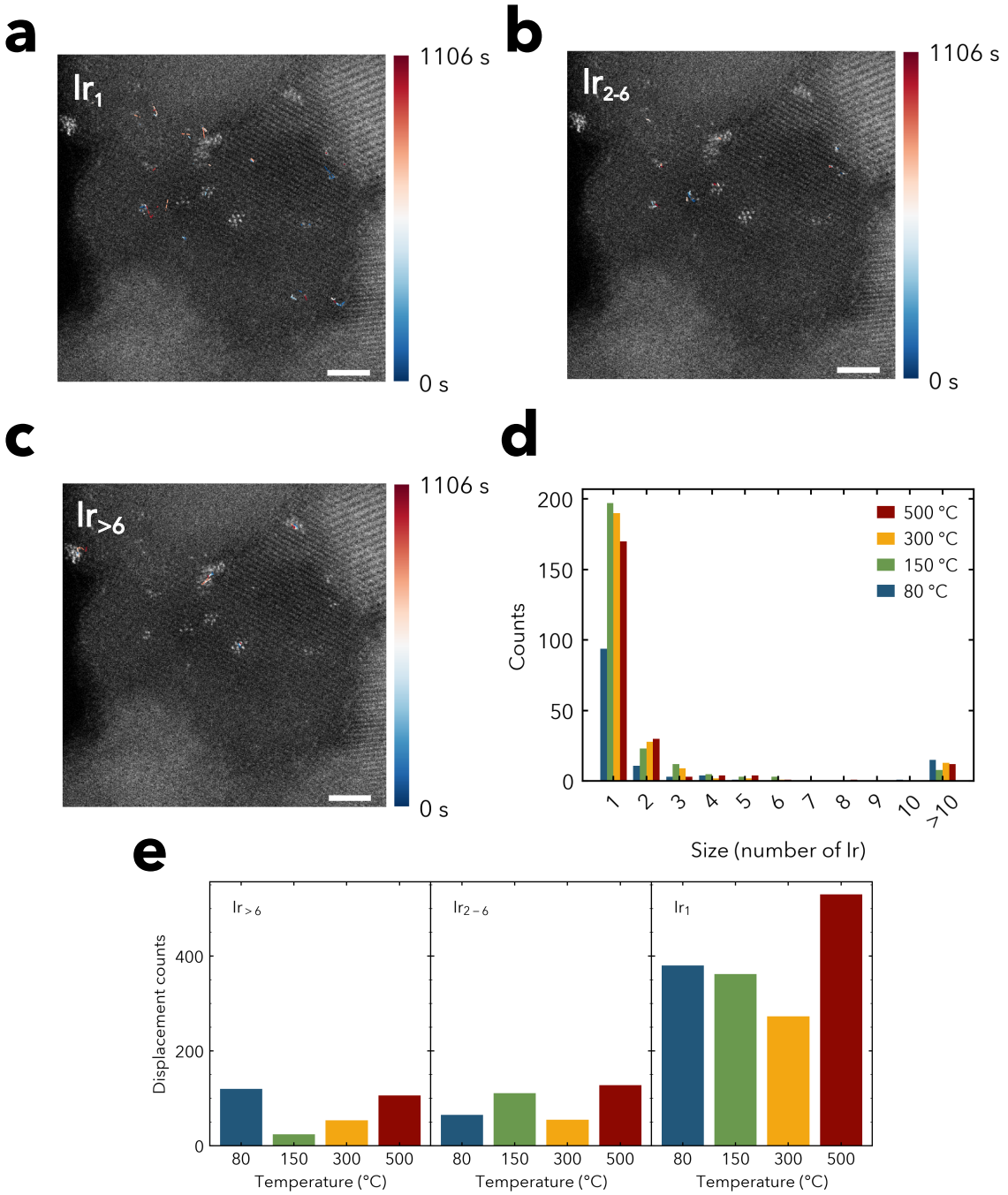


Figure 4.6: Representative set of linked Ir trajectories at 500 °C. (a) Ir_1 trajectories, (b) $Ir_{2\text{-}6}$ trajectories and (c) $Ir_{>6}$ trajectories. (d) Total number of Ir tracked as a function of Ir size (e) Total number of Ir displacements tracked as a function of temperature and Ir size.

Figure 4.7 compares the distribution of displacement velocities for Ir_1, $Ir_{2\text{-}6}$ and $Ir_{>6}$ across all four temperatures. Ir displacements are divided into high- and low-

velocity regions using the displacement velocity of 0.005 nm s^{-1} as the threshold (highlighted with the vertical line in Figure 4.7). Overall, Ir_1 exhibits higher proportion in the high-velocity region than $Ir_{2\text{-}6}$, followed by $Ir_{>6}$, regardless of the heating temperatures. This suggests a higher mobility of Ir_1 compared to $Ir_{2\text{-}6}$ and $Ir_{>6}$, consistent with the qualitative analysis from Figure 4.6a-c.

For $Ir_{2\text{-}6}$ and $Ir_{>6}$, their distribution profiles remain relatively unchanged with increasing temperatures, while the distribution for Ir_1 evolves. Specifically, the displacement velocities for Ir_1 shift towards the low-velocity region when temperature increases from 80 °C and 150 °C to 300 °C and 500 °C, converging towards 0.001 nm s^{-1} with a smaller proportion between 0.004 and 0.008 nm s^{-1}. This shift begins at 300 °C and maintains at 500 °C, suggesting an overall decrease in Ir_1 mobility when the sample is heated at 300 °C and 500 °C.

Note that the displacement of Ir_1 is driven by a combination of energy transfer from the electron beam and the elevated temperature, explaining the strong presence of high-velocity displacements at 80 °C for Ir_1. The experiments were conducted using a 300 kV beam, capable of transferring up to 4.4 eV of electron energy to the Ir_1, as estimated by Zhao and coworkers [11]. This amount of energy is expected to promote displacements of Ir_1 on TiO_2, based on Alghannam and coworkers' density-functional theory (DFT) calculations of the diffusion barriers for precious metal adatoms on TiO_2, which range from 1 to 4 eV. [12] Therefore, the apparent mobility observed in Figure 4.7 cannot be directly correlated with the elevated temperatures to derive a temperature-mobility relationship. Instead, I focus on the evolution of Ir mobility by comparing the displacement velocity profile between different temperatures within the same Ir size, as in these comparisons, the beam energy contribution to the Ir mobility can be offset, assuming negligible variation in the beam energy transfer.

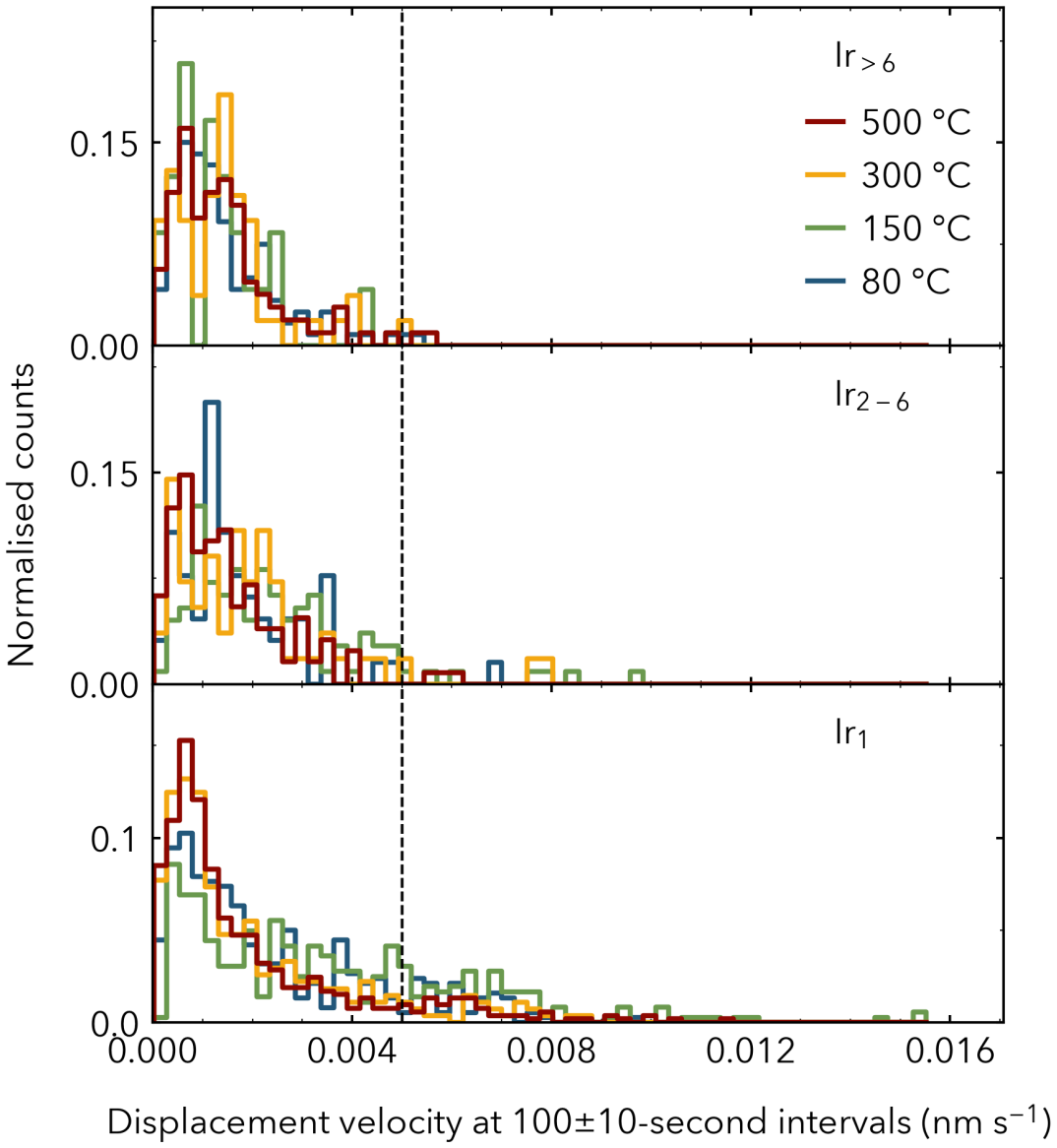


Figure 4.7: Ir mobility analysis as a function of temperature and Ir size. Histograms showing displacement velocities for Ir_1, $Ir_{2\text{-}6}$ and $Ir_{>6}$ across 80, 150 °C, 300 °C and 500 °C. The displacement velocities are calculated over 100 ± 10-second intervals, meaning a displacement velocity of 0.01 nm s^{-1} corresponds to a total 1 nm displacement within this time interval. The vertical line marks the displacement velocities at 0.005 nm s^{-1}.

Figure 4.8 further presents the time-resolved investigation of Ir_1 displacement at 300 and 500 °C, with the 300 °C dataset tracked up to 6000 seconds from the onset of

reaching this target temperature, and the 500 °C dataset tracked up to 9000 seconds. For both temperatures, the datasets are divided into two time groups, namely, 0-1200 seconds and >1200 seconds. Overall, a shift in Ir_1 velocity distribution towards the low-velocity region over time can be observed at both 300 and 500 °C, particularly for 500 °C. Notably, a reappearance of high-velocity displacements occurs upon heating from 300 °C to 500 °C, which is evident by comparing the >1200 seconds group at 300 °C to the >1200 seconds group at 500 °C. This high-velocity component diminishes after 1200 seconds of heating at 500 °C, with the velocity distribution beginning to resemble that observed at 300 °C after 1200 seconds. These observations reveal that the decrease in Ir_1 mobility seen in Figure 4.8 occurs gradually over time, rather than instantaneously upon the temperature increase.

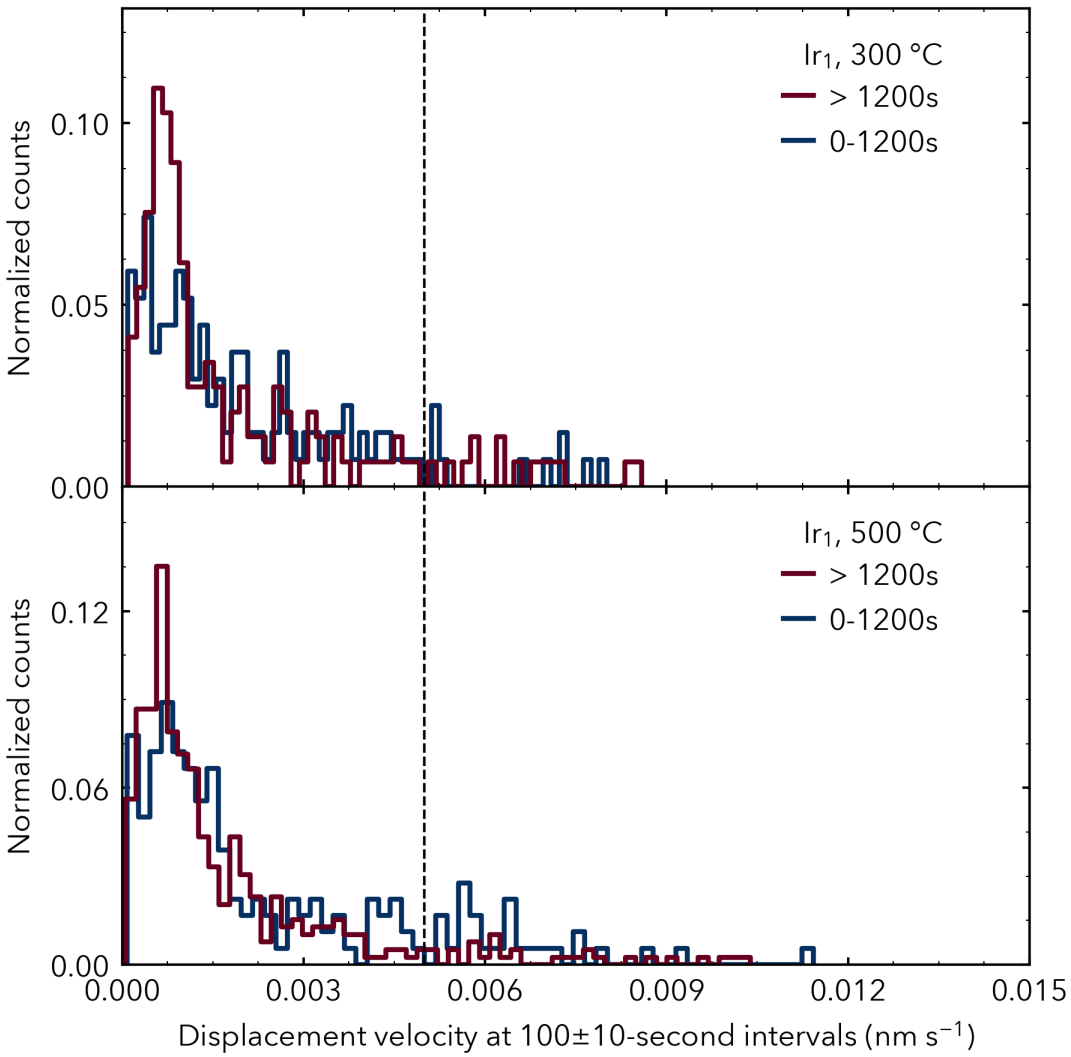


Figure 4.8: Time-resolved Ir_1 mobility analysis. Histograms showing displacement velocities at 300 °C (top) and 500 °C (bottom) as a function of time (0-1200 seconds and >1200 seconds). The vertical line marks the displacement velocities at 0.005 nm s^{-1}.

After the statistical analysis of the Ir mobility, I further establish a qualitative understanding of Ir agglomeration behaviour at different temperatures. At 80 °C, there are instances of two Ir_1 agglomerates, specifically, approaching each other to within the Ir-Ir distance in IrO_2 (3.16 Å), becoming classified as an Ir_2. Yet, this Ir_2 can disassemble over time (Figure 4.9a). In contrast, when three Ir_1 meet one another (Figure 4.9b), they start to stay as an ensemble and move around one another,

staying as an Ir_3. Since XAFS analysis indicates that Ir remains as $[IrCl_6]^{2-}$ at this temperature, the interactions between Ir are expected to be limited to van der Waals forces. The observation in Figure 4.9 implies that van der Waals interaction within an Ir_2 at 80 °C is weak, but starting from Ir_3 the mutual interaction between the Ir appears to strengthen significantly, leading to an ensemble-like behaviour.

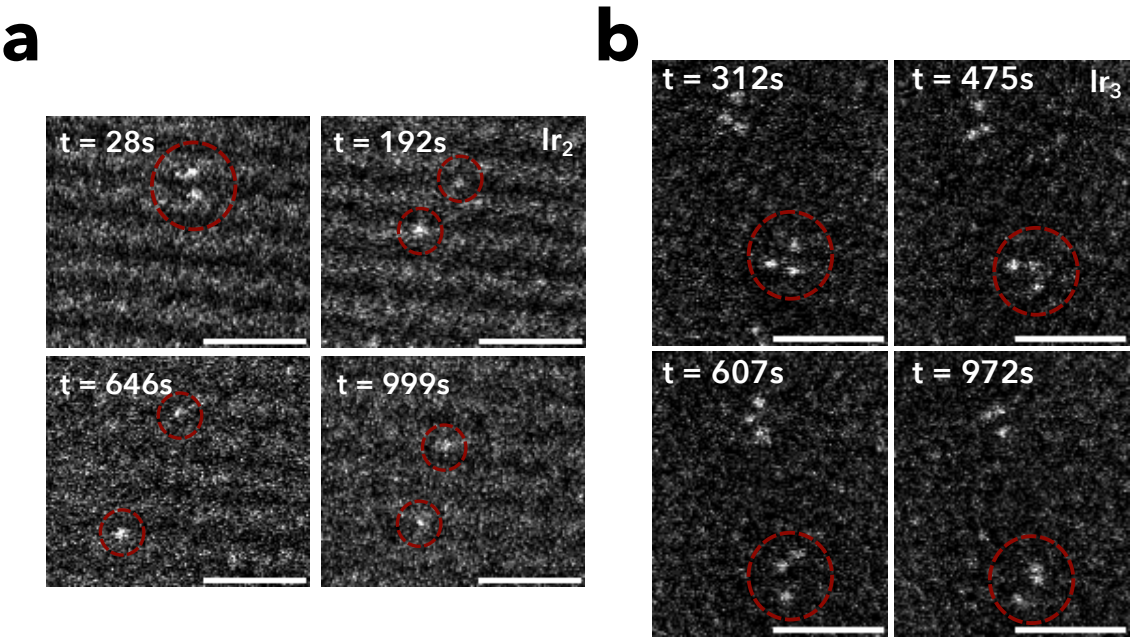


Figure 4.9: Time-resolved ADF-STEM images of a representative (a) Ir_2 and (b) Ir_3 captured at 80 °C. Scale bars are 2 nm. Ir_3 in (b) are highlighted in red dash-line circles of the same sizes in each image set to demonstrate their proximity to one another.

At 300 °C, the two Ir in Ir_2 begins to remain agglomerated when approaching each other (Figure 4.10a). A similar behaviour can be observed for the Ir in Ir_3 (Figure 4.10b). This observation is contrary to Wu and coworkers' theory that the Cl^- remaining on the atomically dispersed Ir prohibit the Ir from interacting with each other, hence stopping them from agglomerating [1].

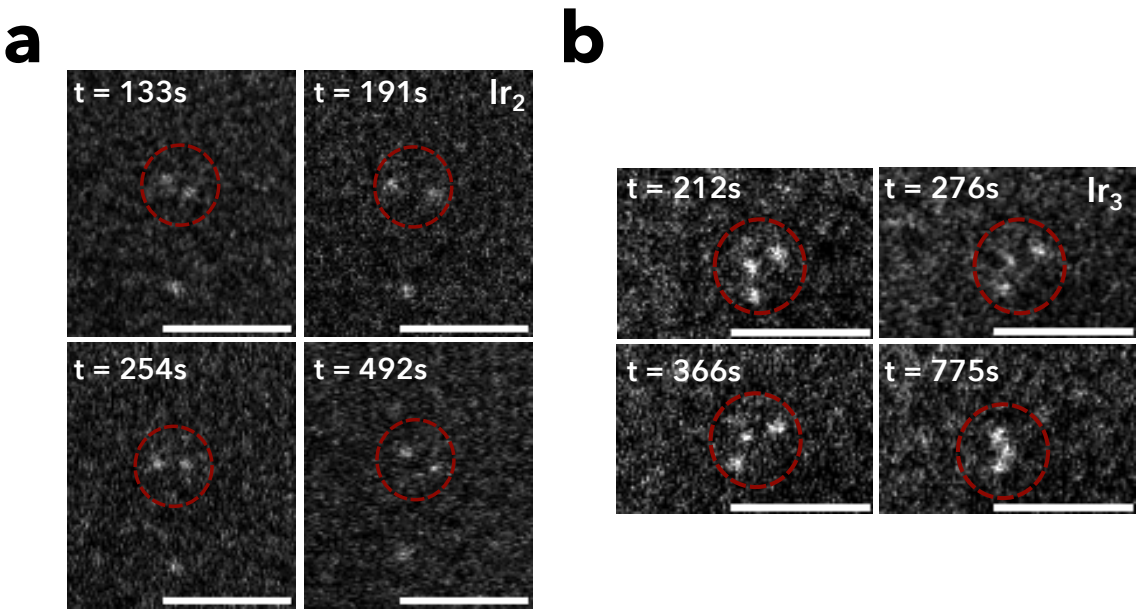


Figure 4.10: Time-resolved ADF-STEM images of a representative (a) Ir_2 and (b) Ir_3 captured at 300 °C. Scale bars are 2 nm. Ir_x are highlighted in red dash-line circles of the same sizes in each image set to demonstrate their proximity to one another.

There is a tendency of finding Ir_1 over the Ti rows beginning of 500 °C, i.e., on the bright fringes in the images, based on an analysis of over 400 counts of these Ir_1 at 500 °C. This result is consistent with previous reports, where Ir_1 adapts to the support's surface termination and preferentially binds on the cations' row of the support [5].

A closer examination of Ir_2 reveals that the two Ir begin to move at a relatively constant Ir-Ir distance between each other, and this distance is dependent on the underlying TiO_2 surface planes. Specifically, the interatomic distance for an Ir_2 is 3.5 ± 0.2 Å on the edge of the (004) planes (Figure 4.11a) and 2.7 ± 0.2 Å on the edge of the (101) planes. Observing the constant distance between the two Ir in Ir_2 implies the presence of a chemical bonding between the two Ir.

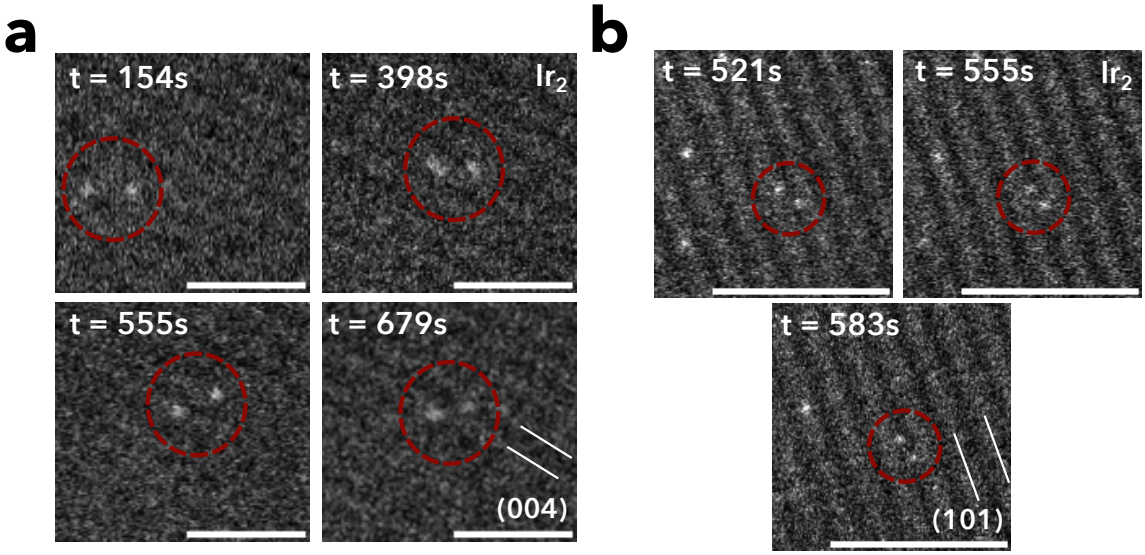


Figure 4.11: Time-resolved ADF-STEM images of a representative Ir_2 on TiO_2 with the edges of (a) (004) planes and (b) (101) planes shown. Images were captured at 500 °C. Scale bars are 2 nm. Ir_2 are highlighted in red dash-line circles of the same sizes in each image set to demonstrate their proximity to one another.

As shown in Figure 4.12, the two Ir clusters move as ensembles at 500 °C and coalesce into one cluster over time. As soon as the size of the clusters exceeds 6, these clusters become immobilised compared to the displacements of the Ir_1 and smaller clusters, as shown in Figure 4.7.

The observation from Figure 4.12 suggests that the sintering of the Ir follows a Smoluchowski-like ripening pathway [13], where single Ir_1 first come in contact with each other and form small clusters, followed by clusters migration as an ensemble and coalescence. The strong, cohesive interactions within the Ir_x, starting from Ir_3 at 80 °C, seem to prevent Ir_1 from detaching from the clusters then sintering with the other clusters, which is the Ostwald ripening [14]. This observation is also consistent with Wang and coworkers' DFT-based predictions of the highest onset temperature of Ostwald ripening for Ir amongst late transition metals on rutile TiO_2 [15].

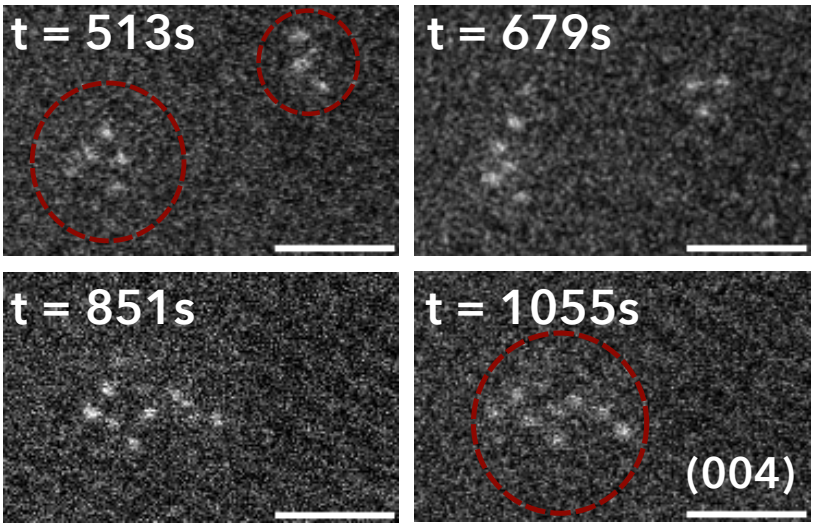


Figure 4.12: Time-resolved ADF-STEM images of two Ir_x coalescing into one large cluster at 500 °C. Scale bars are 2 nm.

Note that the Ir displacements are primarily driven by the electron beam. Therefore, the above qualitatively observed rate of Ir agglomeration at each temperature does not directly correlate to what would be observed during synthesis. However, the agglomeration behaviour, i.e., the Smoluchowski-like ripening demonstrating strong cohesion energy between the Ir in Ir_x, provides valuable insights into how Ir agglomerates during synthesis.

Key summaries of the above XAFS analysis and in-situ heating ADF-STEM analysis are as follows:

- According to the EXAFS analysis, at 300 °C, 1 to 2 Ir-Cl bonds of the $[IrCl_6]^{2-}$ are replaced by Ir-O bonds. At 500 °C, all Cl^- are removed, and a 6-fold Ir-O structure is formed.

- The Ir displacement velocity analysis from in-situ heating ADF-STEM experiments shows a decrease in Ir_1 mobility beginning 300 °C, and this lowered mobility is maintained at 500 °C.

- The above decrease in Ir_1 mobility at both 300 °C and 500 °C is time-dependent.

Specifically, the said decreases in mobility are observed after a certain amount of heating time.

- The agglomeration behaviour of Ir follows a Smoluchowski-like ripening pathway, where Ir_x migrate as ensembles on the TiO_2.

Combining these results, I conclude that the key to minimising Ir agglomeration on TiO_2 is the formation of the Ir-O bond at the first stage of thermal decomposition of $[IrCl_6]^{2-}$ at 300 °C. The partial removal of the Cl^- from $[IrCl_6]^{2-}$ at 300 °C promotes the formation of Ir-O bond that anchors the Ir precursor on the surface of TiO_2, resulting in a decrease in the Ir precursor mobility.

The decomposition of $[IrCl_6]^{2-}$ and the subsequent Ir-O bond formation require time to complete. Therefore, the synthesis heating rate controls the agglomeration of Ir by balancing the following two effects: firstly, the acceleration of the Ir-O bond formation with a higher reaction temperature and secondly, the higher mobility of Ir at the higher temperature before the Ir-O bonds form. For $[IrCl_6]^{2-}$ on TiO_2, the heating rate of 1 °C min^{-1} provides the optimal results compared to higher heating rates.

4.2 Limitations of the in-situ heating ADF-STEM analysis

Using the time-resolved in-situ heating ADF-STEM data correlated with the XAFS analysis of the Ir bonding environment, the synthesis mechanism of the atomically dispersed Ir on TiO_2 has been shown in the first half of this chapter. However, there are several challenges in data collection for both techniques and pitfalls in the in-situ heating ADF-STEM data analysis, which could potentially lead to biased data interpretations. Therefore, I dedicate this following section to a discussion of these

challenges and pitfalls, offering solutions to those I can address and suggestions for those that require further investigation.

4.2.1 Temperature-driven Ir transport dynamics

In this subsection, I discuss my attempt at quantitatively estimating temperature-driven transport dynamics of Ir_1 from the in-situ heating STEM experiments. So far, I have shown the qualitative and comparative investigation of the mobility and agglomeration of the Ir. Further quantitative determination of the Ir transport lengths at different temperatures is valuable for the design of a synthesis strategy to minimise the Ir agglomeration on TiO_2 surface. Such as, hypothetically, should the breaking of the Ir-Cl bond and formation of Ir-O take 1 hour to complete, how far apart of the Ir_1 should be kept from one another to ensure the probability of Ir_1 from colliding into each other is negligible?

For this purpose, the calculation of the mean square displacement (MSD) to describe the Brownian diffusion given by the Einstein–Smoluchowski relationship is the crucial metric, which can be written as:

$$\mathrm{MSD}(t + \Delta t) = \langle [r(t + \Delta t) - r(t)]^2 \rangle = D\Delta t, \tag{4.1}$$

where Δt is the lag time, $r(t)$ is the particle position at time t, D is the diffusion coefficient, and $\langle\rangle$ is the function that averages the ensemble over particles or trajectories [16].

With the MSD calculated, the transport length of Ir at a specific time interval at each critical reaction intermediate temperature may be derived. The estimation of representative MSD that is related to the temperature-driven transport of Ir with my dataset is, however, found to be challenging for the following reasons. Firstly, there is the difficulty of isolating temperature-driven Ir displacements from the knock-on

displacements. As discussed with Figure 4.7, the beam-induced Ir displacements are evident due to the use of the 300 kV electron beam.

I choose the 300 kV beam to increase the spatial resolution while minimising the radiolysis beam damage, which could accelerate the Ir-Cl bond breaking and interfere with the aim of establishing a correlation between Ir bonding environment and mobility [17]. However, the use of a 300 kV electron beam leads to significant knock-on damage to TiO_2 [18, 19], displacing Ti out of the lattice. Therefore, I use a 2 pA beam current with a pixel dwell time of 20 μs to minimise the beam dose, keeping TiO_2 intact for prolonged imaging at increasing temperatures.

As the use of a 300 kV beam is overall beneficial, I plan to offset the Ir mobility contributed to the electron beam by establishing a baseline of the beam-induced displacements at different temperatures, carried out by collecting an extra set of unheated data after each set of heating experiments. However, I found it to be a significant undertaking to collect sufficient images within a reasonable microscope time due to the difficulty in high-throughput image collection using this material system.

Each analysable image takes approximately 20 seconds to collect, as the low beam dose was used at the expense of the images' SNR. During the data collection, I found that 2-fold astigmatism of the beam spontaneously developed within two to three frames, resulting in the loss of atomic resolution images acquired. The cause of the 2-fold astigmatism is likely a local charging of the TiO_2 under the constant electron beam irradiation. I needed to manually correct astigmatism with Ir particles that were out of a field of view and maneuvered back to the same area to continue the image collection. This step is relatively technical, typically taking 1 minute to complete, though it can also take much longer if the astigmatism is strong. The lengthy image collection and the additional effort needed to rectify the 2-fold astigmatism impede a high-throughput data collection.

Moreover, as a result of the need to correct 2-fold astigmatism every few frames, the lag time between frames can hardly be maintained constant. This lag time variation further complicates the analysis of the data collected, as the calculation of the MSD is based on the displacements with a constant lag time. To address this limitation, I allow a 10 % uncertainty in the lag time for the data analysis of Figure 4.7 and report displacement velocities instead of displacement lengths. However, for the calculation of temperature-driven MSD, where the heating temperature's contribution to the total Ir displacements is suspected to be minor, as observed in Figure 4.7, this additional uncertainty of lag time may lead to a significant bias in the interpretation of the temperature-driven Ir_1 mobility.

Since the image collection requires approximately 20 seconds, the time resolution of the experiment is on the order of tens of seconds. For an Ir–O bonding energy of approximately 3 eV [20], the diffusion barrier is estimated to be around 1 eV [12]. At 327 °C, a diffusion coefficient of 10 to 100 $nm^2\ s^{-1}$ is expected with such a diffusion barrier, according to calculations by Yildirim and coworkers for the hopping of a Cu adatom on a Cu surface [21]. This suggests that Ir is likely to diffuse a few nanometers over a timeframe of several seconds. Therefore, the 20-second time resolution that can be achieved in this experiment may be insufficient to fully capture temperature-induced diffusivity.

In summary, I prioritised qualitative analysis with statistical significance, dedicating the microscope time to collecting as many ADF-STEM images as possible at each temperature to obtain a better statistical representation of the Ir mobility (Figure 4.6). This experimental plan enables at least a comparative study of the evolution of Ir mobility on TiO_2 at different temperatures, demonstrating the onset of Ir-O formation at 300 °C is critical to atomic dispersion of Ir.

4.2.2 Temperature relevance to synthesis conditions

In this study, I am correlating the observed mobility of Ir at different temperatures studied at a high vacuum in the STEM (approximately 1.0×10^{-5} pascal during these STEM measurements) to the observation from the synthesis performed in N_2. The validity of this correlation can be challenged. In particular, the reaction temperature and rate of the Ir-Cl bond breaking and the formation of Ir-O bonding on the TiO_2 surface can vary between these two environments.

For the Ir-Cl bond decomposition, the reaction kinetics may be accelerated by a more efficient extraction of the exhaust HCl or Cl_2 gas, compared to the reaction in N_2. This difference in reaction atmosphere may lead to an underestimation of the reaction time needed.

For the formation of Ir-O bonding between Ir and surface O on TiO_2, the difference in the population of surface hydroxyl (-OH) group in UHV and N_2 may have an influence towards the stabilisation of Ir_1 on TiO_2, where heating in UHV is expected to more efficiently remove the majority of these hydroxyl groups and promote Ir-O bonding. This hypothesis is based on Parkinson and coworkers' finding, where they observed Ir_1 to be stabilised on TiO_2 anatase surface in UHV, characterised with scanning tunnelling microscope, but destabilised when moisture was introduced to the TiO_2 surface [22]. The extent of influence of the reaction atmosphere on the Ir-Cl bond breaking and Ir-O bonding formation remains a critical aspect for future investigation, which requires complementary characterisation techniques like environmental STEM.

4.2.3 Accuracy of image registration

In the in-situ ADF-STEM data analysis, the Ir mobility was analysed with respect to the underlying TiO_2 support. Consequently, accurate registration of the TiO_2 support, with errors well below the length scale of the Ir displacements, is crucial

for the analysis of Ir mobility. Acknowledging this, I spent extra effort on finding a suitable method for image registration and attempted to validate the accuracy of the image registration procedure.

Since there are no immobile features in the images to serve as reference points for the validation of the image registration process, I instead plotted the summation of all the displacements for each Ir size as a function of their displacement directions, as shown in Figure 4.13. No strong directional dependency of the Ir displacements can be observed for any Ir size. This result provides evidence of an overall robust image registration that corrects the transnational drifts across the images. Nevertheless, a closer examination of the data reveals a slight tendency of displacements towards two opposing directions ($\sim$+0.75 radians and $\sim$-2.25 radians). This observation is likely due to the deformation of the image from the vibration of the tilting angle with the single-tilt heating holder. With this degree of freedom of the holder, the image can be elongated or compressed along the axis perpendicular to the tilt axis.

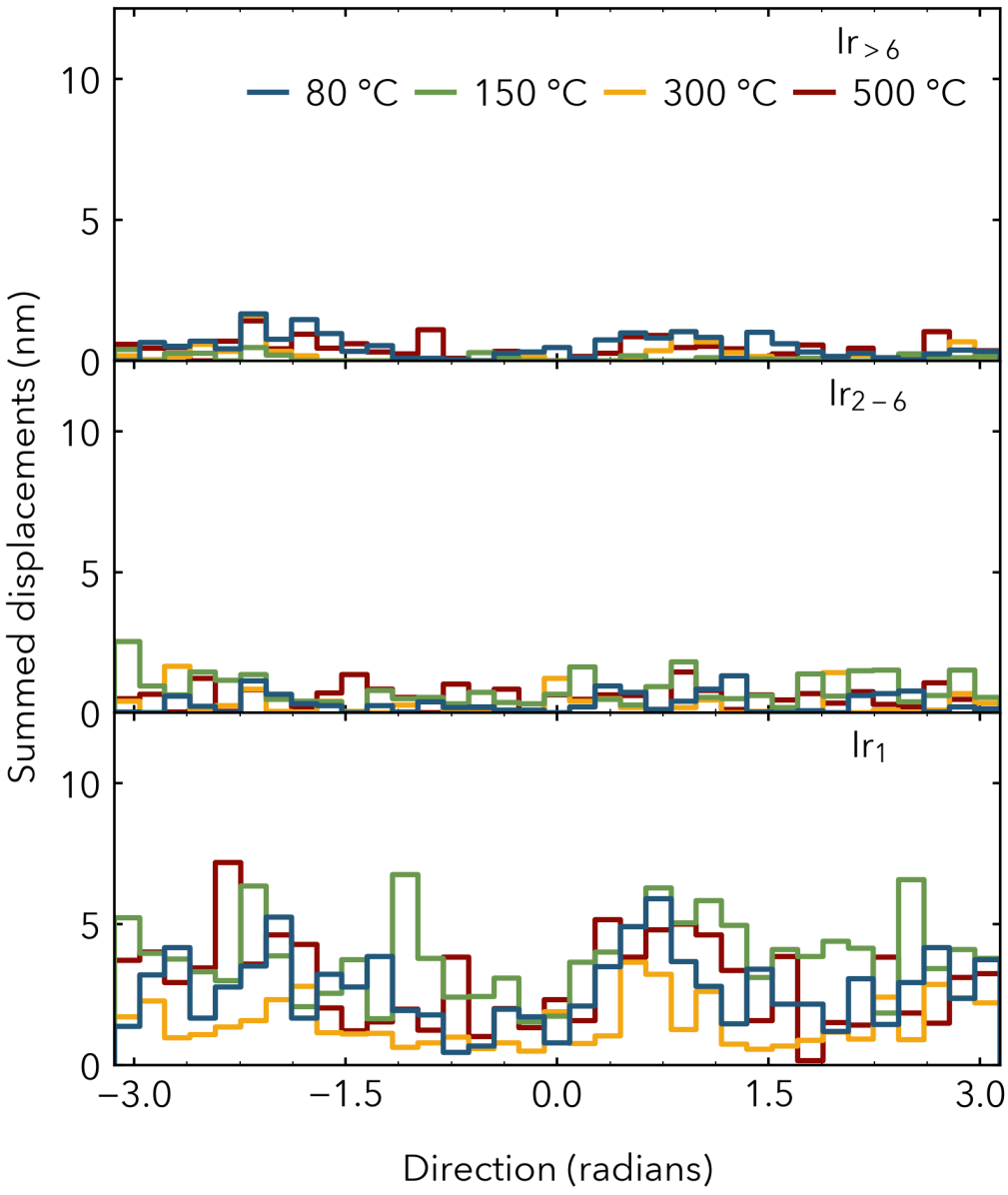


Figure 4.13: Summed Ir displacement lengths as a function of 2D radial directions of the displacement for Ir_1, $Ir_{2\text{-}6}$ and $Ir_{>6}$ across 80 °C, 150 °C, 300 °C and 500 °C.

Upon this observation of potential registration error, I took a closer examination of the datasets and identified possible false Ir displacements as a result of image deformation between frames. Figure 4.14 illustrates one such example. Figure 4.14a and b show the two consecutive image frames captured at 500 °C, each with one presumed to be the same Ir_1 highlighted in the bottom right corner of the image.

Figure 4.14c shows the projected positions of these two Ir_1 on the registered, averaged TiO_2 support. Ideally, if these two Ir_1 are indeed the same Ir_1, their projected position in Figure 4.14c should overlap. However, in this case, these two Ir_1 are separated by approximately 3 Å, resulting in one false count of Ir_1 displacement at 3 Å when these two Ir_1 are linked.

Although this image deformation introduces undesired errors in the mobility analysis, there is no firm evidence of its dependency on temperatures. Specifically, the radial distribution profiles for Ir_1 for all four temperatures resemble each other. Consequently, these errors would be cancelled out when comparing the evolution of displacement velocity at different temperatures, as this supposedly random error would be uniformly distributed to each temperature dataset. Further application of a non-rigid registration method is desired, but the low SNR in the ADF-STEM images without immobile features again complicates this effort.

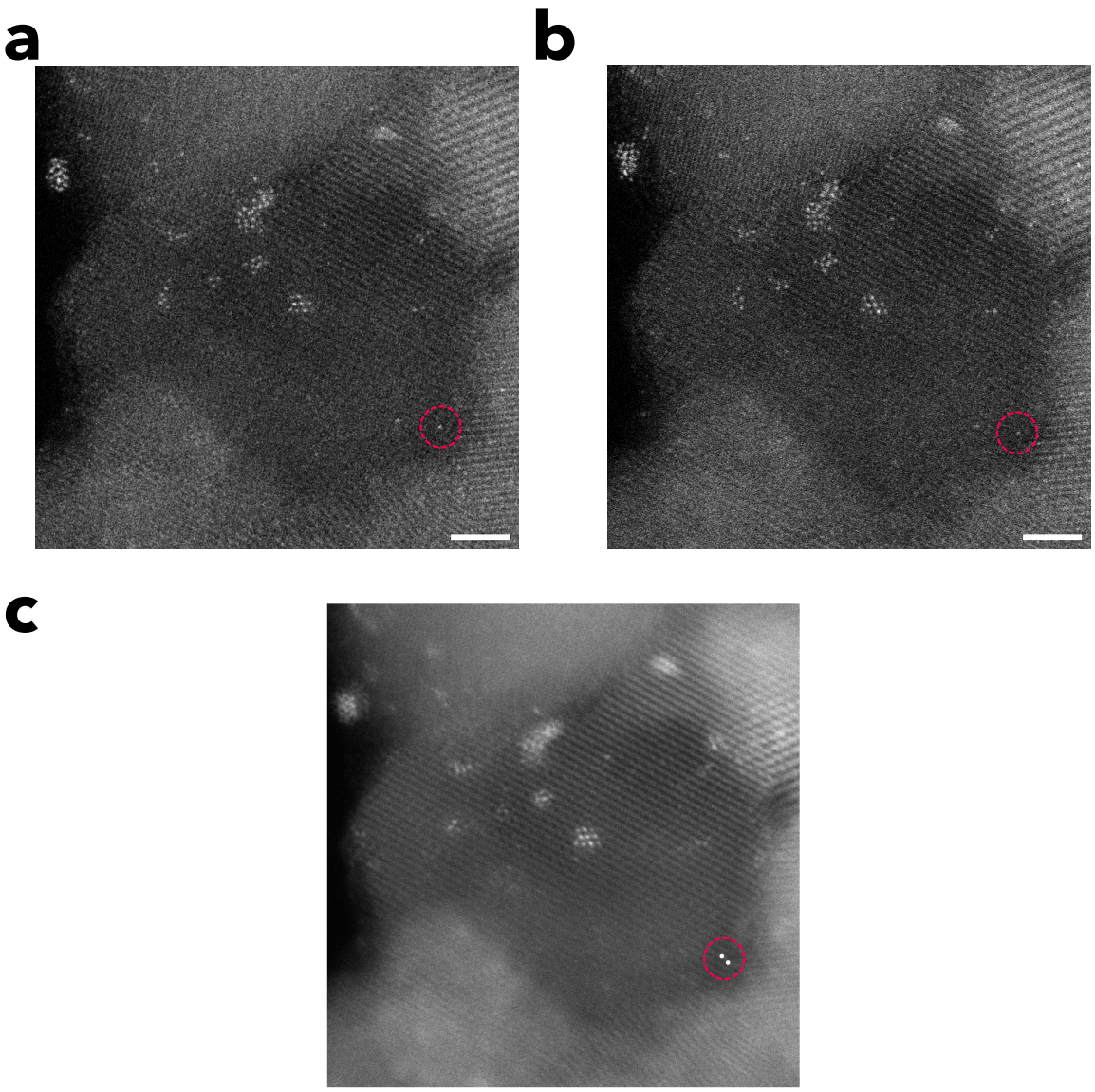


Figure 4.14: (a) and (b) show two consecutive image frames from a registered image stack captured at 500 °C. Highlighted in the red circles are Ir_1, which is presumed to be the same. (c) shows the highlighted Ir_1 in (a) and (b) projected onto the registered and averaged image of the stack.

Conclusions

In this chapter, using in-situ heating ADF-STEM experiments and XAFS analysis, I proposed that the key to minimising Ir agglomeration on TiO_2 is the formation of the Ir-O bond at the first stage of thermal decomposition of $[IrCl_6]^{2-}$ at 300 °C. The heating rate of the synthesis controls the agglomeration of Ir as it provides a balance between the acceleration of the Ir-O bond formation with a higher reaction temperature and the higher mobility of Ir at a higher temperature before the Ir-O bonds are formed.

These results suggest by adjusting the synthesis heating rate, the formation of the coordinatively unsaturated Ir precursor and its binding to the TiO_2 surface can be modulated, thereby controlling the rate of Ir agglomeration.

The limitations in the data interpretation from the in-situ heating ADF-STEM experiments and the data analysis were discussed. Although a quantitative estimation of temperature-driven Ir_1 transport dynamics is in principle derivable from the in-situ heating ADF-STEM experiments, the challenges in a high-throughput collection of the ADF-STEM images for this Ir-TiO_2 sample render this estimation difficult. Therefore, I focus on the qualitative analysis comparing the evolution of the Ir mobility between different temperatures with statistical significance.

The in-situ heating ADF-STEM experiments were performed in a vacuum, while the synthesis of Ir-TiO_2 samples was carried out in N_2. The effect of the different atmospheres on the Ir-Cl bond breaking and Ir-O bonding formation is a critical aspect for future investigation.

Evidence of Ir displacement error was observed due to the image deformation resulting from STEM holder tilting, which was not able to be corrected using the rigid registration method implemented in my Python-based analysis pipeline. These errors can be cancelled out when comparing the evolution of displacement velocity at different temperatures. The use of a non-rigid registration method to improve image

registration is desired, but again, the low SNR in the images significantly complicates the process.

Pipeline for ADF-STEM image processing

This section details the ADF-STEM image processing workflow and its validation. This pipeline not only accelerates the processing of large datasets but also ensures consistency across the time-resolved image sequences acquired at different temperatures, allowing robust statistical analysis, as shown earlier in this chapter.

An overview of the image processing and the effects of each step in the image processing are shown in Figure 4.15 using the same image shown in Figure 4.4 as an example. The image processing consists of four key steps: padding/windowing, bandpass filtering, lattice suppression, and intensity thresholding.

The raw image is first padded and masked with a Tukey window function to smooth the transition at the image edges and minimise the boundary effect that causes the cross-like artefacts after the fast Fourier transform (FFT) of the image. Subsequently, the image is filtered in the Fourier domain by masking its FFT spectrum with a bandpass filter to remove the low-frequency signals, which corresponds to the slowly varying signals from the TiO_2 support, and the high-frequency signals, which is the image noise. Then, the signal variation from the TiO_2 lattice planes is suppressed by masking the lattice reflections that remain in the bandpass-filtered FFT spectrum. Finally, an inverse FFT is performed on the processed FFT spectrum to return the real-space image, followed by thresholding to remove all signals below a set intensity value, leaving only the high-intensity signals.

Figure 4.15a shows a representative raw image padded and windowed, and Figure 4.15b shows its FFT spectrum. No cross-like artefact in Figure 4.15b is observed. This step is crucial for the detection of lattice reflection in the next step.

Figure 4.15c shows the inverse FFT image after bandpass filtering, and Figure 4.15d shows the corresponding intensity line profile along the white dashed line in Figure 4.15c. This line corresponds to the same white horizontal line in the raw image shown in Figure 4.4. Compared to the noisy intensity line profile shown for the raw

image (Figure 4.4c), the intensity line profile after bandpass filtering demonstrates the noise and the background intensities are largely reduced, making Ir signals more easily identifiable from the background.

However, the lattice fringes of the TiO_2 remain clearly observable in Figure 4.15c, causing variations in the Ir signal intensities that are located at different positions with respect to the lattice fringes. In other words, Ir located on the Ti row, where the lattice fringes are present, is showing slightly higher intensity than the Ir that is sitting between the Ti row, as is observed in the different intensities of the two peaks at X pixel number 400 in Figure 4.15d. Therefore, a mask around the lattice reflections is applied to offset this difference. The effect of this lattice suppressing step is demonstrated in Figure 4.15f, with the two Ir signal intensities beginning to align with each other.

After the above steps, the final intensity thresholding in real space is applied, eliminating all the background signals and allowing only the signals of the Ir to pass. This last stage of image processing ensures the following Ir detection algorithm functions appropriately.

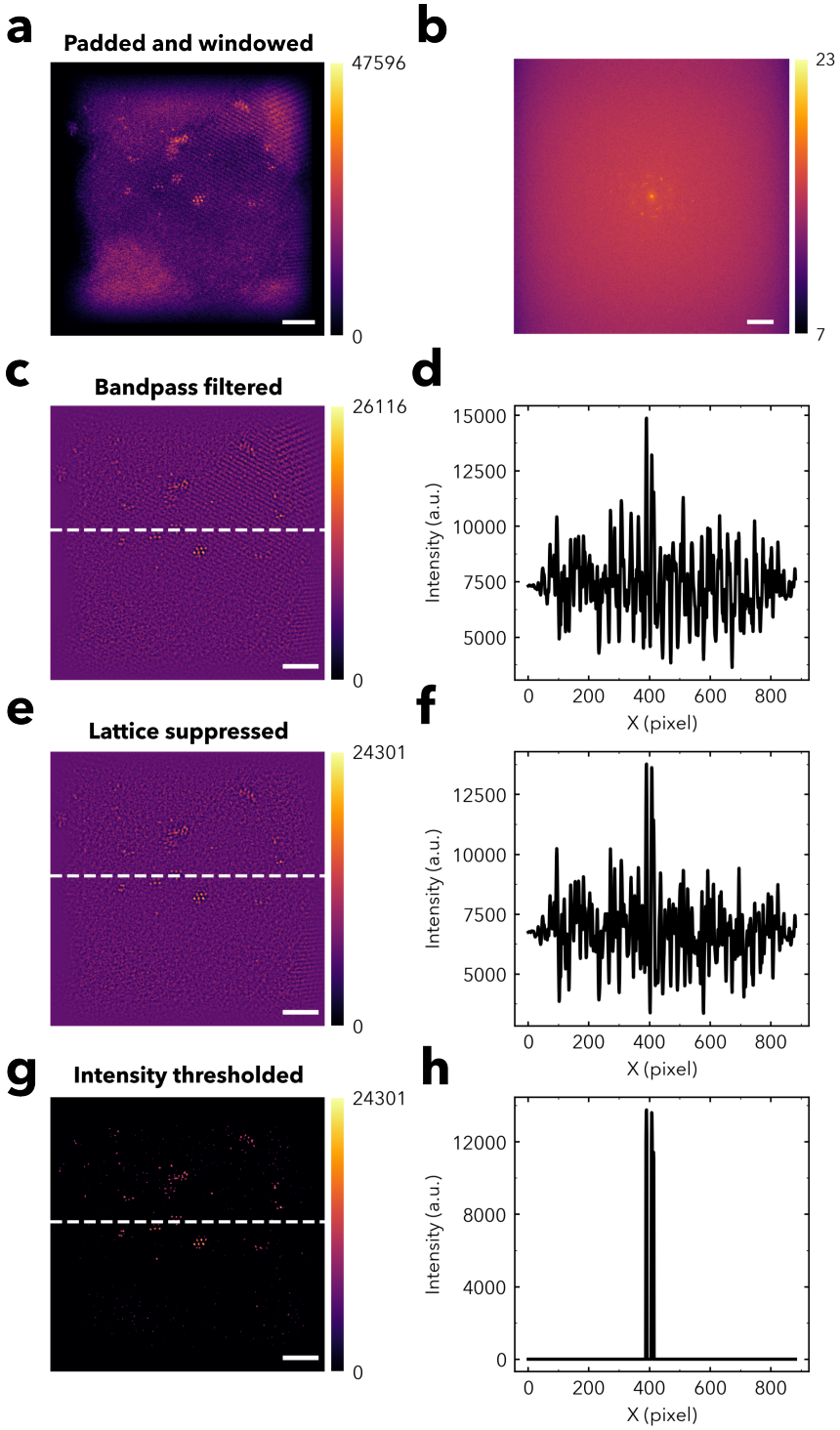


Figure 4.15: Overview of the image processing using the raw image shown in Figure 4.4 as an example. (a) Padded and windowed raw image. (b) FFT spectrum of the padded and windowed image. (c) Inverse FFT image after applying bandpass filtering in Fourier domain. (d) Corresponding intensity line profile along the horizontal white line in (c). (e) Inverse FFT image after lattice suppression in Fourier domain. (f) Corresponding intensity line profile along the horizontal white line in (e). (g) Intensity-thresholded image. (h) Corresponding intensity line profile along the horizontal white line in (g).

The selection of the bandpass filter is manifested in Figure 4.16. Figure 4.16a visualises the bandpass filter that is applied to the FFT spectrum for the detection of the $Ir_{1\text{-}10}$. These filters are constructed by convolving a low-pass Gaussian function (which filters out the high-frequency parts in the FFT spectrum) with a high-pass Gaussian function (where the low-frequency part in the FFT spectrum is cut), creating a ring-shaped filter. The brightest areas of the filter (intensity close to 1) indicate where the intensities in the FFT spectrum can pass through when the filter is applied.

The selection of the cutoff frequency of the filter is guided by the physical meaning of the feature lengths represented in the frequency domain. Figure 4.16b shows the line profile of the bandpass filter for the $Ir_{1\text{-}10}$. Since the averaged size of the Ir_1 observed in the ADF-STEM image is around 0.2 nm, a bandpass filter is centred at this value and steeply drops to 0 to remove high-frequency noise that are smaller than $Ir_{1\text{-}10}$ length. This filter also begins to remove features larger than 1 nm to ensure the removal of the background signal from the TiO_2. In contrast, for $Ir_{>10}$, the filter centres around 1 nm to blur the fine details of the clusters, creating blob-like features that allow me to treat them as ensembles.

The need to separate these two Ir size groups from each other is because, for Ir clusters larger than 10, they begin to have a high chance of stacking on top of each other and not being able to be imaged atom-by-atom, as can be observed in Figure 4.3. This stacking of Ir affects the benchmarking of the Ir detection pipeline in the following section. A better approach to process them is to treat them as ensembles, separating them from the individually resolved Ir for further analysis.

Figure 4.16c-f show examples of the FFT spectra when applied with the $Ir_{1\text{-}10}$ bandpass filter and with the $Ir_{>10}$ bandpass filter and their inverse FFT images. These results demonstrate that after filtering, the background is largely removed, and the contrast of $Ir_{1\text{-}10}$ is enhanced. For the $Ir_{>10}$, after the filtering, the clusters become blobs, bypassing the tricky part where the Ir are not individually separated

in the image.

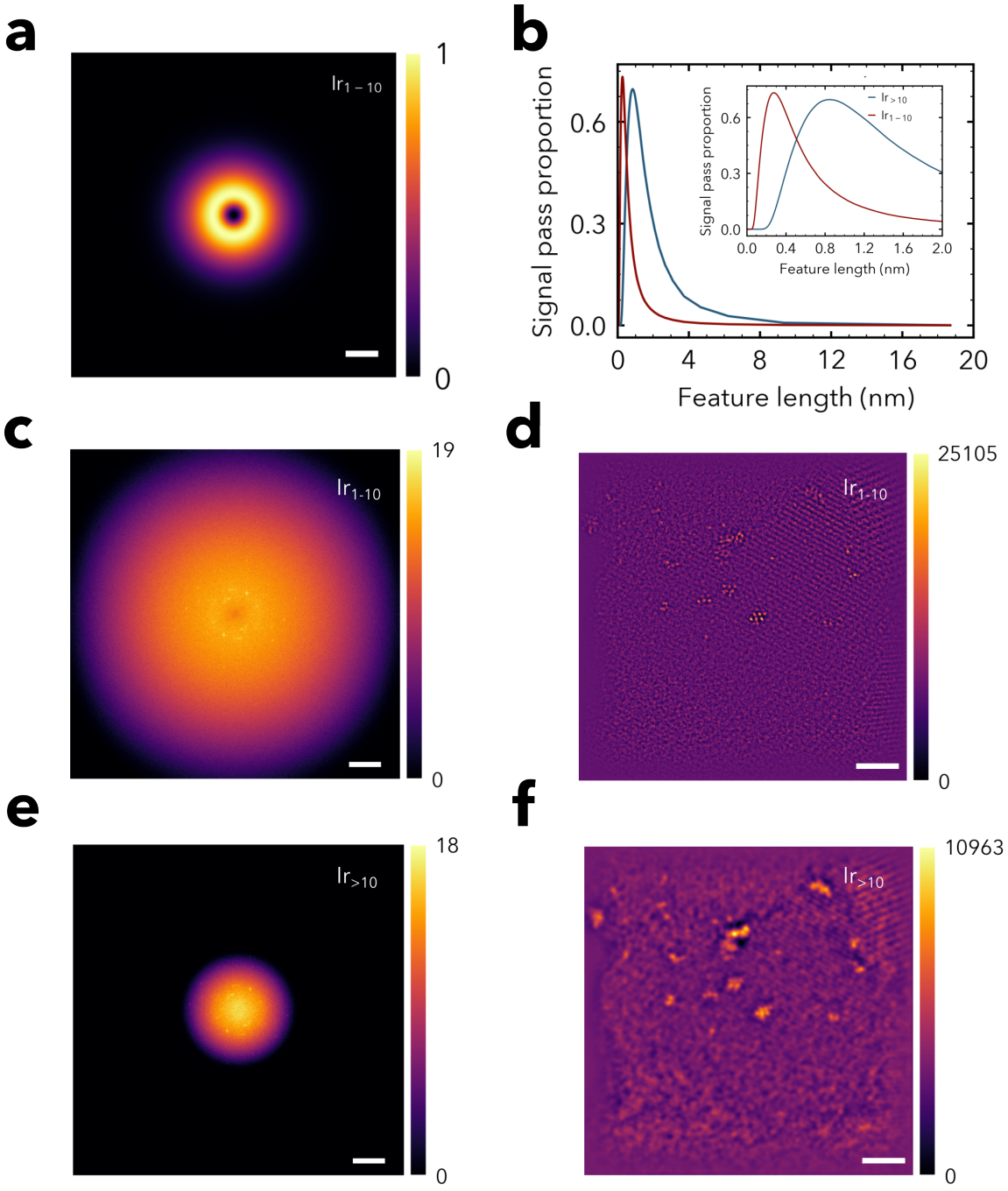


Figure 4.16: Selection of bandpass filter. (a) Bandpass filter for the detection of $Ir_{1\text{-}10}$. (b) Line profile of the proportion of the signal that can pass through the mask as a function of feature length for the $Ir_{1\text{-}10}$ and $Ir_{>10}$ bandpass filters. (c) FFT spectrum of the raw image in Figure 4.4 after the masking with the $Ir_{1\text{-}10}$ bandpass filter and (d) the corresponding inverse FFT image. (e) FFT spectrum of the raw image in Figure 4.4 after the masking with the $Ir_{>10}$ bandpass filter and (f) the corresponding inverse FFT image.

Following bandpass filtering, the lattice suppression is performed. The positions of the lattice reflections are detected by first masking off the centre signal in the FFT spectrum, then thresholding the image, followed by locating the pixels with the highest intensities. The selection of the threshold is the key in this operation, as it determines the number of peaks that can be detected, and the following Ir detection function is based on the search of local maxima of intensities.

To determine the threshold value and to ensure consistency of the TiO_2 lattice reflection points detection, I introduce the concept of the F1 score in the pipeline, a standard metric used in computer vision [23], to find the balance between detection precision and recall, which is defined as follows:

$$\text{Precision} = \frac{\text{TP}}{\text{TP} + \text{FP}} \tag{4.2}$$

$$\text{Recall} = \frac{\text{TP}}{\text{TP} + \text{FN}} \tag{4.3}$$

$$\text{F1} = 2 \cdot \frac{\text{Precision} \cdot \text{Recall}}{\text{Precision} + \text{Recall}}, \tag{4.4}$$

where TP is a true positive, FP is a false positive, and FN is a false negative between the detected features from the pipeline and the true position of the features. The Hungarian method is used to assign the best-matching pairs between the detected and the true positions of the features within a matching distance threshold, enabling the calculation of TP, FP and FN [24].

Since multiple lattice planes are typically present in the image field of view, as seen in Figure 3.8), there is no clear definition of the true location of lattice reflection peaks. Therefore, I rely on manually tagging the reflection peaks as the true positions. For each image stack, I tag a random selection of a quarter of the FFT spectra and calculate the F1 scores. The FFT threshold that yields the highest F1 score is selected and applied to the entire image stack to ensure consistency.

Figure 4.17e shows the precision, recall and F1 scores as functions of the threshold. The precision increases with a higher threshold, as fewer false features are detected, whereas the recall decreases as the number of correctly identified features drops. The combination of this yields a maximum F1 score of 0.8 ± 0.1 at a FFT threshold of 17.25.

With the threshold selected and applied in the FFT spectrum, Gaussian masks to the detected peaks in the FFT spectrum are applied to the post-bandpassing FFT spectrum in the previous step, as shown in Figure 4.17d.

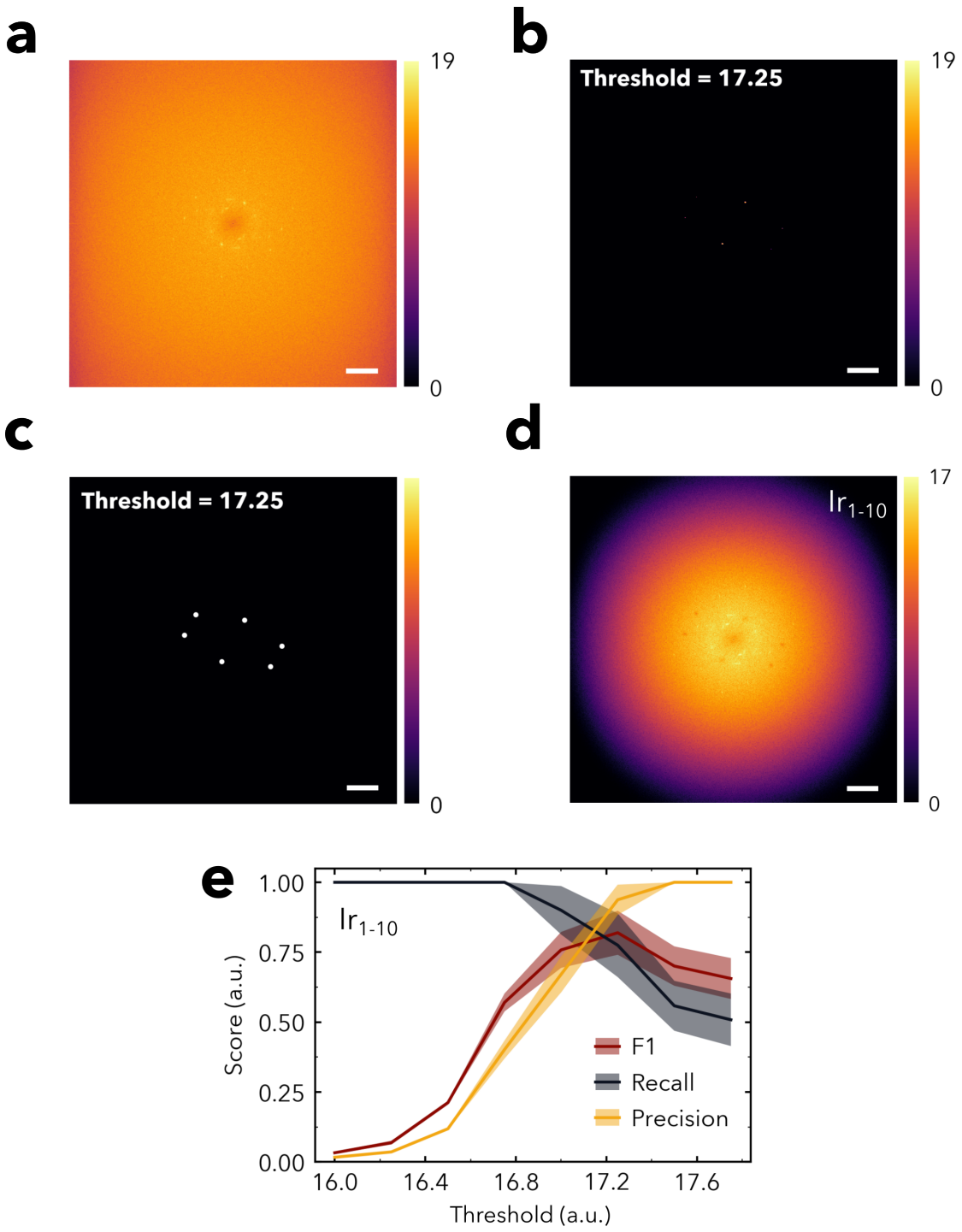


Figure 4.17: Lattice suppression process. (a) FFT spectrum of the raw image in Figure 4.4 with its centre signal masked and (b) the corresponding thresholded image. (c) Detected lattice reflection peaks from (b). (d) FFT spectrum of the Figure 4.16c with lattice reflections masked. (e) F1, recall and precision scores of the detection of the lattice reflection peaks in the FFT spectrum as functions of the threshold.

After lattice suppression, the final image processing step is intensity thresholding, which is performed using the same process as the lattice suppression step described above. There is no prior knowledge of the true position or the intensity of $Ir_{1\text{-}10}$. Therefore, manual tagging of the $Ir_{1\text{-}10}$ in the image stack is performed. The threshold is determined by the calculation of the F1 score with a quarter of the image stack. The choice of a quarter of the image stack (5 out of 19 for this image stack in this example) is to reduce the human input time required to tag the positions of all $Ir_{1\text{-}10}$.

As shown in Figure 4.18a, the maximum F1 score for this particular image stack is 0.80 ± 0.02 at a threshold of 99.9 for the detection of the $Ir_{1\text{-}10}$. For the $Ir_{>10}$, the threshold is otherwise quantified by ensuring the size of the detected blob is within 10 % of the manually measured size in the raw image.

This concludes the image processing procedure. The detection of the Ir is then performed by a simple detection of local maxima in the processed image, and the results have been shown previously in Figure 4.5.

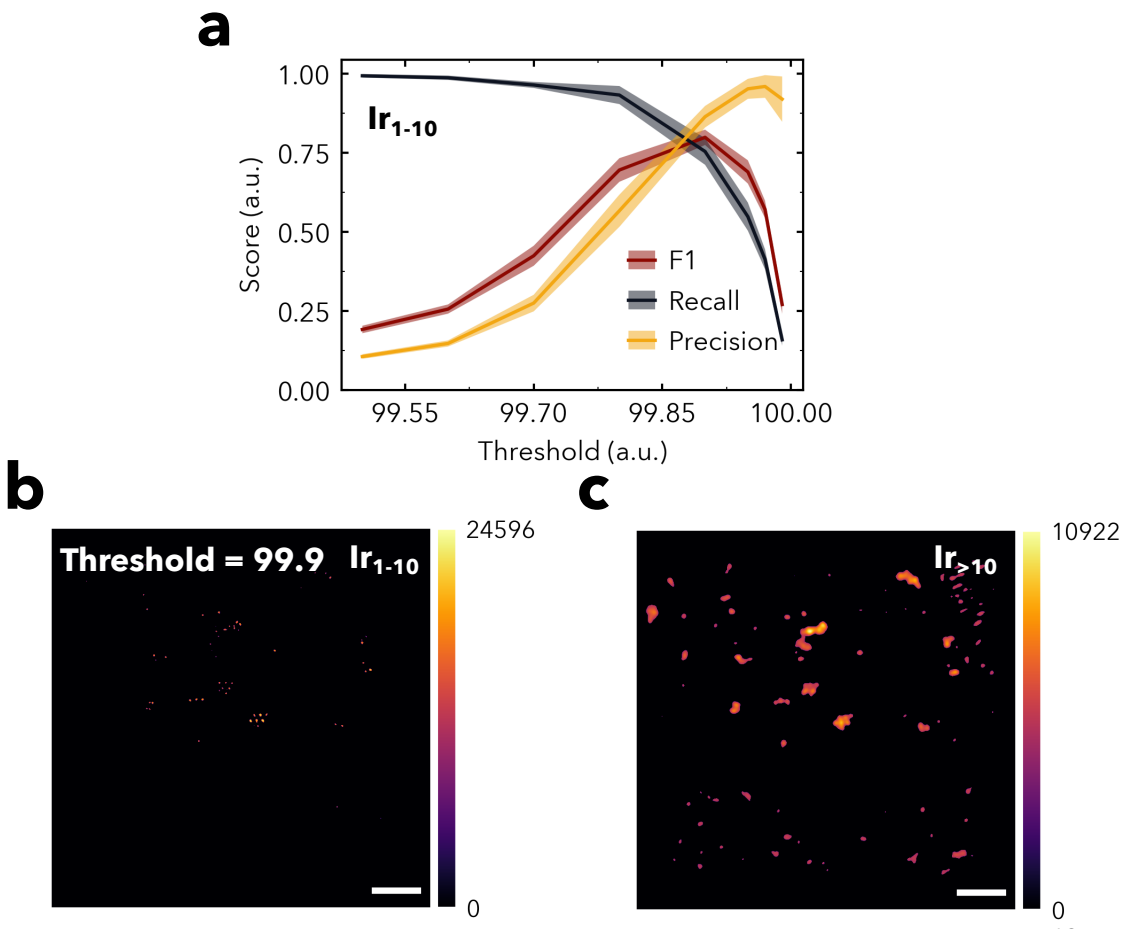


Figure 4.18: Intensity thresholding process. (a) F1, recall and precision scores of the detection of $Ir_{1\text{-}10}$. (b) Thresholded image of $Ir_{1\text{-}10}$ and (c) $Ir_{>10}$ from the raw image in Figure 4.4, both after the padding/windowing and bandpass filtering and lattice suppressing process.

Experimental

In-situ heating annular dark field scanning transmission electron microscopy (ADF-STEM)

In-situ heating ADF-STEM experiments were performed using a JEOL ARM300CF STEM at an accelerating voltage of 300 kV. A CL aperture of 20 μm, convergence semi-angle of 16.4 mrad, a beam current of 1.9 pA, and a detector angle between 41 and 130 mrad were used. Samples were deposited on the DENSsolution Wildfire Nano-Chip, and the Wildfire STEM holder controlled the temperature of the Nano-Chip. Samples were baked using in-situ heating on the Nano-Chip in the microscope at 150 °C overnight before the experiments, except for one sample, which was baked at 80 °C overnight in the microscope for the investigation of Ir mobility at 80 °C. The collection of in-situ heating ADF-STEM data was performed in collaboration with Dr David Hopkinson (Diamond Light Source).

X-ray absorption spectroscopy (XAS)

XAS measurements were performed at the B18 beamline of the Diamond Light Source. 80 °C, 150 °C, 300 °C and 500 °Csamples were prepared using a heating rate of 1 °C min^{-1} and held at the target temperatures for 4 hours in N_2. 8 mm sample pellets were prepared by mixing an appropriate amount of sample with cellulose (Avicel PH-101, Sigma-Aldrich), with the composition calculated using the XAFSmass software [25]. The spectra for the Ir reference samples were collected in transmission mode, while the Ir-TiO_2 samples were measured in fluorescence mode. Si(111) crystal monochromator coupled with Cr-coated collimating mirrors were used. For the fluorescence measurements, the 36-element Ge fluorescence detector was used. Data were analysed using the Larch software [26]. For the reference samples, including Ir metal (99.9% powder, Sigma-Aldrich), IrO_2 (99.9%, Sigma-Aldrich) and $H_2IrCl_6{\cdot}xH_2O$ (99.9%, Sigma-

Aldrich), the k^3-weighted Fourier transform was performed between $k = 3$ and 14 Å^{-1} using a Hanning window. The EXAFS fit was performed between $R = 1.0$ and 4.2 Å. For the Ir-TiO_2 samples, the k^3-weighted Fourier transform was performed from $k =$ 3 to 8.5 Å^{-1} using a Hanning window. The EXAFS fit was performed between $R =$ 1.0 and 3.5 Å. The amplitude reduction factor (S_0^2) for fitting the for Ir-TiO_2 samples was obtained from fitting the rutile IrO_2 reference. The collection of the XAS data was performed in collaboration with Dr Donato Decarolis (Diamond Light Source).

References

[1] Haofei Wu, Zheng Li, Qiwen Zhang, Luozhen Jiang, Chen Hou, Shufen Chu, Jing Feng, Wenwu Xu, Lina Li, Fang Song, Mingwei Chen, and Pan Liu. Chloride ligand stablizes single-atom on nanoporous metal oxides in a pyrolysis process. *Chemical Engineering Journal*, 497, 10 2024.

[2] Nazir Khan, Danil Prishchenko, Yurii Skourski, Vladimir G. Mazurenko, and Alexander A. Tsirlin. Cubic symmetry and magnetic frustration on the fcc spin lattice in K 2 IrCl 6 . *Physical Review B*, 99(14), 4 2019.

[3] A A Bolzan, C Fong, B J Kennedy, and C J Howard. Structural Studies of Rutile-Type Metal Dioxides. *Acta Crystallographica Section B*, 53(3):373–380, 6 1997.

[4] Xueli Zheng, Jing Tang, Alessandro Gallo, Jose A Garrido Torres, Xiaoyun Yu, Constantine J Athanitis, Emily May Been, Peter Ercius, Haiyan Mao, Sirine C Fakra, Chengyu Song, Ryan C Davis, Jeffrey A Reimer, John Vinson, Michal Bajdich, and Yi Cui. Origin of enhanced water oxidation activity in an iridium single atom anchored on NiFe oxyhydroxide catalyst. *Proceedings of the National Academy of Sciences*, 118(36):e2101817118, 9 2021.

[5] Pengxin Liu, Xing Huang, Deni Mance, and Christophe Copéret. Atomically dispersed iridium on MgO(111) nanosheets catalyses benzene–ethylene coupling towards styrene. *Nature Catalysis*, 4(11):968–975, 11 2021.

[6] Dmitry Lebedev, Roman Ezhov, Javier Heras-Domingo, Aleix Comas-Vives, Nicolas Kaeffer, Marc Willinger, Xavier Solans-Monfort, Xing Huang, Yulia Pushkar, and Christophe Copéret. Atomically Dispersed Iridium on Indium Tin Oxide Efficiently Catalyzes Water Oxidation. *ACS Central Science*, 6(7):1189–1198, 7 2020.

[7] Jordan Finzel, Kenzie M. Sanroman Gutierrez, Adam S. Hoffman, Joaquin Resasco, Phillip Christopher, and Simon R. Bare. Limits of Detection for EXAFS Characterization of Heterogeneous Single-Atom Catalysts. *ACS Catalysis*, 13(9):6462–6473, 5 2023.

[8] Daniel B Allan, Thomas Caswell, Nathan C Keim, and Casper M der Wel. soft-matter/trackpy: Trackpy v0.4.2, 10 2019.

[9] Shuhui Liu, Hua Xu, Dongdong Liu, Hao Yu, Fan Zhang, Peng Zhang, Ruolin Zhang, and Wei Liu. Identify the Activity Origin of Pt Single-Atom CatalystviaAtom-by-Atom Counting. *Journal of the American Chemical Society*, 143(37):15243–15249, 9 2021.

[10] Sharon Mitchell, Ferran Parés, Dario Faust Akl, Sean M. Collins, Demie M. Kepaptsoglou, Quentin M. Ramasse, Dario Garcia-Gasulla, Javier Pérez-Ramírez, and Núria López. Automated Image Analysis for Single-Atom Detection in Catalytic Materials by Transmission Electron Microscopy. *Journal of the American Chemical Society*, 5 2021.

[11] Yanyan Zhao, Xingxu Yan, Ke R. Yang, Sufeng Cao, Qi Dong, James E. Thorne, Kelly L. Materna, Shasha Zhu, Xiaoqing Pan, Maria Flytzani-Stephanopoulos,

Gary W. Brudvig, Victor S. Batista, and Dunwei Wang. End-On Bound Iridium Dinuclear Heterogeneous Catalysts on WO3 for Solar Water Oxidation. *ACS Central Science*, 4(9):1166–1172, 9 2018.

[12] Afnan Alghannam, Christopher L. Muhich, and Charles B. Musgrave. Adatom surface diffusion of catalytic metals on the anatase TiO2(101) surface. *Physical Chemistry Chemical Physics*, 19(6):4541–4552, 2017.

[13] Zhe Li, Hsin Yi Tiffany Chen, Koen Schouteden, Thomas Picot, Ting Wei Liao, Aleksandr Seliverstov, Chris van Haesendonck, Gianfranco Pacchioni, Ewald Janssens, and Peter Lievens. Unraveling the atomic structure, ripening behavior, and electronic structure of supported Au20 clusters. *Science Advances*, 6(1), 1 2020.

[14] Thomas W. Hansen, Andrew T. Delariva, Sivakumar R. Challa, and Abhaya K. Datye. Sintering of catalytic nanoparticles: Particle migration or ostwald ripening? *Accounts of Chemical Research*, 46(8):1720–1730, 8 2013.

[15] Qixin Wan, Sulei Hu, Jiangnan Dai, Changqing Chen, and Wei Xue Li. First-Principles Kinetic Study for Ostwald Ripening of Late Transition Metals on TiO 2 (110). *Journal of Physical Chemistry C*, 123(2):1160–1169, 1 2019.

[16] Nick Clark, Daniel J. Kelly, Mingwei Zhou, Yi Chao Zou, Chang Woo Myung, David G. Hopkinson, Christoph Schran, Angelos Michaelides, Roman Gorbachev, and Sarah J. Haigh. Tracking single adatoms in liquid in a transmission electron microscope. *Nature*, 609(7929):942–947, 9 2022.

[17] R. F. Egerton, P. Li, and M. Malac. Radiation damage in the TEM and SEM. In *Micron*, volume 35, pages 399–409, 8 2004.

[18] R. F. Egerton. Radiation damage to organic and inorganic specimens in the TEM. *Micron*, 119(November 2018):72–87, 2019.

[19] Alejandra Garcia, Andres M. Raya, Marcelo M. Mariscal, Rodrigo Esparza, Miriam Herrera, Sergio I. Molina, Giovanni Scavello, Pedro L. Galindo, Miguel Jose-Yacaman, and Arturo Ponce. Analysis of electron beam damage of exfoliated MoS2 sheets and quantitative HAADF-STEM imaging. *Ultramicroscopy*, 146:33–38, 2014.

[20] Satish Kumar Iyemperumal, Thang Duc Pham, Jack Bauer, and N. Aaron Deskins. Quantifying Support Interactions and Reactivity Trends of Single Metal Atom Catalysts over TiO2. *Journal of Physical Chemistry C*, 122(44):25274–25289, 11 2018.

[21] Handan Yildirim, Abdelkader Kara, Sondan Durukanoglu, and Talat S. Rahman. Calculated pre-exponential factors and energetics for adatom hopping on terraces and steps of Cu(1 0 0) and Cu(1 1 0). *Surface Science*, 600(2):484–492, 1 2006.

[22] Lena Puntscher, Kevin Daninger, Michael Schmid, Ulrike Diebold, and Gareth S. Parkinson. A study of Pt, Rh, Ni and Ir dispersion on anatase TiO2(101) and the role of water. *Electrochimica Acta*, 449, 5 2023.

[23] Barbara Zitová and Jan Flusser. Image registration methods: A survey. *Image and Vision Computing*, 21(11):977–1000, 2003.

[24] H.W. Kuhn. The Hungarian Method for the Assignment Problem. *Naval Research Logistics Quarterly*, 5:83–97, 1955.

[25] K. Klementiev and R. Chernikov. XAFSmass: A program for calculating the optimal mass of XAFS samples. In *Journal of Physics: Conference Series*, volume 712. Institute of Physics Publishing, 2016.

[26] Matthew Newville. Larch: An analysis package for XAFS and related spectroscopies. In *Journal of Physics: Conference Series*, volume 430. Institute of Physics Publishing, 2013.

Chapter 5

Oxygen evolution reaction properties of atomically dispersed Ir on TiO_2 nanosheets

Introduction

Atomically dispersed Ir electrocatalysts are promising candidates for the acidic oxygen evolution reaction (OER) due to their high theoretical mass activity. However, like their nanoparticle counterparts, these catalysts suffer from the aggregation of Ir during the reaction, which leads to deactivation [1]. Enhancing catalyst stability requires a deeper understanding of the bonding environment of Ir and its evolution during usage, establishing a structure-activity-stability relationship of the atomically dispersed Ir electrocatalysts for the OER.

In this chapter, I investigate the OER performance of the atomically dispersed Ir on TiO_2 nanosheets shown in Chapter 3. Using the Python-based analysis pipeline described in Chapter 4, I first investigate the Ir dispersion on TiO_2 prepared with the heating rate of 1 °C min^{-1} and 10 °C min^{-1}, leveraging the extended length

scale of the high-angle annular dark field scanning transmission electron microscopy (HAADF-STEM) analysis to establish statistical overviews of Ir dispersion on the TiO_2. Subsequently, I investigate the chemical state and the bonding environments of these two samples using X-ray absorption fine structure (XAFS) analysis. Finally, I characterise the OER activity and stability of these samples and correlate their OER performances with their Ir dispersions and chemical environments, providing an overview of the structure-activity-stability relationship of the atomically dispersed Ir on TiO_2 for the acidic OER.

5.1 Analysis of Ir dispersion on TiO_2

After the investigation of the synthesis mechanism of atomically dispersed Ir on TiO_2, the second part of this thesis focuses on establishing the Ir size-specific structure-activity-stability relationships of the Ir on TiO_2 for the acidic OER by comparing the performance of the atomically dispersed Ir with Ir clusters on TiO_2. As discussed in Section 1.4, the acidic OER mechanism on Ir is strongly dependent on the local environment of the Ir, in particular, if there is a long-range ordering of Ir to induce the cooperative effect and accelerate the reaction. Therefore, a quantitative analysis of the Ir dispersion on TiO_2 is necessary for an accurate interpretation of the structure-activity-stability relationship.

In the first part of this chapter, the analysis of Ir dispersion on TiO_2 is performed. Specifically, the Ir size distribution analysis is carried out using the STEM image processing pipeline detailed in Chapter 4. These results are then compared with those from the extended X-ray absorption fine structure (EXAFS) analysis, which examines the dispersion in the bulk of the sample.

5.1.1 Statistically analysis from HAADF-STEM images

As shown in the Figure 3.11, an Ir cluster-rich (Ir_x) sample was synthesised using a heating rate of 10 °C min^{-1} (Ir-TiO_2-10C) in the thermolysis step, whereas the atomically dispersed Ir (Ir_1) sample was prepared using the heating rate of 1 °C min^{-1} (Ir-TiO_2-1C). Figure 5.1a compares the Ir size distribution of Ir-TiO_2-1C and Ir-TiO_2-10C using the HAADF-STEM images, including the representative ones shown in Figure 3.11. For both samples, more than 1000 Ir counts are analysed to obtain statistical insights into the Ir size distribution. Note that Ir-TiO_2-1C sample here is the same sample labelled as 500 °C in Chapter 4, which was prepared by thermolysis of 500 °C using a 1 °C min^{-1} heating rate. I renamed the sample for clarity in this chapter.

The same clustering criteria used in the in-situ heating annular dark field scanning transmission electron microscopy (ADF-STEM) analysis are adopted here. Specifically, two Ir_1 in the HAADF-STEM images are categorised as one Ir_2 when their separation between each other is within 0.316 nm, the Ir-Ir distance for IrO_2. Since the Ir in the clusters are not always atom-by-atom resolved, the number of Ir in each cluster is estimated by dividing the cluster area by the averaged size of Ir_1 obtained from the image. This approximation assumes that the clusters are monolayered and, therefore, provides a lower-bound estimation of the number of Ir in clusters, as the Ir in clusters can stack in 3D. However, qualitative analysis suggests that the Ir clusters are primarily monolayer.

Figure 5.1 compares the size distribution of Ir-TiO_2-1C and Ir-TiO_2-10C. For Ir-TiO2-1C, a total of 819 counts of Ir_1 and 83 counts of Ir_x were analysed. While for Ir-TiO_2-10C, a total of 559 counts of Ir_1 dispersed Ir and 347 counts of Ir_x were found. The atomic percentage of Ir in the form of Ir_1 and Ir_x are calculated for both samples using the criteria mentioned above to estimate the number of Ir in Ir_x.

This Ir atomic percentage analysis indicates that for all the Ir in Ir-TiO_2-1C, 78 %

of them are in Ir_1 and the rest 22 % are Ir_x, while Ir-TiO_2-10C is composed of 13 % of Ir_1 and 87 % of Ir_x, as shown in Figure 5.1a. The Ir_x for Ir-TiO_2-1C consists of 30 Ir_2, 2 Ir_3 and 9 larger Ir_x, whereas for Ir-TiO_2-10C, there are 6 Ir_2, 1 Ir_3 and 331 larger Ir_x. Figure 5.1b further shows the size distribution of the Ir_x in both samples, where a shift towards the larger degree of clustering is observed for Ir-TiO_2-10C compared to Ir-TiO_2-1C. The average size of Ir is shifting from 0.68 nm to 0.95 nm for Ir-TiO_2-1C to Ir-TiO_2-10C.

The above analyses confirm that Ir-TiO_2-1C is a Ir_1-rich sample, comparing to the Ir_x-rich sample of Ir-TiO_2-10C. This said, there exists a non-negligible proportion of Ir_x (22 % of Ir) in Ir-TiO_2-1C, despite the one representative HAADF-STEM image in Figure 3.11 indicating only a small degree of Ir clustering. This discrepancy between a subjectively qualitative and quantitative analysis of the Ir distribution highlights the importance of the statistical quantification of the Ir dispersion performed in this thesis work, allowing for a more accurate interpretation of Ir morphology.

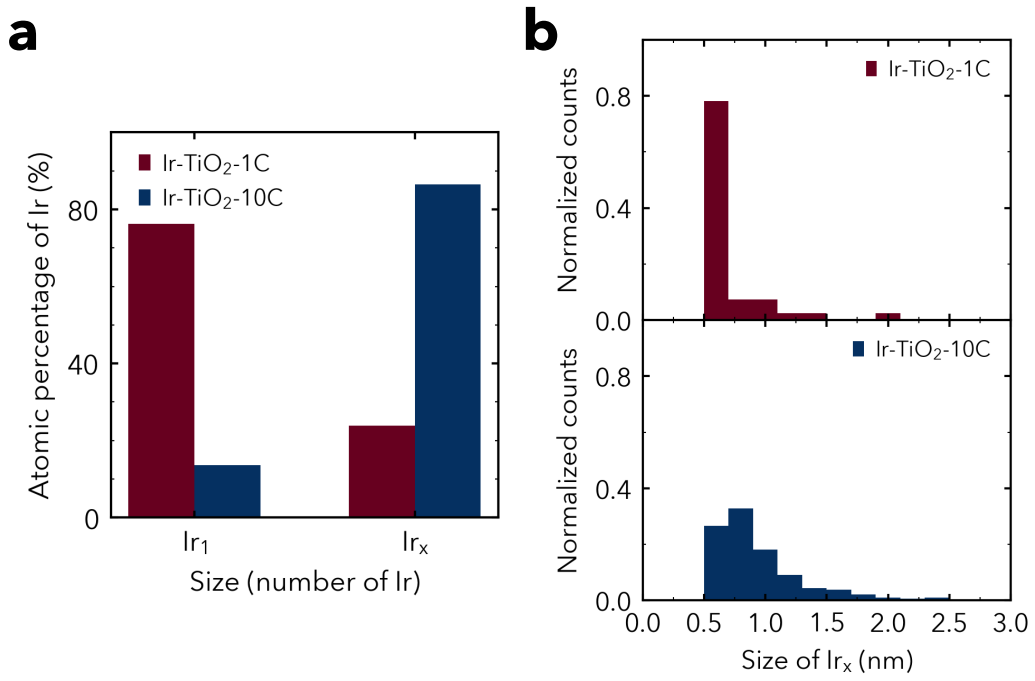


Figure 5.1: Ir size distribution statistics from HAADF-STEM images. (a) Atomic percentages of Ir_1 and Ir_x for Ir-TiO_2-1C and Ir-TiO_2-10C. (b) Size distribution of Ir_x for Ir-TiO_2-1C and Ir-TiO_2-10C normalised to the total counts of Ir_x.

5.1.2 Atomic dispersion analysis from XAFS

After the Ir size distribution analysis from the HAADF-STEM images, I followed the standard practice of utilising the EXAFS analysis to confirm the atomic dispersion of Ir in the bulk of the sample by investigating if scattering signals associated with Ir-Ir or Ir-O-Ir bonds are present in the samples, as discussed in Chapter 1. The absence of these second-shell Ir scattering signals is commonly used as evidence of a lack of Ir clustering.

The bonding environments of the Ir in Ir-TiO_2-1C and Ir-TiO_2-10C are then compared using Ir L_3-edge k^3-weighted Fourier transform (FT)-EXAFS spectra. The fitting of Ir-TiO_2-1C, shown in Figure 4.1 as the 500 °C sample, indicates a 6-fold Ir-O coordination with a bond length of 2.01 Å. The FT-EXAFS spectrum for Ir-TiO_2-10C is only qualitatively analysed, as the fit will produce an averaged Ir model to this two-phase system of metallic Ir(0) and Ir(IV), as supported by the X-ray absorption near edge structure (XANES) linear combination analysis to follow. Such a fit would not be physically meaningful.

As shown in Figure 5.2, the first-shell coordination peak for the Ir-TiO_2-10C sample shifts slightly towards a longer bond length and a lower intensity compared to the Ir-TiO_2-1C, likely a result of the some of Ir(0) clusters in the sample. For both samples, neither scattering signals associated with Ir-Ir or Ir-O-Ir bonds can be observed, suggesting that the Ir in both Ir-TiO_2-1C and Ir-TiO_2-10C samples can be categorised as atomically dispersed.

This conclusion is in stark contrast to the size distribution analysis from the HAADF-STEM images, where Ir-TiO_2-10C is determined to be an Ir_x-dominant sample. This agrees with Finzel and coworkers' density-functional theory prediction that oxidised metal clusters do not show significantly different scattering signals in the second-shell M-O-M bonds, as shown in Figure 1.4b. The lack of a long-range ordering of Ir in the clusters, given the small sizes of the Ir and the monolayer-like structure

from HAADF-STEM images, could potentially produce scattering signals associated with Ir-Ir or Ir-O-Ir bonds. In addition, due to the low Ir loading in the sample, relatively noisy EXAFS spectra were obtained. The insufficient signal-to-noise ratio (SNR) in the high energy second-shell scattering region of the spectra further complicates the analysis, limiting the applicability of using the EXAFS analysis to investigate the Ir dispersion.

In summary, the potential lack of sensitivity of EXAFS in the second-shell M-O-M scattering region for determining Ir dispersion emphasises the importance of a statistical analysis of the Ir dispersion using HAADF-STEM. The use of 2D TiO_2 nanosheets to extend the length scale of the analysis enables a more accurate understanding of the Ir dispersion.

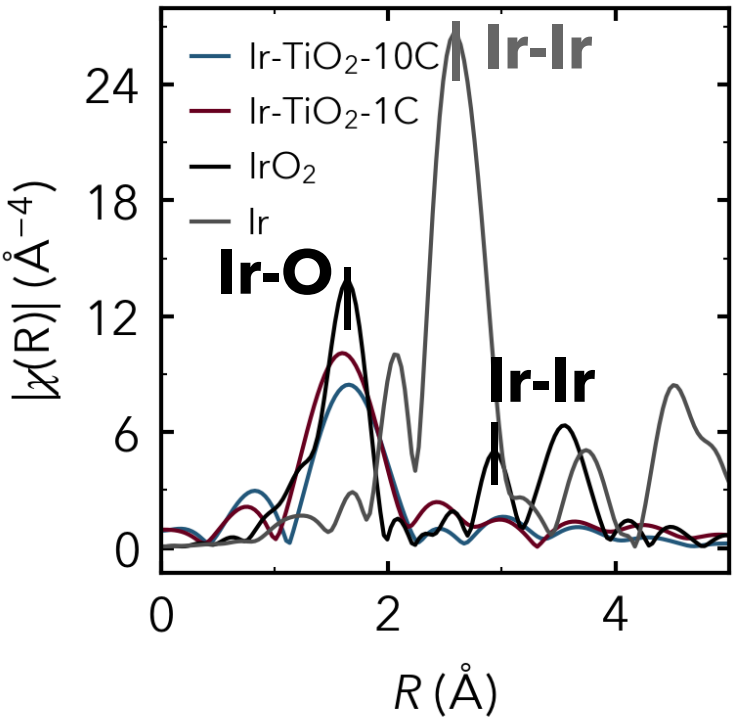


Figure 5.2: Bonding environment analysis of Ir-TiO_2 samples using Ir L_3-edge k^3-weighted FT-EXAFS spectra for Ir-TiO_2-1C and Ir-TiO_2-10C.

5.1.3 Chemical state analysis of Ir-TiO_2

The averaged oxidation state of the Ir in Ir-TiO_2-10C compared with that of Ir-TiO_2-1C is investigated by XANES, shown in Figure 5.3. While WL positions are identical at 11218 eV for both Ir-TiO_2-1C and Ir-TiO_2-10C, the peak intensity of Ir-TiO_2-10C is lower than that of the Ir-TiO_2-1C. This result suggests a lower average oxidation state for Ir-TiO_2-10C. Indeed, the integrated WL intensity of Ir-TiO_2-10C and the fit to the WL intensity/number of 5d hole regression curve shows that the average oxidation state for the Ir-TiO_2-10C is + 3.7 ± 0.2, compared to 4.0 ± 0.2 for the Ir-TiO_2-1C. This result implies that the Ir_x in Ir-TiO_2-10C is a mixture of oxidised Ir clusters with a +4 oxidation state, the same as the Ir_1, and metallic Ir(0), likely a result of the thermolysis in the inert N_2 atmosphere.

To further investigate the degree of the Ir(0) presence in Ir-TiO_2-10C, a linear combination analysis of the XANES spectra was then performed by using the XANES spectra of Ir metal and the Ir-TiO_2-1C (representing Ir_1 with an oxidation state of +4) as the fitting models. As shown in Figure 5.4a, the XANES spectrum of the Ir-TiO_2-10C can be fitted with a linear combination of 85 % of Ir-TiO_2-1C and 15 % of metallic Ir. This fit indicates the majority of the Ir in Ir-TiO_2-10C is at the oxidation state of +4 with a small portion of Ir(0) clusters.

In addition, the high similarity of the XANES spectra between the Ir-TiO_2-1C and Ir-TiO_2-10C suggests that Ir in both samples is in similar local environments, despite the evident Ir clustering in the Ir-TiO_2-10C, as revealed in the HAADF-STEM analysis. This result suggests the Ir clusters are adopting the structure of Ir_1, without Ir-Ir and Ir-O-Ir ordering such as that in metallic Ir or an IrO_2 crystal, consistent with the EXAFS results, where both Ir-Ir and Ir-O-Ir scattering peaks are absent from the spectra. This interpretation is further supported by the failed linear combination fitting of the Ir-TiO_2-10C XANES spectrum using metallic Ir and IrO_2 as the model spectra, shown in Figure 5.4b.

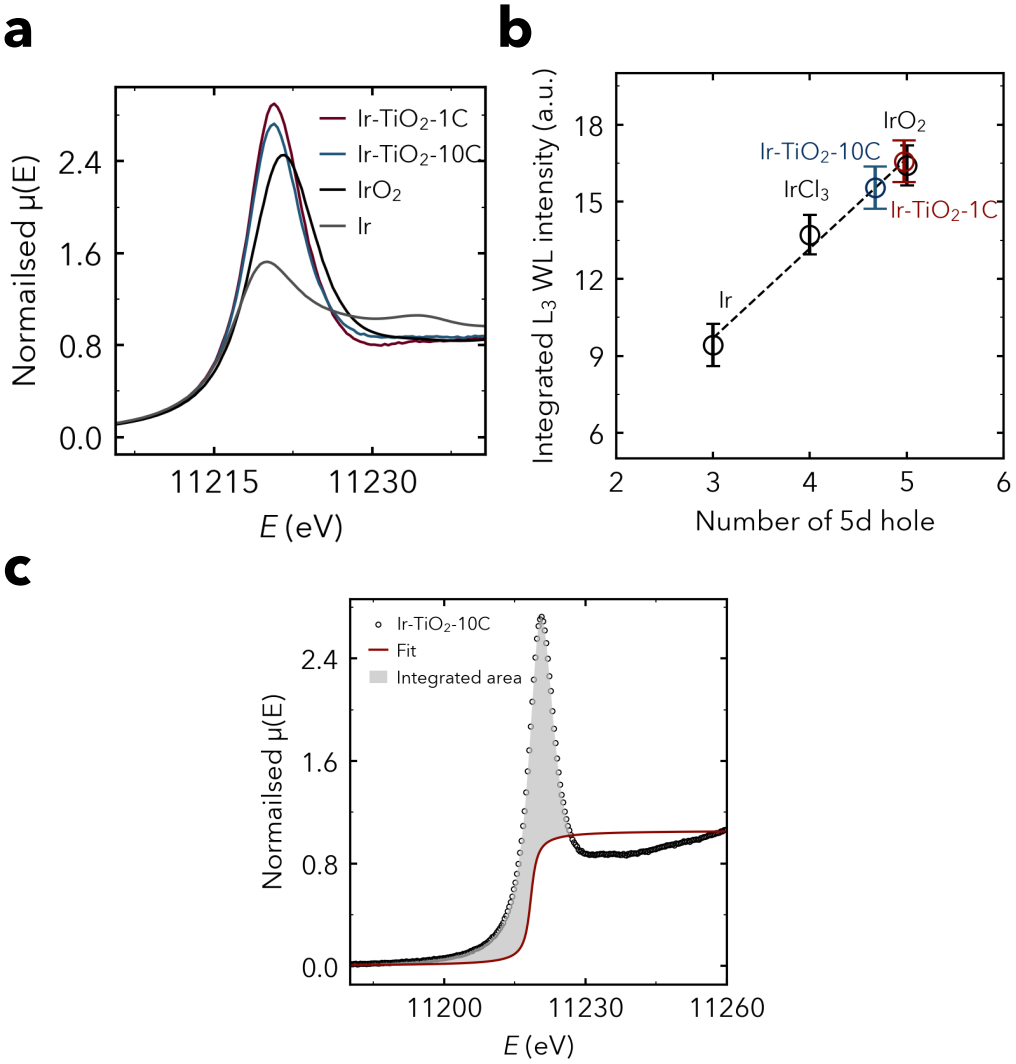


Figure 5.3: XANES analysis of different Ir size distribution. (a) XANES spectra and (b) corresponding fits at Ir L_3-edge for the Ir-TiO_2-1C, Ir-TiO_2-10C and the reference samples. Integration of the WL is shown in (c)for the Ir-TiO_2-10C sample. The raw data of the spectra are plotted with the scattered hollow circles. Background arc-tangent function fitted to the spectra is shown as the red curve, and the integrated area is shown as the grey-shaded region.

To summarise, the XAFS analysis reveals that, despite the difference in their Ir morphology as observed in the HAADF-STEM analysis, the Ir in both Ir-TiO_2-1C and Ir-TiO_2-10C share similar local environments and oxidation states. Specifically, Ir is 6-fold coordinated with oxygen with an oxidation state of +4. The similarity in their local environments and oxidation states enables a fairer assessment of the atomic efficiency of Ir between Ir_1 and Ir_x for the OER without the complication

from different local environments and oxidation states of the Ir. Although again, care should be taken to interpret this XAFS data, as XAFS may be insufficiently sensitive to determine the structural differences between Ir_1 and small Ir_x at a low Ir loading.

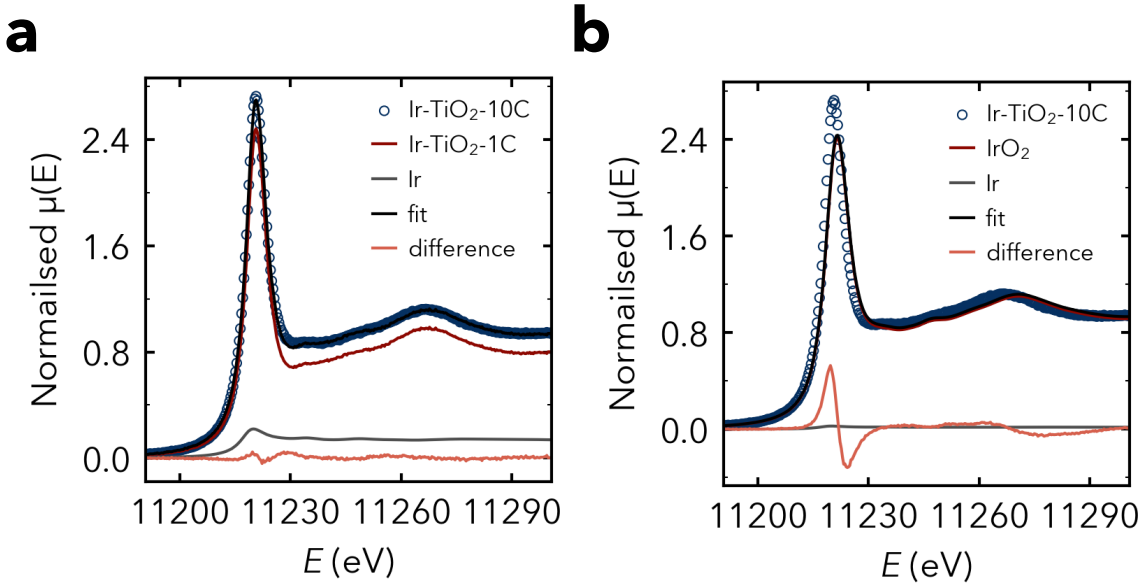


Figure 5.4: XANES linear combination analysis of Ir-TiO_2-10C conducted using (a) a mixture of Ir-TiO_2-1C and Ir metal spectra and (b) a mixture of IrO_2 and Ir metal spectra from 11175 eV to 11315 eV.

5.2 OER performance

5.2.1 Activity

This section assesses the OER performance of the Ir-TiO_2-1C and the Ir-TiO_2-10C. Fluorine-doped tin oxide (FTO) glass was chosen as the electrode to prepare the sample for the OER tests. FTO glass was selected due to its resistance to the acidic OER conditions [2]. As described in Chapter 2, to ensure good electrical contact between the Ir-TiO_2 samples and the FTO layer, the electrode was prepared by calcining a thin layer of TiO_2 on FTO-glass using hydroxypropyl cellulose (HPC) as a binder.

This extra calcination step, along with the use of the binder, can cause the modification to the Ir dispersion to the Ir-TiO_2-1C and Ir-TiO_2-10C if the samples were to be coated on the electrode with the procedure described above. Therefore, instead of directly coating the Ir-TiO_2-1C and Ir-TiO_2-10C onto the FTO glass, I modified the procedure to firstly prepare the bare TiO_2 on the FTO glass, followed by immersing the TiO_2-coated FTO glass into the $[IrCl_6]^{2-}$ precursor solution for the strong electrostatic absorption (SEA) process, then finished with the thermolysis step. The morphology of the Ir dispersion was characterised by scratching the Ir-TiO_2 off the FTO glass and examined it using HAADF-STEM. The images shown in Figure 3.11 are the samples prepared in this manner.

Scanning electron microscopy (SEM) was used to characterise the coating of TiO_2 on FTO glass. Figure 5.5a and Figure 5.5b show the top and cross-sectional view of the TiO_2 coating, respectively. The micrographs reveal a porous matrix consisting of TiO_2 nanosheets, with pores in the size of a few hundred nanometers. These pores should provide the OER reactant, i.e., the water, with access to not only the top part of the casting but also the part that is on the FTO side. In addition, this porous structure provides a pathway for the product, i.e., the oxygen gas, to dissipate. The thickness of the TiO_2 coating is measured at $\sim$ 1 to 2 um. A compact contact between TiO_2 and FTO is confirmed.

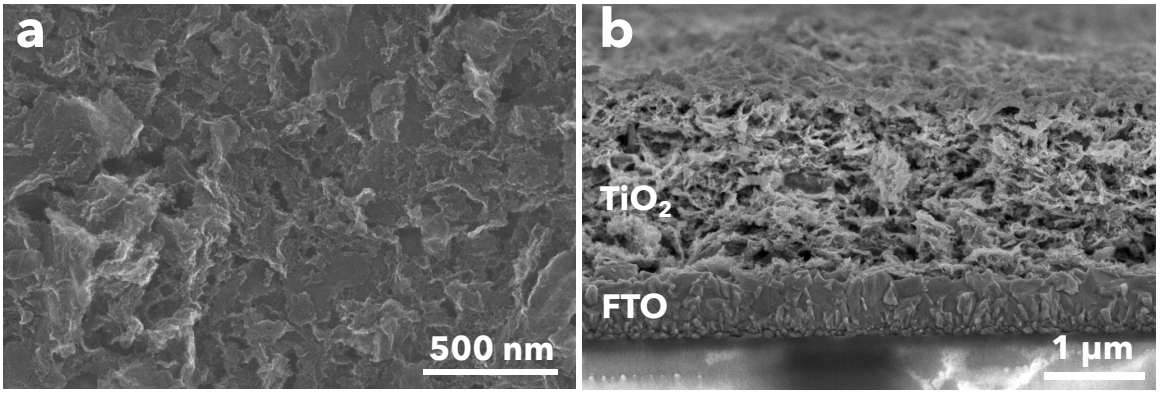


Figure 5.5: Morphology of the TiO_2-coated OER electrode investigated with SEM micrographs. (a) Top and (b) cross-sectional view of the electrode.

Potentiostatic Electrochemical Impedance Spectroscopy (PEIS) was used to follow the reaction kinetics and to extract the high-frequency resistance (HFR) in the system for the iR drop correction. Figure 5.6a shows the PEIS responses of one representative measurement of Ir-TiO_2-1C from the open circuit voltage (OCV), which is usually measured at 0.8 to 0.9 V vs RHE, to 1.96 V vs RHE. Figure 5.6b shows the zoom-in of the low impedance part in Figure 5.6a. From OCV to 1.36 V, the PEIS primarily shows a capacitive behaviour. A semi-circle emerges from 1.56 V and becomes smaller and distorted at 1.96 V. The emergence of the semi-circle at 1.56 V suggests the onset of OER. The distortion of the semi-circle is likely a convolution of the Butler-Volmer kinetics with limiting mass transport of the H_2O and O_2.

The HFR is obtained by fitting the PEIS response at 1.76 V with the equivalent circuit shown in the inset of Figure 5.6b, where the HFR corresponds to the R_1. In this particular case, the HFR is measured at 12.3 Ω and across all repeats, the HFR ranges between 12 to 13 Ω.

Cyclic voltammetry (CV) comparing the bare TiO_2 substrate, Ir-TiO_2-1C and Ir-TiO_2-10C is shown in Figure 5.6c. Strong current cathodic/anodic response at 0.1 V vs RHE is observed for the TiO_2, which can be attributed to the capacitive current from the charging of the conduction band of TiO_2 anatase [3, 4]. Other than the peaks at 0.1 V, there is one extra redox peak at 0.95 V vs RHE for the Ir-TiO_2-1C, which can be attributed to an $Ir^{3+/4+}$ redox, as commonly observed for IrO_2 and for atomically dispersed Ir [1]. The CV for Ir-TiO_2-10C shows a similar profile to that of Ir-TiO_2-1C, with the redox peak at 1.0 V slightly weaker than that of Ir-TiO_2-1C.

The OER activities of both Ir-TiO_2-1C and Ir-TiO_2-10C were examined by 10 CVs between 1.3 to 2.1 V vs RHE with a minimum of three independent measurements performed. A representative dataset is shown in Figure 5.7a-c. The current response was normalised to the total Ir mass on the electrode to examine the Ir use efficiency. Ir-TiO_2-1C shows larger mass-normalised current densities than Ir-TiO_2-10C for the

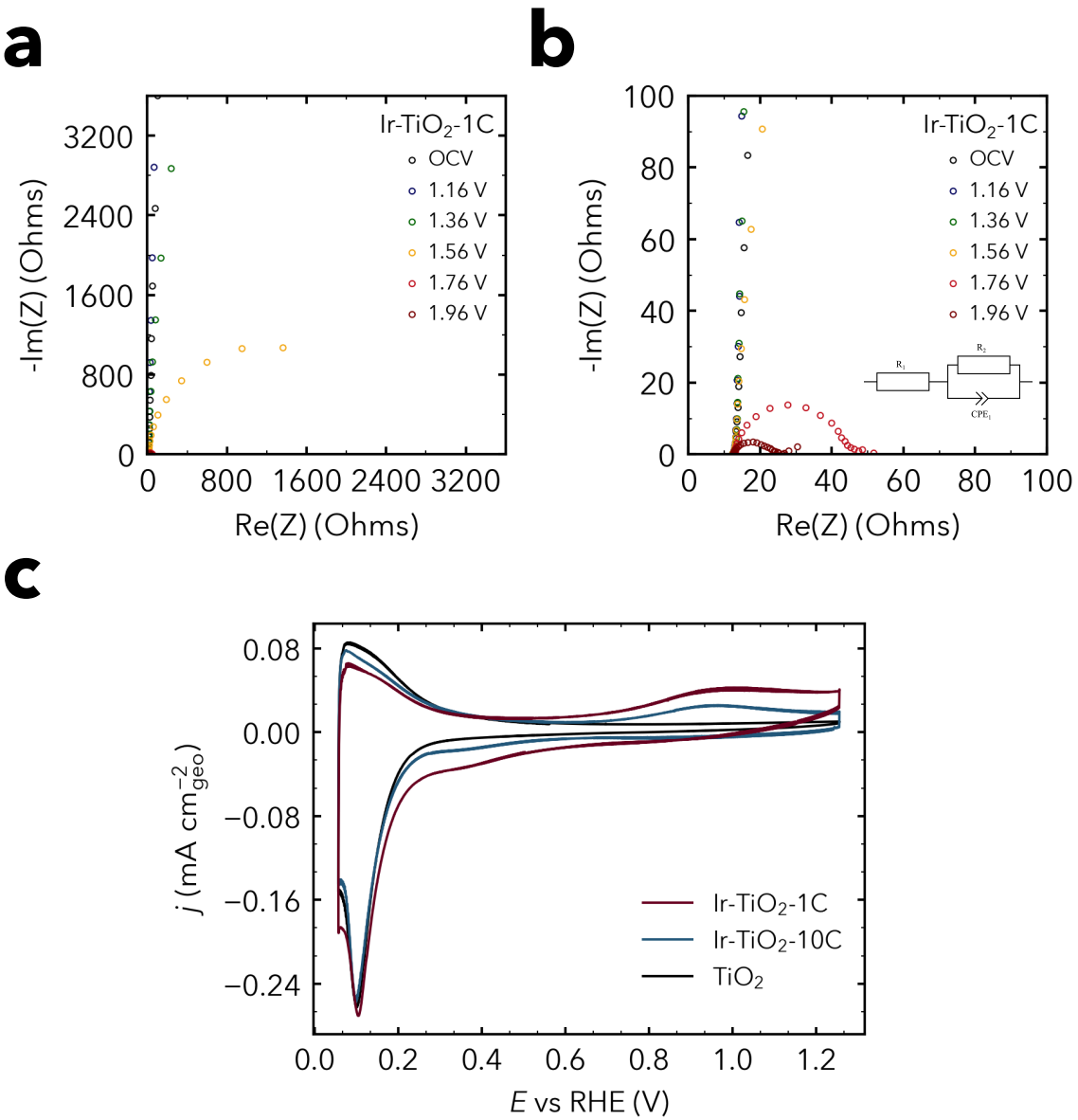


Figure 5.6: Electrochemical properties of the Ir-TiO_2 samples. (a) PEIS of Ir-TiO_2-1C. (b) shows in the low impedance region in (a). Inset showing a R_1-p(R_2-CPE) circuit for the fitting of the spectrum at 1.76 V, with CPE as the constant phase element to represent the non-ideal capacitive behaviour. (c) CV of Ir-TiO_2-1C, Ir-TiO_2-10C and TiO_2 below OER potentials, performed in Ar-saturated 0.5 M H_2SO_4 with a scan rate of 100 mV s^{-1}. The CV scans start from OCV (~0.9 V) first cathodically, then anodically, and finally back to OCV.

1st, 3rd and 10th cycle, indicating a superior Ir use efficiency for the Ir_1-rich Ir-TiO_2-1C sample compared to the Ir_x-rich Ir-TiO_2-10C. A redox peak at 1.85 V vs RHE is observed for both samples. This redox peak can be attributed to the $Ir^{4+/5+}$ redox,

which has been commonly reported to be crucial for the activation of Ir for the OER [5].

To compare with literature-reported Ir-mass activities for OER, specifically to examine if Ir-TiO_2-1C outperforms the commercial IrO_x from Alfa Aesar (see Table 1.3), the averaged mass activity at 1.55 V of the repeated measurements is calculated and shown in Figure 5.7d. An average mass activity of 58 ± 13 and 11 ± 3 A g_{Ir}^{-1} at 1.55 V is measured for the 1st and the 10th cycle of Ir-TiO_2-1C, respectively. For Ir-TiO_2-10C, mass activities of 19 ± 4 and 6 ± 1 A g_{Ir}^{-1} are measured for the 1st and the 10th cycle. Comparing to the mass activity ranging from 100 to 500 g_{Ir}^{-1} reported for the commercial IrO_x from Alfa Aesar, as summarised in Table 1.3, the mass activities for both Ir-TiO_2-1C and Ir-TiO_2-10C are significantly lower. This result suggests that downsizing the Ir into atomically dispersed Ir using TiO_2 nanosheets as a support may not offer a significant improvement for an OER catalyst.

The resistivity (ρ) of the TiO_2 coating can be estimated using the formula:

$$\rho = R \cdot \frac{A}{L} = 2 \cdot \frac{0.5 \times 10^{-4}}{1 \times 10^{-6}} = 100\ \Omega \cdot \mathrm{m}, \tag{5.1}$$

where R is the resistance (2 Ω, determined from the resistance difference between a bare FTO electrode and an Ir-TiO_2 coated FTO glass), A is the cross-sectional area (0.5 cm^2), L is the thickness of the material (1 μm). Therefore, the resistivity of the TiO_2 layer is 100 $\Omega \cdot$ m. As discussed previously, the total Ir loading on the electrode is 1–2 orders of magnitude lower than what is typically used in the literature. If the Ir loading were increased by a factor of 10 to match literature values, this would result in a resistance of approximately 20 Ω. At a current density of 10 mA cm^{-2}, this resistance would produce a 200 mV overpotential. Attempting to correct this using iR compensation could introduce significant errors in the interpretation of the catalytic reactivity.

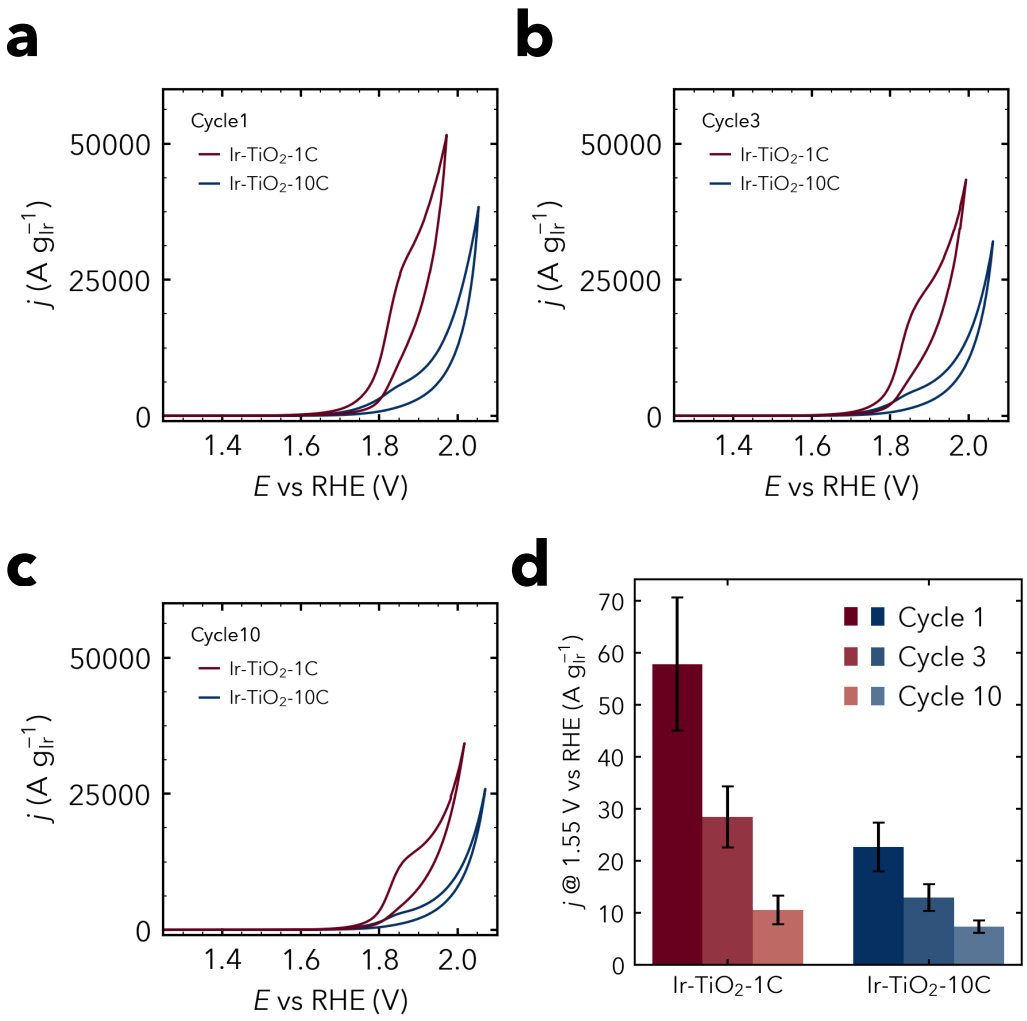


Figure 5.7: Evaluation of OER performance of Ir-TiO_2-1C and Ir-TiO_2-10C performed using 10 consecutive CVs between 1.3 and 2.1 V vs RHE in O_2-saturated 0.5 M H_2SO_4. OER current responses are normalised to the total Ir mass on the electrode, typically ranging from 0.1 to 0.2 μg. (a) shows the 1st, (b) 3rd and (c) 10th CV. (d) summarises the Ir mass-normalised OER activities across all three samples at 1.55 V vs RHE. Averaged OER current densities and error bars are calculated using at least three independent measurements. In each measurement, the OER current density is extracted from the average of the forward and the backward CV sweep to cancel out the capacitive charging in the current response [6].

Practical use of Ir-TiO_2-1C as OER catalysts may be further hindered by its low geometric current density at 1.55 V, which is constrained by low Ir areal densities on the electrodes, which are 1 to 2 orders of magnitude lower than commonly reported in the literature. A thin Ir-TiO_2 layer was coated to minimise the ohmic resistance of

the electrode. Using this thin Ir-TiO_2 geometry, the averaged total mass of 72 ± 22 μg and 65 ± 17 μg is measured for the Ir-TiO_2-1C and the Ir-TiO_2-10C electrodes on a 0.5 cm^{-2} area. Based on the Ir loading of 0.18 wt% estimated from UV-Vis analysis, shown in Chapter 3, this calculates a Ir loading areal density of 0.25 ± 0.07 $\mu g\ cm_{geo}^{-2}$ for Ir-TiO_2-1C and 0.22 ± 0.03 $\mu g\ cm_{geo}^{-2}$ for Ir-TiO_2-10C.

A lower Ir areal loading results in a larger overpotential to reach the same OER current density, as can be derived from the Bulter-Volmer kinetics detailed in Chapter 1. This is reflected in the geometric activities of the Ir-TiO_2 samples, shown in Figure 5.8d. The geometric activity of 0.023 ± 0.008 and 0.0036 ± 0.0010 mA cm_{geo}^{-2} at 1.55 V is measured for the 1st and the 10th cycle of the Ir-TiO_2-1C, respectively. For the Ir-TiO_2-10C, geometric activities of 0.0039 ± 0.0003 and 0.0013 ± 0.0002 mA cm_{geo}^{-2} at 1.55 V are measured for the 1st and the 10th cycle. For the bare TiO_2, geometric current densities of 0.0003 ± 0.0001 and 0.00010 ± 0.00006 mA cm_{geo}^{-2} at 1.55 V are recorded for the 1st and the 10th cycle. The current densities for both Ir-TiO_2 samples are at least one order of magnitude larger than those of TiO_2, confirming the observed current responses correlate with the Ir present.

Significant OER current begins after 1.7 V vs RHE and reaches 10 mA cm_{geo}^{-2} at approximately 1.9 V of the 1st CV for Ir-TiO_2-1C. Comparing to ∼1.45 V to 1.5 V to reach this geometric current density commonly reported for other atomically dispersed Ir catalysts shown in Table 1.2, this performance is less promising for consideration as an alternative OER catalyst in PEM water electrolysers.

Besides the low observed OER activities, the stability of both catalysts suffers. As shown in Figure 5.8, the current densities gradually decrease for both Ir-TiO_2-1C and Ir-TiO_2-10C. The geometric current densities for Ir-TiO_2-1C drops by 6-fold from 1st to 10th cycle. A decrease in activity is also observed for the Ir-TiO_2-10C, where a 3-fold drop in geometric current densities from the 1st to the 10th cycle is shown. This rapid degradation of both Ir-TiO_2 samples requires further investigations and is

discussed in the following section.

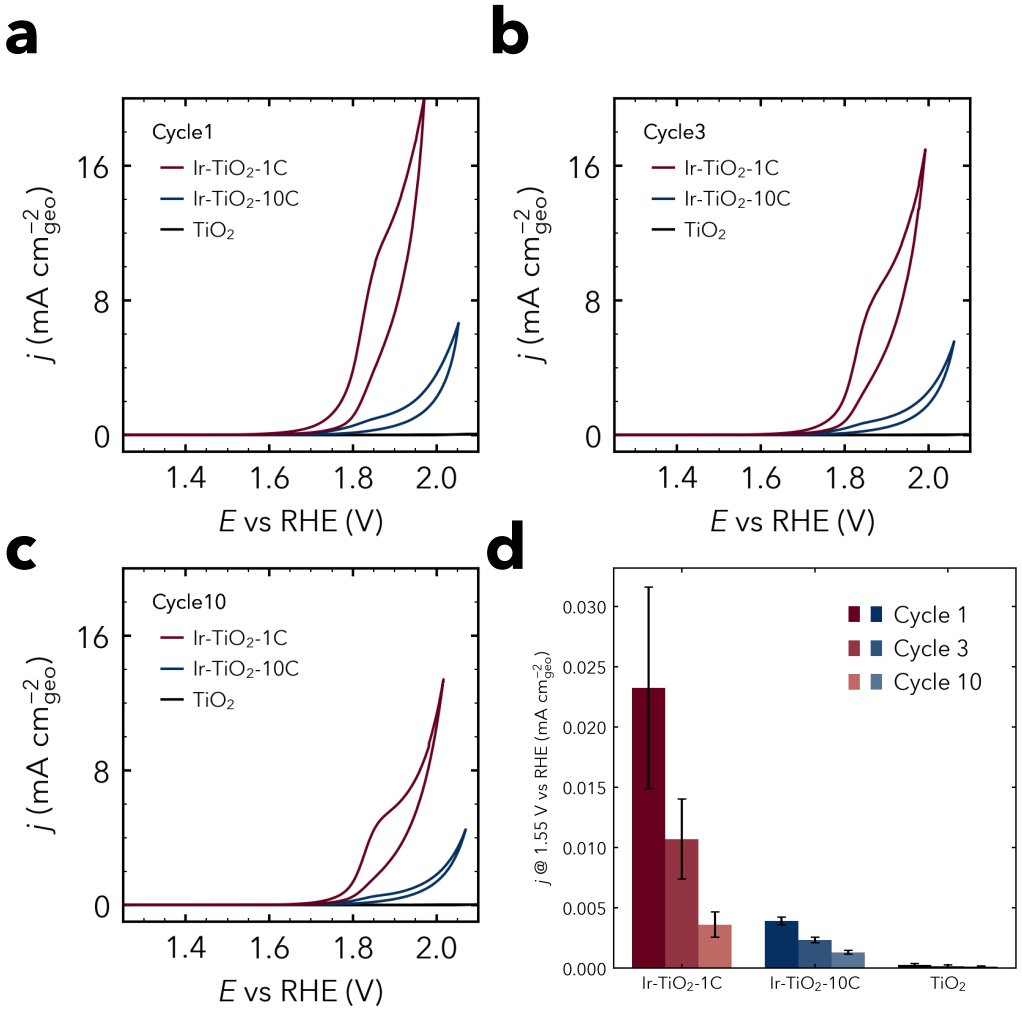


Figure 5.8: Evaluation of OER performance of Ir-TiO_2-1C, Ir-TiO_2-10C and TiO_2 performed using 10 consecutive CVs between 1.3 and 2.1 V vs RHE in O_2-saturated 0.5 M H_2SO_4. OER current is normalised to 0.5 cm^2, the geometric surface area of the electrode. (a) shows the 1st, (b) 3rd and (c) 10th CV. (d) summarises the geometric OER activities across all three samples at 1.55 V vs RHE. Averaged OER current densities and error bars are calculated using at least three independent measurements. In each measurement, the OER current density is extracted from the average of the forward and the backward CV sweep to cancel out the capacitive charging in the current response [6].

5.2.2 Stability

The stability issue was further investigated with post-OER HAADF-STEM images, with representative images for Ir-TiO_2-1C are shown in Figure 5.9a and b and Ir-TiO_2-10C shown in Figure 5.9c and d. Although Ir_1 remains present, significant agglomeration of Ir_1 can be observed in the lower magnification HAADF-STEM image across TiO_2 support. Qualitatively, the Ir dispersion of Ir-TiO_2-1C begins to resemble that of Ir-TiO_2-10C.

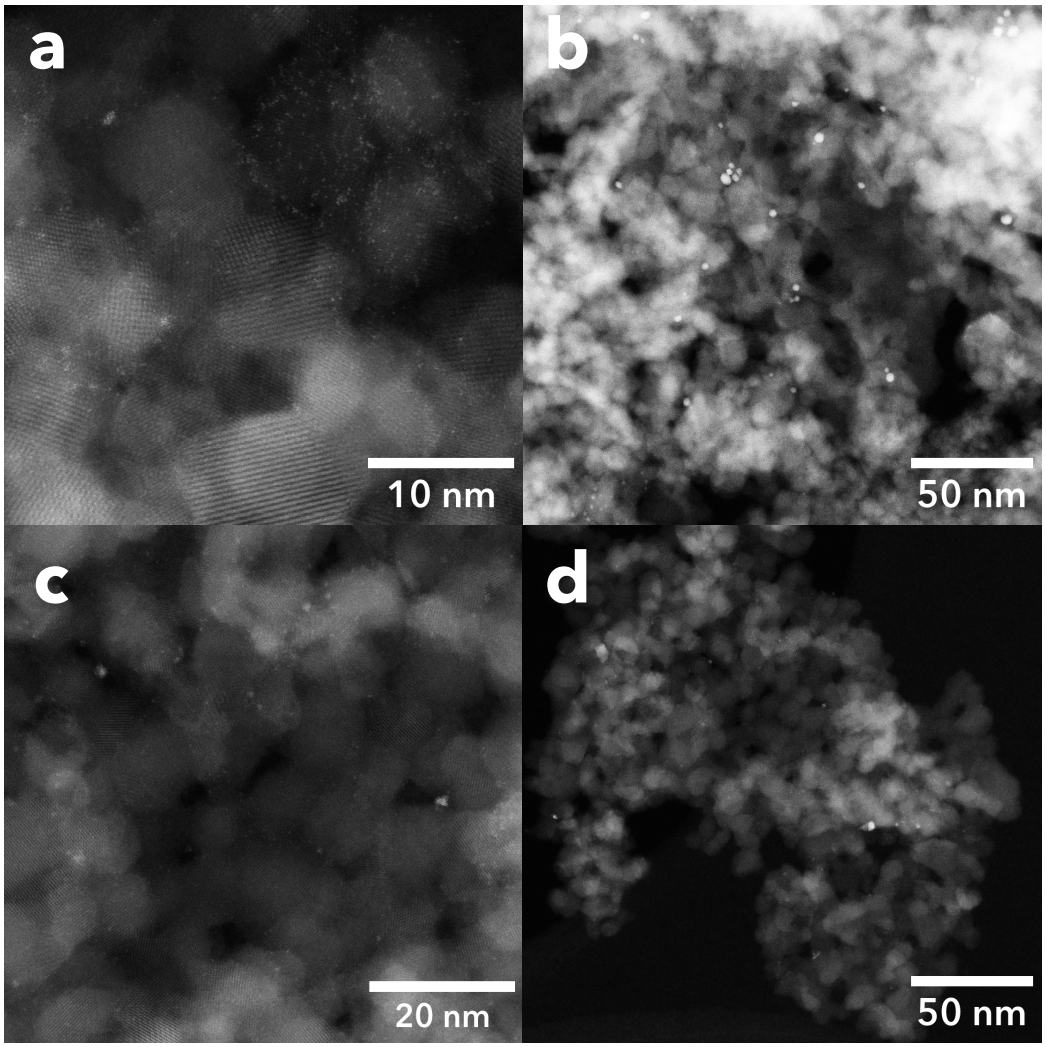


Figure 5.9: HAADF-STEM analysis of the post-OER samples. Representative (a) high- and (b) low-magnification HAADF-STEM images of the post-OER Ir-TiO_2-1C. Representative (c) high- and (d) low-magnification HAADF-STEM images of the post-OER Ir-TiO_2-10C.

Quantitatively, the size distribution analysis of HAADF-STEM images is performed and shown in Figure 5.10. A significant increase in the number of nanosized clusters in the range of 0.5 to 1.5 nm with an average size of 1.1 nm is observed for Ir-TiO_2-1C. This trend of agglomeration is observed for Ir-TiO_2-10C as well, with the average Ir size doubling from 0.95 nm in the pristine sample to 1.9 nm post-OER. Atomic percentage analysis shows that only 28% of the Ir remains as Ir_1 for Ir-TiO_2-1C, whereas for Ir-TiO_2-10C, this value drops to only 10%.

The oxidation state of the post-OER Ir-TiO_2-1C sample was characterised using XPS measurement at Ir 4f since the total Ir loading on the electrode is too low for the collection of the Ir signal in a reasonable time frame (<1 hour) with the synchrotron XAS. The analysis of the Ir 4f peak is, unfortunately, complicated by its overlap with the Ti 3s peak at the binding energy of 60 eV. Therefore, the analysis of the Ir 4f peak is highly dependent on the fitting of the Ti 3s peak. To ensure consistency, I followed the fitting process proposed by Van der Merwe and coworkers [7], constraining the peak shape, position and area of Ti 3s using its physical correlation to the Ti 3p peak at 37.1 eV. The details of this peak fitting process can be found in Chapter 2.

XPS measurements at Ir 4f reveal an Ir $4f_{7/2}$ binding energy of 61.9 eV for both the pristine and post-OER Ir-TiO_2-1C samples, corresponding to an oxidation state of +4 [8] (Figure 5.11). The oxidation state of the pristine sample measured with XPS agrees with the oxidation state of +4.01 estimated with the XANES analysis.

Since the oxidation states of the Ir in Ir-TiO_2-1C remains unchanged, the degradation of its OER activity is unlikely to be due to a change in the chemical state of Ir. A more plausible cause of the degradation is the high degree of Ir agglomeration after the 10 CVs at the OER region, reducing the active surface area of the Ir and thus leading to a decrease in the OER activity.

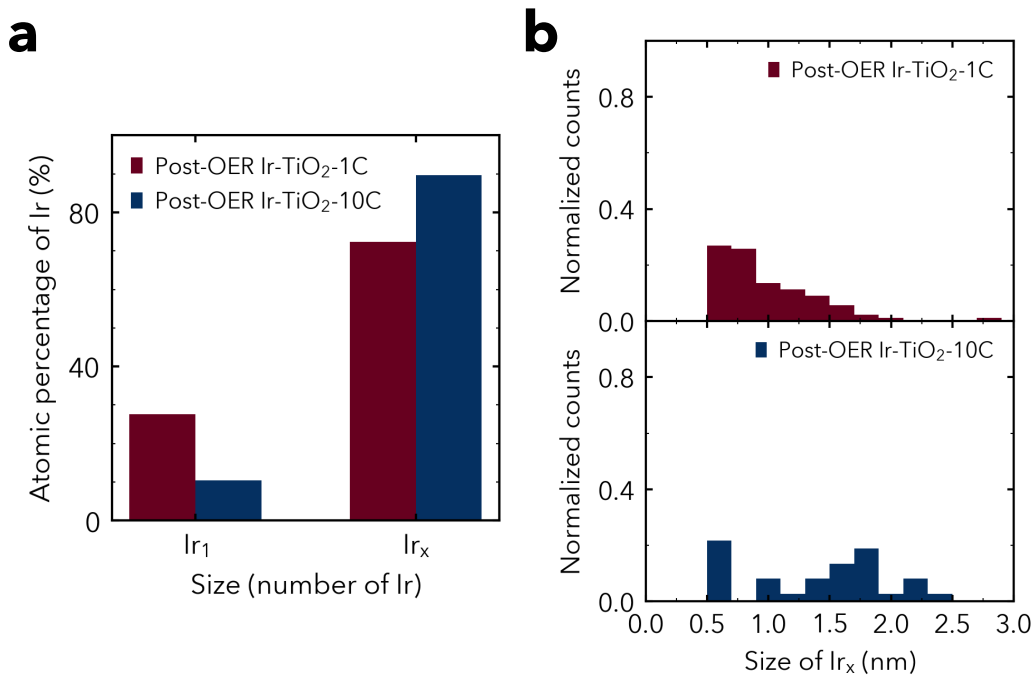


Figure 5.10: Ir size distribution statistics from STEM images. (a) Atomic percentage of Ir_1 and Ir_x for post-OER Ir-TiO_2-1C and post-OER Ir-TiO_2-10C. (b) Size distribution of Ir_x for post-OER Ir-TiO_2-1C and post-OER Ir-TiO_2-10C normalised to the total counts of Ir_x.

5.2.3 Improvements of the support

Assuming the OER activity of the atomically dispersed Ir is limited by the electronic conductivity of the TiO_2 support, strategies to improve the electronic conductivity of the support while meeting all the support requirements discussed in Chapter 1 are desired.

As discussed in Chapter 1, the choice of TiO_2 as the support for the atomically dispersed Ir is based on the Z-contrast in the STEM to allow reliable characterisation, and TiO_2 is the well-known stable support in the OER conditions in PEM water electrolysers. To improve the electronic conductivity of TiO_2, doping is a commonly used strategy that increases the charge mobility in TiO_2 while maintaining its structural robustness to ensure stabilities during OER. Common dopants for TiO_2 used in electrochemical reactions is Nb [9, 10]. Although this dopant has been shown to

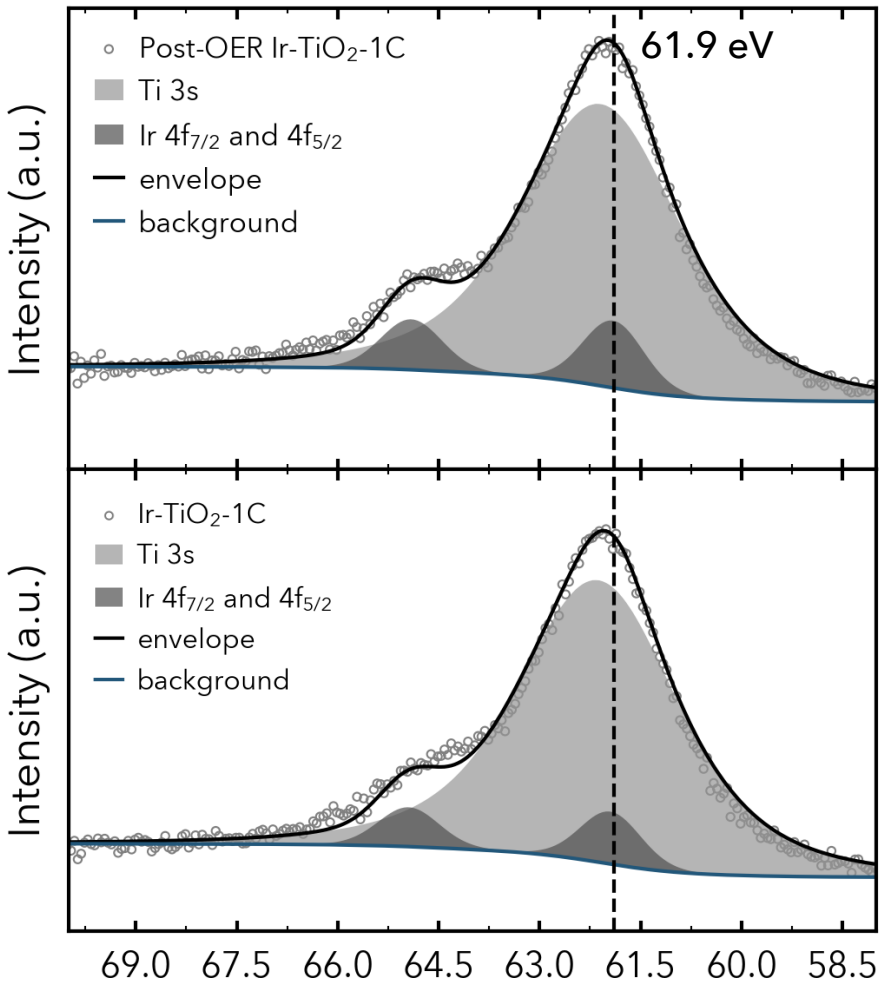


Figure 5.11: Chemical state analysis of post-OER Ir-TiO_2-1C (top) comparing with Ir-TiO_2-1C (bottom) using Ir 4f XPS.

improve the electronic conductivity of TiO_2 and, in turn, improve the overall Ir-TiO_2 system, these dopants also have high Z-contrast against Ti in STEM, and this may result in difficulty in distinguishing the dopants from the Ir in the HAADF-STEM images.

With all requirements considered, nitrogen-doped TiO_2 may be an ideal candidate with improved electronic conductivity [11]. And the N-TiO_2 can be prepared by treating the TiO_2 in NH_3 at elevated temperatures. I used the commercially available 5 nm TiO_2 particles to start synthesising the N-TiO_2.

The synthesis was characterised by XRD, XPS and STEM, shown in Figure 5.12.

Using the XRD, a new peak at 43 degrees corresponds to the formation of a new titanium oxynitride $TiON_x$ starts appearing at 575 °C. Further, increasing the reaction temperature transforms the TiO_2 anatase into the cubic rocksalt ($TiON_x$) structure with partial substitution of O with N.

XPS N 1s spectrum confirms the successful doping of N, with the peak on the left corresponding to interstitial N (N_{int}), where the nitrogen occupies the interstitial site in the TiO_2 lattice before it begins to replace oxygen in the lattice (N_{sub}) [11]. Ti 2p spectrum confirms the Ti remains at +4, and the O 1s XPS shows the O-Ti bonds.

The colours of TiO_2 change from white to yellow (prepared at 575 °C in 50 sccm NH_3), to light brown (prepared at 600 °C in 50 sccm NH_3) and to dark brown (prepared at 600 °C in 200 sccm NH_3), suggesting more absorption of the visible light and thus a good indication of the introduction of defect states in the TiO_2 bandgap.

While promising electronic conductivity may be expected, HAADF-STEM images of the 575 °C 50 sccm NH_3 treated sample shows a significant degree of sintering of the 5 nm TiO_2, with further BET analysis showing a decrease of the surface area from 290 $m^2\ g^{-1}$ to 100 $m^2\ g^{-1}$. This lowering of the surface area limits the total amount of Ir that can be loaded.

However, a preliminary test to synthesise atomically dispersed Ir on N-doped TiO_2 (the 575 °C 50 sccm NH_3 treated sample) using the synthesis method investigated in this work results in a disappearance of the yellow colour of the N-doped TiO_2, suggesting sintering and the removal of the N dopant.

In summary, although N-TiO_2 serves as a promising candidate for the preparation of atomically dispersed Ir, meeting all the requirements that are critical for the study of atomically dispersed Ir, the use of the high-temperature thermolysis studied in this work is not compatible. The N-TiO_2 undergoes sintering, and the dopants are removed after the thermolysis. Other preparation methods that involve a thermolysis step with a lower temperature, such as promoting the Cl^- removal in a hydrogen

atmosphere, may be worth exploring.

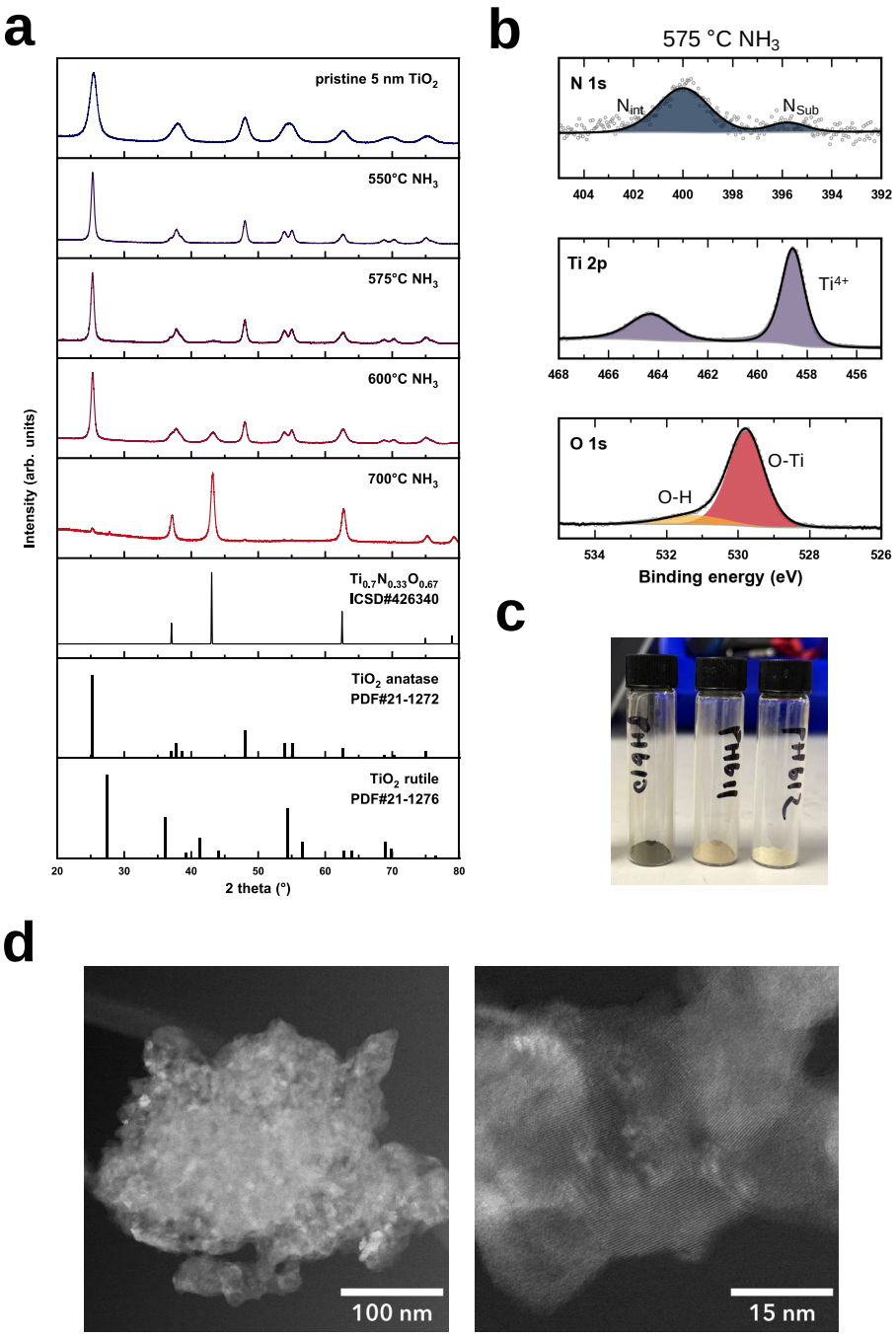


Figure 5.12: Synthesis and physical characterisation of N-TiO_2. (a) XRD of 5 nm TiO_2 treated in 50 sccm NH_3 with increasing temperature. (b) XPS N 1s spectra, Ti 2p and O 1s spectra of the N-TiO_2 prepared at 575 °C with a flow rate of 200 sccm NH_3. (c) A photo showing the TiO_2 treated at different conditions. The sample on the left is at 600 °C with a flow rate of 200 sccm NH_3, the sample in the middle is at 600 °C with a flow rate of 50 sccm NH_3 and the sample on the right is at 575 °C with a flow rate of 50 sccm NH_3. (d) Representative ADF-STEM images of the N-TiO_2 prepared at 575 °C with a flow rate of 50 sccm NH_3.

Conclusions

In this chapter I studied the OER performance of two Ir-TiO_2 samples, one Ir_1-rich Ir-TiO_2-1C sample prepared by a heating rate of 1 °C min^{-1}, and the other Ir_x-rich Ir-TiO_2-10C sample prepared by a heating rate of 10 °C min^{-1}. The Ir dispersions are confirmed by a size distribution analysis of multiple HAADF-STEM images, showing the size of the Ir_x around 1 nm for the Ir_x-rich Ir-TiO_2-10C sample.

The XAFS analysis shows that the Ir bonding environment and the oxidation state of the Ir_x-rich sample resemble those of the Ir_1-rich sample, despite their significant differences in the Ir dispersion. The similarity in their local environments and oxidation states enables a fairer assessment of the atomic efficiency of Ir between Ir_1 and Ir_x for the OER without the complication from different local environments and oxidation states of the Ir. The Ir_1-rich Ir-TiO_2-1C sample indeed exhibits a superior OER activity to the Ir_x-rich Ir-TiO_2-10C, as characterised by the CV in the OER region, validating the idea of increasing atomic dispersion of Ir to increase the Ir utilisation.

Nevertheless, both the Ir-TiO_2-1C and Ir-TiO_2-10C exhibit lower OER mass activities than that of commercial IrO_x benchmark, likely due to low electronic conductivity of the TiO_2 support. In addition, the thin sample layer required for minimising the ohmic resistance of the electrode leads to a low Ir areal loading density, which may limit the practical application of these catalysts in a PEM water electrolyser. In addition, the activities of both Ir-TiO_2-1C and Ir-TiO_2-10C degrade significantly during the OER activity tests, which is attributed to a rapid agglomeration of the Ir, based on the post-OER HAADF-STEM analysis. These results motivate further efforts to improve the electronic conductivity of the TiO_2 support and develop a strategy to mitigate the Ir agglomeration during OER.

Lastly, the use of nitrogen-doped TiO_2 as a support for the Ir_1 with higher electronic conductivity was explored. However, the use of thermolysis of $[IrCl_6]^{2-}$ in N_2

to prepare the atomically dispersed Ir is not compatible with N-TiO_2, as the N-TiO_2 readily sinters at the synthesis temperature, removing the nitrogen dopants. Other preparation methods that require heat treatment with lower temperatures, such as promoting the Cl^- removal with heat treatment in a hydrogen atmosphere, may be worth exploring.

Experimental details

Preparation of Ir-TiO_2 electrodes

The TiO_2 nanosheet-coated electrodes, using fluorine-doped tin oxide (FTO) glass (TEC 10, 1mm thickness, 20 mm x 15 mm, 9.39 ± 0.38 Ω square^{-1}, Ossila) as the backing electrode, were prepared with the protocol reported by Lebedev and coworkers [12]. FTO glasses were cleaned by successive ultra-sonication in 0.01 M KOH in 2-propanol (>99.8%, Sigma-Aldrich) at 70 °C, followed by water, each for 15 minutes and repeated for 3 times. For the coating of the TiO_2 nanosheets, first, a slurry of TiO_2 nanosheets using 10 wt% hydroxypropyl cellulose (HPC, Mw ∼80,000, Sigma-Aldrich) as a binder was prepared. HPC was dissolved and stirred overnight in ethanol (>99.8%, Sigma-Aldrich) before being added to TiO_2 nanosheets dispersed in ethanol and stirred overnight. stirred overnight with . Subsequently, a thin layer of the slurry was coated on the FTO glass using the doctor blade method. Area (0.5 cm^{-2}) and thickness (1-2 μm) of the TiO_2 coating was controlled by masking the FTO glass with one layer of scotch tape before the doctor blade process. Finally, the electrode was calcined in air at 500 °C for 1.5 hours with a heating rate of 1 °C min^{-1} to remove the HPC and promote the electrical contact between the TiO_2 and FTO layer.

For the preparation of the Ir-TiO_2 electrodes, the TiO_2 nanosheets-coated FTO glass was immersed into an $[IrCl_6]^{2-}$ precursor solution (1 mg of $H_2IrCl_6 \cdot xH_2O$ in 3.77 mL of deionized water) for the SEA process for 1 hour under continuous stirring. Subsequently, a washing step using pH 3 HCl solution is used to remove excess $[IrCl_6]^{2-}$ precursor solution. The electrodes were then dried at 80 °C overnight, followed by thermolysis at 500 °C with the desired heating rate.

Electrochemical setup

Electrochemical measurements were conducted using a three-electrode setup. The measurements were recorded with a Biologic SP50e potentiostat at room temperature in 0.5 M H_2SO_4 (Suprapur, Sigma-ALdrich) saturated with O_2 (N5.0 grade, BOC).

Electrical connections to the Ir-TiO_2-coated FTO electrodes were established using an electrode clip, with glassy carbon acting as the electrical contact. The bare FTO part of the electrode, where was not coated with TiO_2, was masked using 3M^{TM} electroplating tape 470 to ensure accurate calculation of the geometric surface area. To accelerate mass transport of the reaction reactant and the removal of the O_2 bubble produced during the oxygen evolution reaction (OER) from the working electrode, the working electrode was continuously bubbled with an O_2 stream.

A mercury/mercury sulfate (Hg/Hg_2SO_4 in satd. K_2SO_4, Supleco, Sigma-Aldrich) reference in a Luggin capillary was used as the reference electrode, placing around 5 mm away from the working electrode. The reference electrode was regularly calibrated using the reversible hydrogen electrode (RHE). This was carried out by performing a cyclic voltammetry measurement in the H_2-saturated cell using the same electrolyte in the potential range where she and the hydrogen oxidation reaction (HOR) are expected to occur. With a Pt sphere and a Pt mesh as WE and CE, respectively, the value for RHE was read by averaging the potential intercepts at zero current for HER and HOR. Such calibration can offset the voltage loss caused by liquid-junction potential, which is in the range of tens of mV and results from the difference in chemical composition between the reference electrode and the electrolyte solution in the cell [13].

A Pt mesh with a significantly larger electrochemically active surface area than the working electrode was employed. To minimise cross-contamination from the Pt at the working electrode, the counter electrode was placed in a fritted glass tube (Ace gas dispersion tube with a porous fritted glass tip, porosity 4-8 μm).

Cyclic voltammetry (CV) was used to characterise the OER activity and stability of the Ir-TiO_2 electrodes. Ten consecutive CVs were performed for each electrode between 1.3 and 2.1 V vs RHE at a scan rate of 10 mV s^{-1}. To extract the OER current density at a specific potential, the averaged current density from the anodic and the cathodic sweep was calculated to offset the capacitive current density, as recommended by Wei and coworkers as an alternative to steady-state chronoamperometry [6]. The obtained CVs were iR drop corrected using the high-frequency resistance (HFR) determined using potentiostatic electrochemical impedance spectroscopy (PEIS) between 100 kHz and 1 Hz with a voltage perturbation of 10 mV voltage perturbation. A typical HFR ranges between 12 to 13 *Omega*. The morphology of the Ir dispersion was characterised by HAADF-STEM by scratching the Ir-TiO_2 off the FTO glass. The images are shown in Figure 3.11.

X-ray absorption spectroscopy (XAS)

XAS measurements were performed at the B18 beamline of the Diamond Light Source. The Ir-TiO_2-1C and Ir-TiO_2-10C samples were prepared by heating the post-SEA, as-synthesised sample at 500 °C in N_2 using a heating rate of 1 °C min^{-1} and 10 °C min^{-1}, respectively. 8 mm sample pellets were prepared by mixing an appropriate amount of sample with cellulose (Avicel PH-101, Sigma-Aldrich), with the composition calculated using the XAFSmass software [14]. The spectra for the Ir reference samples were collected in transmission mode, while the Ir-TiO_2 samples were measured in fluorescence mode. Si(111) crystal monochromator coupled with Cr-coated collimating mirrors were used. For the fluorescence measurements, the 36-element Ge fluorescence detector was used. Data were analysed using the Larch software [15]. For the reference samples, including Ir metal (99.9% powder, Sigma-Aldrich), IrO_2 (99.9%, Sigma-Aldrich) and $H_2IrCl_6 \cdot xH_2O$ (99.9%, Sigma-Aldrich), the k^3-weighted Fourier transform was performed between $k = 3$ and 14 $Å^{-1}$ using a Hanning window.

The extended X-ray absorption fine structure (EXAFS) fit was performed between R = 1.0 and 4.2 Å. For the Ir-TiO_2 samples, the k^3-weighted Fourier transform was performed from $k = 3$ to 8.5 Å^{-1} using a Hanning window. The EXAFS fit was performed between R = 1.0 and 3.5 Å. The amplitude reduction factor (S_0^2) for fitting the for Ir-TiO_2 samples was obtained from fitting the rutile IrO_2 reference. The collection of the XAS data was performed in collaboration with Dr Donato Decarolis (Diamond Light Source).

High-angle annular dark field scanning transmission electron microscopy (HAADF-STEM)

HAADF-STEM measurements were performed using a JEOL ARM200F microscope at an accelerating voltage of 200 kV. A CL aperture of 20 μm, convergence semiangle of 14.38 mrad and the detector, beam current of 69 pA, and detector angle between 78 and 271 mrad were used. Samples were deposited on a Cu TEM grid and baked at 150 °C in a vacuum overnight before the measurements.

Scanning electron microscopy (SEM)

SEM measurements were performed using a high-resolution Merlin field-emission scanning electron microscope (Zeiss, Germany). A 3 kV accelerating voltage and a 100 pA beam current were used.

X-ray photoelectron spectroscopy (XPS)

XPS measurements were performed using a Physical Electronics (PHI) VersaProbe III instrument. An Al K-alpha (1486.8 eV) source at 25 W and a chamber vacuum below 10^{-7} Pascal was used. A pass energy of 55 eV was used for the measurements. All measurements were performed with the neutraliser turned off. 400 minutes of

measurement time were used to collect the Ir 4f spectra, while for the Ti 2p, 20 minutes were used. Data analysis was performed using CasaXPS software (Casa Software Ltd) [16]. Shirley backgrounds were used, and Gaussian-Lorentzian line shapes were selected for the peak fitting. Charge calibration was conducted by shifting the energy of Ti $2p_{3/2}$ to 458.6 eV.

References

[1] Dmitry Lebedev, Roman Ezhov, Javier Heras-Domingo, Aleix Comas-Vives, Nicolas Kaeffer, Marc Willinger, Xavier Solans-Monfort, Xing Huang, Yulia Pushkar, and Christophe Copéret. Atomically Dispersed Iridium on Indium Tin Oxide Efficiently Catalyzes Water Oxidation. *ACS Central Science*, 6(7):1189–1198, 7 2020.

[2] Jesse D. Benck, Blaise A. Pinaud, Yelena Gorlin, and Thomas F. Jaramillo. Substrate selection for fundamental studies of electrocatalysts and photoelectrodes: Inert potential windows in acidic, neutral, and basic electrolyte. *PLoS ONE*, 9(10), 10 2014.

[3] Francisco Fabregat-Santiago, Ivan Mora-Seró, Germà Garcia-Belmonte, and Juan Bisquert. Cyclic voltammetry studies of nanoporous semiconductors. Capacitive and reactive properties of nanocrystalline TiO2 electrodes in aqueous electrolyte. *Journal of Physical Chemistry B*, 107(3):758–768, 1 2003.

[4] Karin Rettenmaier, Gregor Alexander Zickler, Günther Josef Redhammer, Juan Antonio Anta, and Thomas Berger. Particle Consolidation and Electron Transport in Anatase TiO2 Nanocrystal Films. *ACS Applied Materials and Interfaces*, 11(43):39859–39874, 10 2019.

[5] Nataša Diklić, Adam H. Clark, Juan Herranz, Dino Aegerter, Justus S. Dier-

cks, Alexandra Beard, Viktoriia A. Saveleva, Piyush Chauhan, Maarten Nachtegaal, Thomas Huthwelker, Dmitry Lebedev, Paula Kayser, José Antonio Alonso, Christophe Copéret, and Thomas J. Schmidt. Surface Ir+5 Formation as a Universal Prerequisite for O2 Evolution on Ir Oxides. *ACS Catalysis*, 13(16):11069–11079, 8 2023.

[6] Chao Wei, Reshma R. Rao, Jiayu Peng, Botao Huang, Ifan E.L. Stephens, Marcel Risch, Zhichuan J. Xu, and Yang Shao-Horn. Recommended Practices and Benchmark Activity for Hydrogen and Oxygen Electrocatalysis in Water Splitting and Fuel Cells. *Advanced Materials*, 31(31):1806296, 2019.

[7] Marianne van der Merwe, Raul Garcia-Diez, Leopold Lahn, R. Enggar Wibowo, Johannes Frisch, Mihaela Gorgoi, Wanli Yang, Shigenori Ueda, Regan G. Wilks, Olga Kasian, and Marcus Bär. The Chemical and Electronic Properties of Stability-Enhanced, Mixed Ir-TiOx Oxygen Evolution Reaction Catalysts. *ACS Catalysis*, 13(23):15427–15438, 12 2023.

[8] Ailong Li, Shuang Kong, Kiyohiro Adachi, Hideshi Ooka, Kazuna Fushimi, Qike Jiang, Hironori Ofuchi, Satoru Hamamoto, Masaki Oura, Kotaro Higashi, Takuma Kaneko, Tomoya Uruga, Naomi Kawamura, Daisuke Hashizume, and Ryuhei Nakamura. Atomically dispersed hexavalent iridium oxide from MnO2 reduction for oxygen evolution catalysis. *Science*, 384(6696):666–670, 5 2024.

[9] Luu Manh Quynh, Nguyen Thi Tien, Pham Van Thanh, Nguyen Minh Hieu, Sai Cong Doanh, Nguyen Tran Thuat, Nguyen Viet Tuyen, Nguyen Hoang Luong, and Ngoc Lam Huong Hoang. Optical and electrical responses of magnetron-sputtered amorphous Nb-doped TiO2 thin films annealed at low temperature. *Physica B: Condensed Matter*, 532:200–203, 3 2018.

[10] Wenjie Sun, Xiaojuan Dong, Pingping Huang, Jia Shan, Lei Qi, and Jun Zhou.

Solvothermal synthesis of Nb-doped TiO2nanoparticles with enhanced sonodynamic effects for destroying tumors. *RSC Advances*, 11(58):36920–36927, 10 2021.

[11] Christopher Foo, Yiyang Li, Konstantin Lebedev, Tianyi Chen, Sarah Day, Chiu Tang, and Shik Chi Edman Tsang. Characterisation of oxygen defects and nitrogen impurities in TiO2 photocatalysts using variable-temperature X-ray powder diffraction. *Nature Communications*, 12(1), 12 2021.

[12] Dmitry Lebedev, Yuliana Pineda-Galvan, Yuki Tokimaru, Alexey Fedorov, Nicolas Kaeffer, Christophe Copéret, and Yulia Pushkar. The Key RuV=O Intermediate of Site-Isolated Mononuclear Water Oxidation Catalyst Detected by in Situ X-ray Absorption Spectroscopy. *Journal of the American Chemical Society*, 140(1):451–458, 1 2018.

[13] Allen J. Bard and L. R. Faulkner. *Electrochemical Methods: Fundamentals and Applications*, volume 2nd. 1995.

[14] K. Klementiev and R. Chernikov. XAFSmass: A program for calculating the optimal mass of XAFS samples. In *Journal of Physics: Conference Series*, volume 712. Institute of Physics Publishing, 2016.

[15] Matthew Newville. Larch: An analysis package for XAFS and related spectroscopies. In *Journal of Physics: Conference Series*, volume 430. Institute of Physics Publishing, 2013.

[16] N. Fairley. CasaXPS VAMAS Processing Software, 2010.

Chapter 6

Conclusions and future work

This work focuses on understanding the synthesis and structural-activity-stability relationship of atomically dispersed Ir on TiO_2 anatase for acidic OER. In Chapter 3, a synthesis methodology combining the strong electrostatic absorption (SEA) of $[IrCl_6]^{2-}$ with a thermolysis step in N_2 was demonstrated for the preparation of the atomically dispersed Ir on TiO_2 anatase. The agglomeration of Ir during synthesis was minimised by lowering the heating rate of the thermolysis. Specifically, using a heating rate of 1 °C min^{-1}, an atomically dispersed Ir (Ir_1)-rich sample was prepared, compared to Ir cluster (Ir_x)-rich sample prepared using a heating rate of 10 °C min^{-1}.

Chapter 4 focuses on further gaining insights into the synthesis mechanism. In this chapter, the results from the in-situ heating ADF-STEM experiments were discussed in detail, showing the investigation of the Ir agglomeration behaviour and mobility with increasing temperature on TiO_2. Combined with the temperature-dependent XAFS analysis of the evolution of the bonding environment and oxidation state of the Ir, it was concluded that the formation of the Ir-O bond at the first stage of thermal decomposition of $[IrCl_6]^{2-}$ at 300 °C reduced the mobility of Ir precursor before reaching the target synthesis temperature, therefore minimising Ir agglomeration TiO_2. The reason why the heating rate of the synthesis controls the agglomeration

of Ir was attributed to the balance between the acceleration of the Ir-O bond formation with a higher reaction temperature and the higher mobility of Ir at a higher temperature before the Ir-O bonds are formed.

Chapter 5 assessed the OER performance of the atomically dispersed Ir on TiO_2. Using the image analysis pipeline developed in this work combined with the HAADF-STEM characterisation at an extended length scale enabled by the use of the 2D nanosheet morphology of the TiO_2, statistically significant representations of the Ir dispersion were established for the Ir-TiO_2 samples synthesised. This analysis confirmed the sample prepared at the heating rate of 1 °C min^{-1} was indeed an Ir_1-rich sample, compared to Ir_x-rich sample prepared using a heating rate of 10 °C min^{-1}.

Further XAFS analysis showed that the Ir_1-rich sample has a 6-fold Ir-O bonding environment and an oxidation state of +4. The analysis for the Ir_x-rich sample showed that the Ir_x shared similar bonding environments and oxidation states with the Ir_1. This similarity in the chemical environment of the Ir species enabled a more fair comparison of the Ir use efficiency for the OER without a major complication due to their differences in chemical environments.

The Ir_1-rich sample showed a higher mass activity than the Ir_x-rich sample, validating the idea of increasing atomic dispersion of Ir to increase the Ir use. However, both catalysts produced low current densities at the low overpotential regions, which might hinder their application as an alternative catalyst in PEM water electrolysers. This poor activity was primarily due to the ultralow total Ir loadings on the electrodes, which were resulted from the thin TiO_2 coating used to limit the ohmic resistance of the poorly conducting TiO_2 support. Furthermore, the stabilities of both of these catalysts were low, with their OER current densities dropping significantly within 10 CV cycles in the OER region. This was attributed to significant agglomeration of the Ir_1 after the OER test, as evidenced by the post-OER HAADF-STEM analysis.

The synthesis of nitrogen-doped TiO_2 was lastly explored, attempting to increase

the electronic conductivity of the TiO_2 support for an overall enhancement in the OER activity. However, it was realised that these nitrogen-doped TiO_2 were not compatible with the synthesis method developed in this study, as the 500 °C thermolysis readily sintered the nitrogen-doped TiO_2 and removed the dopants.

To discuss the intrinsic OER activity of atomically dispersed Ir for the acidic OER, systematic theoretical investigations of the overpotential for atomically dispersed Ir on various metal oxide supports are required. The theoretical overpotential represents the minimum thermodynamic barrier required to complete the OER cycle and can be calculated from first principles using the reaction mechanism proposed by Nørskov and coworkers [1]. However, such studies are currently lacking in the literature. In particular, the behaviour of Ir on TiO_2 explored in this thesis remains to be explored and requires future research.

For the alkaline OER, Zheng and coworkers reported a theoretical overpotential of 0.2 eV for atomically dispersed Ir on NiFe oxyhydroxide, which is significantly lower than the 0.6 eV observed for the IrO_2 surface [2]. Their findings suggest that atomically dispersed Ir not only maximises the utilisation of the Ir active surface area but also benefits from the enhanced intrinsic activity of the dispersed Ir species, leading to improved overall OER performance. Whether these conclusions extend to the acidic OER remains a topic for further investigation.

Overall, this thesis work provides new insights into the synthesis and the electrochemical properties of atomically dispersed Ir on TiO_2 anatase for the acidic OER. Although the OER activity of this atomically dispersed Ir on TiO_2 electrocatalyst may not be suitable for practical applications in the PEM water electrolysers due to limitations of the TiO_2 support, the insights into Ir agglomeration mechanism during synthesis gained from this study offer a critical ground for the synthesis of atomically dispersed Ir electrocatalysts onto a more suitable support for the OER. In addition, the synthesis controls over the Ir dispersion, which enables the preparation of atomi-

cally dispersed Ir electrocatalysts and oxidised Ir clusters on the same support, lays the foundation for future OER mechanistic studies comparing how OER is catalysed on these two different Ir dispersions. These OER mechanistic studies will further help researchers understand the complex acidic OER mechanism.

References

[1] J. Rossmeisl, Z. W. Qu, H. Zhu, G. J. Kroes, and J. K. Nørskov. Electrolysis of water on oxide surfaces. *Journal of Electroanalytical Chemistry*, 607(1-2):83–89, 9 2007.

[2] Xueli Zheng, Jing Tang, Alessandro Gallo, Jose A Garrido Torres, Xiaoyun Yu, Constantine J Athanitis, Emily May Been, Peter Ercius, Haiyan Mao, Sirine C Fakra, Chengyu Song, Ryan C Davis, Jeffrey A Reimer, John Vinson, Michal Bajdich, and Yi Cui. Origin of enhanced water oxidation activity in an iridium single atom anchored on NiFe oxyhydroxide catalyst. *Proceedings of the National Academy of Sciences*, 118(36):e2101817118, 9 2021.

Appendix

Additional HAADF-STEM images for the Ir-TiO_2 samples

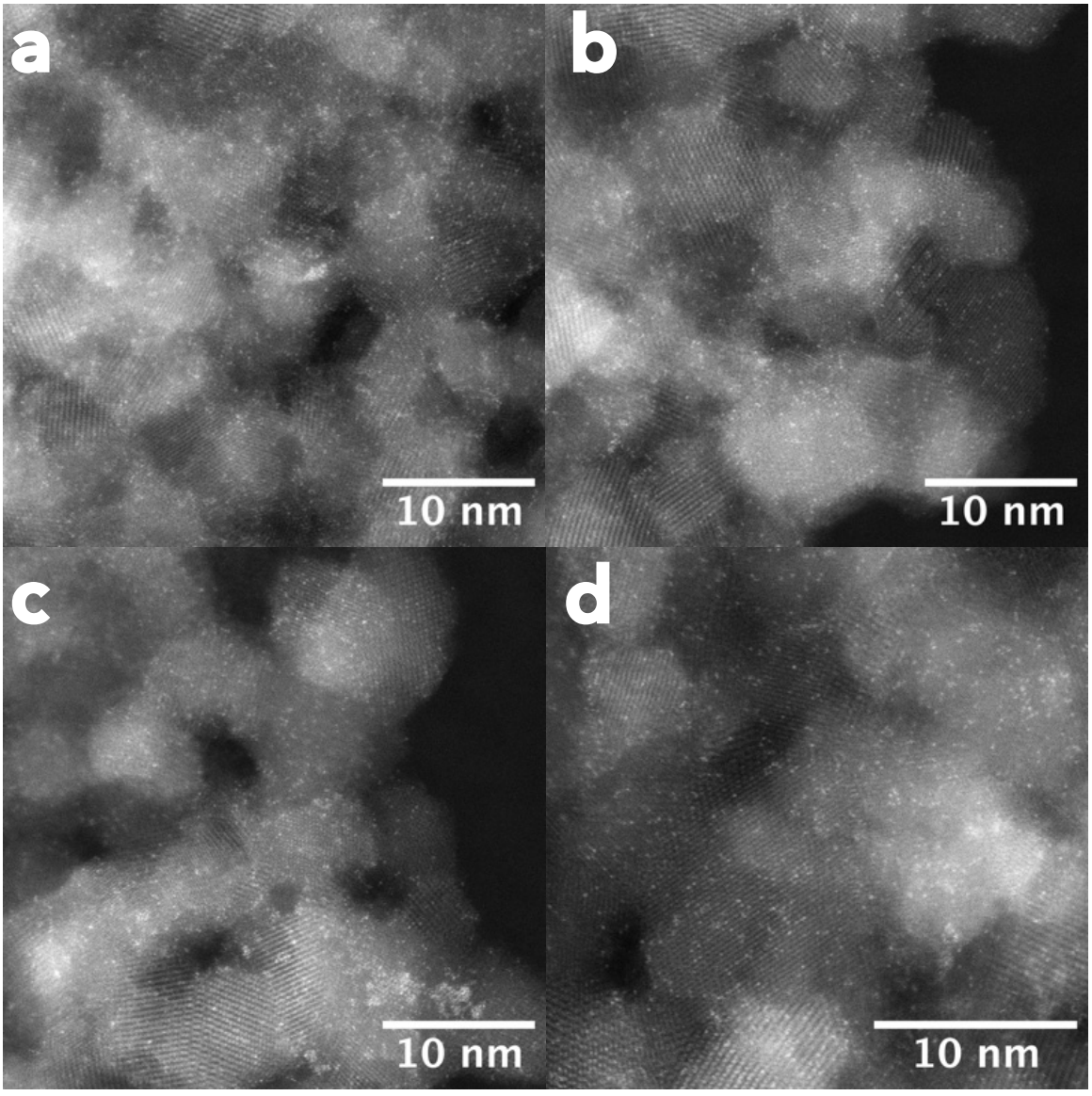


Figure 1: HAADF-STEM images of Ir-TiO_2-1C.

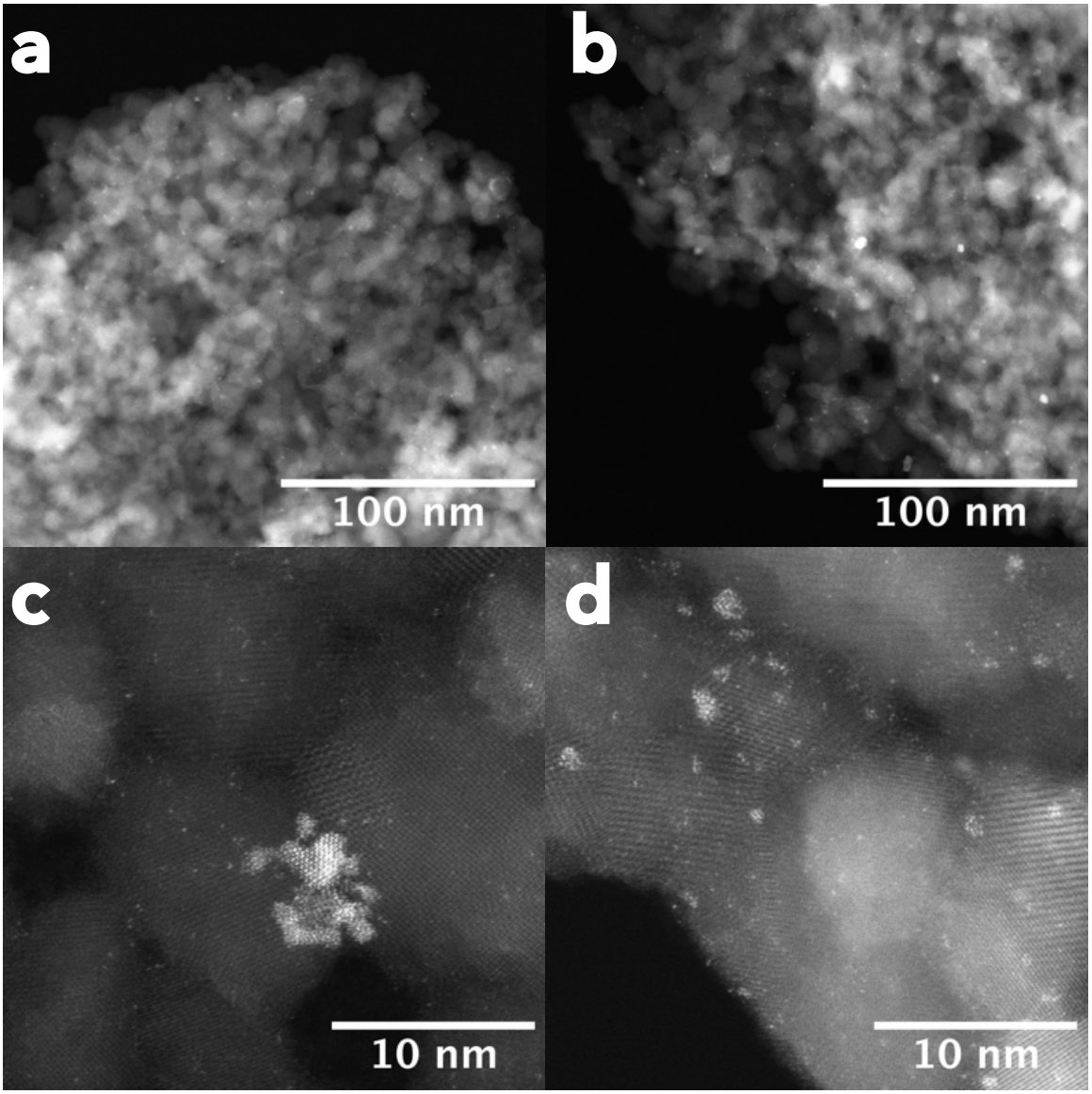


Figure 2: HAADF-STEM images of Ir-TiO_2-10C.

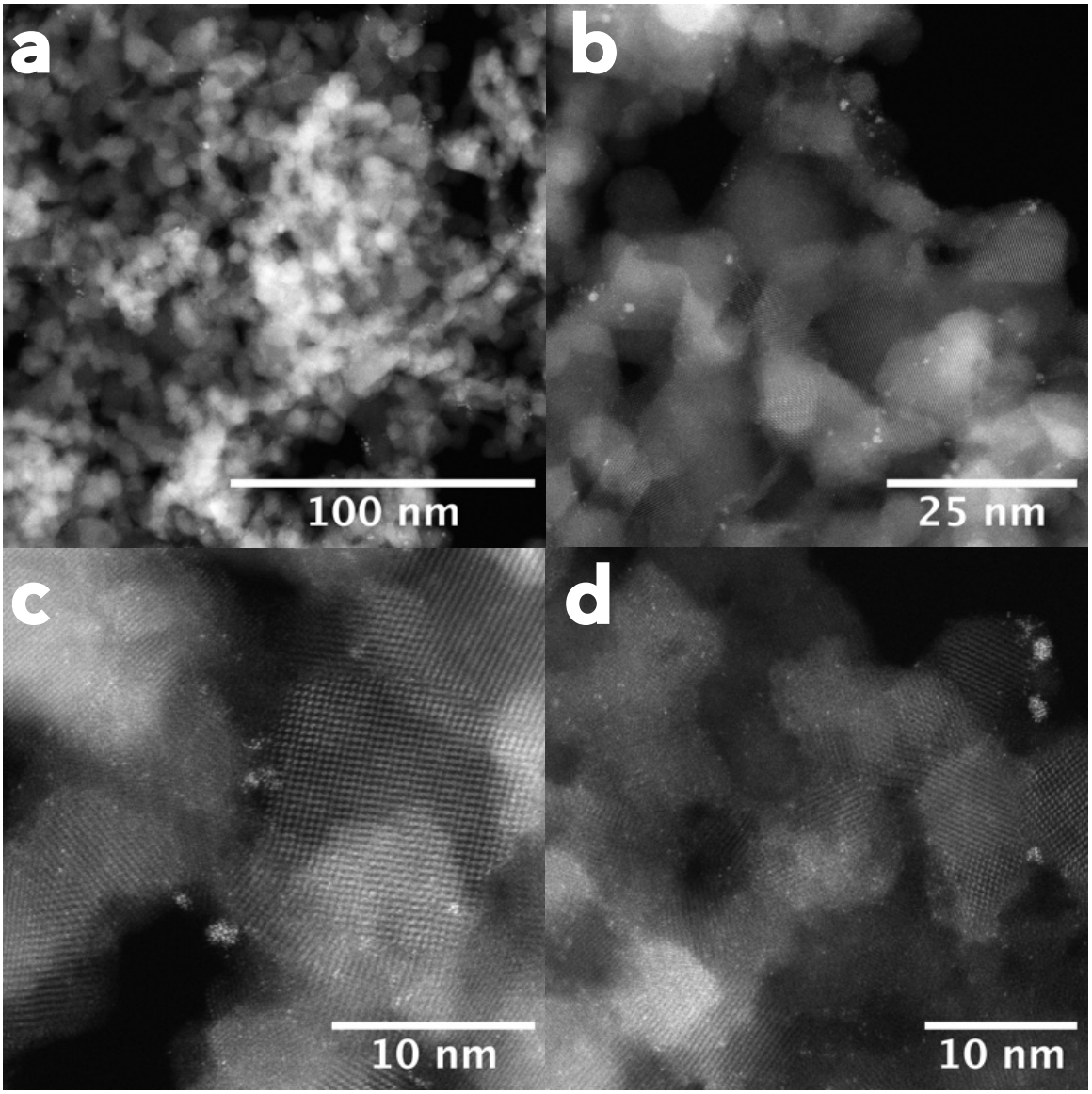


Figure 3: HAADF-STEM images of Ir-TiO_2-flash.

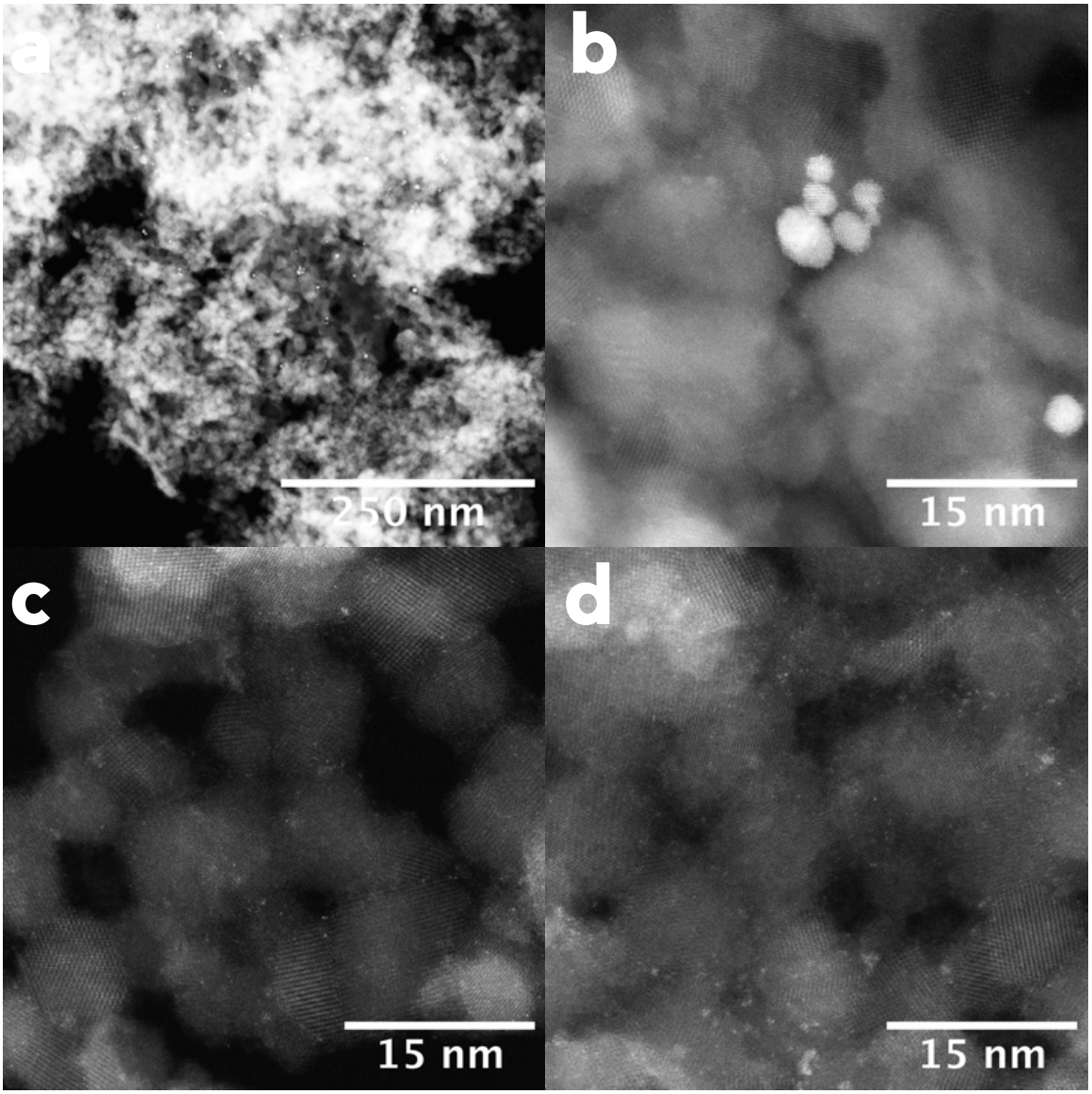


Figure 4: HAADF-STEM images of post-OER Ir-TiO_2-1C.

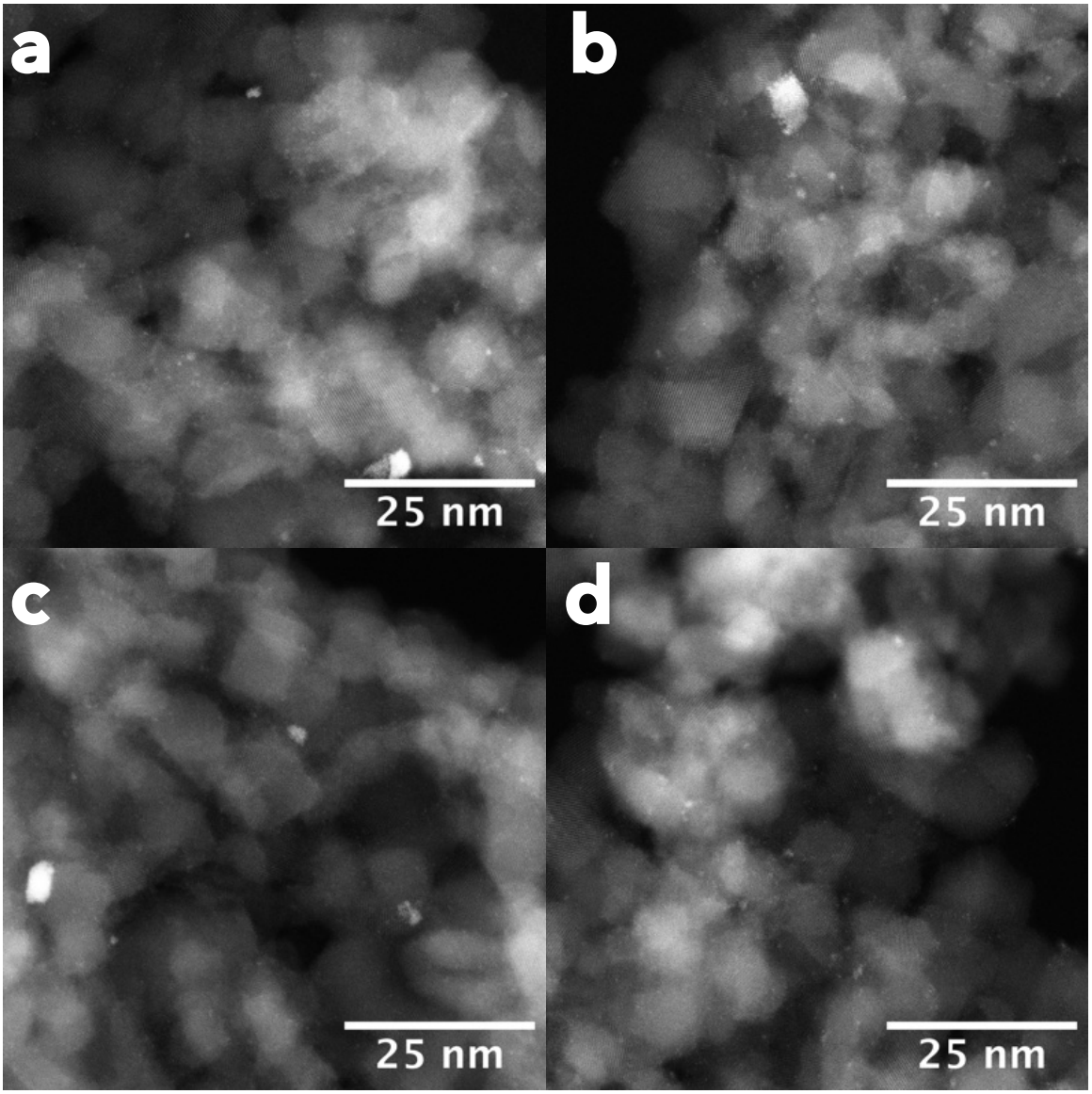


Figure 5: HAADF-STEM images of post-OER Ir-TiO_2-10C.

Implication of W impurity in the TiO_2 nanosheets

Signals associated with tungsten L_2 absorption are observed from the Ir 4f XAFS spectra for all Ir-TiO_2 samples [1], as shown in Appendix Figure 6 using the Ir-TiO_2-1C sample as an example. This W impurity is likely from the rGO powder, as the detailed analysis of the rGO surface using HAADF-STEM shows traces of high-contrast atomically dispersed species and very occasionally clusters on the parts of the as-received rGO surface (Appendix Figure 7a and b). When the rGO was combusted during the heat treatment, the W was suspected to be transferred and sintered with the TiO_2 nanosheets. The implications of this W impurity for the data analysis are discussed in the following sections. 11544.0

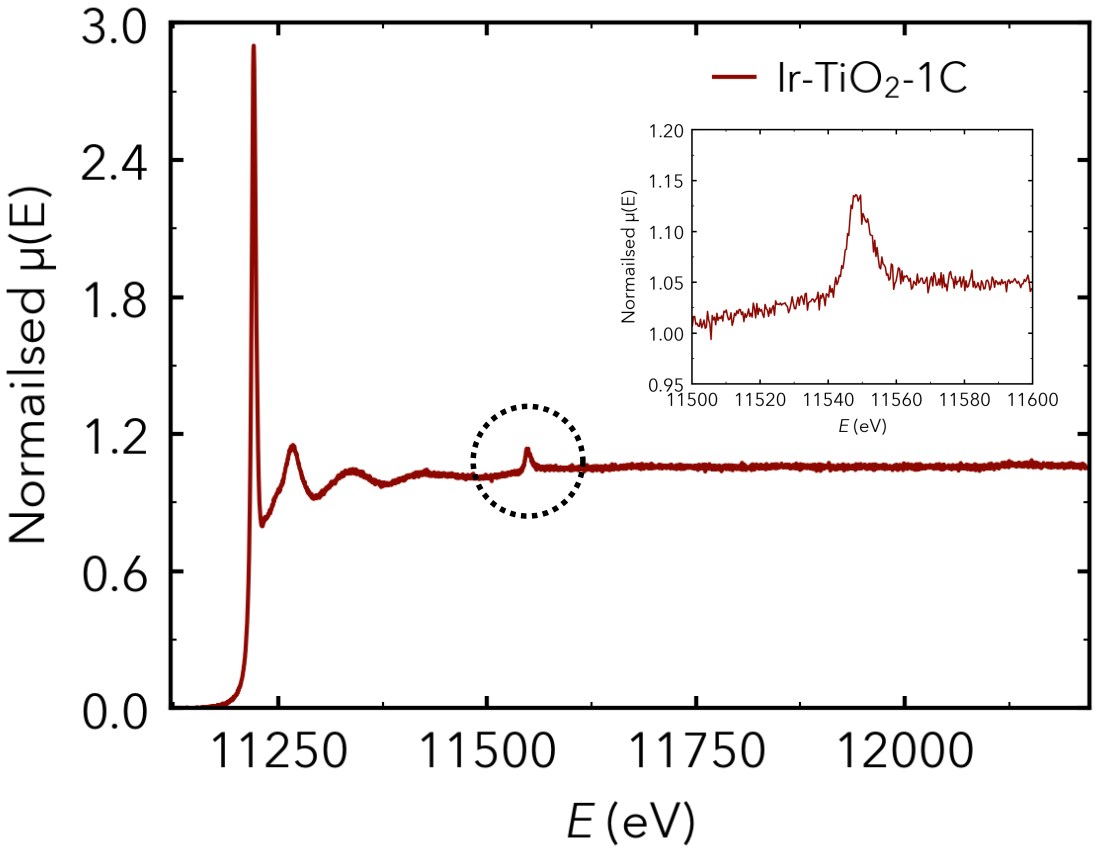


Figure 6: Experimental EXAFS spectrum of the Ir-TiO_2-1C sample. The black circle and the inset highlight the signal between 11540 and 11560 eV, which corresponds to the W L_2 edge [1].

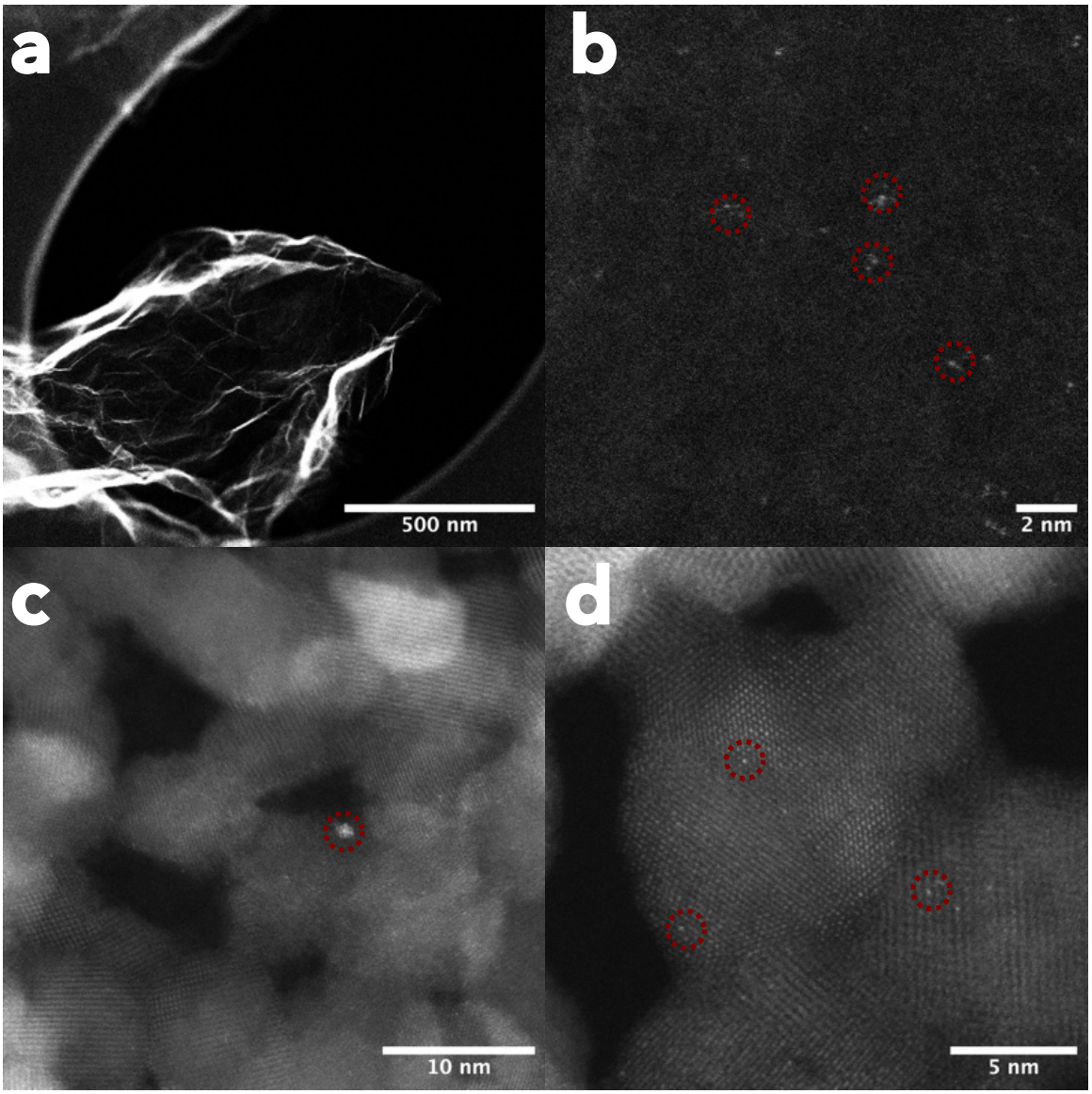


Figure 7: HAADF-STEM image of as-received rGO at (a) low magnification and (b) high magnification. (c) and (d) HAADF-STEM images of the TiO_2 nanosheets. The red circles highlight the high-contrast atomically dispersed species and clusters, which can be attributed to the presence of W impurity.

Range of EXAFS fitting

Since an absorption signal attributed to W occurs approximately at 9 $Å^{-1}$ above the Ir L_3 absorption edge, the fitting of the EXAFS for all the Ir samples (80 °C, 150 °C, 300 °C and 500 °C) are carried out before the sharp rise in signal around 9 $Å^{-1}$ due to the presence of W to avoid convolution between the W bonding environment with

that of Ir (Appendix Figure 8a-d). Specifically, the fitting are carried out between k = 3 to 8.5 Å^{-1} masked with a Hanning window of δk = 0.5 Å^{-1}. The EXAFS fits are performed over a R range between 1.0 and 3.5 Å.

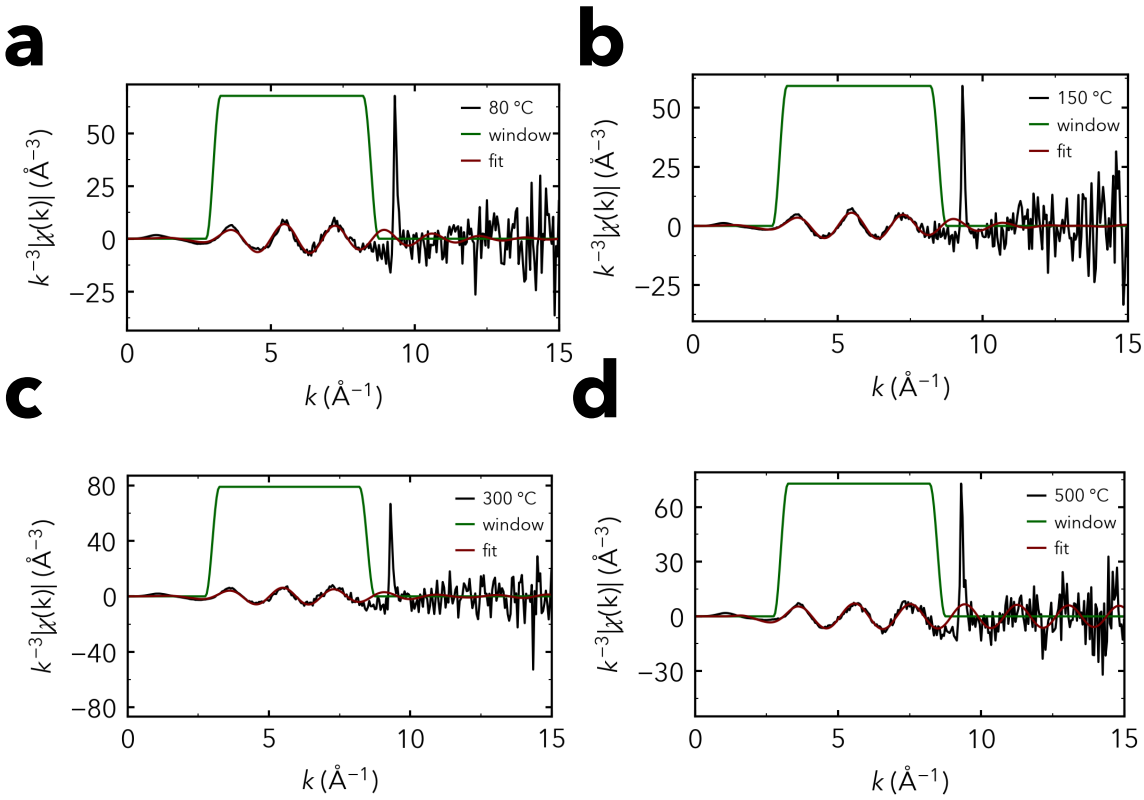


Figure 8: k^3-weighted experimental EXAFS data (black), fit (red) and masking window (green) for the (a) 80 °C, (b) 150 °C, (c) 300 °C and (d) 500 °C sample.

The S_0^2 for the fitting is extracted from the fitting of the rutile IrO_2 reference. For consistency, S_0^2 should ideally be obtained using the same fitting range as for the Ir-TiO_2 samples. However, the constrained k-range limits the resolution of the peaks in the R space, making the fitting of multiple scattering paths highly uncertain, resulting a S_0^2 value of 0.80 ± 0.14 with high uncertainty in the σ^2 and ΔE_0 for the Ir-Ir scattering path, as shown in Appendix Table 1.

In contrast, the fitting of the IrO_2 reference conducted with the k = 3 to 14 Å^{-1} with a R range between 1.0 and 4.2 Å using 5 scattering paths, masked with a Hanning window of δk = 3 Å^{-1} shows smaller uncertainty, as shown previously in Chapter 4

Table 4.1. Therefore, I utilise $S_0^2 = 0.83$ from this fitting and perform the fitting of the Ir-TiO_2 samples. The spectra fits using these above two different fitting ranges for the IrO_2 are shown in the Appendix Figure 9.

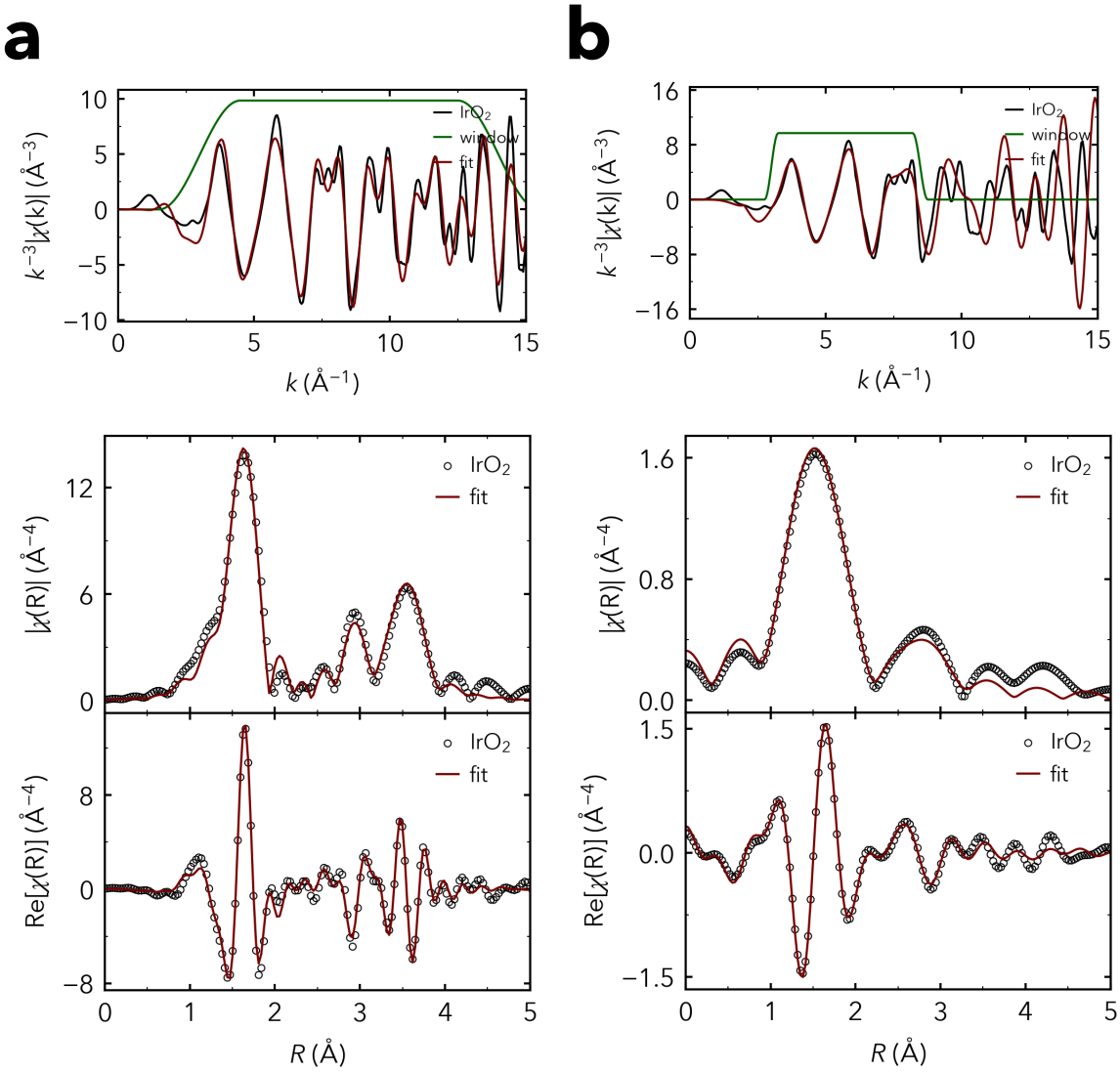


Figure 9: k^3-weighted experimental data (black), fit (red) and masking window (green) for the IrO_2 reference. (a) Fitting conducted with k = 3 to 14 Å^{-1} masked with a Hanning window of δk = 3 Å^{-1}. The EXAFS fit was performed over a R range between 1.0 and 4.2 Å, utilising the first 5 single scattering paths from a rutile IrO_2 reference structure [2]. (b) Fitting conducted with k = 3 to 8.5 Å^{-1} masked with a Hanning window of δk = 0.5 Å^{-1}. The EXAFS fit was performed over a R range between 1.0 and 3.5 Å, utilising the first 3 single scattering paths from a rutile IrO_2 reference structure [2].

Table 1: EXAFS fitting results for IrO_2 with $k = 3$ to 8.5 Å^{-1} masked with a Hanning window of $\delta k = 0.5$ Å^{-1}. The EXAFS fit was performed over a R range between 1.0 and 3.5 Å, utilising the first 3 single scattering path from a rutile IrO_2 reference structure [2].

Paths	**N**	**R (Å)**	σ^2 **(Å^2)**	ΔE_0 **(eV)**	S_0^2	**R-factor**
Ir-O.1	6	1.96 (0.02)	0.0015 (0.0022)	15 (3)		
Ir-Ir.1	2	3.02 (0.23)	1.783e-11 (0.0050)	2 (36)	0.80 (0.14)	0.005
Ir-O.2	4	3.45 (0.06)	0.0392 (0.0649)	15 (3)		

Ir mobility analysis from the in-situ heating ADF-STEM experiments

Since W and Ir have similar atomic numbers, they are indistinguishable from each other in a HAADF-STEM image, provided they are on the same Z-plane. Although the presence of W can convolute with the analysis of the Ir mobility, the areal density of the W is only one-tenth of the Ir: an Ir_1 areal density of 0.06 ± 0.003 nm^{-2} is calculated in the in-situ heating ADF-STEM (see Chapter 4), whereas the W_1 areal density is estimated to be at 0.006 ± 0.001 nm^{-2}, analysed from the ex-situ HAADF-STEM images shown in Appendix Figure 7c and d. Since the W is the minority species in the analysis, their existence should not alter the analysis and interpretation discussed in the main text.

Enhancement of the electronic conductivity of TiO_2

Should the W is sintered and submerged into the bulk of the TiO_2 nanosheets, it effectively serves as a dopant that introduces defects into the TiO_2 lattice and can increase the electronic conductivity of the TiO_2. However, this is unlikely to have a significant effect on the TiO_2 due to the low total loading of W. The Ir loading is 0.18 wt% and the W is x times lower, this much lower than the usually used heavy doping of W in the range of tens of atomic percentage of the TiO_2 in literature [3].

Synergetic effect between Ir and W for the OER

Synergetic effects between Ir and W have been reported previously to show enhanced OER activity, where parts of Ir in a IrO_2 are cationically displaced by W [3]. Nevertheless, this effect only becomes pronounced when the Ir and W are sufficiently close to one another (ideally within the first coordination shell of the Ir and W) [4]. For the samples shown in this study, this effect is expected to be insignificant due to the low Ir and W loadings, which are likely to lead to large distances between the Ir and W from one another.

References

[1] Upul Jayarathne, Perumalreddy Chandrasekaran, Angelique F. Greene, Joel T. Mague, Serena Debeer, Kyle M. Lancaster, Stephen Sproules, and James P. Donahue. X-ray absorption spectroscopy systematics at the tungsten L-edge. *Inorganic Chemistry*, 53(16):8230–8241, 8 2014.

[2] A A Bolzan, C Fong, B J Kennedy, and C J Howard. Structural Studies of Rutile-Type Metal Dioxides. *Acta Crystallographica Section B*, 53(3):373–380, 6 1997.

[3] Jiajian Gao, Xiang Huang, Weizheng Cai, Qilun Wang, Chunmiao Jia, and Bin Liu. Rational Design of an Iridium-Tungsten Composite with an Iridium-Rich Surface for Acidic Water Oxidation. *ACS Applied Materials and Interfaces*, 12(23):25991–26001, 2020.

[4] Dongxi Cai, Jie Zhang, Zhe Kong, and Zesheng Li. Synergistic Effect of Single-Atom Catalysts and Vacancies of Support for Versatile Catalytic Applications, 9 2024.